THE UNIVERSITY *of* EDINBURGH

SERS Substrates for Sensing in Pathology and Physiology

Holly Fleming

Doctor of Philosophy with Integrated Study in

Optical Medical Imaging with Healthcare Innovation and Entrepreneurship

The University of Edinburgh and The University of Strathclyde

THE UNIVERSITY *of* EDINBURGH

University of Strathclyde Glasgow

2019

Declaration of Authorship

This thesis has been composed by the author and has not been previously submitted for examination which has led to the award of a degree. The work, data, and interpretation presented here are those of the author unless there was significant collaborative contribution made, in which case it has been clearly recognised. Where published work has been consulted the source has been clearly cited.

Parts of the work presented herein have been published as:

- K. Ehrlich, A. Kufcsák, S. McAughtrie, H. Fleming, N. Krstajić, C. J. Campbell, R. K. Henderson, K. Dhaliwal, R. R. Thomson, and M. G. Tanner, ***Optics Express***, 2017, **25**, 25: 30976-30986
- K. Ehrlich, H. Fleming, S. McAughtrie, A. Kufcsák, N. Krstajić, C. J. Campbell, R. K. Henderson, K. Dhaliwal, R. R. Thomson, and M. G. Tanner, ***Proc. SPIE 10685, Biophotonics: Photonic Solutions for Better Health Care VI,*** 2018, **106850Q**
- H. Fleming, S. McAughtrie, B. Mills, M. G. Tanner, A. Marks, C. J. Campbell, ***Analyst***, 2018, **143**, 5918-5925

Signed:

Date: 30th March 2020

Acknowledgements

I would like to thank my supervisors Dr Colin Campbell and Professor Mark Bradley who gave me the opportunity to work on this project and have provided advice, support and encouragement throughout my PhD, for this I am incredibly grateful.

I would like to thank members of Proteus, in particular Sarah, Beth, Mike, Katjana, Fuad, Sheelagh, and Emma, for their support. Above all Sarah, for which without her support my experience would likely have been much different (and definitely more PG).

To all the past and present members of the Campbell group and Bradley group who have provided support, encouragement and much entertainment, thank you.

To everyone in Optima CDT who have provided support, encouragement and friendship, without which my experience would have not gone as nearly as smoothly. Special thanks go to Jean O'Donoghue, who has been a source of invaluable advice and encouragement throughout my PhD, and to Sam Brown, who has never failed to help. Katie and Lulu, you have provided great company, motivation, and excellent cooking, thank you both. Special thanks to Cat, Joe, Alisia, Rachael, and Sam, I could not have picked a better group to go through this PhD with. You have been the source of many great times.

Thanks to the University of Edinburgh for funding my research and providing many opportunities to develop further.

Finally, and most importantly, I would like to thank my family. Mum, Dad, Mel, Elizabeth and Louise, you have all helped enormously through lots of encouragement (and much needed distractions). And to Eddy, you have provided endless support throughout my PhD, without which this would have been impossible. Thank you.

Abstract

Monitoring physiological parameters such as pH at the site of a disease are important in determining the health status in patients.

Current approaches are based on the analysis of arterial blood to measure systemic blood pH along with other parameters such as PO_2 and PCO_2, to allow assessment of gaseous exchange and ventilation efficiency. There has been a drive to develop improved sensors capable of continuous and dynamic monitoring of these aspects. Optical sensing devices have gained popularity as they can be designed to incorporate inexpensive optical fibres and miniaturised and mass-produced detectors and LED-based light sources.

In addition to monitoring pH in a clinical situation, the development of physiological sensing tools for use at a cellular level has been critical in being able to non-invasively assess cellular response to a host of insults be it drug treatment or other cellular modulation strategies. The move towards three-dimensional (3D) cell culture has become increasingly attractive as a mimic of the 3D architecture and gradients found *in vivo*. The development of spatially selective sensors capable of measuring these physiological features could provide a tool in understanding cell-drug responses.

In this thesis, multiple approaches were developed to enable SERS pH sensing based on both an optical fibre as well macroscopically entrapped SERS sensors applied as a means of observing extracellular pH within a 3D cell culture system. This included the use of pH responsive reporter molecules on nanoparticles (Chapter 2), their entrapment within macro-scale supports such as polymer beads and (Chapter 3), and paper (Chapter 4).

Lay Abstract

All life exists in a delicately balanced state. There are trillions of chemical reactions happen simultaneously in the body, driving the processes that keep a human body 'alive'. Specific organs and tissues work together to control and maintain this balance which ensures that the body continues to function normally. For example, the lungs are responsible for gas exchange to and from the blood, and in doing so keeps the oxygen concentration and blood pH levels constant. pH is a measure of how acidic or alkaline a solution is, and by measuring physiological parameters such as blood pH or the pH within the lungs, the health status of a patient can be monitored. On a much smaller scale, looking at pH on a cellular level can indicate if the cells are functioning correctly.

There has been a drive to develop improved sensors capable of continuous monitoring of these parameters. Optical sensing devices have gained popularity as they can be designed to incorporate inexpensive optical fibres and miniaturised and mass-produced detectors and LED-based light sources.

In this thesis, a technique called surface enhanced Raman scattering (SERS) is used to measure pH. Raman scattering detects molecular vibrations and the addition of gold nanoparticles boosts the vibration signals. Molecules sensitive to pH are bound to gold nanoparticles and the nanoparticles were attached to the end of an optical fibre, using either a glassy-like glue, 3D polymer beads, or filter paper.

In addition to measuring pH through an optical fibre using SERS, it was used to measure pH on a cellular level. Multicellular tumour spheroids (MTS) are small bunches of cells that mimics the environment of tissue much better than typical cell cultures which are grown in a 2D layer. Here, SERS was used to monitor the pH gradients between the central and outer regions of the MTS before and after the addition of a drug. The development of these spatially selective sensors offers a means to understanding cell-drug responses.

Contents

List of Figures

Abbreviations

μL	Microlitre
2D	2-Dimensional
2-MPY	2-Mercaptopyridine
3D	3-Dimensional
4-ATP	4-Aminothiophenol
a.u.	Arbitrary units
ANOVA	Analysis of variance
AUC	Area under curve
AuNP	Gold nanoparticles
CCD	Charge coupled device
CFU	Colony forming units
CLSM	Confocal laser scanning microscopy
cm^{-1}	Raman shift
CMOS	Complementary metal-oxide-semiconductor
DC	Dark counts
DCM	Dichloromethane
dH_2O	Deionised water
DIPEA	N,N-Diisopropylethylamine
DLS	Dynamic light scattering
DM	Dichroic mirror

DMEM	Dulbecco's modified Eagle’s medium
DMF	Dimethylformamide
DMSO	Dimethyl sulfoxide
E. coli	*Escherichia coli*
ECM	Extracellular matrix
EDTA	Ethylenediaminetetraacetic acid
EM	Extracellular matrix
eq	Equivalents
EtOH	Ethanol
FCS	Foetal calf serum
HSPyU	Dipyrrolidino(N-succinimidyloxy)carbenium hexafluorophosphate
ICP-MS	Inductively coupled plasma mass spectrometry
ICP-OES	Inductively coupled plasma optical emission spectrometry
LB	Lysogeny broth
ln	Natural log
LOD	Limit of detection
MBA	4-Mercaptobenzoic acid
MeOH	Methanol
min	Minute
MMF	Multimode fibre
MM-MCF	Multimode multicore fibre
MPY	4-Mercaptopyridine

MTS	Multicellular tumour spheroids
MTT	3-(4,5-dimethylthiazol-2-yl)-2,5-diphenyltetrazolium bromide
mW	Milliwatt
MW	Molecular weight
NA	Numerical aperture
NIR	Near infrared
NQ	1,8-diaza-4,5-dithian-1,8-di(2-chloro-[1,4]-napthoquinone-3-yl)octane
Ø	Diameter
P. aeruginosa	*Psuedomonas aeruginosa*
PBS	Phosphate buffered solution
PDMS	Polydimethylsiloxane
PEG	Polyethylene glycol
pH	Potential of hydrogen (measure of acidity)
PLL	Poly-L-Lysine
ROS	Reactive oxygen species
rpm	Revolutions per minute
SEM	Scanning electron microscopy
SERRS	Surface enhanced resonance Raman spectroscopy
SERS	Surface enhanced Raman spectroscopy
SESORS	Surface enhanced spatially offset Raman spectroscopy
SF	Serum free
SORS	Spatially offset Raman spectroscopy

SPAD	Single photon avalanche diode
STS	Staurosporine
TCSPC	Time correlated single photon counting
TEM	Transmission electron microscopy
TG	TentaGel® beads
TMOS	Tetramethyl orthosilicate
UV	Ultraviolet
λ	Wavelength
RNA	Ribonucleic acid
DNA	Deoxyribonucleic acid
IR	Infrared
CAIX	Carbonic anhydrase IX

1. Introduction

1.1 The Role and Control of pH in Biological Systems

In the early 1900's, Lawrence Henderson studied blood and the respiratory function. At the time it was known that blood was able to resist changes in pH, though the relationship between buffering capacity and the hydrogen ion concentration had not yet been realised. It was he who put forward an equation linking the composition of a buffer and $[H^+]$ (**equation (1.1)**).[1]

$$[\mathrm{H}^+] = K_a \frac{[\mathrm{acid}]}{[salt]} \quad (1.1)$$

It was not until 1916, that Karl Hasselbach merged Henderson's formula with Sørensons pH scale to express a formula now known as the Henderson-Hasselbach equation (**equation (1.2)**). Over physiological ranges, pH can be calculated using the Henderson-Hasselbach equation where K_a is the dissociation constant of the weak acid, pK_a = -log K_a, and [HA] and $[A^-]$ are the molarities of the weak acid and its conjugate base.[1] **Equation (1.3)** is the dissociation equilibrium of the weak acid to the conjugate base of the acid (A^-) and hydrogen ions (H^+).

$$pH = pK_a + log \frac{[A^-]}{[HA]} \quad (1.2)$$

$$HA \rightleftharpoons A^- + H^+ \quad (1.3)$$

Both intracellular (pH_i) and extracellular pH (pH_e) are tightly regulated, any slight deviation from the norm (centred around pH 7.4) can result in the widespread disorder of cell function.[2] Intracellular pH (pH_i) regulation is critical for most cellular processes including cell volume regulation, vesicle trafficking, cellular metabolism, cell membrane polarity, muscular contraction, and cytoskeletal interactions, to name but a few.[3] Extracellular pH (pH_e) is known to affect ion transport processes, and is a key biomarker of diseases such as breast and liver cancers.[4,5]

Due to the importance of pH regulation there exist several large scale mechanisms to prevent pH deviation, each operating on different timescales; physiological buffers offer a swift and localised pH correction, the respiratory system can correct on the medium-term (minutes), while renal acid-base control occurs on a much longer time-frame (days).[2]

1.1.1 Respiratory System and pH

A recent analysis of deaths relating to respiratory illnesses has shown that the UK has the highest proportion of deaths among the EU-28 average, at 14.1% compared to 8.5%.[6,7] These deaths result from a variety of conditions such as pneumonia, chronic obstructive pulmonary disease, and asthma.[7] Improving health through a better understanding of the fundamental disease processes would be of great value in the drive to improving the capability of diagnosis and treatment.

The respiratory system's main purpose is gas exchange, allowing the intake of oxygen (O_2) and removal of carbon dioxide (CO_2) to and from the blood (**Figure 1.1**) This process occurs within the small air sacs known as alveoli and the surrounding microvasculature. There are millions of these alveoli within the lung, providing a large surface area for gas exchange to occur. Through diffusion, the O_2 can pass

through from the alveolus, where the O_2 concentration is high, to the deoxygenated blood, which has a lower O_2 concentration. The reverse occurs for CO_2, where it passes from the blood to the lungs to be expelled. The walls of the alveolus and capillary are one cell thick allowing for rapid transport of the gases.

The mechanisms employed by the body to correct the pH imbalance include increased ventilation in an attempt to reduce the formation and expel excess CO_2, often resulting in the blood pH returning to normal within minutes. The kidneys can also compensate for acidosis, through excretion of excess acid. [2]

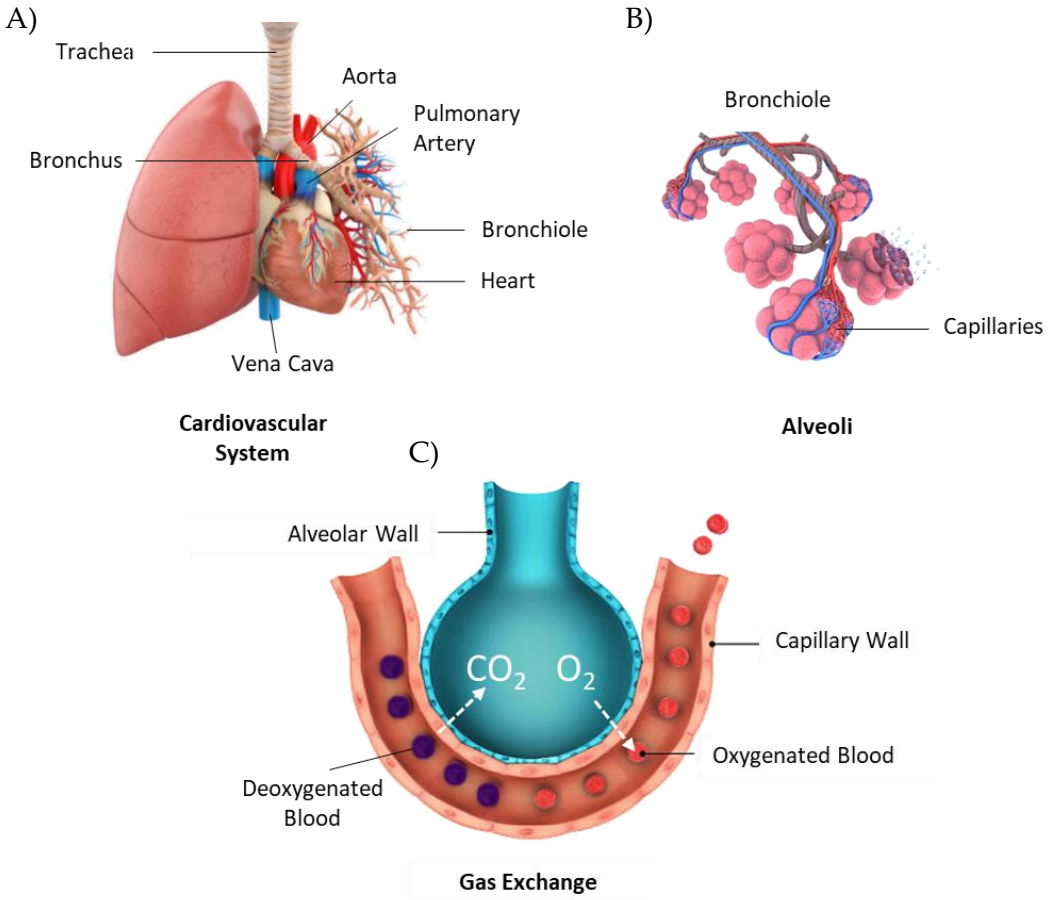

Figure 1.1 Cardiovascular system delivering O_2 to tissues. A) Cardiovascular system comprising the lungs, heart, and blood vessels. Deoxygenated blood is delivered from the body into the heart and pumped to the lungs *via* the pulmonary artery. Gas exchange occurs and oxygenated blood is delivered back to the heart to be pumped round the body. B) Alveoli which are situated at the ends of the bronchiole are covered in capillaries. C) Illustration of gas exchange between an alveolus and capillary. Images retrieved and adapted from istockphoto.com

If the ability of the lungs to carry out efficient gas exchange is disturbed, the outcome is that an insufficient amount of O_2 will reach the blood, in combination with the accumulation of CO_2. The build-up of CO_2 can cause acidosis, where the pH of the blood falls below pH 7.35.[2]

In healthy lungs, the alveoli should be sterile compartments, devoid of any infiltrating bodies such as inflammatory cells and pathogens. However, diseases such as pneumonia result in immune cells invading into the alveoli. These cells employ an assortment of killing mechanisms to target pathogens, including the secretion of oxidative and proteolytic proteins. The microbicidal mechanisms do not only destroy pathogens, but are also capable of disrupting the delicate balance of the alveoli and causing damage to host tissue.[8]

Studies conducted by Vukovac et al. have shown that pH can be indicative of the local inflammatory burden in patients suffering from the acute exacerbation of COPD (AECOPD), finding the pH of the lung to be higher than that in stable COPD patients.[9,10] Notably, *in situ* pH measurements were conducted using pH indicator test strips, placed onto a region of interest. While a simple process, there are limitations to using these test strips: the test strips are unable to offer dynamic pH sensing and are sent through the working channel of the bronchoscope individually, increasing the procedural time significantly; while the quantification of the strips relies on a colorimetric interpretation by eye, therefore introducing sources of error.[11]

A thin (100 μm) mucus gel-aqueous sol complex lines the surface of the airways in the lungs, known as the airway surface liquid (ASL). In the alveoli, it is alveolar subphase fluid (AVSF) with a pulmonary surfactant that lines the surfaces.[12] Compared to the pH of blood (pH 7.35-7.45), the pH of the ASL is acidic, having been measured as pH 6.6 *in vivo* in healthy humans using an electrode based pH meter, that was capable of being deployed through a bronchoscope.[8,12,13] In patients with a pneumonia infection, the pH of the bronchi was found to be significantly lower than that of healthy patients, at around pH 6.5 compared to pH 6.7, respectively.

While the environmental pH may play a role in the innate defence against pathogens, the lowering of the pH during infection can encourage bacterial growth and promote resistance by decreasing the effectiveness of some antimicrobials, particularly aminoglycosides, a class of antimicrobials used to treat a range of respiratory infections, including tuberculosis.[13–15] The ability to monitor pH in the alveolar regions, specifically the AVSF, could offer a key biomarker of the lungs' innate defence while also allowing clinicians to select optimal therapies.

1.1.2 Cancer and pH

1.1.2.1 The Hallmarks of Cancer

As previously discussed, pH has a significant role among many disease states. Considering its role within cancer specifically, it's important to regard the characteristics of cancer. Hanahan and Weinberg examined the so-called "Hallmarks of Cancer" which characterise ten biological indicators which present during the development of tumours (**Figure 1.2**).[16,17] While it is thought that cancers must demonstrate all the hallmarks, the order of acquiring these capabilities varies between cancer types.

Sustaining proliferative signalling: One of the most fundamental features of cancer cells is the ability to undergo continual proliferation. Typically, healthy cells carefully control the release of signalling molecules, such as growth factors and extracellular matrix components, which promote cell growth. Cancer cells, however, can evade control and regulation through a number of channels, they may produce growth factors themselves; mimic growth signals to stimulate normal cells; or increase the number of receptor proteins, causing the cells to become "hyperresponsive".[17]

Evading growth suppressors: As well as promoting proliferation, cancer cells must also be able to avoid the mechanisms used to restrict proliferation through tumour suppressor genes. There are two notable proteins, retinoblastoma-associated protein (RB) which responds to signals occurring extracellularly, and tumour protein p53 (TP53), which reacts to intracellular signals to prevent uncontrolled proliferation. Cancer cells may exhibit defects along the protein production pathways, meaning that the tumour suppressing capabilities normally carried out are not properly functioning.[17]

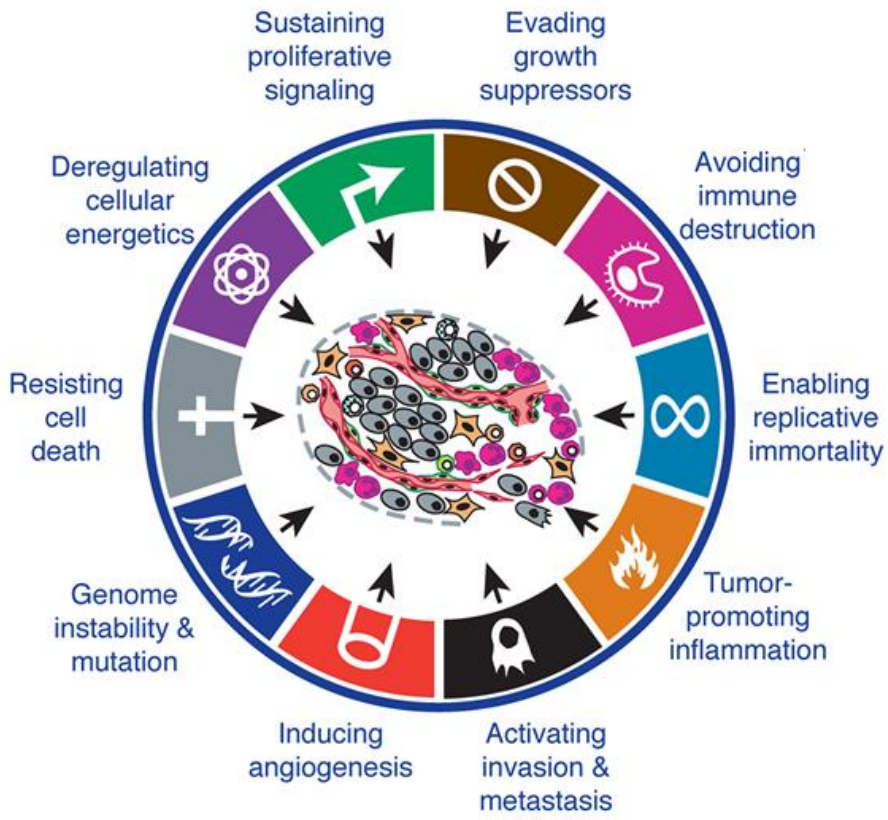

Figure 1.2 Illustration of the ten "Hallmarks of Cancer", characterising biological features during cancer development, as defined by Hanahan and Weinberg[17]. Image reproduced from Hanahan and Weinberg, Cell, Volume 144, Issue 5, 4 March 2011, Pages 646-674 with permission from Elsevier.

Avoiding immune destruction: Despite cancer cells going through constant immune selection pressure, some will emerge and 'escape' immune surveillance. Three of the major escape mechanisms are: lack of tumour-antigen recognition; resistance to cell death; induction of immunological tolerance *via* immunosuppressive factors secreted by tumour cells. Cancer cells can modify the cytotoxic mechanisms of the immune system through secretion of immunosuppressive factors or recruitment of immunosuppressive inflammatory cells.[17,18]

Enabling replicative immortality: Healthy cells typically have a finite number of growth and division cycles, with the lifespan of the cell ending in non-proliferative, but viable state called senescence. Some cells which can circumvent senescence undergo a second phenomenon known as crisis, where the majority of the cells in the population will die. Occasionally, cells emerge from a population in crisis showing the ability to continually replicate, known as immortalisation. It is thought that this ability is due to the increased production of telomerase, an enzyme which maintains the telomere length by adding repeat segments of hexanucleotides to the ends of chromosomes. In normal functioning cells, the telomeres become shorter with each growth cycle, it is the telomere length which determines the number of cycles the cell can undergo. In cancer cells, the increase in telomerase activity offsets the progressing telomere loss that would otherwise occur.[17]

Tumour promoting inflammation: Immune cells, primarily tumour associated macrophages (TAMs), can contribute to multiple hallmark capabilities by supplying bioactive molecules to the tumour microenvironment, such as growth factors that can sustain proliferation, proangiogenic growth factors, and matrix-degrading enzymes that aid invasion. TAMs can also release immunosuppressive molecules, allowing the tumour to evade the immune system.[17]

Activating invasion and metastasis: The ability to invade and metastasize distant sites is a key hallmark of cancer progression. A growing tumour will eventually generate cells which move out of the original tumour site to invade adjacent tissues followed by the migration to distant sites where new colonies are formed. The

function of cell-to-cell adhesion molecule, E-cadherin, is lost in invading cancer cells, whereas N-cadherin shows increased levels in migrating cancer cells, a molecule that aids cancer cells to pass through blood vessels during invasion.[17]

Inducing angiogenesis: As with normal tissues, tumours require a blood supply to transport nutrients and remove waste. The arrangement of blood vessels is usually fixed, with angiogenesis typically switched off, and it is only switched on for processes such as wound healing. Cancer cells have angiogenesis activated constantly, stimulated by growth factors such as vascular endothelial growth-factor (VEGF). The newly formed vasculature are not well organised and considered to be "leaky" compared to healthy blood vessels.[17]

Genome instability and mutation: Considered an enabling characteristic, the mechanisms responsible for the detection and resolution of DNA defects ensures that the degree of spontaneous mutations occurring remains very low during each cell growth cycle. However, when these mechanisms are compromised, the rate of mutations increases. As cancer cells evolve, mutations which can overcome these anticancer defences in genes that normally function in maintaining the stability of the genome are selected. Genomes vary widely between different tumour types, but nearly all of them have DNA repair defects. Thus, genome instability and mutation are essential to tumour progression.[17]

Resisting cell death: Faults and defects in cells, such as DNA damage, would typically result in the cell undergoing apoptosis. The most common strategy found among cancer cells to avoid apoptosis is the loss of the p53 tumour suppressor function, which is involved in signalling for apoptosis. Without this protein functioning correctly, the cell may not be able to resist apoptosis, and may also be able to evade growth suppressors as mentioned above.[17]

Deregulating cellular energetics: The Warburg effect refers to an observation that cancerous cells tend to produce lactate *via* the glycolytic pathway, regardless of oxygen concentrations, instead of producing energy through oxidative phosphorylation.[5,19] Although seemingly counterintuitive, as there is much less ATP

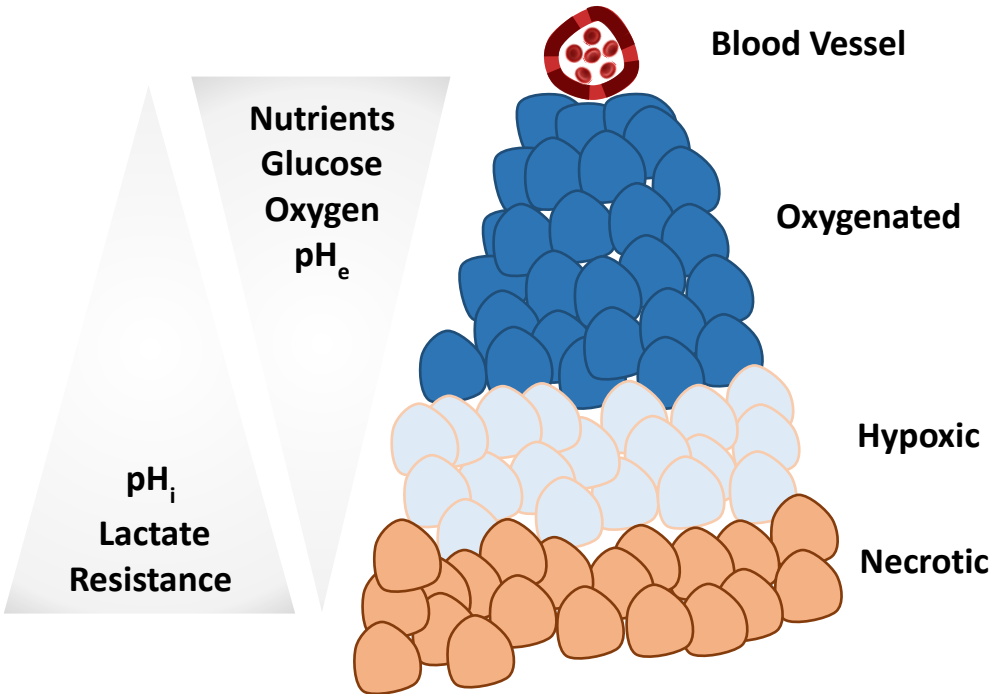

Figure 1.3 The tumour microenvironment. Gradients form as the tumour grows further away from vasculature.

produced through glycolysis compared to oxidative phosphorylation, cancer cells have increased uptake and utilisation of glucose, meaning that there is an increased rate of production of ATP, allowing rapid and sustained proliferation. Further, cancer cells undergoing aerobic glycolysis also produce many intermediate biosynthetic precursors. These molecules are used as building blocks to produce proteins, lipids and DNA required by the rapidly dividing cells. The hypoxia inducible factor (HIF) is not only a response to low oxygen levels, it may be stimulated in response to a variety of triggers, such as radiation induced DNA damage, signalling from other proteins, growth factors and the occurrence of pyruvate. Once activated, HIF can go on to activate genes that support aerobic glycolysis and repress genes involved in normal respiration.[17]

1.1.2.2 The Role of pH in Cancer

The role of pH along with the development of the tumour microenvironment is a further important consideration of cancer. It is well known that cancerous tissues are associated with a hypoxic and more acidic microenvironment than found in non-cancerous tissues.[4] Studies carried out in the 1950s recognised that tumours beyond a distance of around 200 μm from a blood supply can become necrotic.[20] It is this poor vascular perfusion which contributes to the heterogeneity of the tumour microenvironment. Poor vasculature prevents waste removal and regional hypoxic gradients can occur. With the increased metabolic demand of cancer cells, this can all lead to a decreased extracellular pH: extracellular acidosis, where the pH has been reported as low as pH 6.5.[19,21] Conversely, if the pH_e is acidic, the pH_i will be slightly alkaline ($pH_i > 7.4$), which is not typically observed in healthy cells (pH_i ~7.2).[19,22,23]

The pH_e changes on a more drastic scale than the pH_i as there are several mechanisms responsible for regulating pH_i, many of which efflux protons to the extracellular space. There are a number of mechanisms contributing to the acidification of the tumour microenvironment through the maintenance of pH_i, including Carbonic Anhydrases (CAs); Vacuolar-ATPase; monocarboxylate transporters (MCTs); HCO_3^- transporters; and Na^+/H^+ exchangers (NHEs) .[19] CAs are metalloenzymes, which maintain the acid-base balance both intra- and extracellularly by converting CO_2 to bicarbonate and protons. In particular, CAIX, is an important regulator of tumour pH, making it a potential therapeutic target.[19,22] Vacuolar-ATPases transport protons from the cytoplasm to intracellular vesicles (e.g. lysosomes). Mono-carboxylic acids such as lactate and pyruvate are transported across plasma membranes *via* monocarboxylate transporters (MCTs). Importantly, MCTs are often over expressed in cancer cells, leading to an increased efflux of glycolytic by-products (lactate and protons), and therefore causing a reduction in pH_e.[19,22] The HCO_3^- transporters regulate movement of HCO_3^- across the plasma membrane, allowing either acidification or alkalinisation of the pH_i. Finally, the NHE family can be considered one of the most active transporters in pH_i regulation, especially NHE1 which

hyperactively ferries protons extracellularly. It is thought that the increased activity of NHE1 is largely responsible for increased invasion and metastasis.[19,22] As the maintenance of pH_i is permissive to cancer progression, these transporter families have become attractive therapeutic targets, with pH_e changes used as an approach to monitor drug efficacy.[24]

1.1.3 Challenges

There are two main approaches typically employed to determine pH in biological samples: electrochemical and optical based techniques. Currently, glass electrode-based measurements can be considered as the gold standard for pH sensing due to their selectivity and reliability over a wide pH range.[25,26] However, using electrode sensors presents several challenges, hindering their translation into biomedical applications. These challenges can be overcome by optical based methods. Comparing the two approaches: a glass electrode is fragile and can be difficult to miniaturise, conversely, it is relatively easy to miniaturise optical devices using optical fibres; electrochemical sensors require an reference electrode, whereas internal standards can be applied to optical sensors; optical devices can employ multiple wavelengths to provide multiplexing capabilities, and do not suffer from electronic interference.[26,27]

Considering the advantages of optical vs electrochemical devices in the context of the space limited regions of the lung, an optical platform for sensing physiological parameters was investigated.

1.2 Raman and Surface Enhanced Raman Spectroscopy

1.2.1 Raman Spectroscopy

Inelastic scattering of light was originally theorised by A. Smekal in 1923, and was first observed in 1928 when C. V. Raman detected a change in the frequency of scattered light arising from the incident light through focusing sunlight on a series of liquids and their vapours.[28,29] The phenomenon has since been known as Raman spectroscopy. In general, spectroscopy is the study of the interaction between matter and electromagnetic radiation, where photons may be absorbed, emitted, scattered, or non-interacting. Different energy transitions within a molecule can be explored by employing certain types of radiation; electronic transitions may be studied by ultraviolet (UV) and visible light, vibrational transitions by infrared (IR), and rotational transitions by far-IR and microwaves.[28–30]

The process of absorption requires a matching of the energy of the incident photon and the energy gap between a molecule's ground state and the excited state, whereas scattering requires no such suitable pairing. IR spectroscopy is typically used to study vibrational transitions by measuring the absorbance (or emission) of radiation, however the incident radiation may also be scattered. It is this scattered light that is measured in Raman spectroscopy. Rayleigh scattering is the predominant type of scattering, where there is no change in frequency between the incident and scattered light. A small proportion of photons (approximately 1 in 10^7) undergo an energy change in a process known as inelastic scattering. These photons can either lose energy to the molecule, known as Stokes scattering, or gain energy from the molecule, known as anti-Stokes scattering. It is possible to gain information from both vibrational and rotational transitions with carefully selected incident light sources; however only vibrational Raman scattering has been used in this project. **Figure 1.4** compares the process of Raman scattering with fluorescence emission and IR absorption.

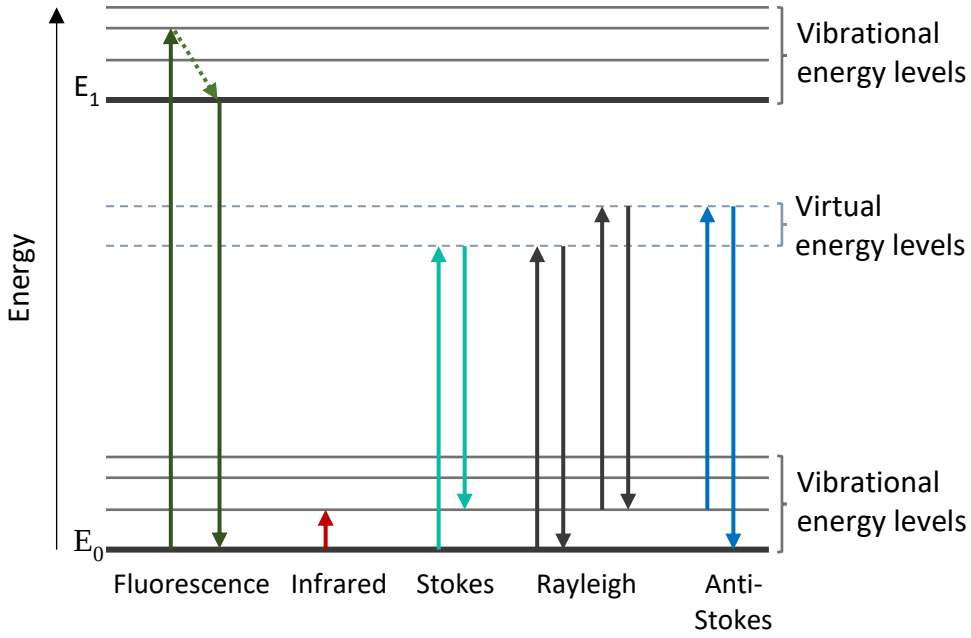

Figure 1.4 Jablonski diagram illustrating transitions between energy levels between fluorescence, infrared absorption, and light scattering processes.

Raman spectroscopy can provide several advantages over more conventional methods such as fluorescence or chemiluminescence approaches, which offer limited characteristic structural information and broad emission spectra, often requiring multiple wavelengths of light. Generally, optical detection techniques that employ the use of fluorophores give rise to broad emission bands, provide little characteristic structural information and large spectral overlap when multiple molecules are present. Using Raman spectroscopy, specifically surface enhanced Raman spectroscopy (SERS), can produce sharp fingerprint spectra, that are molecularly specific, providing a way to gain multiparameter information using a single wavelength of light.[31,32]

1.2.2 Surface Enhanced Raman Spectroscopy (SERS)

A significant enhancement of Raman signals can be seen when an analyte is adsorbed on to a roughened metal surface, this phenomenon is known as surface enhanced Raman spectroscopy (SERS).[33–37] The SERS effect was first observed in 1974 by Fleishmann *et al.* when an increase in the Raman signal intensity of pyridine was seen when adsorbed onto a roughened silver electrode.[33] Early theories proposing the origin of the enhancement were in disagreement, with Van Duyne and Jeanmaire suggesting enhancement was due to an electromagnetic effect, whereas a chemical enhancement was proposed by Albrecht and Creighton.[34,35,38] While detailed mechanisms on enhancement effects are still relatively unknown, it is widely acknowledged that the enhancement results from a combination of electromagnetic and chemical enhancements.

1.2.2.1 Electromagnetic Enhancement

The electromagnetic effect requires the analyte to be held in close proximity, or adsorbed, onto a roughened metal surface, such as a nanoparticle. Following laser irradiation, the delocalised electrons on a metal surface collectively move, it is this movement which is known as surface plasmon resonance.[29] The incident light causes the surface electrons to oscillate, increasing the local electromagnetic field experienced by the adsorbed analyte, and thus intensifying polarisation of the molecule resulting in significantly enhanced scattering efficiency (**Figure 1.5**).[29,37,39] This enhancement does not happen evenly around a nanoparticle, the greatest enhancement occurs at points where the nanoparticles are in contact, forming "hot spots" which afford a strong SERS signal, enabling single molecule detection.[40–42]

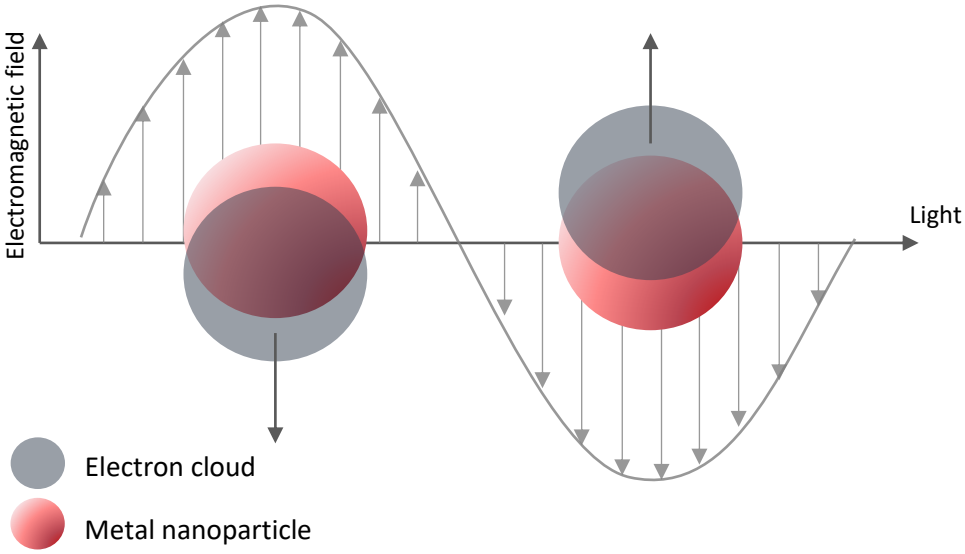

Figure 1.5 Free electrons responding to an external electric field, resulting in oscillations of the electrons, a phenomenon known as surface plasmons, which create regions of strong intensity electromagnetic fields at the surface of the nanoparticle. The molecules held near the nanoparticle experience increased polarisation, resulting in enhanced Raman scattering efficiency

1.2.2.2 Chemical Enhancement

In addition to electromagnetic enhancement, thought to be the primary contributor to enhancement in SERS signal, a contribution from chemical (or charge transfer) enhancement can also occur. New electronic states form as the analyte adsorbs onto the surface of the metal nanoparticle, where there is a charge transfer in the analyte being probed from the highest occupied molecular orbital (HOMO) to the lowest unoccupied molecular orbital (LUMO) of the electronic energy levels.[37,39,43,44]

1.2.2.3 Materials used for SERS

A range of materials exist that are capable of achieving a SERS effect. The most common materials typically consist of colloidal suspensions made by reducing Au or

Ag salts, however other metals including Cu, Al, Li, Na, K, and In have also been used.[45–47] A diverse range of substrates such as electrodes,[33–36] planar surfaces,[48] and nanoparticles in a variety of shapes (e.g. spheres, stars, shells, rods)[49–51] have also been employed as SERS substrates.

Some of the major advantages of using nanoparticles include their high surface area and ease of functionalisation, allowing simple preparation of sensitive and selective nanosensors, which are amenable to biological probing.

1.3 Raman Spectroscopy in Biology and Medicine

While this thesis primarily focuses on the application of SERS, it is also worth mentioning the progress in Raman spectroscopy within the field.

1.3.1 Raman Spectroscopy for *in vitro* Analysis of Cells

As the basic biological unit of all living organisms, the cell and the study of them as individual and cell populations to better understand cellular dynamics and processes is undeniably important, particularly when analysing indicators of disease. As a non-destructive and label free technique requiring minimal sample preparation, Raman spectroscopy is a popular method to interrogate biological samples, particularly live cells. Imaging techniques have been developed to combine spectral information with spatial information, making it possible to distinguish the cellular architecture such as proteins, lipids, and DNA, without requiring staining.[52–54]

Majzner et al. used 3D confocal Raman imaging to examine endothelial cells, illustrating the heterogeneity within a single cell. The size, volume, shape and biochemical composition of cellular organelles inside a single cell was defined

without the need for special sample preparation and so did not disrupt the spatial integrity.[53]

Heraud et al. demonstrated the advantage of Raman spectroscopy as a tool for live cell imaging, investigating the phenotypic changes of oocytes through their maturation. Differences between live oocytes and fixed oocytes were studied, identifying any fixation induced architectural changes (**Figure 1.6**).[55] As such, they were able to identify a spectral marker only found in live cells, providing a method to assess the health of the oocytes.[55]

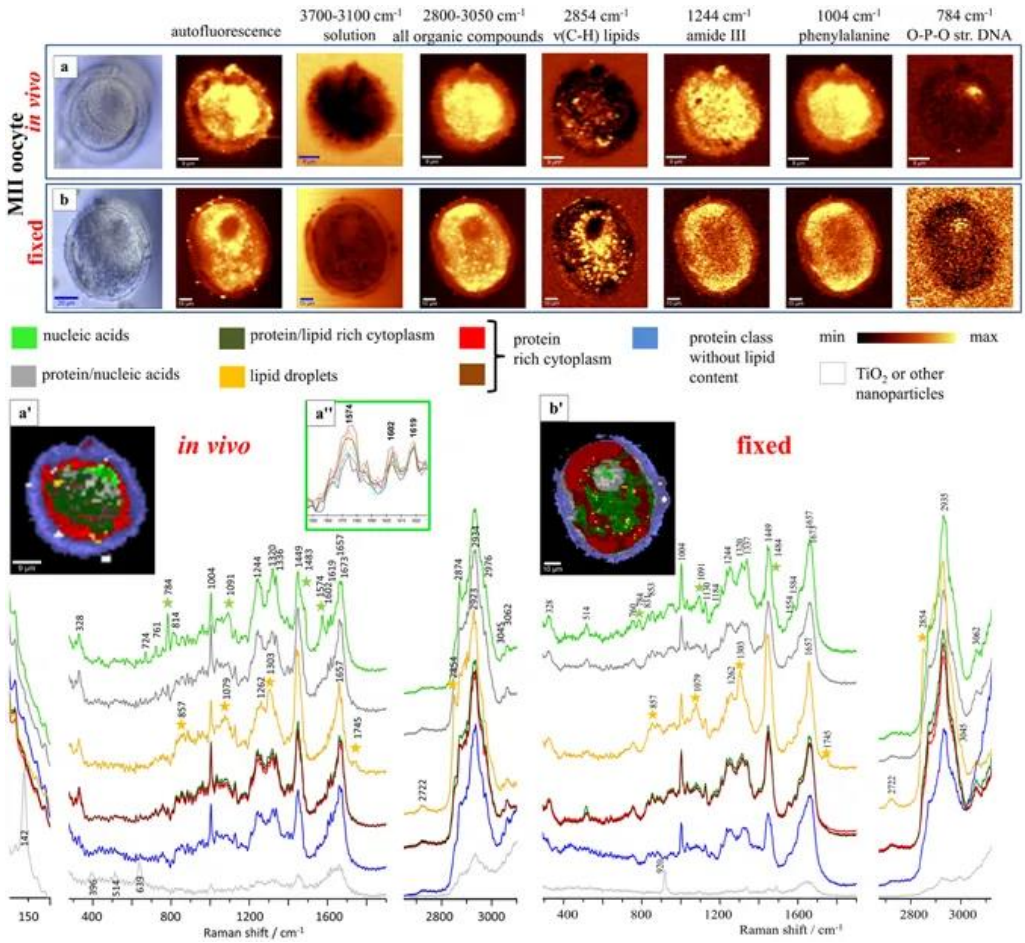

Figure 1.6 A photomicrograph of (**a**) functional and (**b**) fixed oocytes in the MII stages; Integration Raman maps of a specific bands were obtained with 532 nm excitation; K–means Clustering (KMC) results with 8 main classes were presented with an average spectrum for each class. In a", presented is the zoom-in of the spectral region showing the band at 1602 cm^{-1} for the single spectra extracted from the nucleic acid class, which is only observed in the *in vivo* state. The Raman intensities in the region of 300–1900 cm^{-1} were scaled by factor of 2 comparing to CH-stretching region and lower region below 300 cm^{-1}. (Adapted with permission from reference 55 under the Creative Commons Attribution 4.0 Unported Licence)

1.3.2 Raman Spectroscopy for *Ex Vivo*/*In Vivo* Analysis

Transitioning from *in vitro* to *in vivo* studies presents a range of technological hurdles to overcome. Clinical applications of Raman spectroscopy can employ optical fibres due to the ease of access to *in vivo* locations, facilitating the technique as a minimally intrusive tool for monitoring and detection of disease. Due to relatively weak scattering properties, the Raman signals can be hidden by a range of background signals originating from fluorescence, scattering, or even the measurement systems themselves, as the signals can be easily influenced by instrumentational and fibre probe designs. Employing near-infrared lasers can reduce the autofluorescence arising from tissue, while clever fibre designs can minimise the signals from the silica fibres (as mentioned in Section 1.4.5).[8,56,57]

As a diagnostic tool, Raman spectroscopy has proven its effectiveness for the accurate identification of healthy and diseased tissues in a wide range of cancers, including skin[58,59], oesophageal[60,61], cervical[62], colorectal and bladder cancer[57,63], using both *ex vivo* and *in vivo* sample analysis.

Other non-cancerous application examples include using Spatially Offset Raman Spectroscopy (SORS) to measure bone composition *in vivo*.[64] Several biofluids have proven to be useful samples in disease and infection identification through Raman spectroscopy, analysing the spectra obtained from fluids such as sputum[65,66], serum, blood, or urine.[57,67–71]

1.4 Surface Enhanced Raman Spectroscopy in Biology and Medicine

While Raman spectroscopy offers advantages in that it is label-free and non-invasive, meaning that there is no need for external markers such as stains or labels to detect a response, the signal is inherently weak, leading to either longer acquisition times, or the use of high laser powers which are not always suitable for biological samples. Combining the molecular specificity of Raman spectroscopy with the improved sensitivity due to the plasmonic nanostructures, SERS provides a method of probing biological samples to examine disease processes. SERS reporters, or tags, are commonly used in detection and imaging applications.[49,54] SERS can be used as a

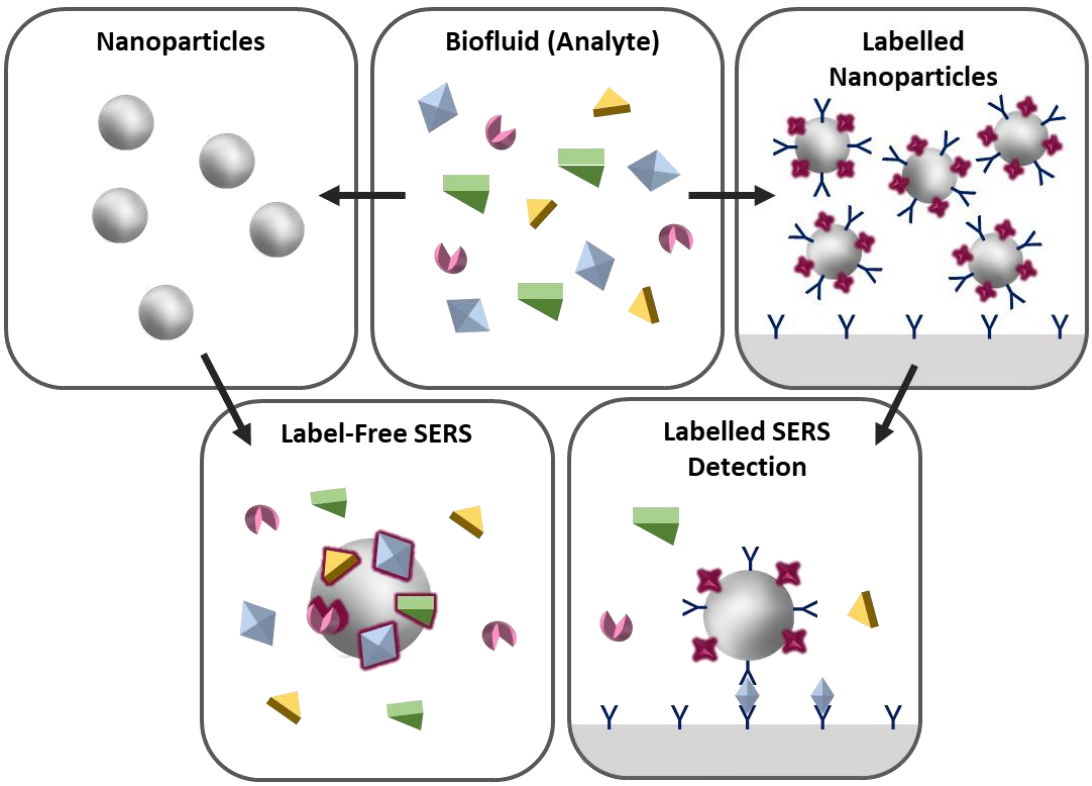

Figure 1.7 Direct and indirect approaches to surface enhanced Raman spectroscopy. Label-free nanoparticles can be used to directly measure the analyte's intrinsic Raman signals, whereas nanoparticles functionalised with reporter molecules offer an indirect measurement approach, for instance with an immunoassay.

direct or indirect method, i.e. using label-free or labelled nanoparticles, to measure biological processes (**Figure 1.7**).

1.4.1 Surface Enhanced Raman Spectroscopy for *In Vitro* Analysis

1.4.1.1 Unlabelled Nanoparticle Investigations

The intrinsic analysis of cells *via* label free SERS investigations (using unlabelled nanoparticles - without reporter molecules) can provide a wealth of information relating to both cellular components as well as cellular processes occurring in the direct vicinity of the nanoparticles.

Components of cells can be identified by analysing intrinsic spectral bands. Kneipp et *al* measured signals originating from the native cell constituents such as DNA, RNA, amino acids, and proteins demonstrating the distribution of DNA and protein by the presence of their respective spectral peaks found at ~1120 cm^{-1} and ~1004 cm^{-1}.[72] It is worth noting that the distribution of the cell components was only detected in regions where nanoparticles were present, and the non-uniformly distribution of nanoparticles throughout the cell will not provide a complete depiction of the cell in its entirety.[72]

While exploring the molecular composition of native cell constituents is an interesting application, label-free SERS also offers a way to observe biological processes and functions such as endocytosis.[73–75] Huefner et *al* characterised spectral features associated with the maturation process of endosomes to lysosomes such as the decrease of pH along the transition pathway, the degradation of lipids and proteins, and the breakdown of nucleic acids within the lysosomes.[74,75]

The study of biological processes and functions using label-free SERS typically relies on the intracellular uptake of nanoparticles. However, intercellular signalling

pathways often result in the secretion of a small number of molecules, whilst extracellular chemical signalling pathways are involved in many biological and physiological processes. Using a glass nanopipette covered with nanoparticles, metabolites secreted from Madin-Darby canine kidney (MDCKII) epithelial cells, namely pyruvate, lactate, ATP, and urea, were detected simultaneously.[76] Additionally, this approach has been used to measure ATP, glutamate, acetylcholine, γ-aminobutyric acid (GABA) and dopamine, among other neurotransmitters by placing the SERS probe near mouse dopaminergic neurons.[77]

In a similar way to using Raman spectroscopy, to differentiate between cancerous and non-cancerous tissues as described in Section 1.3, nanoparticles may be introduced into tissue samples to enhance intrinsic signals, therefore aiding discrimination between cell types.[78,79]

Gaining information from cells using label-free SERS approaches can be challenging, the irregular dissemination of nanoparticles throughout the cell, the formation of variable sized nanoparticle aggregates, and the generation of large and complex data sets requires advanced analysis to extract important features, all require careful consideration.

1.4.1.2 Labelled Nanoparticles

Functionalising nanoparticles with reporter molecules facilitate the active imaging or sensing of biological targets. Simple nano-labelling systems are most common, where a single reporter molecule is used to functionalise the nanoparticle surface. More complicated arrangements of nanoparticle functionalisation range from multiple reporter molecules on a single nanoparticle, to combining reporter molecules with specific targeting compounds such as oligomers[80,81], peptides[82,83], or antibodies.[49,84–86]

SERS has been applied to biological samples in various formats to detect disease *in vitro*. Combining targeted SERS approaches with live cell microscopy enables further

capabilities such as high spatial resolution imaging of specific cellular biomolecules. Targeting approaches such as the conjugation of antibodies to nanoparticles can provide information on the presence and distribution of biomarkers within cells. Lee et al. reported the use of gold or silver nanoparticles functionalised with monoclonal antibodies specific to phospholipase Cγ1, which is overexpressed in hyperproliferating tissues and found in many cancers.[84]

In addition to the detection of biomarkers found in diseased human tissues, pathogen detection is critically important as antimicrobial resistance increases. Kearns et al. demonstrated the use of silver nanoparticles functionalised with a Raman reporter with bacterial strain specific antibodies. Employing a sandwich-type assay, bacterial cell concentrations as low as 10 CFU/mL were detected in single pathogen tests, and using the multiplex system, three bacterial strains were isolated and detected: *Escherichia coli* (*E. coli*), *Salmonella typhimurium (S. typh*), and methicillin-resistant *Staphylococcus aureus (*MRSA).[86]

While targeting of biomolecules provides high spatial resolution imaging of specific cellular biomolecules, nanoparticles functionalised with only reporter molecules can provide information on the intracellular distribution of the particles. McAughtrie et al. reported the first combined 3D Raman and SERS imaging in cells. Cells were treated with a mix of nanoparticles, functionalised with a range of reporter molecules, and their location within the cell determined. In addition to SERS imaging, intrinsic Raman signals from the cells were also analysed, demonstrating SERS imaging and the simultaneous confirmation of nanoparticle uptake along with multiple cellular component detection.[54]

Blood, sputum, and urine are common biofluids analysed for indications of infection and disease. Indirect detection is the predominant approach to employing SERS in biofluid based assays (**Figure 1.7**). Much of the early work was established by Vo-Dinh et al., reporting on the first DNA-SERS probe, where labelled nucleic acid sequences were used to target specific complementary nucleic sequences.[87] This has enabled

SERS to be used as a tool in the detection and identification of viral and bacterial DNA for possible disease diagnosis.[80,81,88–90]

1.4.1.3 3-Dimensional Cell Culture and Surface Enhanced Raman Spectroscopy

There is no doubt that cell culture has become a crucial tool in understanding fundamental biological mechanisms which underpin cell behaviour. These behaviours such as differentiation, migration and growth can be affected by the cell's microenvironment. Cell culture is an accepted approach to study cell behaviour, however, there is much evidence to suggest that the behaviour of cells grown as 2D culture diverge significantly from the response seen *in vivo*.[91,92] **Figure 1.8** illustrates the difference between 2D and 3D environments and the biophysical cues cells receive. In traditional 2D cell culture a stiff, flat surface provides support for the cells to adhere. These 2D cell culture supports (typically polystyrene or glass) provide an easy way to handle cells in a homogenous manner, with the cells grown as monolayers. This aids growth reproducibility as the cells receive comparable amounts of nutrients, or drugs, applied to the cells. What these supports lack, however, is the ability to offer a means of allowing the cells to "find" a niche comparable to their natural environment. The external support can influence cell shape, which in turn affects the regulation of biophysical cues determining cell behaviours, such as migration, proliferation, and in some cases, differentiation. In addressing this issue, there has been much effort made in recent years to investigate methods which move away from the growth of monolayer cell cultures to look at more complex "cell structures" which can mimic the behaviours seen *in vivo*.[91–94]

Advances in the fields of cell biology and tissue engineering have provided a range of methods in which to culture cells in three dimensions. Self-organising models such as multicellular tumour spheroids (MTS), or models that employ scaffolds (such as hydrogels), both provide a relatively simple and scalable method of production,

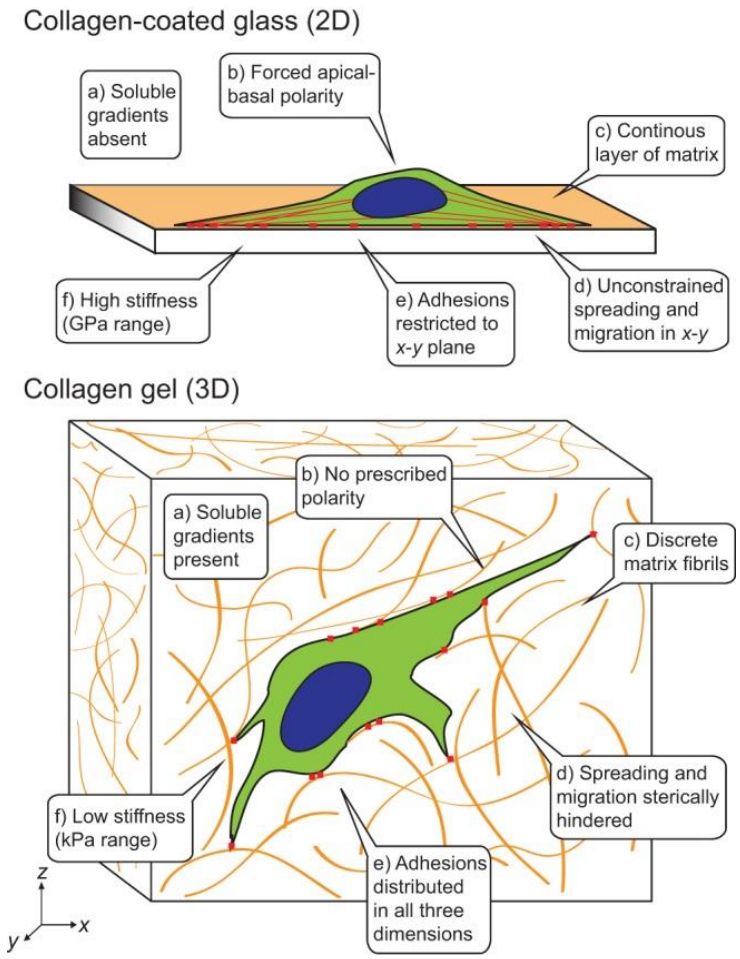

Figure 1.8 Missing cues. The physical, mechanical and chemical cues cells encounter is considerably different between 2D and 3D microenvironments. Reprinted from reference 92 with permission from Journal of Cell Science.

offering high reproducibility, the possibility of co-culture, and are also amenable to high throughput for drug screening.[92,94–96] However, with their simplicity lies several drawbacks; the architecture of these cultures can lack the complexity seen in tissue, while some commercial scaffolds can have significant variations between batches due to their biological origin.[94] Techniques such as 3D bioprinting offer the ability to create custom *in vivo*-mimicking architectures with physical and chemical gradients.[94,95] Most recently, Noor et al. printed thick cardiac patches, matching the biochemical and immunological fingerprint of a patient.[97]

Current methods used to analyse physiological parameters in 3D culture models often involve destruction of the sample.[98–100]

Combining SERS with 3D cell culture models presents several challenges, including excitation of SERS probes through "tissue" and the corresponding signal detection. As 3D cell culture becomes more popular, Raman techniques are being employed as an identification method as well to monitor the physiological environment in a spatially resolved and quantitative manner.

The use of Raman techniques in 3D cell culture is still in its infancy. However, as multicellular tumour spheroids (MTS) are a simple production method of 3D cell culture, several studies have implemented SERS in this setting.[23,101,102] Jamieson et al. used a regional targeting approach to investigate the intracellular pH and redox gradients that occur across live MTS (outer, intermediate, and centre regions, **Figure 1.9**), and the subsequent response to drug or radiation treatments.[23]

Altunbek et al. demonstrated the cellular responses to Doxorubicin (Dox) and Paclitaxel treatments on HeLa cell spheroids. Due to apoptosis, an increase in the cholesterol peak at 555 cm^{-1} was attributed to the destabilisation of the endolysosomal membrane, while the activation of GTPases resulted in an increase in a signal associated to the guanine (675 cm^{-1}). A drug specific response was also noted with the increased cholesterol peak intensity at 705 cm^{-1} after Dox treatment, due to the induced cholesterol synthesis on the endolysosomal membrane.[102]

As a way to improve signal obtained through tissue, Nicolson et al. used surface enhanced resonance Raman spectroscopy (SERRS). NIR Raman reporters in resonance with the excitation wavelength, enabling detection through tissue barriers using conventional Raman spectroscopy. Through their biological model nanoparticles were taken up by cells in an MTS arrangement then placed behind porcine tissue. The SERRS signals were detected at a depth of 5 mm of tissue.[101]

1.4.2 Surface Enhanced Raman Spectroscopy for Molecular Sensing

Biological systems exist in a balanced state and alterations to parameters such as pH, redox potential, and the concentration of reactive oxygen species (ROS) can have significant impact on cell functions, with changes to the physiological homeostasis observed in disease processes. As such, SERS reporters have been developed to measure these parameters. Early work by Lyandres et al. created glucose sensors using silver coated spheres functionalised with mercaptohexanol and decanethiol, creating "holes" where glucose molecules could position themselves and the resulting response measured by SERS.[103] The group reported the quantification of glucose within a clinically relevant range of 0.56–25 mM, under physiological pH and in the presence of interfering analytes.

Measuring intracellular pH by SERS often employs the pH sensitive molecules 4-mercaptobenzoic acid or 4-mercaptopyridine as both display ratiometric peak changes.[51,104] Using this approach, SERS-based investigations have explored the endocytic pathway by monitoring pH changes in vesicles.[72,74,105] Through measuring intracellular pH, Pallaoro et al. found that the majority of nanoparticle containing locations within the cell registered pH values between 4-5, with a smaller number of sites measuring pH 6, and even fewer at pH 7-8. From this, they hypothesised that the main pathway by which nanoparticles enter cell was through receptor mediated endocytosis, as the other pathways, caveolae mediated endocytosis or micropinocytosis, would tend to result in higher pH compartments.[106] The intracellular pH has also been shown to be affected by external influences such as the extracellular pH and inflammation.[107] Jaworska et al. demonstrated that intracellular acidosis occurred in endothelial cells treated with tumour necrosis factor-α (TNFα), a cell signalling protein involved in systemic infection.[107]

In addition to pH, cellular redox potential has been investigated due to its involvement in a number of biochemical processes.[108] Previous work by Campbell et

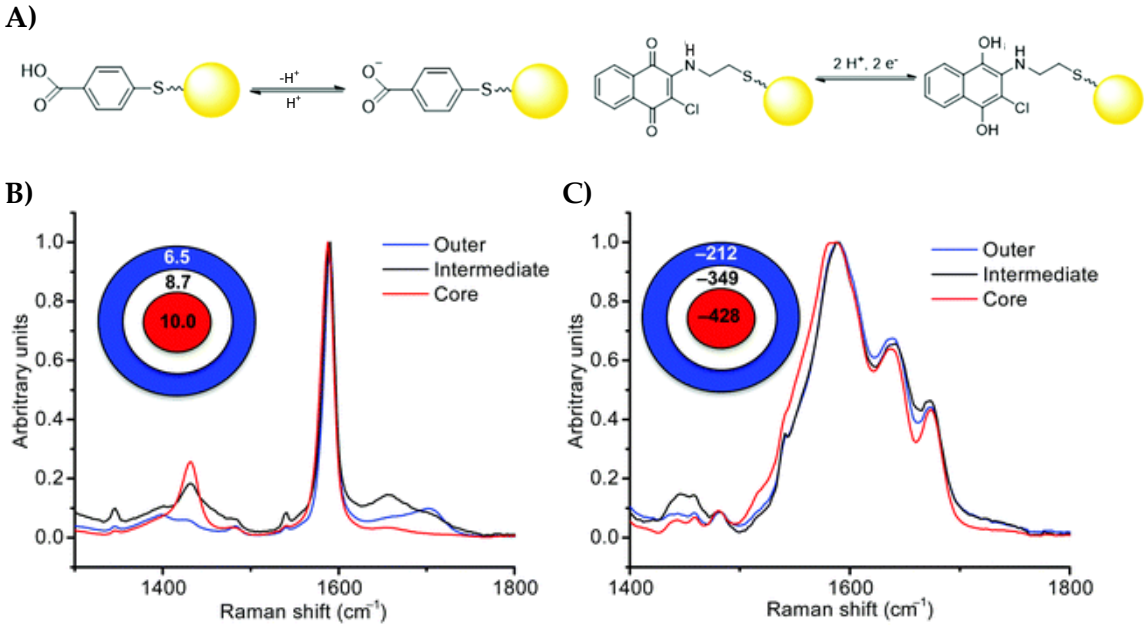

Figure 1.9 A) Molecular structure of 4-MBA and NQ with its electron transfer scheme. B) pH and C) redox potential gradients in MCF7 MTS measured by SERS. Average SERS spectra acquired for core, intermediate and outer regions of MTS with targeted MBA-functionalised nanoshells (B) and NQ-functionalised nanoshells (C) along with a schematic showing average pH and average adjusted redox potential values for each condition (Adapted with permission from reference 23 under the Creative Commons Attribution 3.0 Unported Licence).

al. has included the synthesis of a suite of redox probes, consisting of small molecules sensitive to redox potential, attached to gold nanoparticles (**Figure 1.9**).[109,110] These SERS redox probes have been used to measure intracellular redox potential in a number of cell lines under stresses such as hypoxia or oxidative stress.[109–111] In addition, simultaneous measurements of intracellular pH and redox potential, along with the application of the nanosensors to 3D multicellular tumour spheroids (MTS) models has been reported (**Figure 1.9**).[23,112]

Involved in many physiological mechanisms such as cell signalling and the regulation of gene expression, reactive oxygen species (ROS) such as •OH, hydrogen peroxide and singlet oxygen, are important in biological systems.[113] In instances where ROS are overproduced, cell components such as proteins, DNA, and lipid membranes can be

damaged. As such, the detection and quantification of ROS can be indicative of cell health.[75] Sensitive and selective SERS H_2O_2 probes have been developed using boronic acid sensors, based on 4-carboxyphenylboronic acid (4-CA) and, which decorate the

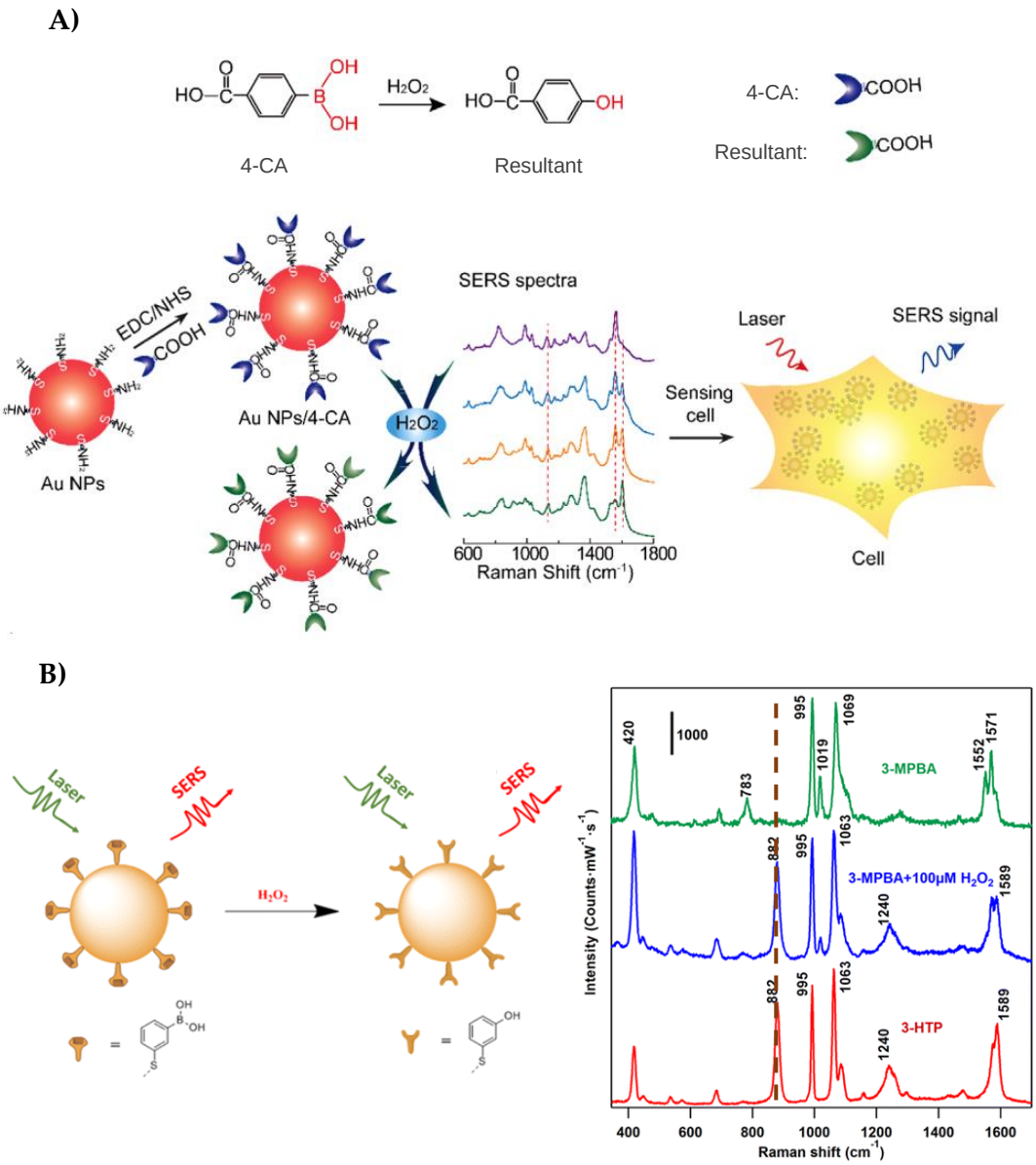

Figure 1.10 A) Illustration of the nanoparticles functionalised with 4-CA for H_2O_2 sensing in living cells (Adapted with permission from reference 114. Copyright 2015 Elsevier B.V.). B) SERS-based scheme for detecting H_2O_2 by a boronate nanoprobe. H_2O_2 selectively oxidizes 3-MPBA (green spectra) to 3-HTP (red spectra), which yields easily distinguished changes in the SERS spectra (Adapted with permission from reference 115: X. Gu, H. Wang, Z. D. Schultz and J. P. Camden, Anal. Chem., 2016, 88, 7191–7197. Copyright 2016 American Chemical Society).

surface of gold nanoparticles (**Figure 1.10**).[114] Gu et al. used 3-mercaptophenyl boronic cid (3-MPBA), which upon reacting with H_2O_2 produces 3-hydroxythiophenol (3-HTP), with each species affording a distinct spectral fingerprint (**Figure 1.10**). From this, it was possible to detect and quantify both endogenous and exogenous H_2O_2 in live cells. Further, combining these nanosensors with glucose oxidase (GOx), they reported the quantitative and selective detection of glucose in human serum.[115]

Other sensing targets include the detection of gaseous signalling molecules, carbon monoxide (CO) and nitric oxide (NO). These have been highlighted as potential therapeutic agents with CO becoming accepted as cytoprotective, and NO has emerged as a potential therapy for acute respiratory distress syndrome (ARDS), because it decreases pulmonary arterial pressure without affecting the systemic blood pressure.[116,117] Novel sensing compounds for CO and NO which can be assembled onto a nanoparticle surface have been developed. The CO detection approach employed nanoparticles modified with a cyclic palladium complex, while the NO sensor used nanoparticles functionalised with *o*-phenylenediamine (OPD). These nanosensors have been used to detect endogenous CO and NO in living cells.[118,119]

1.4.3 Surface Enhanced Raman Spectroscopy and Tissue Imaging

The current gold standard for analysing patient biopsy samples is by immunohistochemical practices. Using nanoparticles in place of fluorescent probes enables SERS to complement current practice. Several advantages that SERS demonstrates are that background contributions are less of an issue than with an intrinsic Raman method, aiding in quicker image acquisitions. Further, multiplexing abilities facilitate the detection of multiple markers in a single measurement, using a single laser line.

Applying SERS to tissue imaging and subsequent disease detection was first reported by Schlücker et al., a system comprising a small molecule reporter linking the nanoparticle and antibody was used to detect and locate prostate-specific antigen (PSA) in patient tissue samples.[120] Further work by the group used this technique to assess and monitor PSA expression in tissues.[121] Drawing attention to the

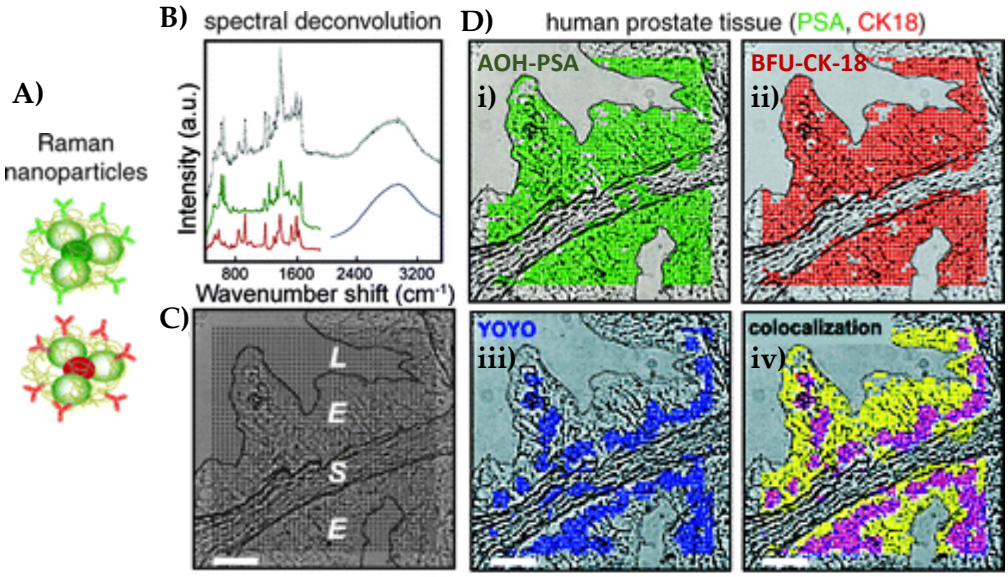

Figure 1.11 A) Illustration of the composite organic-inorganic nanoparticles (COINs). B) Spectral deconvolution from a single point in the map. The measured spectrum (grey) and best-fit spectrum (black, beneath grey spectra) are shown in the upper spectrum. Extracted spectra for BFU-CK-18 (red), AOH-PSA (green), and YOYO (blue) are given below. C) Brightfield image of a section of prostate tissue, targeted with antibody-labelled SERS probes. The image spans the tissue features: gland lumen *(L)*, epithelia *(E)* from two separate prostate glands, and stromal tissue *(S)* between the glands. D) Component and co-localisation of SERS probes. The COIN probe for detection of (i) PSA *via* conjugation with anti-PSA antibody and the Raman dye acridine orange (AOH-PSA, green), and (ii) CK-18 *via* conjugation with anti-CK-18 antibody, and the Raman dye basic fuchsin (BFU-CK-18, red). (iii) A DNA fluorescent dye (YOYO) labelled nuclear regions. (iv) Co-localisation of the combined COIN and DNA signals. Scale bars 10 μm. Adapted with permission from reference 122 B. R. Lutz, C. E. Dentinger, L. N. Nguyen, L. Sun, J. Zhang, A. N. Allen, S. Chan and B. S. Knudsen, ACS Nano, 2008, 2, 2306–2314. Copyright 2008, American Chemical Society.

multiplexing capabilities of SERS, Lutz et al. developed composite organic-inorganic nanoparticles (COINs), applied them to tissues samples, demonstrating the ability to simultaneously target two different antibodies, cytokeratin-18 (CK-18) and PSA (**Figure 1.11**).[122]

1.4.4 Surface Enhanced Raman Spectroscopy and *In Vivo* Imaging

The utilisation of both targeted and non-targeted SERS probes, where SERS probes are either functionalised with a molecule which binds to a specific biomarker or are left without the biorecognition molecule, have been studied for *in vivo* applications. Early SERS *in vivo* studies compared the tumoral uptake of targeted vs non-targeted SERS probes. Antibodies conjugated to gold nanoparticles were introduced into mice *via* tail injection, and SERS signals recorded from tumour and liver locations. The results showed that targeted probes accumulated in the tumour up to 10 times more efficiently than the non-targeted probes, and that there was some non-specific uptake of both types of nanoparticles by the liver and spleen.[123]

With disease processes complex, it is likely that no single targeting probe will provide enough information for complete disease diagnosis. As such, multiplexed imaging *in vivo* has become a research focus, with the aim of detecting disease at an earlier stage. Simultaneous detection of two non-target probes *in vivo* was demonstrated by Gambhir in 2008.[124] Further work by the group extended the multiplexing capabilities to 10 different SERS probes, administered at separate injection points, and the identification of 5 probes administered intravenously (**Figure 1.12**).[50]

Aside from cancer detection, SERS has been used to detect biomarkers of inflammation *in vivo*. Here, nanoparticles were conjugated to anti-intercellular

adhesion molecule 1 (ICAM-1) antibodies, as ICAM-1 expression in vasculature is an early indication of inflammation and atherosclerosis. After inflammation was induced in the ear pinnae of a mouse, by administering lipopolysaccharide, the SERS signals were measured demonstrating significantly higher detection over the isotype control. It was also reported that, compared to conventional fluorophore-antibody conjugates, SERS reporters produce higher sensitivity detection of ICAM-1.[125]

SERS imaging can offer improvements in spectral definition, depth resolution, and significant signal-to-noise ratio gains in vitro, ex vivo, and in vivo.

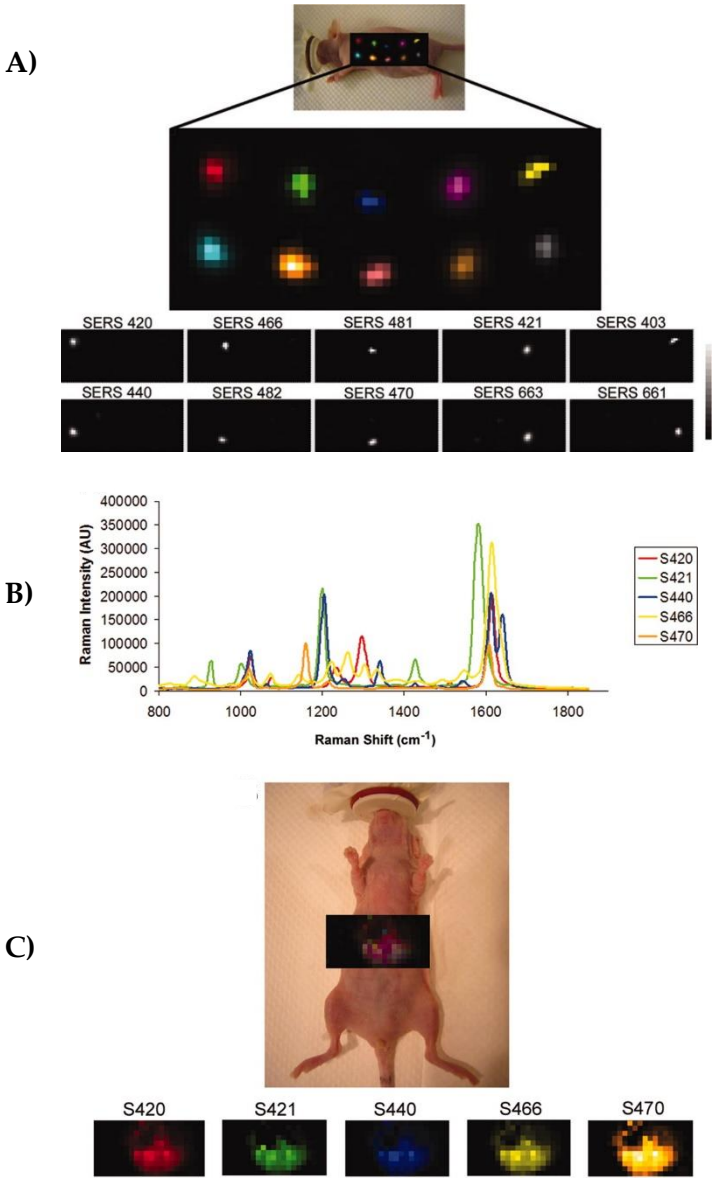

Figure 1.12 Multiplexing *in vivo*. A) Detection of 10 different SERS particles injected subcutaneously in a murine model. The grayscale bar to the right depicts the Raman intensity. B) Spectra of five unique Raman SERS tags. C) Deep-tissue multiplexed imaging 24 h after intravenous injection of five unique SERS nanoparticle batches simultaneously. Raman image of liver overlaid on digital photo of mouse, showing all five SERS probes accumulating in the liver after 24 h. Panels below depict separate channels associated with each of the injected SERS nanoparticle batches. Adapted with permission from reference 50.

1.4.5 Fibre-based Raman Sensors

In addition to conventional microscopy-based instruments, there have been massive efforts to use remote sensing techniques, i.e. sensing and imaging through an optical fibre. Remote sensing allows for identification and detection of disease at sites located away from the spectrometer and other optical measurement devices, without which access would be impractical and unreasonable (e.g. *in vivo* procedures). The fibre-based Raman sensors can be used for direct sensing measurements, for example, when it is possible to obtain the Raman signal from tissue itself, or the sensing fibres can measure analytes indirectly, using reagent mediated sensors. Reagent mediated sensors are useful when the sample has no intrinsic optical properties, and so the analyte will instead interact with a chosen reagent, resulting in an observable change to the optical properties of the reagent. The fibre-based work in this thesis explores reagent mediated sensing.

1.4.5.1 Fabrication of Optical Fibres

Optical fibres are usually employed because they offer a way to sense remotely. Often, this requires the fabrication of fibres, flexible and robust enough to be able to be placed *in vivo*. These characteristics provide constraints around which novel fibres can be designed.

Typically, an optical fibre consists of the core, the cladding, and a polymer coating (**Figure 1.3**). The core through which light propagates, is most commonly made from fused silica glass[126–128], however, they can also be plastic[129–131], or even hollow[56,132–135]. In this thesis, I have used silica-based optical fibres. The cladding has a lower refractive index than the core and thus confines light to the core through total internal reflection, known as a step-index fibre. Frequently, germanium (Ge) doped silica is used as the core combined with a pure silica cladding, as it lowers the core's refractive index.[136,137] Alternatively, to produce a core with a lower refractive index, fluorine can

be employed as a dopant. The step index fibres can be further classified as being either single mode or multi-mode. A single mode fibre has a much smaller diameter core than a multi-mode fibre, often <10 μm, which can only guide a single spatial mode of light. A multi-mode fibre (**Figure 1.3**) typically has much larger core diameters, capable of guiding multiple spatial modes of light along the fibre.

The role of the fibre can be considered as being either inert or active. In inert optical fibre sensors, it is only the optical signals which are transported to and from the sample environment, be it using a single unmodified fibre bundle or two fibre, bifurcated bundles (for excitation and collection). In active optical fibre sensors, the fibre itself is altered to include analyte sensing reagents. The fibre tips can be modified depending on the sensing application, affording either a flat-surface (unmodified), pitted cores, or a sharpened fibre tip (**Figure 1.14**). The modified cores are typically achieved through an etching process where hydrofluoric acid is able to etch Ge-doped

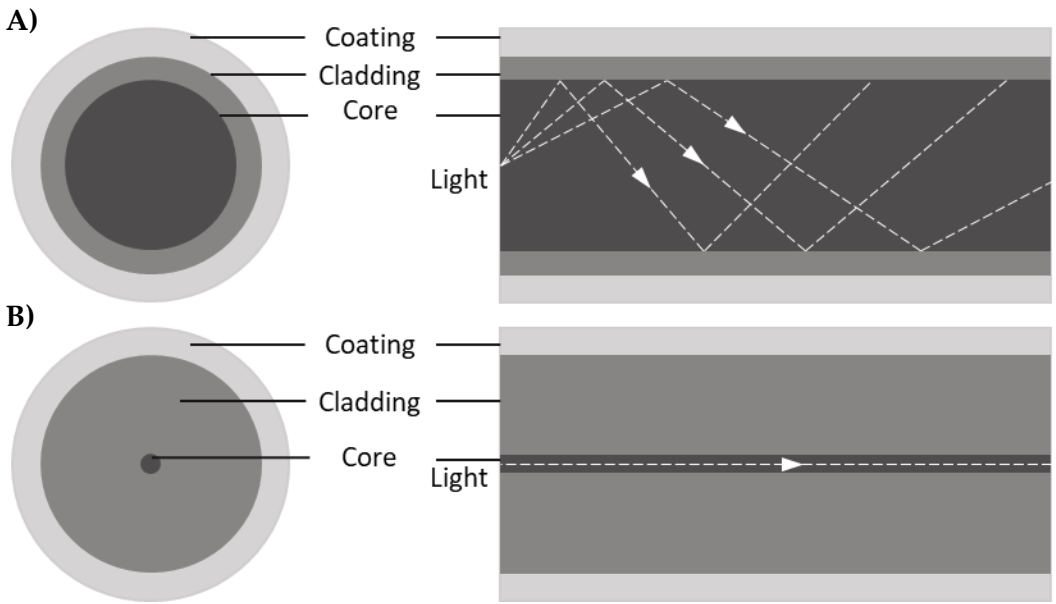

Figure 1.13 Illustration of A) multimode and B) single mode fibre showing the coating, cladding, and core, along with light propagation through the fibre.

silica at a faster rate than pure silica, likely due to the disruption the Ge causes between the SiO_2 bonds.

The sensing reagents frequently employed for fibre-based Raman sensing are nanoparticles functionalised with a reporter molecule. The immobilisation of nanoparticles to the distal end of the optical fibre is commonly carried out using a sol-gel based material, allowing retention of the nanoparticles whilst being porous enough for analytes to pass through.

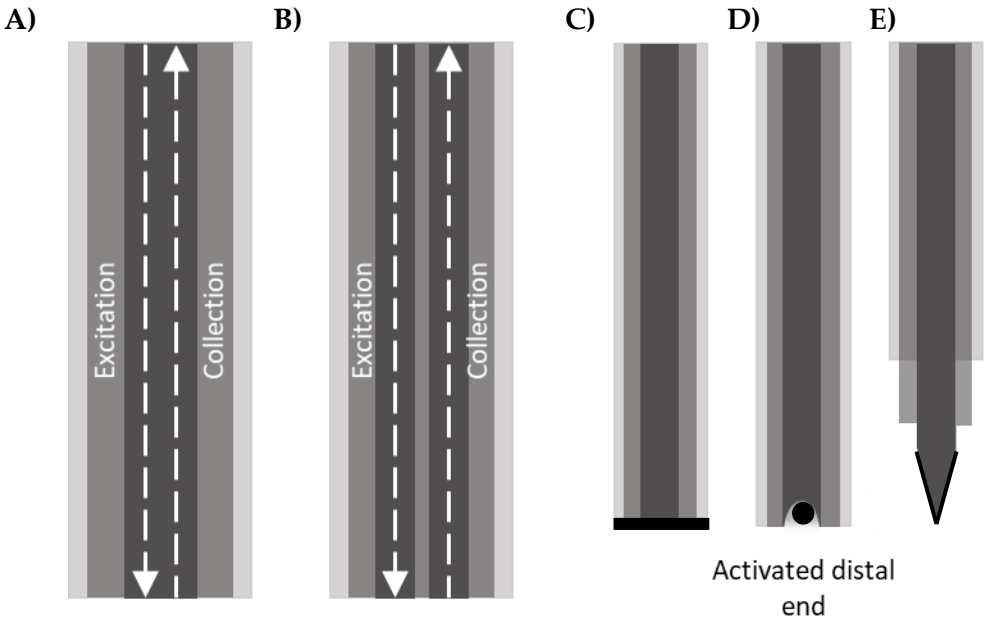

Figure 1.14 Possible optical fibre configurations: A) single fibre bundle used for excitation and collection, B) bifurcated fibre bundle with separate excitation and collection fibres. Activated distal ends with either a C) flat-surface tip, D) etched fibre to leave a pitted core, and E) an etched fibre resulting in a sharpened needle probe.

1.4.5.2 Fibre-Based Applications of Surface Enhanced Raman Spectroscopy

Instrumental design is often a limiting factor in the translation of Raman and SERS to *in vivo* applications, where microscopes or traditional spectrometers may not be ideal. Advances in instrumentation have facilitated remote sensing through an optical fibre.[126,128,138]

When combining SERS with an optical fibre, the fibre can be considered as either active or passive. Employing an endoscopic probe to image and detect SERS particles applied to a biological model (e.g. intravenously or topically) would be considered as passive, where functionalising the fibre probe itself with SERS active particles can be considered active.

Passive fibre applications include imaging SERS particles *in vivo* using a fibre. This can enable the reliable detection of premalignant lesions in animal models that closely mimic disease development in humans.[139–143] Garai et al. developed an endoscope where a rotating mirror enables intraluminal imaging (**Figure 1.15**).[141] Further work by Harmsen et al. used surface-enhanced resonance Raman spectroscopy (SERRS) to enhance sensitivity of particle detection *in vivo*.[139] This technique facilitated the clear definition of tumour margins, with the SERRS-NP signals enabling the detection of much smaller lesions. In particular, SERRS detection does not depend on the morphology of the lesions, or the presence of biomarkers, so that even flat lesions (usually missed with conventional white-light endoscopy) can be seen.[139]

Active optical fibre sensors, where the SERS nanoparticles are attached to the distal end of the fibre, provide an alternative way to measuring physiological parameters.[8,144,145] Typically, modified fibre tips have been developed to measure physiological parameters label-free, dynamic, and in real-time.[128,138,144–146]

There have been methods described in literature detailing the fabrication of SERS fibre probes, from noble metal evaporation or sputtering,[147,148] photo-induced

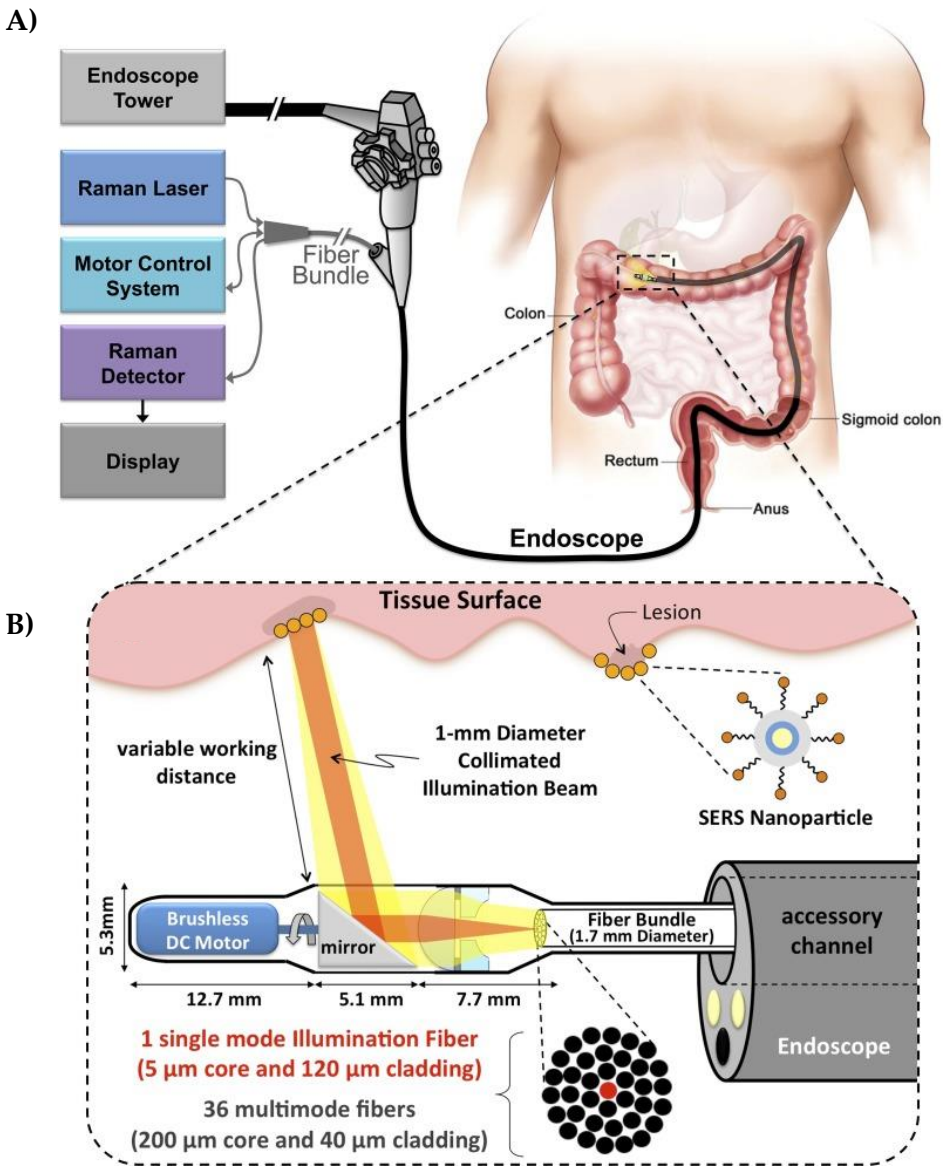

Figure 1.15 Illustration of a Raman-imaging system for the detection of SERS particles. (A) Shows the Raman fibre can be integrated with a clinical endoscope. (B) Schematic of the distal end of the device. The rotating motor allows the mirror to sweep 360 degrees, enabling luminal imaging without requiring tissue contact. (Adapted with permission from reference 141. Copyright 2015 Garai et al.)

deposition of metal nanoparticles,[149,150] and assembly or growth of metal colloidal nanoparticles.[8,76,138,145,151,152] Shape and structure of fibre tips have also been investigated for SERS applications.[138,148] Tapered optical fibre probes have been employed in several remote sensing applications.[145,147,151,152] Liu et al. demonstrated the

remote detection of levofloxacin lactate, and Jin et al. established a method for identifying expired tetracycline hydrochloride, both using tapered optical fibre tips coated in gold nanoparticles.[153,151]

Choudhury et al. developed an endoscope deployable optrode to sense pH within the alveolar regions of an *ex vivo* ovine lung model.[8] Here, an asymmetric dual core fibre consisting of a 2 μm pump core and a 28 μm collection core was used to remove the intrinsic silica background with gold nanoshells functionalised with 4-MBA were attached to the distal end of the fibre (**Figure 1.16**). Using the device, the authors were able to monitor the consequence of ceasing ventilation, which led to the acidification of the alveolar surface fluid over time.[8]

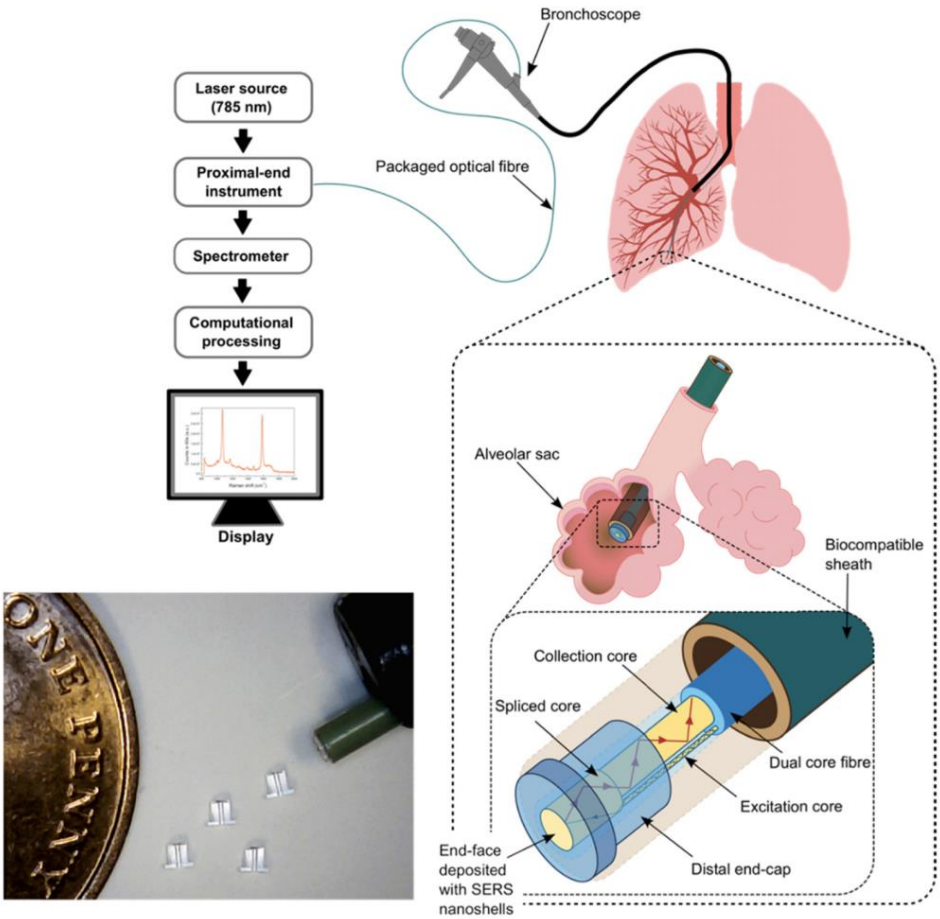

Figure 1.16 Illustration of the optical fibre sensing system for measuring pH. The optrode can be deployed through a conventional bronchoscope, reaching the alveolar region. The sensing fibre consists of 2 cores, a 2 μm excitation core and 28 μm collection core. The face of the distal endcap (outer diameter 1.2 mm) was coated in gold nanoshells functionalised with 4-MBA. (Adapted with permission from reference 8 under the Creative Commons Attribution 4.0 Unported Licence)

1.5 Aims of Thesis

The aim of this thesis was to develop a range of substrates to extend the use of SERS nanosensors in several pH sensing applications: combining nanosensors with an optical fibre, and to also use them within a live 3D cell culture environment.

Fibre-based physiological sensing, particularly within the lungs to reach the alveolar space, presents as a challenge for *in vivo* sensing applications as they are still limited by the size of the sensors. This research presents the development of simple SERS-based optical-fibre sensors to provide a compact and miniaturised sensing system, capable of measuring physiological parameters locations remote to the optical system.

In addition to fibre-based sensing, the substrates for the SERS nanosensors have been utilised as a way of measuring pH of the extracellular space within multicellular tumour spheroids (MTS). MTS are an important tool in cell culture, mimicking the *in vivo* tumour microenvironment more closely than traditional monolayer culture techniques. However, much of the research employing SERS sensing in biological applications focusses on the delivery of nanoparticles intracellularly, measurements concerning the extracellular spaces are somewhat lacking. Thus, these SERS nanosensors substrates have been investigated as a way to measure the extracellular pH within MTS, providing a quantitative tool which could be used to monitor pH changes in response to drug delivery or other types of cancer therapy.

2 Nanosensors

2.1 Surface Enhanced Raman Spectroscopy Nanosensor Selection

There exists a range of molecules capable of responding to changes in pH, where observed spectral changes correspond to either the protonation or deprotonation of the reporter molecule,[51,154] and others where pH alters the aggregation of nanoparticles resulting in an intensity change (*via* formation of hot-spots).[155] The most extensively used SERS pH reporter molecules are 4-mercaptobenzoic acid (4-MBA),[51,105,154,156] 4-mercaptopyridine (4-MPY),[104,157,158] and 4-aminothiophenol (4-ATP).[159,160]

The way in which these SERS nanosensors report on pH is by alterations in peak intensities within their spectra, typically in response to protonation or deprotonation of the sensor molecule. An ideal pH reporter molecule would demonstrate multiple strong SERS signals with ratiometric spectral changes. This could be with a single peak changing with pH against a static reference peak or by means of 2 peaks which change in opposite directions to one another with pH. The sensing range of reporters typically covers ca. 2-3 pH units, centred on the pKa of the sensing moiety. An important point to note when selecting appropriate pH reporters for SERS applications, is that the pKa measured in solution may shift when bound to the surface of a nanoparticle, therefore basing sensor choice solely on the solution pKa's of the unbound molecules may not be helpful.

2.2 Aims of the Chapter

The aims of this chapter are to set out the selection and characterisation of a suitable SERS pH reporter and characterise its spectral responses to pH, followed by the combination of the nanosensors with an optical fibre and similarly demonstrating the response to pH through fibre.

2.2.1 Calibration Set Up

A selection of pH SERS sensors were evaluated by attachment to a particle surface, followed by drying them onto a substrate for analysis with respect to pH. Due to the high Raman signal given by glass slides (**Figure 2.1**), an alternative which eliminates this background signal was prepared. Microscope slides cut to approximately 1 x 1 cm "chips", sputter coated with Cr and Au (3 and 150 nm respectively, by Dr Andrew Garrie (University of Edinburgh, UK)). **Figure 2.1** illustrates the reduction in signal originating from glass when coated with Au.

The set up for pH calibrations (**Figure 2.2**) consisted of the Au coated glass chip glued to a microscope slide, with a self-sealing PDMS superstructure (Schott Nexterion, US) surrounding the chip. Poly-L-lysine (PLL) was used to adhere the functionalised AuNPs by electrostatic forces with the AuNPs. PLL (50 μL, 0.1 mg mL^{-1}) was pipetted onto the gold surface, left for approximately 2 h then rinsed with dH_2O. Functionalised AuNP (~$1.8x10^8$ particles) were added and left to dry completely. Buffers (pH or redox) were then placed within the chamber, and spectra recorded from the submerged chip. Between each buffer, the chip was rinsed with dH_2O. All pH calibration-on-chip experiments involved obtaining the Raman spectra of AuNP (150 nm) functionalised with a reporter molecule (either 4-MBA, 4-MPY, or 4-ATP) while in the presence of different pH buffers. Prior to each experiment, the pH of each buffer was measured using an electrochemical based pH meter (Mettler-Toledo).

Spectrometer choice and its set-up is also an important variable that needs to be controlled. Here, three spectrometers were used; a Renishaw In Via system, an Ocean Optics QE Pro spectrometer, and an in-house built spectrometer.[161] The Renishaw In Via system can achieve a spectral resolution of ~1 cm^{-1}, whereas the Ocean Optics kit has a resolution of 6 cm^{-1}, but has the advantage of being modular and therefore much more portable than the In Via system. The spectrometer built in-house had a 25 cm^{-1} resolution, however it had the advantage of being able to carry out time-resolved measurements.[161–163]

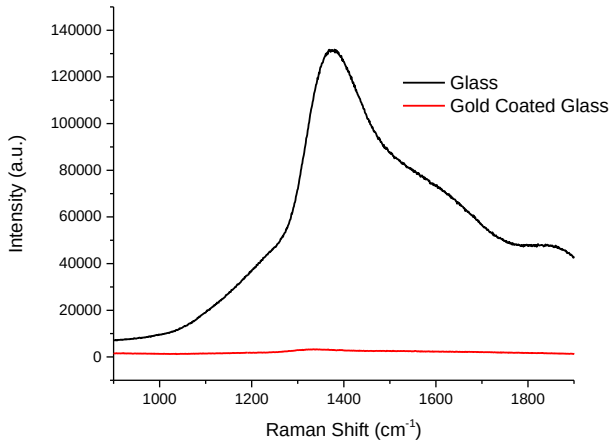

Figure 2.1 Removing Raman glass signal. Raman spectra of glass and gold coated glass (both from microscope slides). Spectra obtained using a Renishaw In Via system, with 785 nm illumination, ~100 mW, 5 accumulations with a 7s integration time.

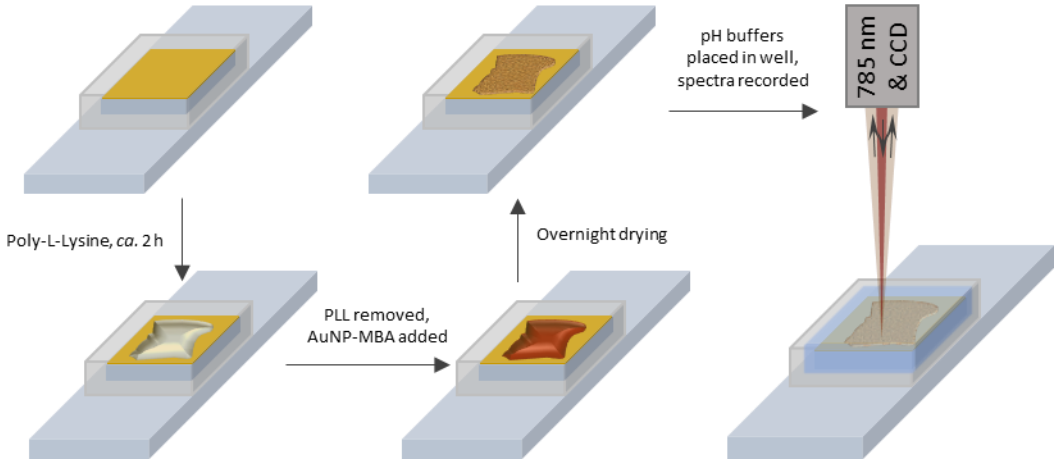

Figure 2.2 Illustration of the calibration set-up. A gold coated glass chip was attached to a microscope slide, surrounded by an adhesive PDMS chamber. Poly-L-lysine (50 µL; 0.1 mg mL^{-1}) was left for *ca.* 2 h, rinsed with dH_2O and functionalised AuNPs (50 µL; 1.8 $x10^8$ particles) and left to dry on the gold surface overnight. The pH buffer (1 mL) was placed in the chamber and the spectra recorded. The buffer was removed, the chip rinsed with dH_2O (1 mL) and new buffer added to the chamber.

2.2.2 4-Mercaptobenzoic Acid as a pH Sensor

4-MBA has been a popular choice for pH based SERS sensing and has been shown to be useful for biological sensing, with many research efforts focussed on intracellular pH measurements.[107,112,147,164]

The Raman modes of 4-MBA have been well characterised and the spectra of 4-MBA on AuNP can be found in **Figure 2.3**.[51,154,164,165] The most prominent features in the SERS spectra are the two intense peaks at 1076 cm^{-1} and 1598 cm^{-1}, due to ring breathing modes[154,164] (**Figure 2.3 (A)**). The visibly less intense peaks at 1400 cm^{-1} and 1707 cm^{-1} exhibit variable intensities dependent on the pH of the surrounding environment (**Figure 2.3 (B)**). These peaks have been assigned to a COO^- stretching mode at 1400 cm^{-1} ($\nu_s(COO^-)$), and a C=O stretching mode of non-dissociated COOH groups at 1707 cm^{-1}.[154,164] A summary of these observations can be found in **Table 2.1**.

The 1st derivative of these spectra ((**Figure 2.3 (C), (D)**) can aid in locating the peak positions, making it easier to see a peak shift occurring between 1396 to 1421 cm^{-1} with increasing pH. An 8-point baseline was subtracted, and peak heights were determined using the peak finding function and the 1st derivative method.

Analysing the spectrum using different peak combinations would provide varied accuracies, so a range of peak combinations were considered for comparison (**Figure 2.4** -**Figure 2.6**). A Boltzmann fit was applied to the calibration data, using equation **2.1**. This equation can be employed to determine pH in a range of biological models, where A_1 = initial y value, A_2 = final y value, $x0$ = calculated pKa (midpoint of the curve), dx = time constant.[166]

A summary of the calculated pKa (with adjusted R^2 values) is given in **Table 2.2**. The calibration plots showed peak combinations vs pH that seemed to demonstrate a wide range of pKa values, largely between 8.99-7.59, with the exception of the plots 1396 / 1076 cm^{-1} and 1396 / 1589 cm^{-1} which gave lower pKa values of around 6.6 (coupled with lower adjusted R^2 values). From these plots, **Figure 2.5 (A)** gave the best fit, with the Boltzmann fit giving an adjusted R^2 of 0.99732 and apparent pKa of 8.9. From the calibration plot in **Figure 2.5 (A)**, pH values between approximately 6 and 10 should be able to be measured accurately. Outside this range the gradient of the curve decreases significantly making measurements less accurate.

$$y = A_2 + \left(\frac{A_1 - A_2}{1 + e^{\left(\frac{x - x0}{dx}\right)}} \right) \qquad \textbf{(2.1)}$$

Rearranged to give pH:

$$x = \ln\left(\left(\frac{A_1 - A_2}{y - A_2} \right) - 1 \right) dx + x_0 \qquad \textbf{(2.2)}$$

$$pH = \ln\left(\left(\frac{A_1 - A_2}{ratio - A_2} \right) - 1 \right) dx + x_0 \qquad \textbf{(2.3)}$$

Deriving pH measurements from the 150 nm AuNP-MBA using the Renishaw In Via system, the ratio between 1397 cm^{-1} ± 25 cm^{-1} (COO^-) and 1707 cm^{-1} ± 40 cm^{-1} (COOH) was used with the following equation **2.4**.

$$pH = \ln\left(\left(\frac{-3.2653}{ratio - 3.5226}\right) - 1\right) 1.02468 + 8.90 \qquad \textbf{(2.4)}$$

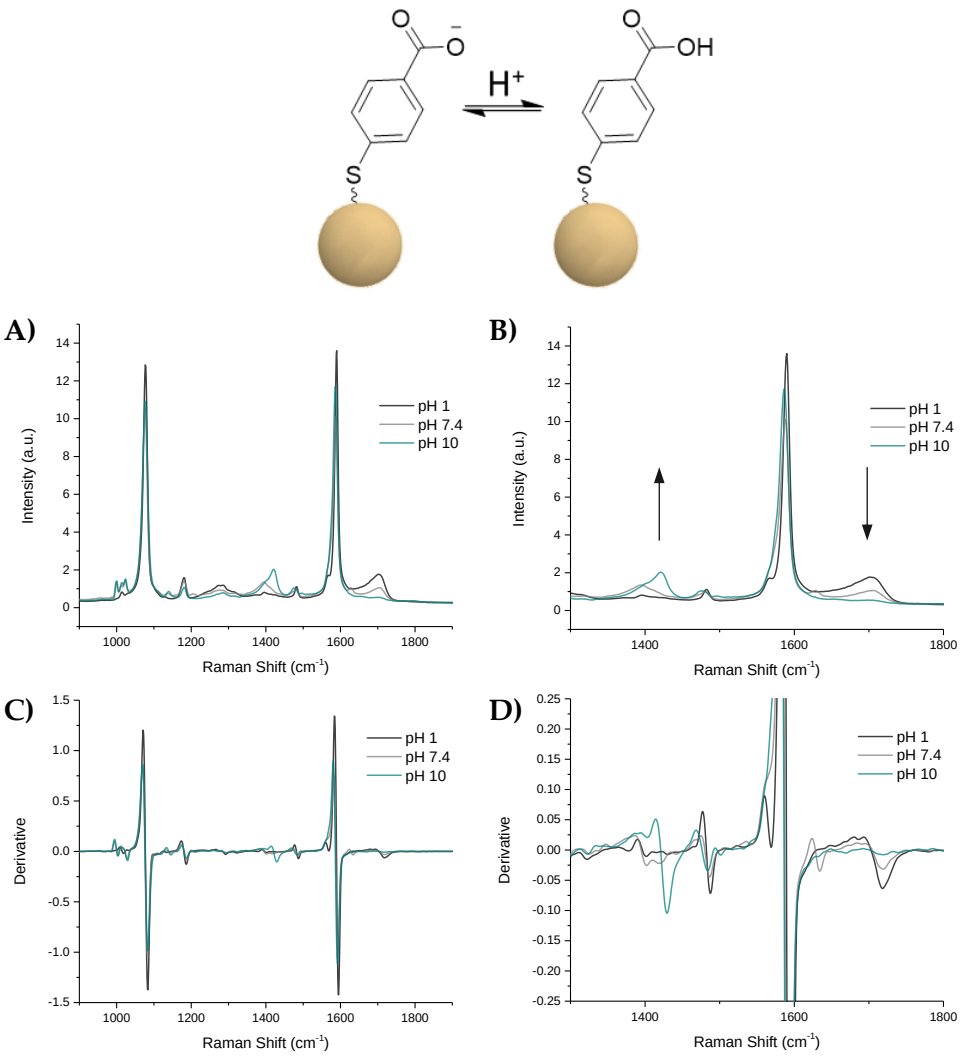

Figure 2.3 Examples of spectral changes of 4-MBA. A) is the general spectrum recorded from 4-MBA, B) is a zoom section highlighting the spectral changes found at 1397 cm^{-1} and 1707 cm^{-1} in more detail, with arrows indicating the direction of change with increasing pH. C) and D) are the 1st derivatives of A) & B) on the same Raman shift scale. Spectra obtained using a Renishaw In Via system, with 785 nm illumination, at 0.1 mW, 60x objective, and 1s integration time.

Table 2.1 Summary of main peaks found from SERS spectra of 4-MBA

Observed Peak Position (cm^{-1})	Assignation	Responsive to pH
1076	Ring breathing	No
1396-1421	COO^- stretch	Yes
1589	Ring breathing	No
1707	C=O stretch	Yes

Table 2.2 Peak and area under curve (AUC) combinations used in calibration plots of 4-MBA.

Calc. Basis	Peak Combination	pKa (from plot)	Adjusted R^2 Value	Figure
AUC	1372-1423 / 1677-1729 cm^{-1}	8.99	0.99082	**Figure 2.4**
AUC	1362-1453 / 1677-1729 cm^{-1}	8.93	0.98496	**Figure 2.4**
AUC	1372-1423 / 1665-1744 cm^{-1}	8.90	0.99732	**Figure 2.5**
AUC	1362-1453 / 1665-1744 cm^{-1}	8.85	0.98744	**Figure 2.5**
Intensity	1396 / 1677 cm^{-1}	8.74	0.99350	**Figure 2.6**
Intensity	1396 / 1076 cm^{-1}	6.66	0.91629	**Figure 2.6**
Intensity	1396 / 1589 cm^{-1}	6.56	0.93951	**Figure 2.6**
Intensity	1707 / 1076 cm^{-1}	7.61	0.98866	**Figure 2.6**
Intensity	1707 / 1589 cm^{-1}	7.59	0.99726	**Figure 2.6**

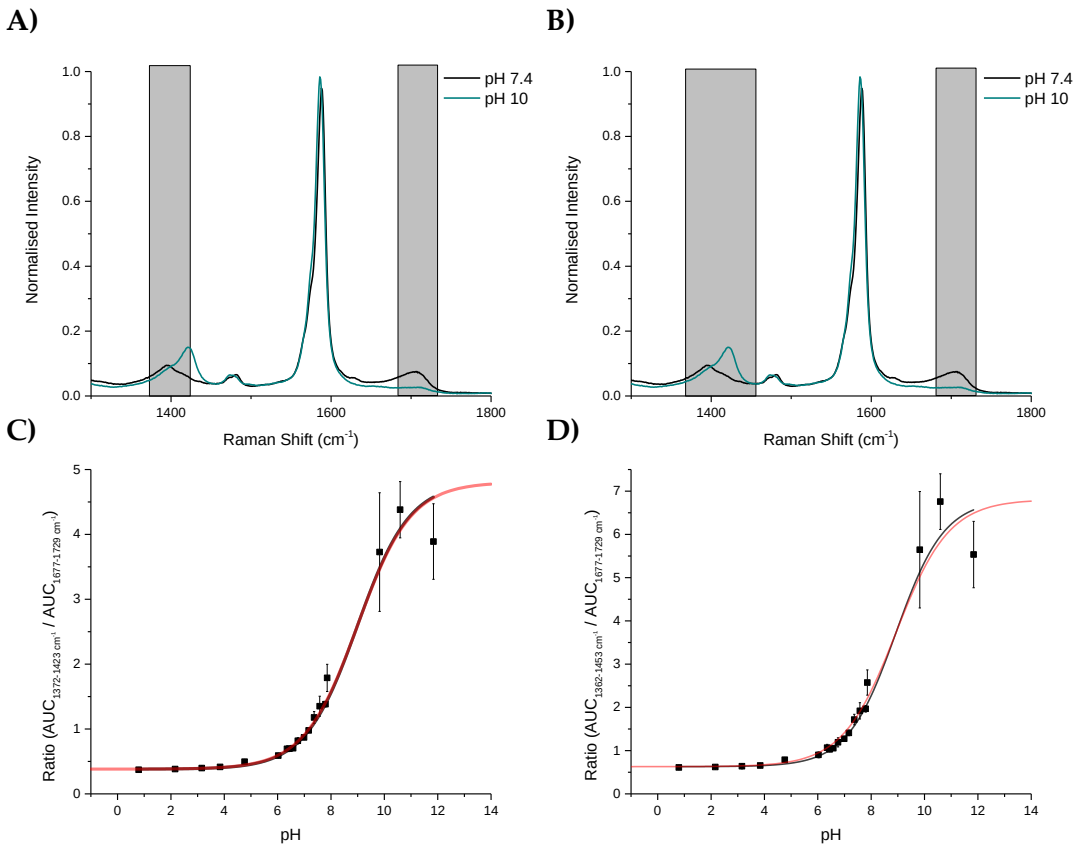

Figure 2.4 Calibration plots using area under the curve (AUC). All spectra were normalised to between 0-1 before integrating pH changing regions at ~1400 cm^{-1} and ~1707 cm^{-1}. Plots A) and B) illustrate the differences between using an integration window of ± 25 cm^{-1} about the 1707 cm^{-1} peak against a ± 25 cm^{-1} window about peak position at pH 7.4 and an integration of the full changing peak area at around 1400 cm^{-1}. Plots C) and D) are derived from the integration of regions highlighted in A) and B) vs pH. The black curve represents a Boltzmann fit to the plotted data, the red curve is the theoretical Henderson-Hasslebach plot derived using the experimentally determined pKa (x0). Spectra obtained using a Renishaw In Via system, with 785 nm illumination, at 0.5 mW, 60x objective, and 1s integration time.

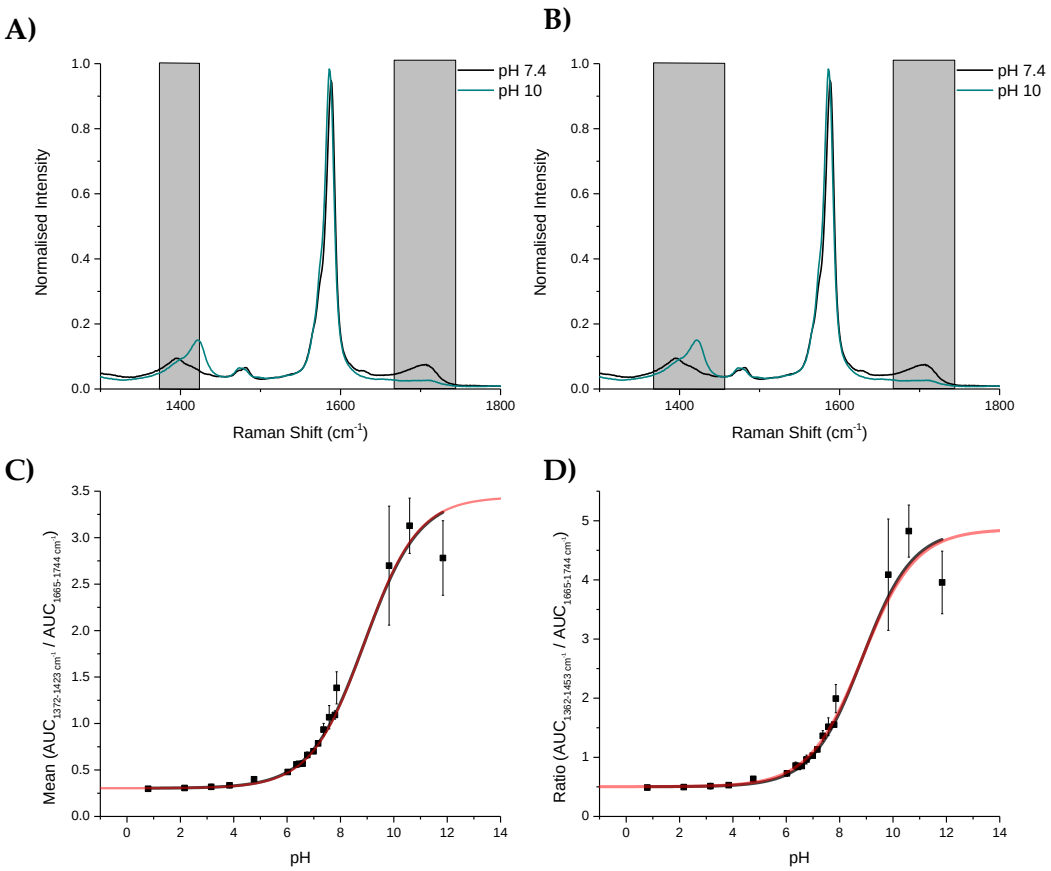

Figure 2.5 Calibration plots using area under the curve (AUC) calculations. All spectra were normalised between 0-1 before integrating pH changing regions at ~1400 cm^{-1} and ~1707 cm^{-1}. Plots A) and B) illustrate the differences between using an integration window of the full changing peak area around the 1707 cm^{-1} peak against a ± 25 cm^{-1} window or the full changing peak area at around 1400 cm^{-1}. Plots C) and D) are based on the integration of regions highlighted in A) and B) vs pH. The black curve represents a Boltzmann fit to the plotted data, the red curve is the theoretical Henderson-Hasslebach plot derived using the experimentally determined pKa (x0). Spectra obtained using a Renishaw In Via system, with 785 nm illumination, at 0.5 mW, 60x objective, and 1s integration time.

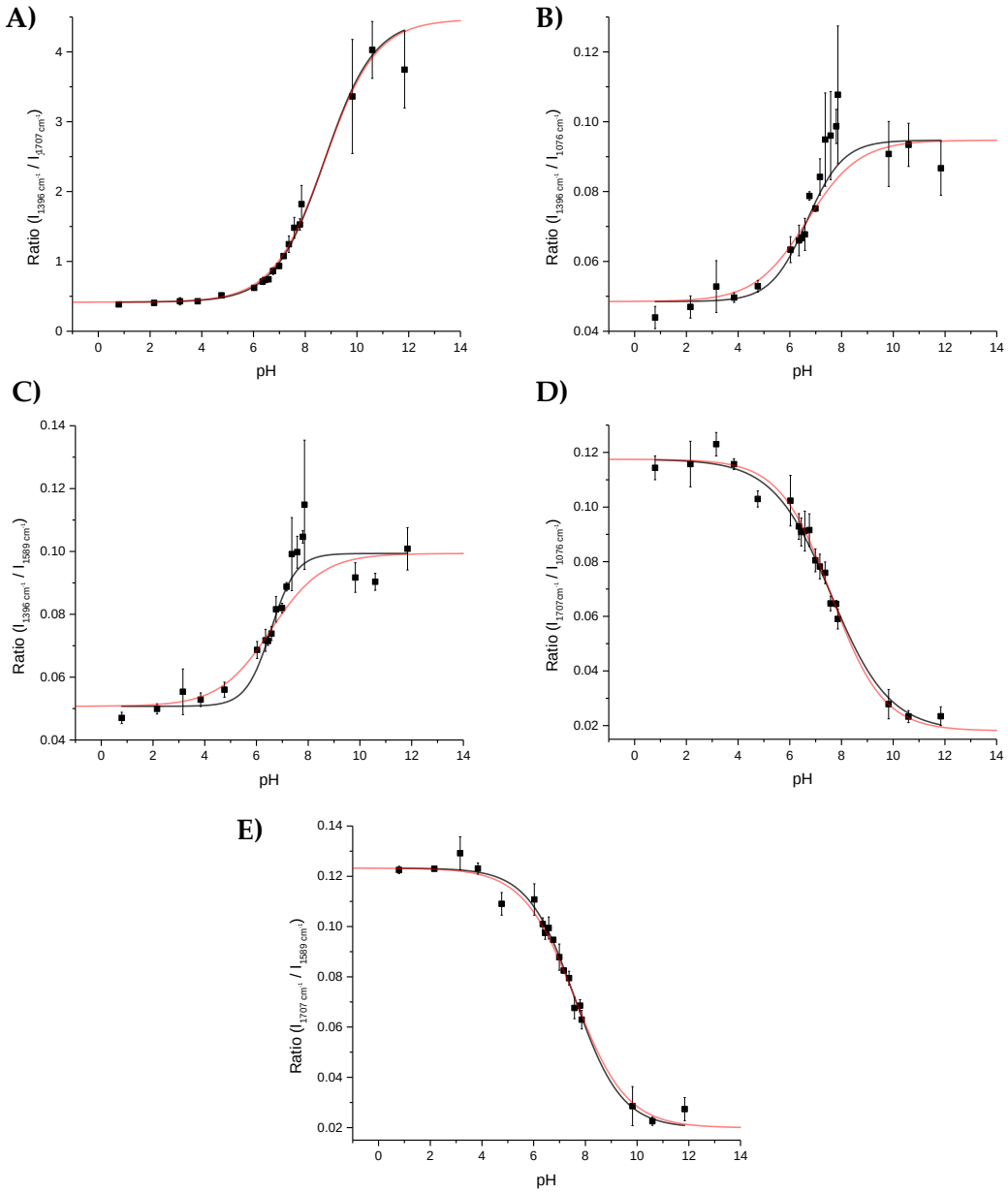

Figure 2.6 Calibration plots using area peak intensities. All spectra were normalised to between 0-1 before integrating pH changing regions at ~1400 cm^{-1} and ~1705 cm^{-1} The black curve represents a Boltzmann fit to the plotted data, the red curve is the theoretical Henderson-Hasslebach plot derived using the experimentally determined pKa (x0). Plots A) represents peak intensity of the 1396 cm^{-1} peak against the peak at 1707 cm^{-1}. B) represents peak intensity of the 1396 cm^{-1} peak against the peak at 1076 cm^{-1}. C) represents peak intensity of the 1396 cm^{-1} peak against the peak at 1589 cm^{-1}. D) calibration plot based on 1707 cm^{-1} peak against 1076 cm-^{1} reference peak, and E) 1589 cm^{-1} reference peak. Spectra obtained using a Renishaw In Via system, with 785 nm illumination, at 0.5 mW, 60x objective, and 1s integration time.

2.2.3 4-Mercaptopyridine and 4-Aminothiophenol as pH Reporters

Other small molecule SERS reporters which respond to pH include 4-aminothiophenol (4-ATP) and 4-mercaptopyridine (4-MPY). **Figure 2.7** illustrates the equilibrium between the protonated and neutral states of 4-MPY and 4-ATP, along with spectra acquired for each reporter at an acidic and basic pH.

2.2.3.1 4-MPY

Five peaks were chosen for calibration calculations, with their peak combinations detailed in **Table 2.3**. The most obvious spectral changes seen between low and high pH in **Figure 2.7** correspond to the relative intensities between the ~1000 cm^{-1} and ~1100 cm^{-1} peaks, the splitting of the peak at ~1600 cm^{-1}, and the varying intensities of the peaks between 1200-1300 cm^{-1}. The observed peaks at 1000 cm^{-1} and 1100 cm^{-1} correspond to ring breathing, with the latter coupled with a C-S stretch. The 1055 cm^{-1} and 1200 cm^{-1} peaks are due to C-H in plane bending of the ring, with the peak at 1600 cm^{-1} due to C=C stretching.

The calibration plots showed peak combinations vs pH that seemed to demonstrate a wide range of pKa values, largely between 7.48-7.90, although there were some pKa values as low as 4.34. While pKa values around 7.5 are relevant for biological applications, their fits to the Boltzmann derived curves were generally much poorer than those of 4-MBA.

2.2.3.2 4-ATP

Five peaks were chosen for calibrations, with the peak combinations detailed in **Table 2.4** Peak combinations for used in calibration plots of 4-ATP. The peak at ~1500 cm^{-1} appeared to be most sensitive to pH, assigned to a b_2-type mode. The peaks at 1077 cm^{-1} and 1581 cm^{-1} are due to ring breathing modes, considered to be insensitive to pH changes.

Calibrations carried out with 4-ATP showed widely variable responses, however, it is known that 4-ATP can dimerize under certain conditions. It has been reported that dimerization (either between nanoparticles or on the same particle) could occur under thermal influences, or under basic conditions.[167,168] This behaviour may add complexity to the sensing ability and as such was deemed to be a less appropriate pH reported that either 4-MBA or 4-MPY.

All calibration plots for both 4-MPY and 4-ATP generally had a poorer fit than those from 4-MBA. For this reason, 4-MBA was selected as a pH reporter for all further work. Further calibration plots based on a range of peak combinations can be found in Chapter 8, Section 8.1, in **Figure 8.1**-**Figure 8.2**.

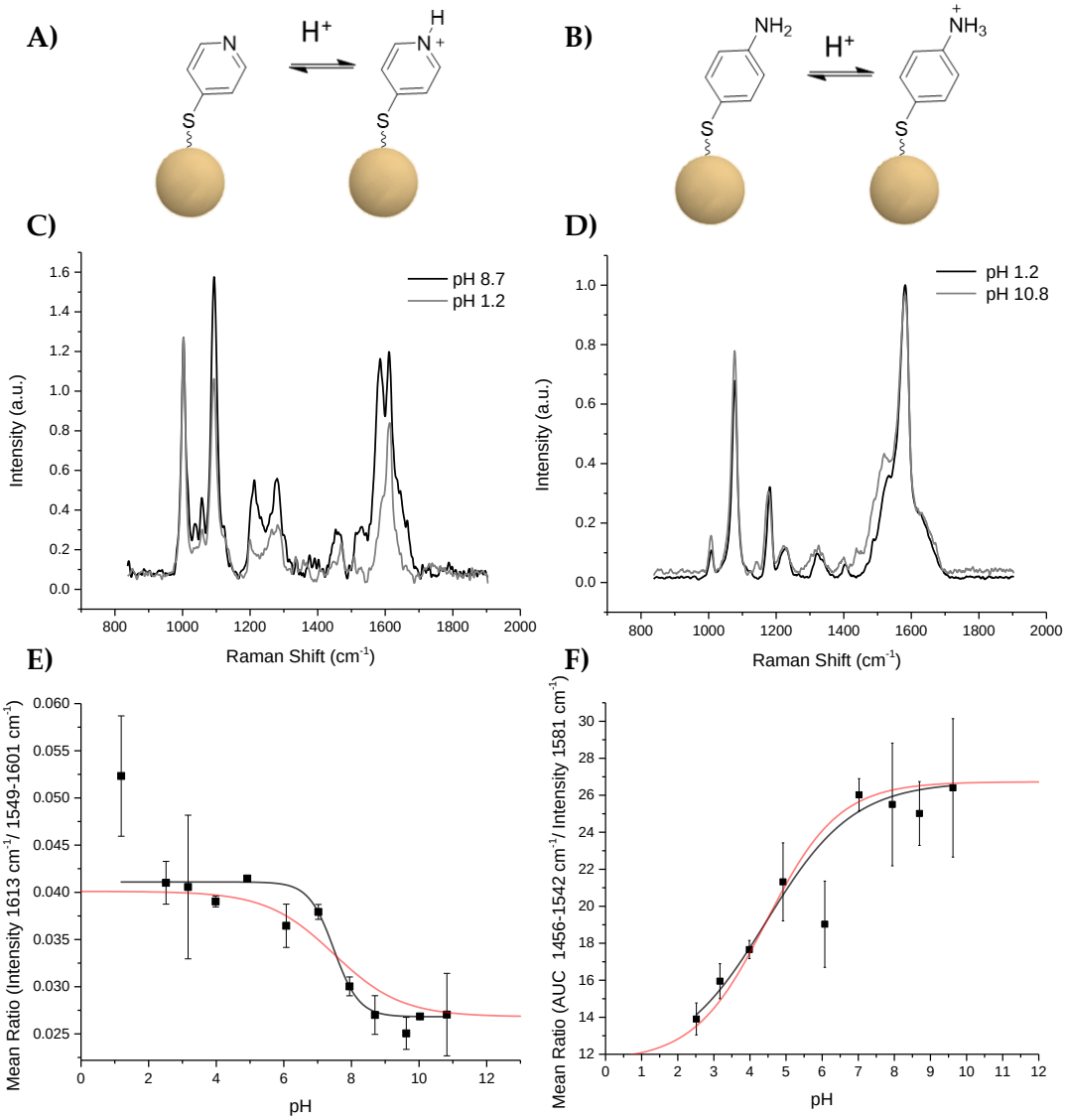

Figure 2.7 Evaluating 4-MPY and 4-ATP as SERS pH sensors. Calibration plots using area and peak intensity. All spectra were normalised to between 0-1 before integrating pH changing regions at the specified points. The black curve represents a Boltzmann fit to the plotted data, the red curve is the theoretical Henderson-Hasslebach plot derived using experimentally determined pKa (x0). Illustrations A) and B) represent protonation of 4-MPY and 4-ATP respectively. Plots C) and D) show spectral changes between an acidic and basic environment. Plots E) and F) peak intensity ratios of the 1613 cm^{-1} peak against area under curve (AUC) between 1549-1601 cm^{-1} for 4-MPY, and AUC between 1456-1542 cm^{-1} against 1581 cm^{-1} for 4-ATP. All spectra recorded using a Renishaw InVia system, with 785 nm illumination, ~0.5 mW, and with a 1 s integration time.

Table 2.3 Peak combinations for used in calibration plots of 4-MPY

Calc. Basis	Peak Combination	Apparent pKa (from plot)	Adjusted R^2	Figure
AUC	1613 / 1549-1601 cm^{-1}	7.48	0.98815	**Figure 2.7**
AUC	1002 / 1549-1601 cm^{-1}	7.66	0.77973	**Figure 8.1**
AUC	1549-1601 / 1002 cm^{-1}	7.83	0.65418	**Figure 8.1**
AUC	1549-1601 / 1613 cm^{-1}	7.59	0.98601	**Figure 8.1**
Intensity	1092 / 1002 cm^{-1}	4.34	0.93636	**Figure 8.2**
Intensity	1002 / 1092 cm^{-1}	4.67	0.89648	**Figure 8.2**
Intensity	1055 / 1002 cm^{-1}	4.96	0.83882	**Figure 8.2**
Intensity	1585 / 1613 cm^{-1}	7.90	0.67106	**Figure 8.2**
Intensity	1613 / 1585 cm^{-1}	7.78	0.80920	**Figure 8.2**

Table 2.4 Peak combinations for used in calibration plots of 4-ATP

Calc. Basis	Peak Combination	Apparent pKa (from plot)	Adjusted R^2	Figure.
AUC	1456-1542 / 1581 cm^{-1}	4.45	0.93093	**Figure 2.7**
Intensity	1077 / 1581 cm^{-1}	3.16	0.90104	**Figure 8.3**
Intensity	1581 / 1077 cm^{-1}	3.88	0.88774	**Figure 8.3**
Intensity	1179 / 1581 cm^{-1}	4.01	0.84741	**Figure 8.3**
Intensity	1439 / 1581 cm^{-1}	7.58	0.47230	**Figure 8.3**

2.3 Surface Enhanced Raman Spectroscopy through an Optical Fibre

As mentioned in Chapter 1, combining SERS sensing with fibre-based sensing would offer advantages as it would allow remote environmental sensing of difficult regions such as the alveolar space. Unfortunately, however, endoscopic sensing has several limitations, such as the strong intrinsic Raman signal generated from the fibre itself (**Figure 2.8**). This is due to when light travels through an optical fibre, it is scattered by silica throughout the whole length of the fibre (**Figure 2.8**). The signal of interest, from a sample in close proximity to the distal end, can be masked by the fibre background. Interference from auto-fluorescent tissue may also cause Raman signals to be masked. There has been some effort to overcome this problem by introducing specialised fibre design, or suppression of background through complex processing methods.[8,169] Through the use of nanosensors and consequently the SERS effect, the signal can be enhanced and so overcome the fibre background issue.

2.3.1 Deposition Variability

As briefly described in Chapter 1, fibre-based Raman sensing must overcome certain challenges in order to become a reliable tool for measuring physiological parameters. These include generating a large enough signal in order to be seen above the often high, intrinsic fibre background.

Using nanoparticles attached to the distal end of a fibre would allow generation of a SERS response to address the limitations outlined above, such as enhancing signal. However, attempts to reliably deposit them onto fibre tips afforded their own difficulties.

Initial studies carried out involved dipping a fibre tip, pre-functionalised with poly-L-lysine, into a concentrated solution of AuNP-MBA (3.6×10^{11} particles mL^{-1}). Though

a simple strategy, the signal afforded from this approach was intense (**Figure 2.8**), easily overcoming the fibre background. However, functionalising the fibre with

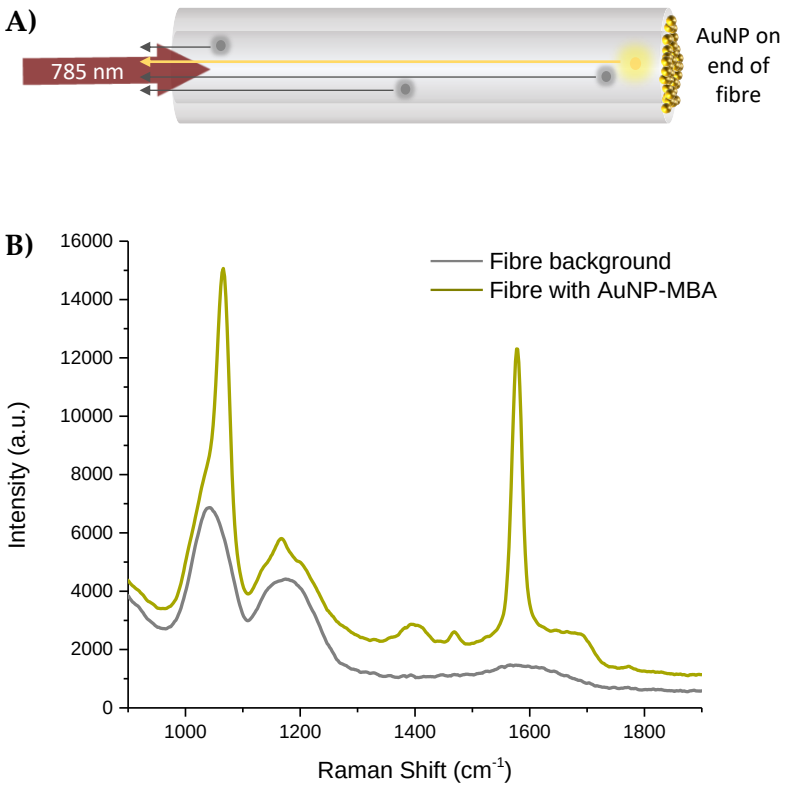

Figure 2.8 SERS signal generated from AuNP-MBA attached to the end of an optical fibre. (A) Light (red arrow) interacts with the fibre core material at every stage, generating a Raman signal (grey). The light continues to the end of the fibre where the AuNP-MBA sensors are located and a SERS signal generated (gold). (B) AuNP-MBA on a fibre. Spectra of the intrinsic background from a 1 m length of fibre (200 μm core diameter, 0.39 NA), and of the same fibre with AuNP-MBA attached onto the distal end. Spectra were recorded using an Ocean Optics QE Pro spectrometer, exciting with a 785 nm laser (ThorLabs), 0.8 mW output power, and 30 s integration time.

AuNPs using this approach often resulted in substantial variability as there is little way of controlling how many nanoparticles were transferred on to the distal end in any single dip. This added a further complication to the functionalisation of the fibre as the addition of nanoparticles to the fibre tip needed to be carried out "live",

meaning that the fibre must first be coupled to the spectrometer to allow real time monitoring of AuNP deposition. It was observed that 3-4 dips of the fibre into concentrated AuNP-MBA solutions was optimal, with additional dipping frequently resulting in loss of signal (**Figure 2.9**).

2.3.2 Effects of Contact

It is realistic to reason that the distal end of the fibre will be in contact with tissue surfaces as well as biological fluids if used *in vivo*. Yet, the transfer of AuNP to the

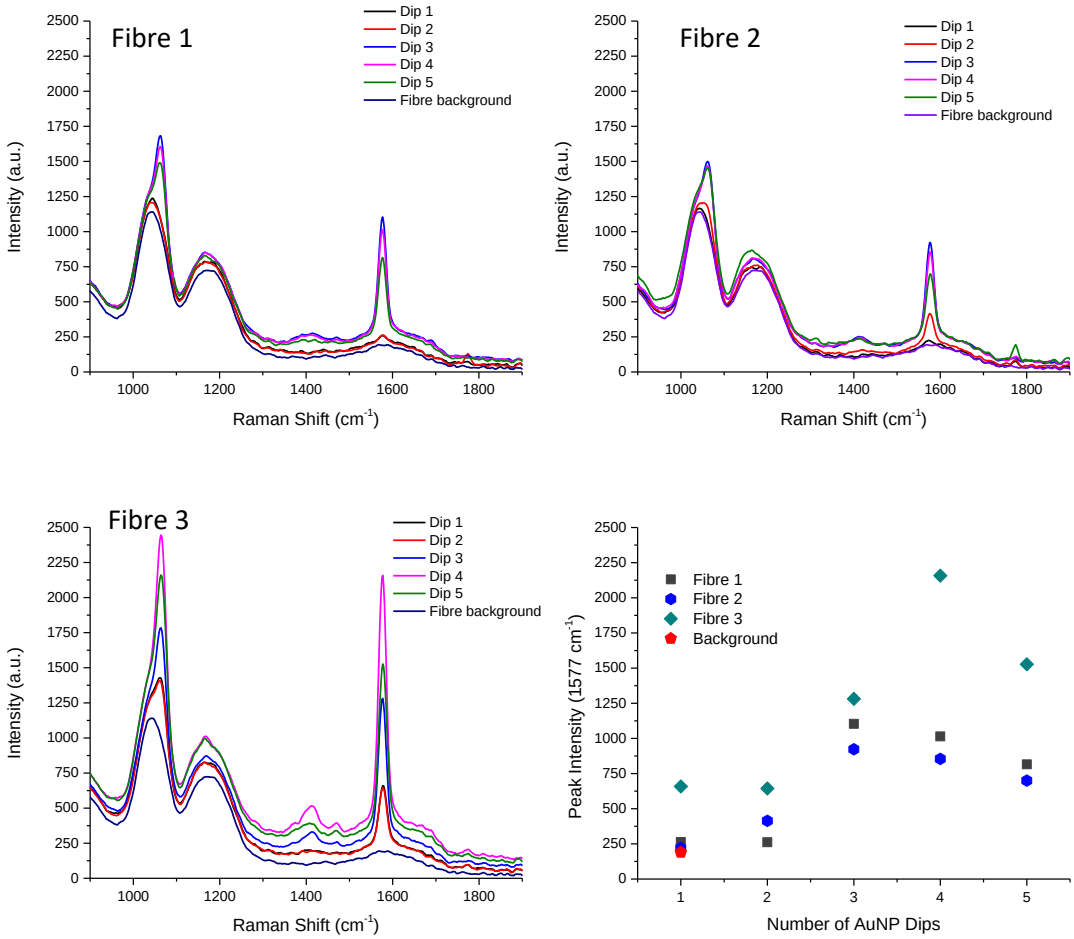

Figure 2.9 Dip coating variation in signal intensity. Measurements taken from 3 fibres, each dipped into a concentrated AuNP solution (3.6 x10^{11} particles mL^{-1}) and their spectra recorded. Spectra obtained using 0.8 mW output power and 30 s integration time. Ocean Optics QEPro spectrometer with a 785 nm excitation source.

sample must be limited. A protective layer (for the fibre and sample) was thus implemented. In addition, use of the fibre without coatings or a protective layer results in significant reduction in signal intensity *via* AuNP loss.

After AuNP deposition (Blot 0, **Figure 2.10**) it can be seen by both the white light image and the Raman map that the AuNPs concentrate around the edges of the fibre, with irregular signals arising across the distal face, however there is a strong signal seen through the fibre which overcomes the background. The unevenness of the AuNPs illustrates the inherent variability of employing a dip coating method. Placing the functionalised fibre into solutions followed by contact with a surface, conditions which might be expected for *in vivo* pH sensing, resulted in a significant transfer of the AuNP from the fibre to the solution or surface and thus a reduction in signal. Spectra recorded after dipping the fibre tip into water and gently blotting against filter paper also demonstrated a substantial reduction of the SERS signal, further exemplified by Raman mapping of the tip of the fibre after each submersion/blot cycle (**Figure 2.10**). The greatest loss of signal was found to be following the first blot, after which the subsequent signal was considered too weak to use carry out pH calibrations using the current commercial system (Ocean Optics QE Pro spectrometer).

As a means to prevent AuNP loss from the end of the fibre, the distal end was coated with a layer of Sol-Gel. Prepared by the hydrolysis of tetramethyl orthosilicate (TMOS) under acidic conditions leads to the formation of SiO_2, first going through a gel state followed by the dehydration to a glass. Sol-Gel provides a porous glassy layer which prevents direct contact between the AuNP and sample while supporting sufficient fluid exchange to allow dynamic sensing. The Sol-Gel layer was prepared *via* the method set out by Grant et al[170] and applied in a similar way to the AuNP deposition, by dipping the distal end of the fibre into an iced solution of the Sol-Gel mixture and allowing to dry overnight under ambient conditions. Though simple in preparation, the resultant surface appears cracked and flaky (**Figure 2.11**) which may pose a risk if in contact with a sample, such as tissue. There are similar considerations to those arising from dip coating the fibre with AuNPs, notably the reliably of the

coating the end in a suitable manner taking in aspects such as the reproducibility of the coating thickness, porosity, while the potential of the of the sol-gel layer to flake may limit the potential scale-up if further translation to an *in vivo* environment is to be considered.

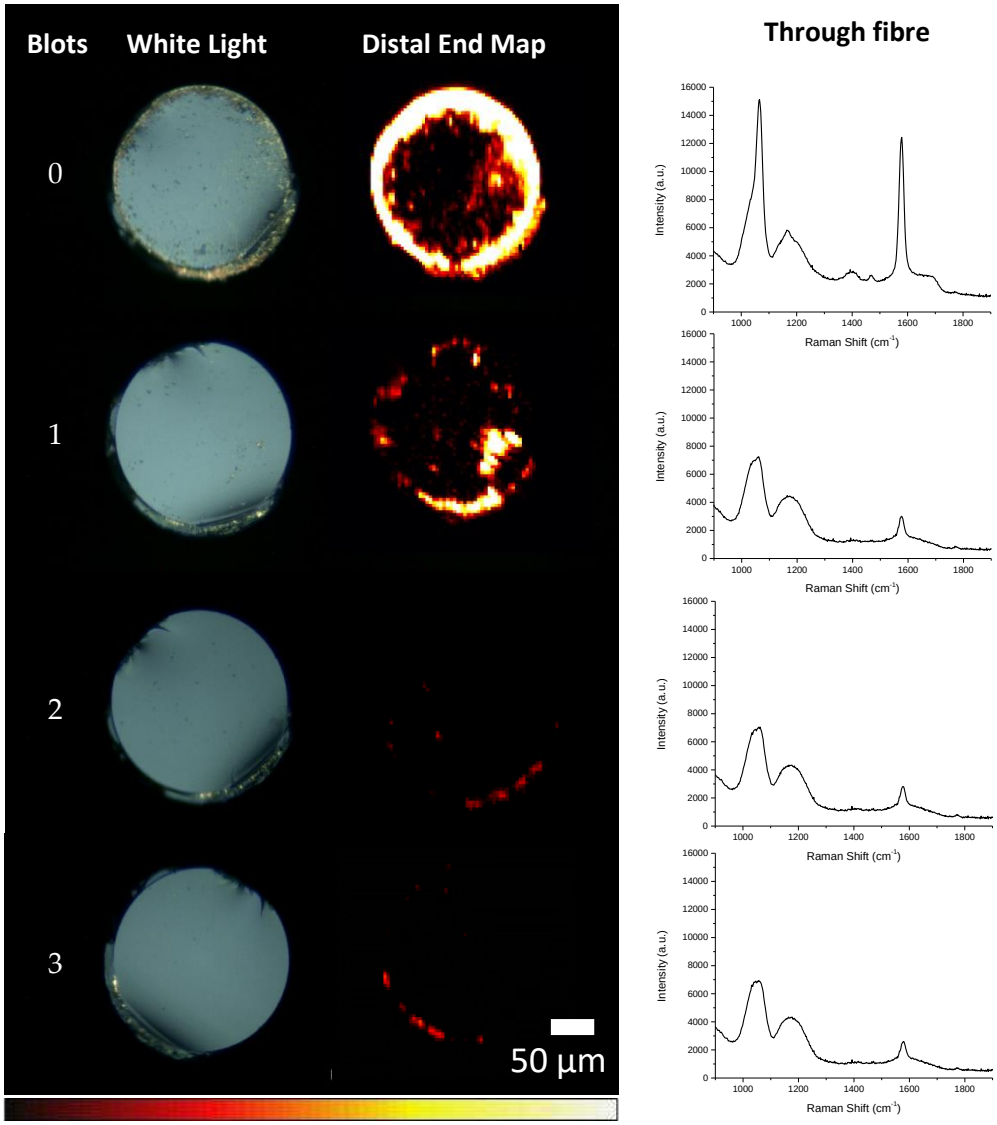

Figure 2.10 Signal over multiple blots. Distal end of an optical fibre (200 µm core diameter, 0.39 NA) dipped into concentrated solution of AuNP-MBA (~3.6 x10^{11} particles mL^{-1}). The fibre was dipped in H_2O and gently blotted on to filter paper. Spectra were recorded after each blot. White light images and distal end maps taken using a Renishaw In Via spectrometer, using StreamLine function, 785 nm laser with ~10 mW power. Colour intensity bar represents arbitrary lower and upper values of 5000 and 100000 respectively. The through fibre spectra were recorded using an Ocean Optics QE Pro spectrometer, 785 nm laser (ThorLabs), 0.8 mW output power, and 30s integration time.

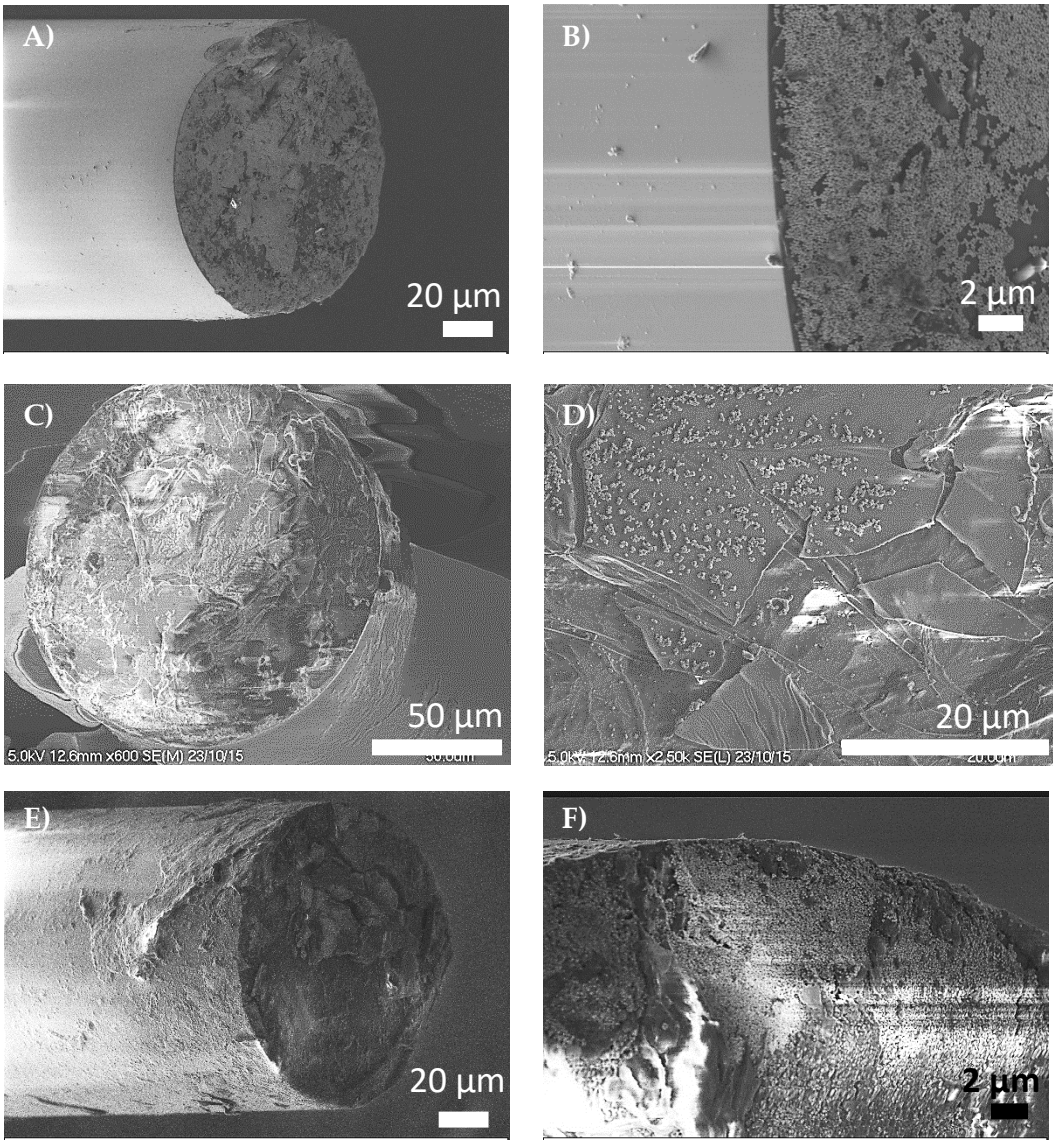

Figure 2.11 SEM image of sol-gel coatings on the distal end of the fibre. A) Fibre with AuNS without a sol-gel coating. B) Close up of AuNS on distal end. C) Fibre tip with sol-gel coating before measurements. D) Expansion of C) showing cracked and flaking nature of the sol-gel coating. E) Distal end after multiple pH calibration experiments. F) Close up of distal tip showing the AuNS still attached.

2.3.3 Overcoming Background

As described above, challenges in combining SERS with a fibre-based approach for dynamic pH sensing applications originate in overcoming the intrinsic fibre background and the entrapment of the SERS sensors. One approach to overcoming this challenge is to employ a sophisticated set up such as time-correlated single photon counting (TCSPC) spectroscopy, to enable a background free Raman spectrum to be produced from a miniaturised fibre probe and enhanced signal from the AuNP to be separated by time.

Work relating to the use of time-resolved spectroscopy was carried out in collaboration with Katjana Ehrlich (Heriot-Watt University, UK) and has been published.[161,171]

TCSPC is typically used for fluorescence lifetime measurements. It allows the measurement of how long a molecule stays in its excited state (following excitation). However, it can be applied to Raman spectroscopy to separate the signal of interest generated from the sample from the background signal generated from the optical fibre thus affording a background free signal.

This approach to reducing the fibre background is a move away from complex fibre designs aimed at tackling the same issue, as it has been shown to work with commercially available optical fibres, providing a low cost means of optical sensing, making it an attractive option.

Raman signal is generated from the interaction of light with the fibre core material when the signal of interest is produced from a relatively small area (**Figure 2.12**). Taking advantage of the different time profiles of fibre Raman scattering and SERS signal, temporal separation of these signals can be achieved. In addition to fibre background suppression, TCSPC can be utilised to separate the SERS signal from fluorescence (**Figure 2.12**).[161]

In a similar way to Section 2.3.1, the distal end of a fibre (2.7 m, 50 μm diameter, 0.22 NA) was functionalised with poly-L-lysine, followed by dipping the end into a concentrated solution of 4-MBA functionalised gold nanoshells (AuNS) while monitoring the signal intensity using a commercial spectrometer. A sol-gel layer was applied before recording measurements.

Comparing non time-resolved measurement obtained from the commercial spectrometer and the time-resolved spectrometer (**Figure 2.13**), it can be seen that the spectra appear visually similar. While demonstrating a higher efficiency (signal amplitudes are larger overall) the slight loss of peak visibility and broadening of the 4-MBA peaks as seen in the spectrum obtained by the time-resolved spectrometer are due to reduced spectral resolution. Post-processing time-gating* allows time windows to be applied after measurements are recorded (**Figure 2.14**) so the fibre

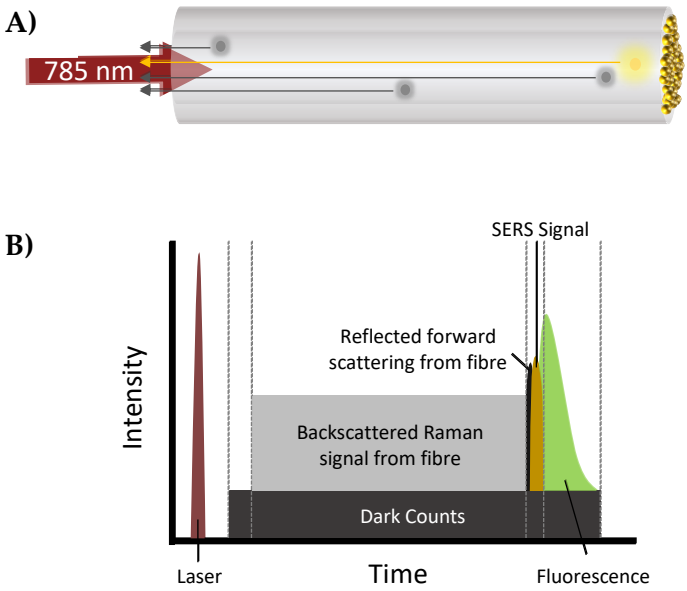

Figure 2.12 Time profiling signals through an optical fibre. A) Light (red arrow) interacts with the fibre core material at every stage, generating a Raman signal (grey). The light continues to the end of the fibre where the nanosensors are located and SERS signal generated (red). B) Illustration of the progression of time signals through an optical fibre (not to scale).

* Measurements obtained and processed by K. Ehrlich (Heriot-Watt University, UK)

background can be removed, resulting in an increase in the signal to noise of the 4-MBA peaks. It is possible to "recover" the true 4-MBA spectra by the subtraction of the measured fibre signal (from the appropriate time window) from the SERS signal **(Figure 2.14)**.

As demonstrated above in **Section 2.2.2**, some of the spectral features of 4-MBA change in response to environmental pH. By taking the ratios of the AUC, within a spectral window of ± 30 cm^{-1} (±4.75 nm) about the peaks of 1380 cm^{-1} (880 nm) and 1700 cm^{-1}(906 nm), and plotting against pH, the advantages to applying TCSPC can be clearly observed (**Figure 2.15**). Comparing the time-gated data with the non-time-resolved data (**Figure 2.15** (A)), the time-gated data clearly shows improved selectivity and a reduction in the standard deviation of the mean, over 3 replicate measurements. Further improvement can be made by increasing the integration time from 10 s to 60 s (**Figure 2.15** (B)).

The ability to separate the signal of interest (e.g. 4-MBA) from the fibre background has other advantages in other applications where there is a large separation between

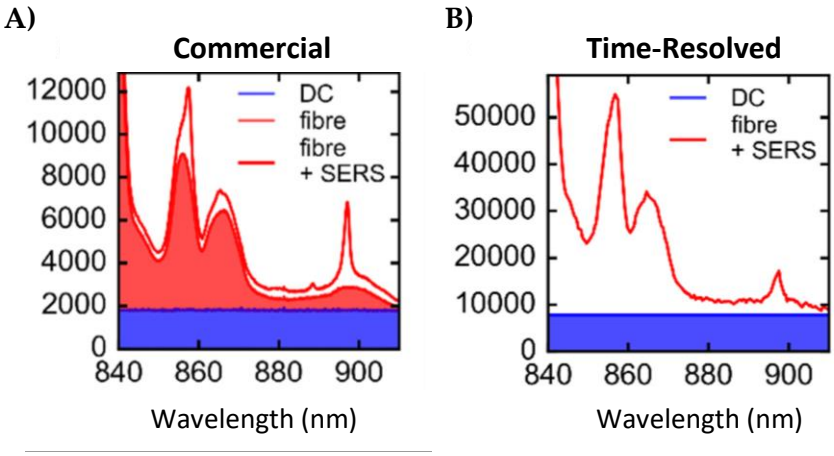

Figure 2.13 Commercial vs time-resolved spectrometers. 10s measurement of a 2.7 m optical fibre with AuNS-MBA at the distal end. A) Spectra of non-functionalised fibre and functionalised fibre obtained using a commercial spectrometer (Ocean Optics, QE Pro). B) Non-time resolved spectra of functionalised fibre obtained using the time-resolved spectrometer. DC: Dark counts. Figures reproduced from K. Ehrlich et *al*. (2017), Optics Express with permission *via* the Creative Common Attribution 4.0 License.

the sample and spectrometer (e.g. oil and gas remote sensing) the fibre background is known to scale with length, and so it becomes more difficult to observe a signal of interest that can overcome the background signal.

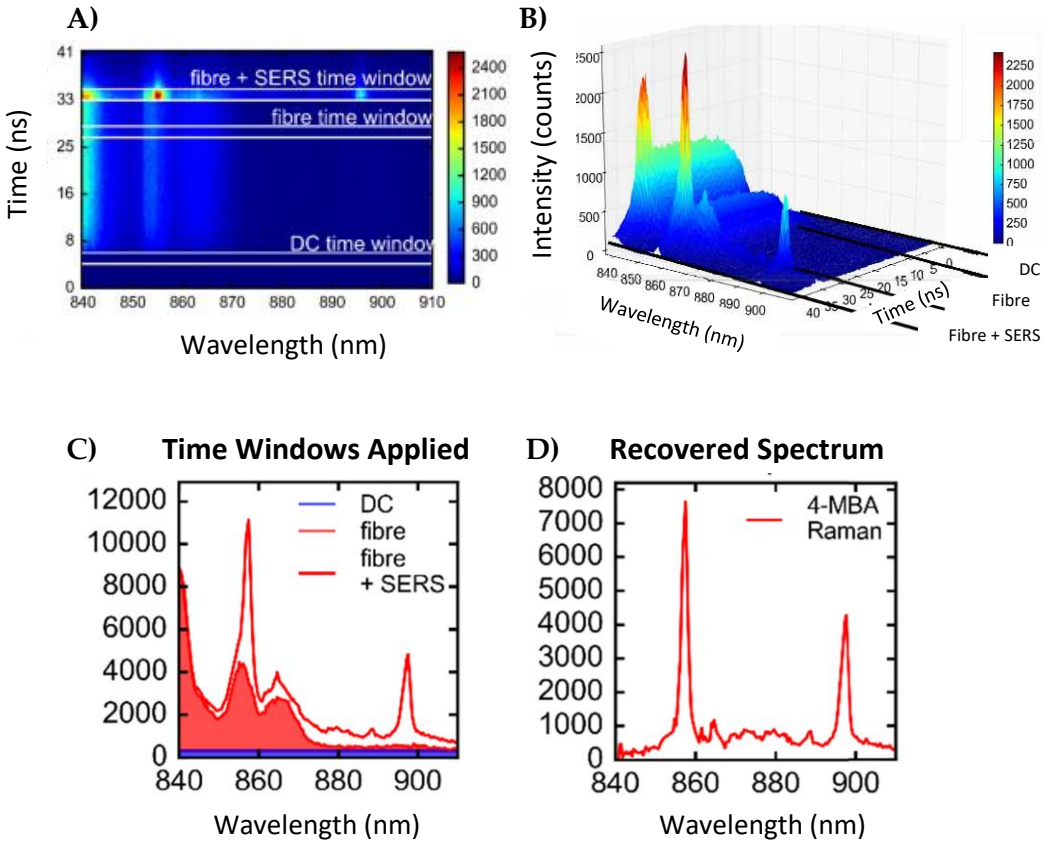

Figure 2.14 Time resolved SERS signal through an optical fibre. 10s measurement of a 2.7 m optical fibre with AuNS-MBA at the distal end. A) Time-resolved measurement represented using colour as an indicator of Raman intensity. B) Time-resolved measurement in a 3-D representation. C) Time-resolved spectra from indicated time windows in A); each window is 2.1 ns. D) Recovered spectrum of 4-MBA on AuNS by subtraction of fibre signal. Figures reproduced from K. Ehrlich et *al*. (2017), Optics Express with permission *via* the Creative Common Attribution 4.0 License. Figure B) reproduced from K. Ehrlich et al., Proceedings Volume 10685, Biophotonics: Photonic Solutions for Better Health Care VI; 106850Q (2018).

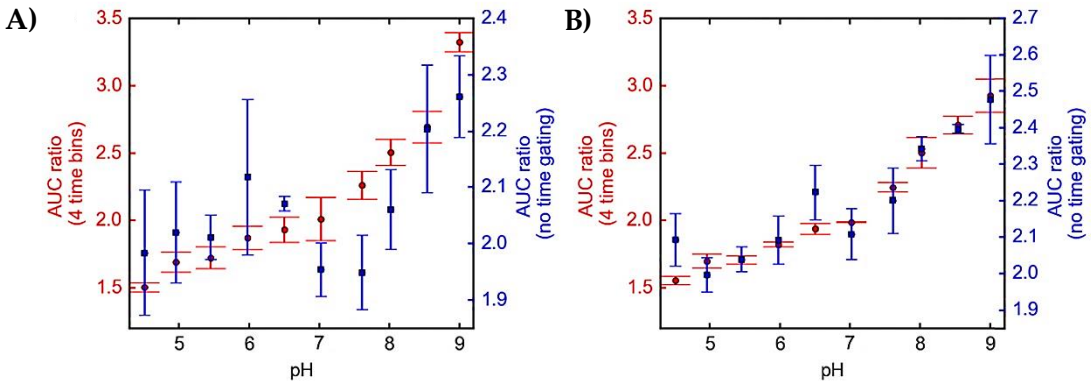

Figure 2.15 Conventional vs time resolved pH sensing. AUC ratios (± 30 cm^{-1} around 1380 cm^{-1} and 1700 cm^{-1} peaks) against pH, between pH 4.5-9.0. Red data points represent time-resolved measurements, blue data points represent non-time-resolved measurements. Measurements obtained using average excitation power of 0.8 mW and 20 MHz pulse repetition rate. A) 10 s integration time. B) 60 s integration time. Figure reproduced from K. Ehrlich et *al*. (2017), Optics Express with permission *via* the Creative Common Attribution 4.0 License.

2.4 Conclusions

Here, several small molecules were evaluated as potential SERS pH reporters (4-MPY, 4-ATP, and 4-MBA). AuNP functionalised with 4-MBA demonstrated the best pH sensitivity over a physiological range (pH 4-9), and thus proved to be the most suitable pH SERS reporter molecule for biological applications.

Following nanosensors selection, AuNP-MBA were deposited on the end of an optical fibre for remote sensing. During this process several limitations were overcome: preventing the loss of AuNPs from the distal end of the fibre, and the intense signal from the fibre background.

Loss of AuNPs was negated by the application of a Sol-Gel layer, providing a porous layer enabling fluid exchange to occur. Overcoming the intrinsic fibre background was achieved by combining time correlated single photon counting spectroscopy (TCSPC) with SERS fibre-based sensing. TCSPC facilitated the temporal selection of the SERS signal, thereby diminishing the impact of the signal generated by the silica fibre. The TCSPC set up clearly demonstrates a strong improvement in sensing capabilities over conventional Raman spectroscopy, despite the sophisticated set up.

3 Polymeric Substrates for Nanosensors

3.1 3D Surface Enhanced Raman Spectroscopy Substrates

SERS sensing substrates while applied to a variety of surfaces, are usually deposited on to a 2D surface, making them easier to locate. Here macroscopic particles (5-300 μm) were loaded with functionalised NPs for SERS-based sensing as a means of forming localised hot-spots of NPs in a controllable manner, while also providing a method to locate and track particles easily due to their size, offering robust SERS-based sensors.

The immobilisation or encapsulation of nanoparticles into a larger microsphere has been demonstrated to have a wide variety of uses, in part due to ease of tracking as well as the potential for multiplexed measurements. Applications include high-throughput suspension arrays, biological labelling, drug delivery, magnetic resonance imaging (MRI) contrast enhancement, and catalysis.[172–178] However, the use of macroscopic substrates for SERS sensors is still relatively uncommon. The immobilisation of nanoparticles onto a larger resin bead has been demonstrated for so-called "barcoding" applications, largely related to solid-phase peptide synthesis, using this approach to monitor reaction progression.[179–181]

3.2 Aims of the Chapter

In this chapter, a method of producing spherical macroscopic scaffolds loaded with SERS sensors for fibre-based sensing applications as well as cellular analysis within 3D culture is demonstrated.

3.3 Development of Spherical SERS Scaffolds

Resins typically used for solid-phase peptide synthesis have proven to be an incredibly useful basis for 3D SERS scaffolds. Amine functionalised polystyrene-PEG-based beads have proven to be an easy to handle tool which allowed simple manipulation of the NPs for SERS based sensing applications.

3.3.1 Loading Efficiencies

The amine functionalised TentaGel beads (0.5 mg, 10 μm) were incubated with citrate capped AuNPs (150 nm, 1.5 mL, 3.6 $x10^9$ particles mL^{-1}). The AuNP uptake was readily observed by eye, with the beads generating a strong red colour within a few hours (**Figure 3.1**) indicating substantial uptake of the AuNPs by the beads. Due to the relatively large size of the TG beads sedimentation of the TG-AuNP conjugates occurred on a timescale of minutes, allowing simple visual inspection of the supernatant to assess loading. It was found that adding 1.4 $x10^{10}$ particles AuNPs to 1 mg of TG resin resulted in saturation of the beads, leaving some AuNPs in the supernatant (**Figure 3.1**). Also noticeable was the colour intensity of the sedimented pellet, which unsurprisingly afforded a more intense colour with increasing addition of AuNPs.

SEM images of the TG-AuNP beads showed a fascinating surface morphology (**Figure 3.2**) with the protrusions of the nanoparticles clearly visible across the beads' surface. To examine this in more detail the beads were "sliced" and imaged by TEM.

This showed that the beads had not penetrated deeply into the bead due to their size (TentaGel beads have a molecular weight cut off of about 2000-3000 Da)[182,183] but were immobilized on the surface of the beads. As **Figure 3.2** shows, the AuNPs formed small aggregates, which is known to enhance the SERS effect.[29] Thus, having the AuNPs localised to the surface of the TG beads is actually preferable as opposed to dispersing them throughout the bead. In addition, there is confidence that a true representation of the bead's environment will be recorded in regards to pH analysis.[182–184]

Further characterisation of loading was carried out by assessing signal intensity of the 1587 cm^{-1} peak vs number of AuNPs added per 1 mg of TG resin (**Figure 3.3**). SERS maps show representative spectra taken from each map illustrating the intensity of the reference peak at 1587 cm^{-1}, with a darker red colour indicating a lower signal

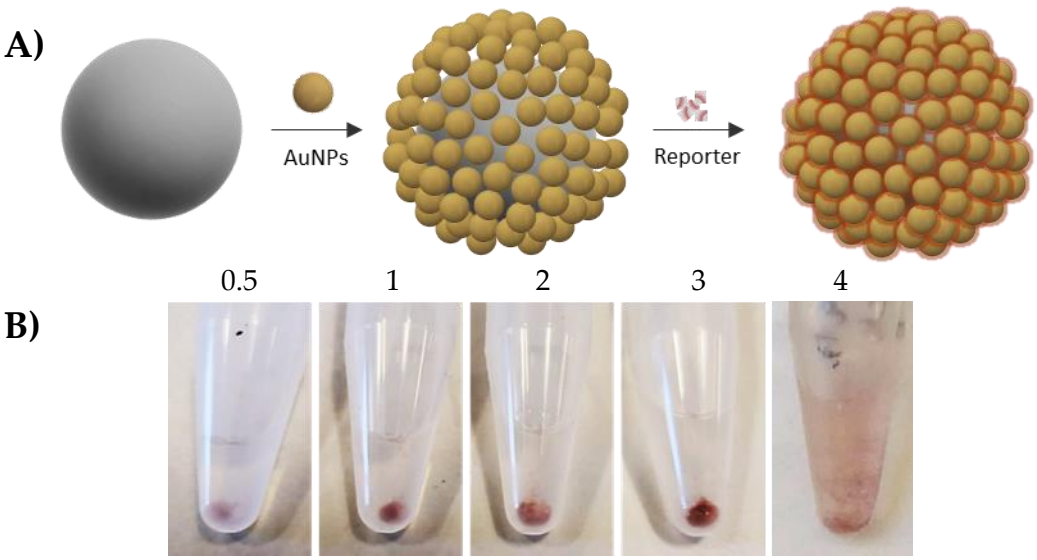

Figure 3.1 AuNPs incubated with TentaGel beads. A) Generic preparation method of labelled TG-AuNP conjugates. B) Loading of AuNPs *via* increasing ratio of AuNPs (150 nm) to TG beads (10 μm, 0.1 mg). L-R: AuNP:TG (v:w), 0.5:1, 1:1, 2:1, 3:1, 4:1.

intensity, and the lighter yellow colours indicating a higher signal intensity. **Figure 3.3** shows an obvious difference between samples 0.5 to 2, with a somewhat less obvious intensity increase between samples 2 and 3. The intensity increase between 2 and 3 was confirmed by looking at individual spectra from the maps. From this data, most of the work was carried out with a ratio TG:AuNP of 1:3 (w/v; 1 mg: 1.1 x 10^{10} particles AuNP).

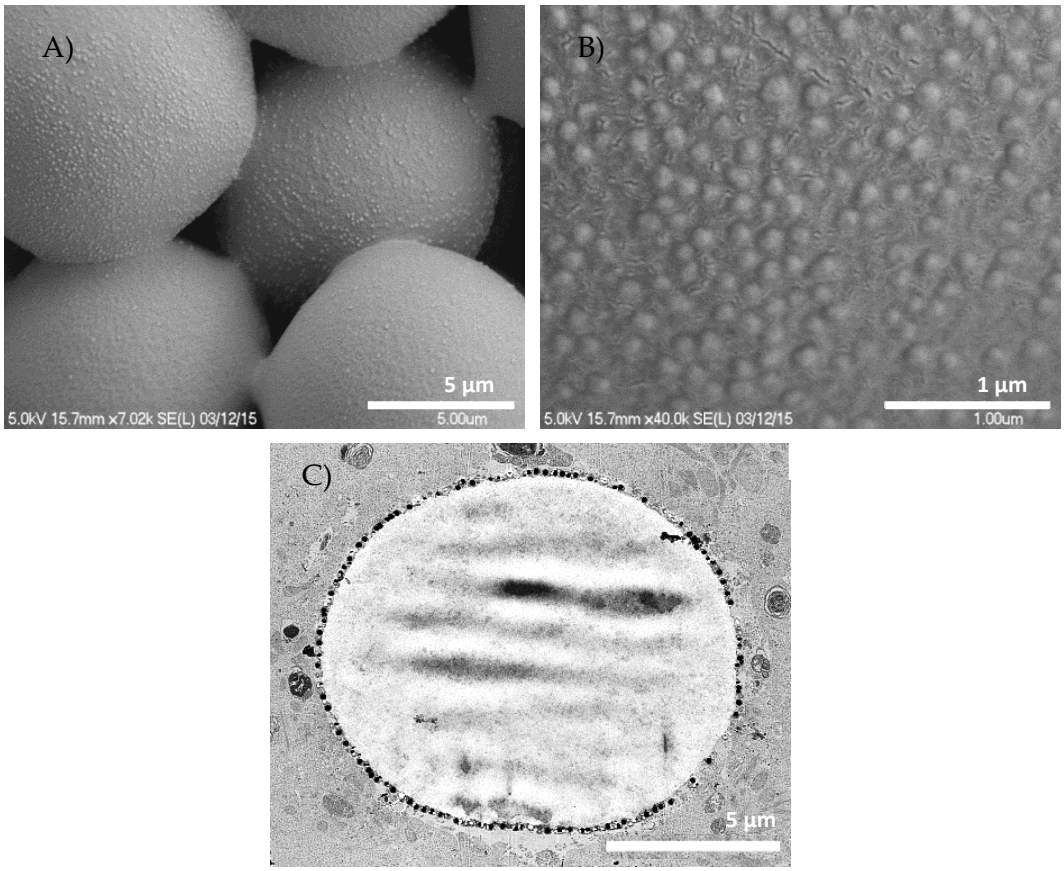

Figure 3.2 SEM and TEM images of TG-AuNP. A) and B) SEM images of 10 µm TentaGel beads loaded with 150 nm AuNPs showing a high density of AuNPs embedded on the surface of the resin particles. C) TEM image of a 10 µm cross-section through a 10 µm TG bead loaded with unlabelled 150 nm AuNPs showing a strong localisation of the AuNPs on the outer surface of the microsphere.

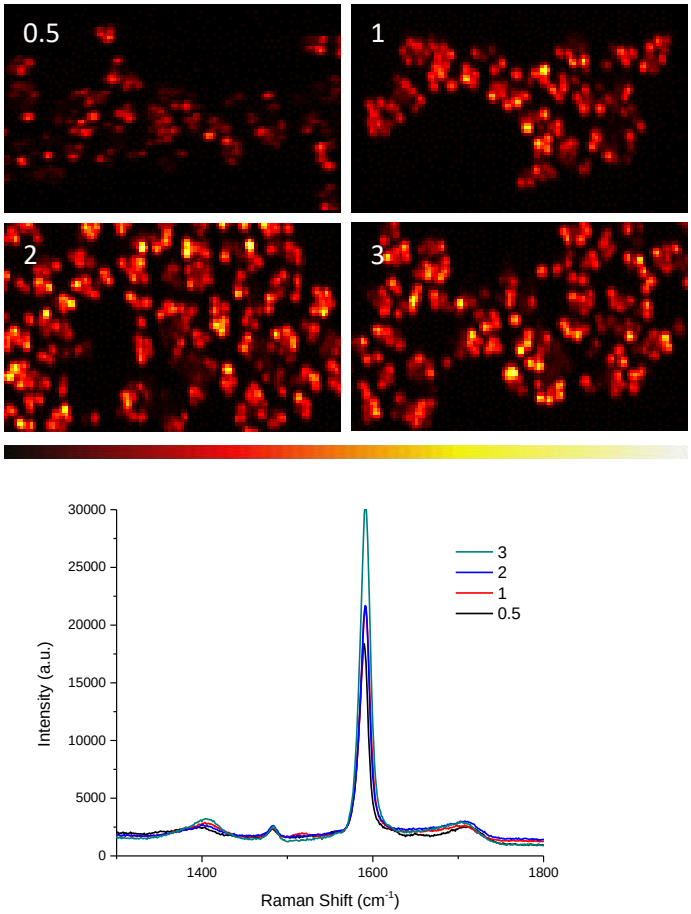

Figure 3.3 TGs loaded with varying concentrations of AuNPs. AuNPs (150 nm) conjugated to TentaGel beads (10 μm) in various ratios; AuNP:TG (v:w), 0.5:1, 1:1, 2:1, 3:1. Intensity Raman maps and representative spectra are shown for each condition are shown. StreamLine configuration used with 785 nm excitation source, 2 s integration time, 0.1 mW, 20x objective. Colour bar represents the 1587 cm^{-1} peak intensity with upper and lower limits of 0 and 700000 respectively.

3.3.2 Effects of Surface Charge on TentaGel-Nanoparticle Loading

To investigate the effect of surface charge on loading efficiency, the amino functionalised TentaGel beads were modified by capping with either an acetyl group (TG-Ac) or a carboxylic acid group (TG-C_4H_8-COOH or TG-PEG-COOH). The amino group (TG-NH_2) is protonated at physiological pH and the beads displayed a positive zeta potential (+14.6 ± 1.89 mV), which upon capping with acetic anhydride (to produce an amide: TG-Am) gave beads with a zeta potential of 5.76 ± 1.33 mV. The coupling of adipic acid or PEG bis(carboxymethyl) ether induces a negative charge on the beads at physiological pH with the resulting TentaGel beads (TG-C_4H_8-COOH or TG-PEG-COOH) having a zeta potential of -22.9 ± 1.52 mV and -22.1 ± 1.95 mV respectively (**Figure 3.4**). When treated with the citrate capped AuNPs (-29.7 ± 1.32 mV, **Figure 3.5**) the "surface change" was shown to have a dramatic effect on AuNP uptake (**Figure 3.4 (C)**) – with only the original TG-NH_2 beads showing uptake (likely due the positive charge on the TentaGel beads and the negative charge on the citrate coated AuNPs).

To explore further the effect of whether surface charge was the driving force behind uptake, or the physisorption of the amine groups on the TGs interacting with the gold, the AuNPs were functionalised with 4-MBA (0.1 mM) or PLL (0.1 mM), resulting in zeta potentials of -27.45 ± 2.61 and +17.78 ± 1.92 mV respectively (**Figure 3.5**). After combining the modified TGs with the functionalised AuNPs overnight (TG:AuNP 1:2, w/v), forcing the conjugates back into suspension, the particles were allowed to settle over a period of about an hour (**Figure 3.5 (B)**). The best uptake, as observed by the formation of a pellet, is from the combination of 4-MBA functionalised AuNPs with the positive zeta charged beads (TG-NH_2 and TG-Am). There was a slight appearance of conjugates forming in a pellet from the combination of positively charged AuNPs (PLL) and negatively charged TGs (TG-C_4H_8-COOH and TG-PEG-COOH), again hypothesized due to the complementary charges on the particles. However, all modified samples contained a reddish supernatant, indicating that not

all AuNPs were taken up by the TGs. This is in contrast to combining, in the same proportion (TG:AuNP, 1:2), unfunctionalised AuNPs with unmodified TGs (TG-NH_2) which results in a complete uptake of the AuNPs, leaving a clear supernatant (**Figure 3.4 (C)**).

While complementary surface charges have been shown to affect AuNP uptake, it is well known that certain functional groups such as thiolates, amines, and phosphines

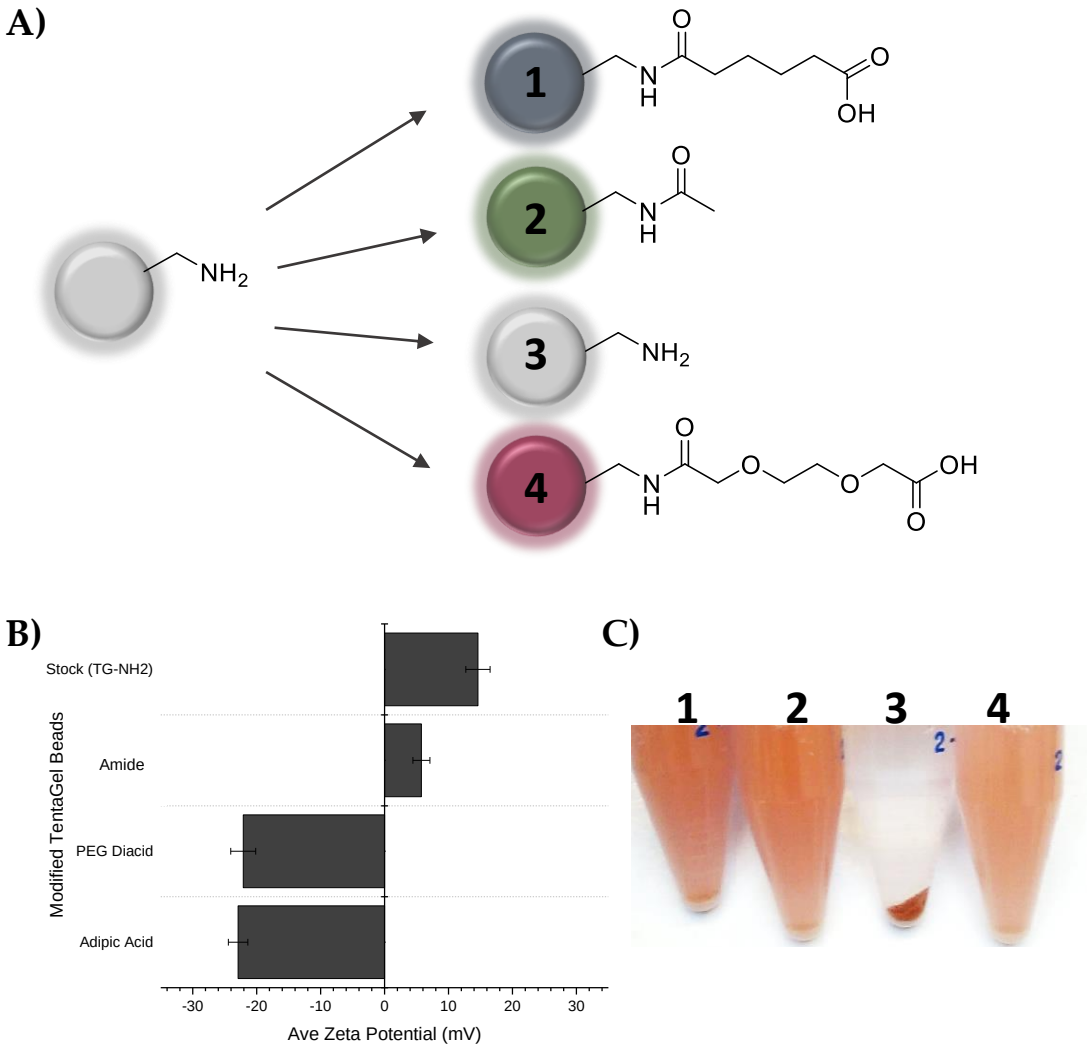

Figure 3.4 Modification of TG Beads. A) Amino functionalised TG beads were modified with adipic acid or poly(ethylene glycol) bis(carboxymethyl) ether (1 and 4, respectively), with an amide group (2), or left unmodified. B) Zeta potential measurements of the modified TG beads. C) Images of the corresponding modified TG beads combined with unfunctionalised AuNPs after an overnight incubation, showing AuNP uptake is best with the unmodified TGs (NH_2).

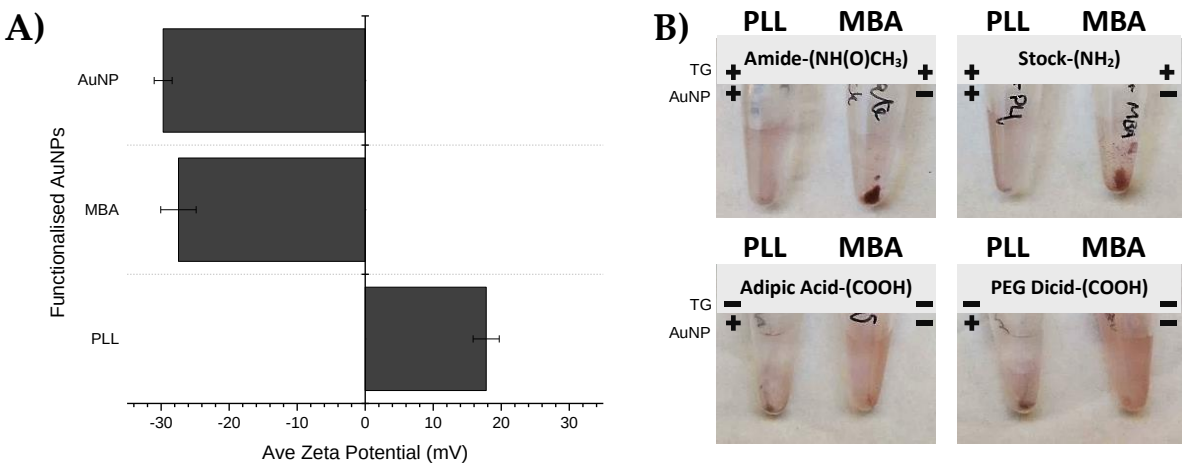

Figure 3.5 Effect of surface charges on AuNP uptake into the TG beads. A) Zeta potential measurements of unfunctionalised, 4-MBA, or PLL functionalised AuNPs. B) Visual illustration of uptake between functionalised TG beads with PLL or MBA functionalised AuNPs. The +/- denote zeta potential of the TG beads (in grey rectangle) and of the AuNPs (overlaid in image).

have a strong affinity for gold.[185–191] Considering this, it is simpler to combine TG-NH_2 with unfunctionalised AuNPs prior to functionalisation with a SERS reporter. However, for TG-AuNPs functionalised with multiple SERS reporters another strategy may be required.

Concentration studies were carried out on unmodified TG beads loaded with AuNPs, functionalising the TG-AuNPs with between 0.1 mM to 1.0 mM 4-MBA. All samples were analysed in solution as well as dried on to gold substrate, displays the intensity across concentration at 1587 cm^{-1}. This peak, due to ring breathing, was chosen to measure intensity as it the strongest peak present in the 4-MBA spectrum, and remains constant across changes in its environment.[51,112] Six separate spectra were recorded across the samples then averaged. The nature of drying TG-AuNPs down onto a solid surface can lead to a non-uniform layer consisting of large aggregates.

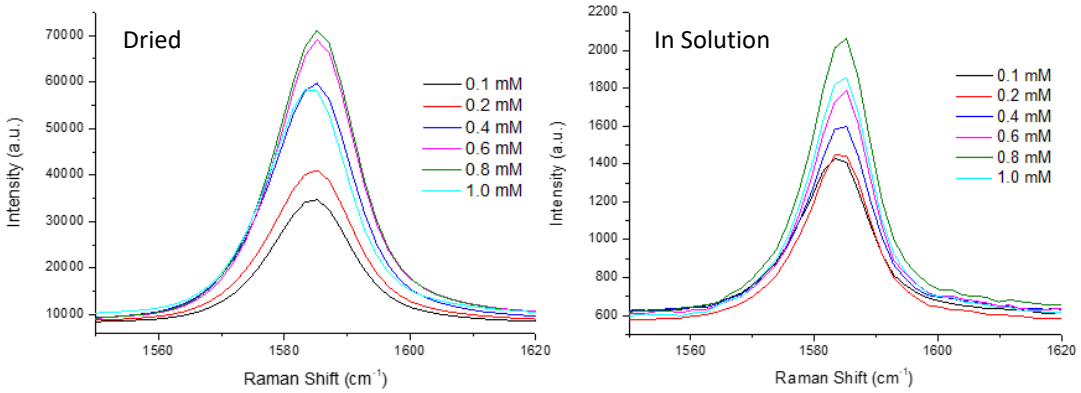

Figure 3.6 Effect of 4-MBA concentrations on signal intensity in TG-AuNPs. Change in 1587 cm^{-1} peak intensity in Raman spectra of TG-AuNP-MBA measured in dried form (left) and in solution (right) showing optimised loading of AuNPs to be 0.8 mM. Spectra recorded using Ocean Optics QE Pro spectrometer with accompanying probe, with a 10 s integration time and 19.7 mW output. All spectra were normalised to background at 950 cm^{-1}.

The formation of these aggregates creates so called "hot-spots" which can further enhance the SERS signal intensity, far outweighing the enhancement contributions arising from the reporter concentrations. Therefore, to support findings from the dried samples, labelled TG-AuNPs in solution were also measured. A 50 μL droplet was placed onto the gold substrate immediately prior to the measurement being taken. The labelled TG-AuNPs in solution follow a similar trend in that a concentration of 0.8 mM MBA in EtOH afford the highest signal intensity. All spectra were normalised to the background at 950 cm^{-1}.

3.3.3 Versatility of Microsphere Size

While initially focussing on 10 μm TG particles, **Figure 3.7** shows employing a microsphere as a substrate for AuNPs can be extended, with AuNPs successfully taken up by a variety of different sized amino-functionalised microspheres. Here, six sizes of microsphere were investigated (ranging from 5 to 300 μm). This approach proved versatile, as the conjugates could be tuned as a "pick and mix" type selection. Nanoparticles may be chosen for their SERS ability at a chosen wavelength, with the size of the microsphere selected based on application. It was observed that for beads above 150 μm the SERS intensity per bead dropped (**Figure 3.7**), while small beads (5 – 30 μm) begin to reach AuNP saturation at around 3 mL AuNP (1.1×10^{10} particles) per 1 mg of TG. The larger sizes (above 150 μm) tend to reach saturation far below this level, at around 0.5 mL AuNP (1.8×10^{9} particles). Even once saturated, the larger sizes have a lower intensity (**Figure 3.7**).

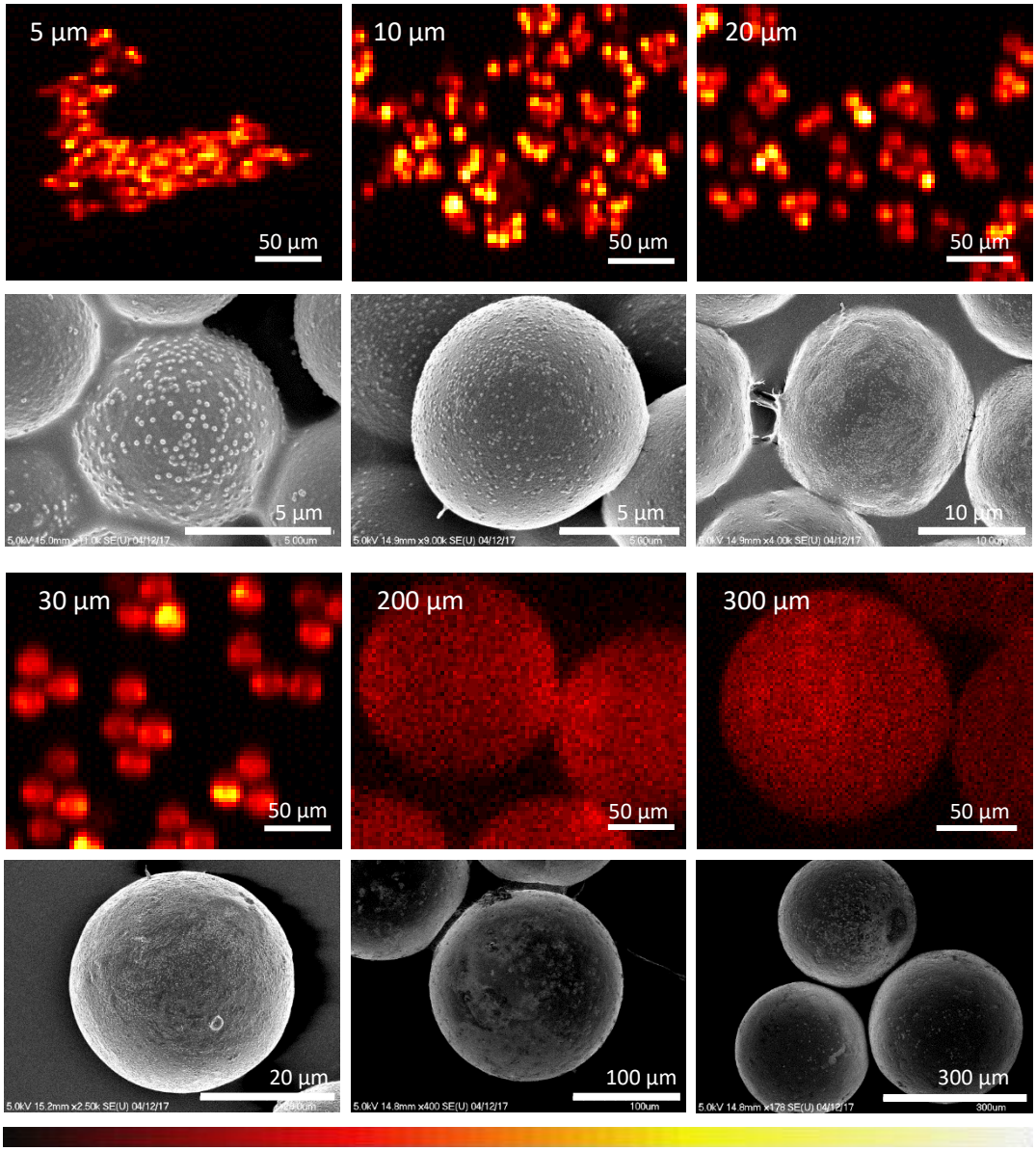

Figure 3.7 Size versatility of TG Beads. Raman intensity maps and SEM images of amino functionalised TG beads of various sizes loaded with AuNP-MBA (150 nm). StreamLine configuration used with a 785 nm excitation, 2 s integration time, 0.1 mW, 20x objective. Colour bar represents 1587 cm^{-1} peak intensity with upper and lower limits of 0 and 500000 respectively for beads 5, 10, 20 and 30 µm, and upper and lower limits of 0 and 50000 for beads

3.3.4 pH Response of TentaGel-Nanoparticle Beads

To assess their pH response of the TG-AuNP-MBA conjugates were analysed. submerged in pH buffers was carried. A gold coated glass chip was prepared with poly-L-lysine (50 μL, 0.1 mg mL^{-1}; as described in Section 2.2.1). The TG-AuNP-MBA conjugates were then pipetted onto the same area as the PLL and left to dry completely. The functionalised chip was submerged with pH buffers and spectra recorded. Between each buffer, the chip was rinsed with dH_2O. All pH calibration-on-chip experiments involve obtaining the Raman spectra of TG beads (10 μm) loaded with gold nanoparticles (150 nm, 1.1 x 10^{10} particles) functionalised with 4-MBA, while in the presence of a range of different pH buffers, carried out in a random order. A total of 57 measurements were recorded. Prior to each experiment, the pH of each buffer was measured using an electrochemical based pH meter (Mettler-Toledo).

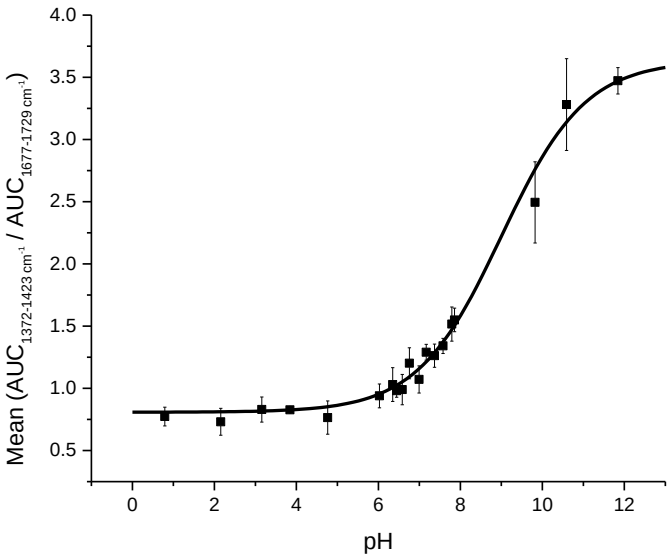

Figure 3.8 pH calibration plot for TG-AuNP-MBA (10 μm TG with 150 nm AuNP, 1.1 x 10^{10}) using area under the curve (AUC) calculations. 3 replicate calibrations were carried out, measuring pH in a random order each time. All spectra were normalised before integrating the pH changing regions at 1400 cm^{-1} and 1707 cm^{-1}. The black curve represents a Boltzmann fit to the plotted data. All spectra recorded using Renishaw InVia, 60x objective, 785 nm, ~0.5 mW, 1 s integration time.

The data set had an 8-point baseline subtracted and peak heights were determined using the peak finding function and the 1st derivative method. The data was normalised by scaling between 0 and 1, with the peak at 1587 cm^{-1} used as the reference peak as it had the maximum intensity value. Using a spectral window of ± 50 cm^{-1} around the peaks at 1400 cm^{-1} and 1707 cm^{-1}, the area under curve (AUC) of these regions was measured across the range of pH buffers (**Figure 3.8**). From the data plotted in **Figure 3.8** a Boltzmann fit was applied, providing a pKa of 8.99 (with and adjusted R^2 value of 0.992).

A Boltzmann fit was applied to the calibration data, using equation **(3.1)** to determine pH in a range of biological models, where A_1 = initial y value, A_2 = final y value, $x0$ = calculated pKa (midpoint of the curve), dx = time constant.[166]

$$y = A_2 + \left(\frac{A_1 - A_2}{1 + e^{\left(\frac{x - x0}{dx}\right)}} \right) \qquad \textbf{(3.1)}$$

Rearranged to give pH:

$$x = \ln\left(\left(\frac{A_1 - A_2}{y - A_2} \right) - 1 \right) dx + x_0 \qquad \textbf{(3.2)}$$

$$pH = \ln\left(\left(\frac{A_1 - A_2}{ratio - A_2} \right) - 1 \right) dx + x_0 \qquad \textbf{(3.3)}$$

Deriving pH measurements from the 10 μm TG beads decorated with 150 nm AuNP-MBA using the Renishaw In Via system, the ratio between 1396.7 cm^{-1} ±25 cm^{-1} (COO^-) and 1707 cm^{-1} ±25 cm^{-1} (COOH) was used with the following equation **(3.4)**.

$$pH = \ln\left(\left(\frac{-2.82687}{ratio - 3.63468} \right) - 1 \right) 1.02468 + 8.99946 \qquad \textbf{(3.4)}$$

The calibration data shows that the 4-MBA functionalised AuNPs incorporated into the TG beads were capable of dynamic pH sensing, making them attractive macro-scale SERS sensors.

3.4 Analysing Multicellular Tumour Spheroids Using TentaGel-Nanoparticle Sensors

3.4.1 3D Culture Challenges

Currently, 2D cell culture remains the most common strategy in which to initially test a wide range of novel drug candidates. However, there are major limitations to this methodology as it stands; cells grown in monolayer are known to behave in a different way to tissue, and thus reduces its parallels to *in vivo* studies. Many techniques have been employed to measure nutrient gradients have been designed using monolayer culture. However, the methods used to interrogate the health of the multicellular tumour spheroids (MTS) are limited by *z* penetration depths of current imaging techniques, and so often require breaking up the spheroid therefore making it difficult to monitor physiological changes over time.[98,192]

Acidosis, where the extracellular pH falls, is a key feature of tumour tissue with the production of acidic metabolites, such as lactic acid, caused by anaerobic glycolysis.[5] The Warburg Effect theorises that lactate is produced *via* the anaerobic glycolytic pathway instead of oxidative phosphorylation, irrespective of whether there is sufficient oxygen for energy production. In contrast to monolayer cultured cells, MTS afford a gradient, radiating from the core outwards (**Figure 3.9**). Access to nutrients, oxygen, and the reduced ability to remove waste build up from the centre of the MTS can hasten the formation of a necrotic core.

3D cell culture provides a way to monitor the biological activity of compounds. Here, TG-AuNP conjugates were employed to measure the pH gradient of multicellular

tumour spheroids (MTS). MTS can be either grown as clusters of cells from single cell suspensions, or grown in a hanging-drop, using gravity to drive self-assembly.

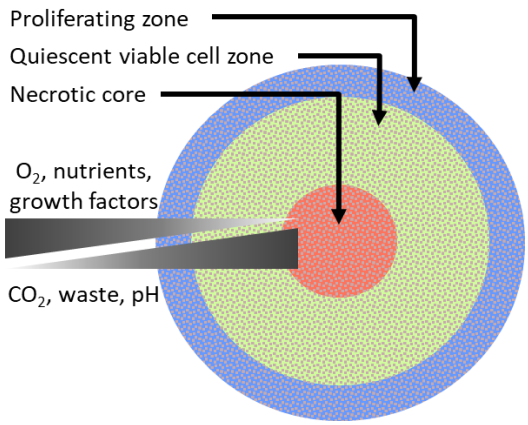

Figure 3.9 MTS microenvironments. MTS grow in organised spherical structures containing proliferating, quiescent and dead cells. Gradients develop due to insufficient mass transport of nutrients and waste. Adapted from Lin et *al*.

3.4.2 2D Sensing

Before investigation the TG-AuNP-MBA beads in MTS, an MTT assay was carried out to assess the effect on the viability of MCF-7 cells after an overnight incubation with either AuNP, AuNP-MBA, TG, TG-AuNP, or TG-AuNP-MBA. **Figure 3.11** demonstrates that the treated MCF-7 cells showed no significant impact compared to the control.

An attempt to measure the extracellular pH of MCF-7s in a monolayer culture was conducted. TG-AuNP-MBA (10 μm/150nm respectively) beads were dried down onto PLL coated to CaF_2 windows and placed in a 6-well plate of MCF-7 cells (1 x10^5 cells per well) overnight. Each well had the culture medium exchanged for fresh medium containing staurosporine (STS; 1 μM, 2 mL), a strong tyrosine kinase inhibitor, used to induce apoptosis. Raman spectra were obtained from samples incubated with STS between 0-1, 1-2, 2-3, 4-5, and 6-7 hours. For each condition between 25-50 samples

were recorded, the ratio calculated using equation **(3.4)** determined from using the Renishaw In Via system. To avoid differing atmospheric conditions, each sample was incubated until immediately prior to recording spectra, minimising the time the sample was out of the incubator. There was no significant difference (as measured by a one-way ANOVA) between the untreated and treated samples (**Figure 3.10**). This is likely due to the buffering capacity of the medium dominating the pH measurements, demonstrating that this method is not appropriate for 2D culture.

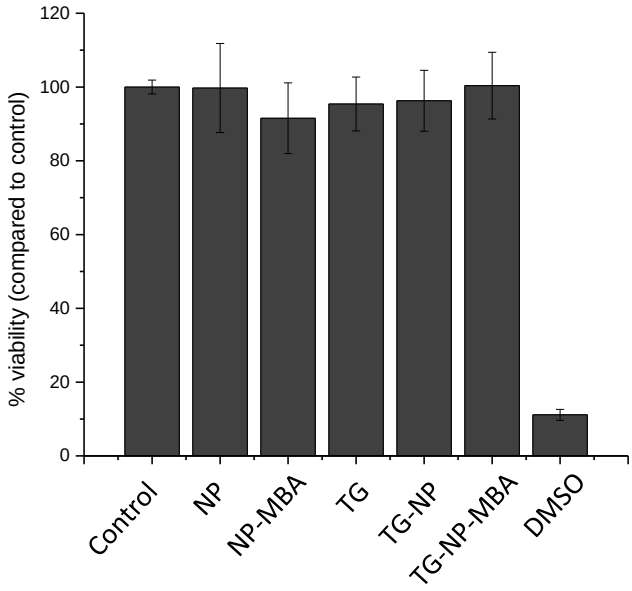

Figure 3.11 Cytotoxicity results for MCF-7 cells treated with TGs and AuNPs. % Viability is compared to the controls.

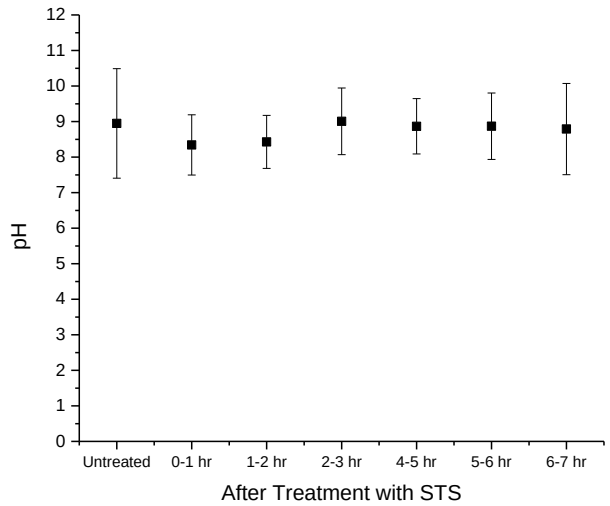

Figure 3.10 Distribution of pH in monolayer culture of MCF-7 cells, and the difference in pH between populations untreated and treated with staurosporine over time. pH calculated using TG-AuNP-MBA.

Table 3.1 Average pH as measured using TG-AuNP-MBA in MCF-7 monolayer culture after treatment with staurosporine

Treatment with STS	Average pH
Untreated	8.95 ± 1.54
0-1 hr	8.34 ± 0.85
1-2 hr	8.43 ± 0.75
2-3 hr	9.01 ± 0.94
4-5 hr	8.87 ± 0.78
5-6 hr	8.87 ± 0.94
6-7 hr	8.77 ± 1.28

3.4.3 Loading Beads into Multicellular Tumour Spheroids

MTS were grown using the hanging drop method (as detailed in Chapter 6 Section 6.4.8), typically seeded with 6000 MCF-7 cells and harvested after 9 days of growth. The efficient number of beads per spheroid sample was investigated. Ideally, it would be beneficial to have many beads dispersed evenly throughout a spheroid in order to collect data on the pH gradient. The TG-AuNPs-MBA were combined with MCF-7 cells at the seeding stage of MTS formation. In contrast to the preparation of zoned SERS active cells in spheroids, where AuNP treated cells are introduced throughout the growth phase of MTS formation,[23] it was found that introducing the TG-AuNPs-MBA during seeding resulted in them being dispersed throughout the spheroid. If required, the beads could be introduced to spheroids after 5 days to position them solely on the outer regions of the spheroid.

Initial attempts at loading with high concentrations of around 1800-9000 TG-AuNP-MBA beads per spheroid (**Figure 3.12**) showed intense loading, too high to be useful, as the signal generated from a single TG-AuNP-MBA bead is often so intense that signal can be picked up from surrounding areas of the particles, thus is difficult to differentiate 1 bead from another. By reducing the laser power, the resolving

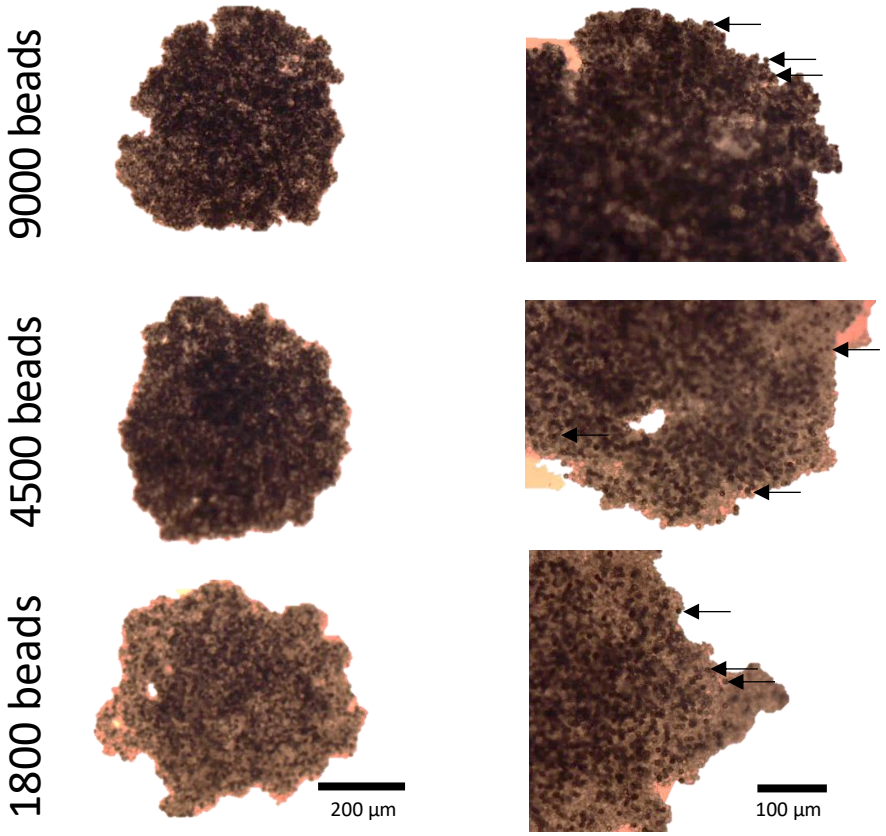

Figure 3.12 Microscope images of MCF-7 spheroids with high TG-AuNP-MBA (10 µm/150nm) bead loadings of between 1800-9000 beads per spheroid. The beads are seen as dark spherical objects heavily dispersed throughout the spheroids (arrows indicate example locations).

capabilities between beads may be improved, although at a cost of reduction in signal intensity. This would primarily benefit imaging in 2D, as trying to image a volume would complicate matters further, where it is much more difficult to differentiate beads on multiple planes, not to mention the huge increase in total measurement time required for 3D imaging compared to 2D. Instead, lowering the TG-AuNP-MBA loading to a number where a relatively fast 2D map can be acquired on a timescale of minutes (rather than hours required for a 3D map). **Figure 3.14** shows Raman intensity maps (4-MBA peak at 1587 cm^{-1}) of MCF-7 MTS loaded with either ~180 or ~20 beads. While the beads are not solely constrained to a particular "zone" within the spheroid,

the MTS treated with approximately 180 beads shows clumping in the centre, making it difficult to resolve a single bead. The MTS treated with ~20 beads shows a much more even dispersity. **Figure 3.13** is a representative spectrum obtained from the Raman map in **Figure 3.14** .

Table 3.2 gives the approximate number of beads in 1-0.001 mL of the prepared TG-AuNPs, with the equivalent number per spheroid sample. Having a relatively low number of beads per spheroid coupled with a higher laser power ensures that signal is gained from beads dispersed throughout the spheroid and not simply on the surface. TEM analysis was carried out on sections of MTS containing TG-AuNP-MBA to examine the location of the beads within the spheroid in relation to an intracellular or extracellular setting.

Figure 3.15 illustrates the TG-AuNP-MBA beads are not taken up by cells (most likely due to their size) and are still located in the extracellular space of the spheroids, and that the AuNPs are held on the surface of the polymer beads.

Table 3.2 Number of TG-AuNP-MBA beads per MCF-7 spheroid

Aliquot from Stock TG-AuNP (mL)	Beads (40000 cells/mL)	Beads (per spheroid (6000 cells/15 μL))
1.0	1,200,000	18,000
0.5	600,000	9000
0.25	300,000	4500
0.1	120,000	1800
0.01	12,000	180
0.001	1,200	20

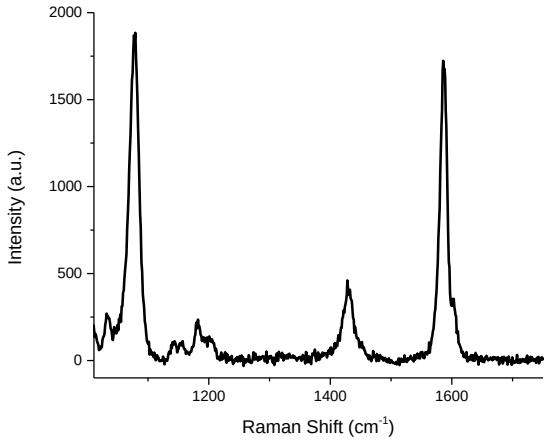

Figure 3.13 Representative spectrum of TG-AuNP-MBA within a spheroid. Obtained with a 785 nm excitation source, 2 s integration, 10 mW, 5x objective.

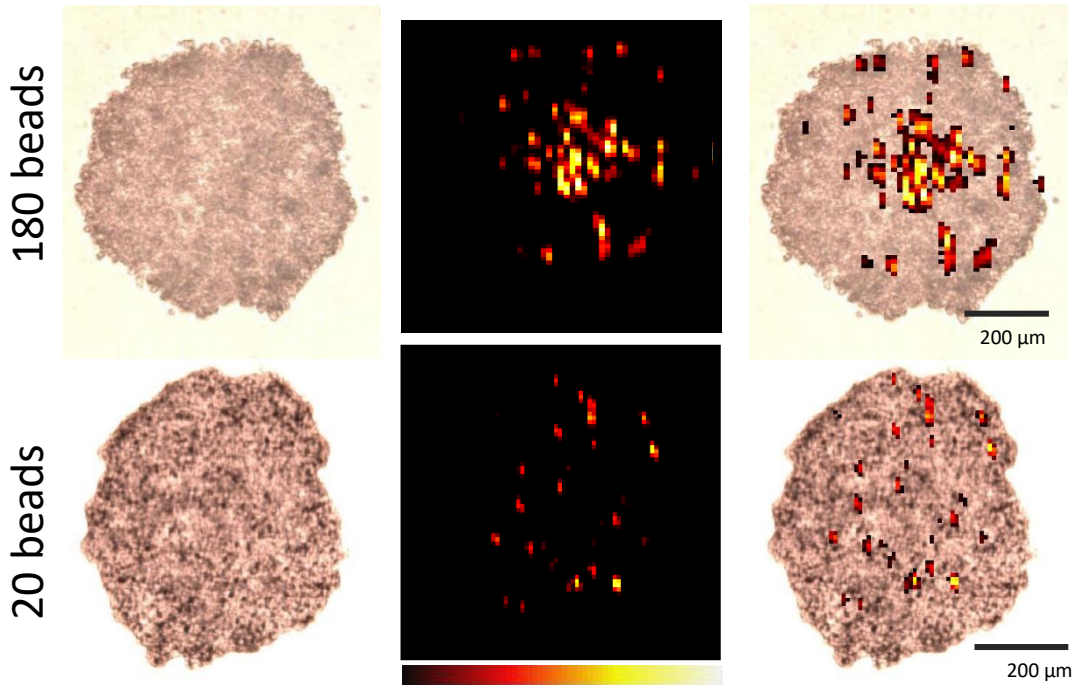

Figure 3.14 Raman intensity maps of MCF-7 MTS loaded with 20 or 180 TG-AuNP-MBA beads per spheroid. StreamLine configuration used with 785 nm excitation, 2 s integration time, 10 mW, 5x objective. Colour bar represents 1587 cm^{-1} peak intensity with upper and lower limits of 10000 and 50000 respectively.

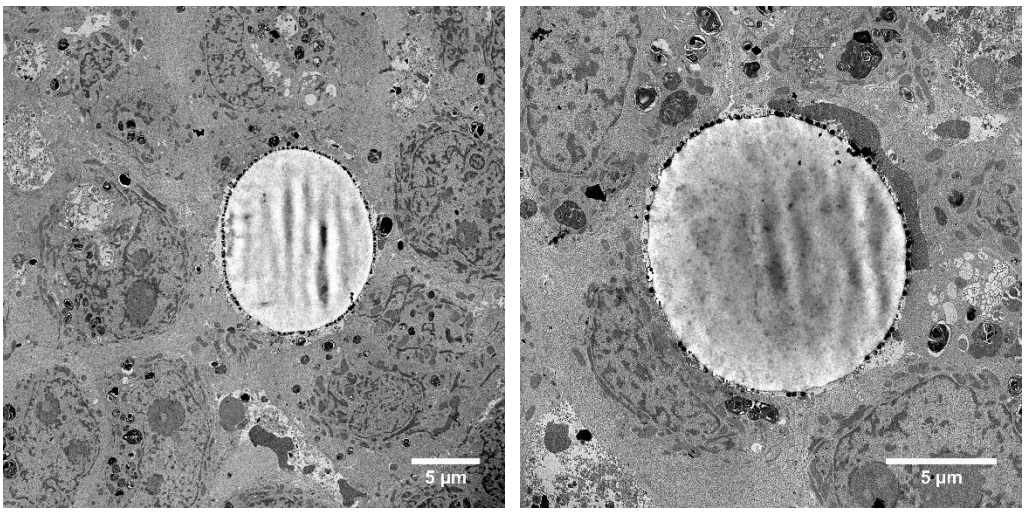

Figure 3.15 TEM images of TG-AuNP beads located in MTS. MTS grown with 10 µm beads confirms beads are located extracellularly.

3.4.4 Measuring pH in MCF-7 MTS

Having successfully shown that the TG-AuNP-MBA beads can be incorporated into MCF-7 MTS, the next step was to assess pH across different regions (central or outer). Intensity maps were made (as such in **Figure 3.14**) with MTS loaded with around twenty 10 µm TG-AuNP-MBA beads. For the purpose of this study, the spheroids were treated as 2 separate "zones": outer or central. The outer regions relate to the proliferation zone, where nutrient and waste gradients have not yet formed. The central region refers to the quiescent zone, which encompasses the necrotic core (if formed), where the development of nutrient and waste gradients can form.

The MTS formed in hanging drops had the medium removed (15 µL) and replaced with either fresh medium, or staurosporine (STS, 10 µM, 15 µL), then left to incubate for 5-6 hours in a humidified environment with 5% CO_2. Following incubation, the samples were removed and immediately mapped. **Figure 3.16** shows the difference in distribution of pH values (calculated using equation **(3.4)**) between outer and central regions, and between untreated samples and those treated with STS. For both conditions (STS treatment) there was a significant difference in pH between the zones.

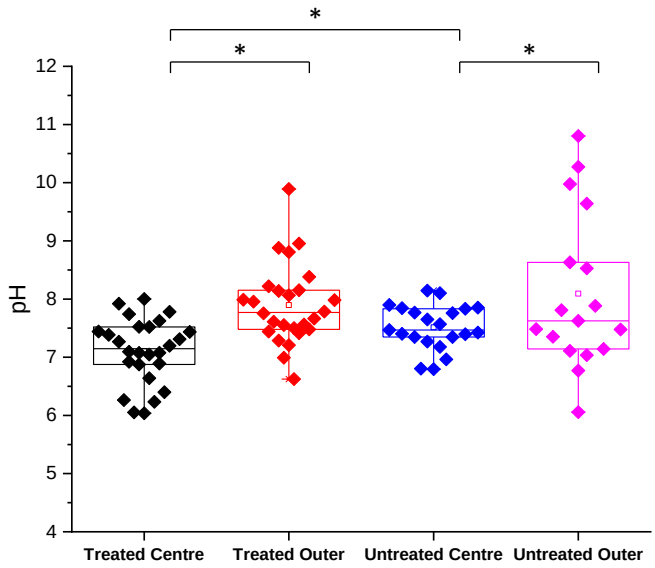

Figure 3.16 Distribution of pH between central and outer regions of MCF-7 spheroids, and the difference in pH between untreated and treated with staurosporine (10 μM, 5-6 hour incubation) populations. pH was calculated using 10 μm TG-AuNP-MBA in MCF-7 cells in spheroids.

The untreated samples afforded average pH values of 7.51 ± 0.38 and 8.09 ± 1.34 relating to the central and outer regions, respectively. Likewise, after treatment with STS the central regions had a lower pH than that of the outer region (7.11 ± 0.56 and 7.90 ± 0.68). A Shapiro-Wilke test was used to assess the normality of distribution across the populations, followed by a one-way ANOVA used to assess if the populations showed a difference to a significance at the 0.05 level (as indicated by * in **Figure 3.16**).

Table 3.3 pH of central and outer zones in MCF-7 MTS

Position	Untreated	Treated STS
Centre	7.51 ± 0.38	7.11 ± 0.56
Outer	8.09 ± 1.34	7.90 ± 0.68

Previous work carried out by other members of the group used SERS to investigate intracellular pH in MCF-7 MTS, showing that cells in the central region of the spheroids exhibited an increased pH.[23] Combined with the results presented here, a reduced pH_e was found within the centre of the spheroid, these match findings presented in the literature,[193–196] demonstrating that SERS can be used to measure intra- and extra-cellular pH, as well as the dissipation of the pH gradient with drug treatments.

This approach allows for the easy discrimination of zones and simultaneous monitoring of inner and outer regions, with the potential to observe the response to a drug treatment as a function of pH. While demonstrated in a breast cancer cell line here, extracellular acidity is also a pathological feature of inflammation.[197,198]

Providing that there are suitable reporter molecules available, this technique may be extended to simultaneous intracellular and extracellular sensing applications, as well as multiplexed sensing for parameters such as, redox potential, oxygen, as well as metabolites of interest.

3.5 Fabrication of a Multicore pH Sensing Fibre

3.5.1 Multimode Multicore Optical Fibres

Multicore optical fibres offer great sensing versatility. Through selectively etching pits into the distal end of the optical fibre, the ability to load pH and redox sensor TG-AuNPs into differing cores could be achieved. This sensing architecture has the potential to extend to other sensing probes (for example, oxygen).

For this body of work, multimode-multicore fibres were used. Each fibre consisted of 19 cores with a core diameter of 10 μm and a core separation of 21 μm. The fibres were prepared by the draw and stack method as described in Chapter 6, Section

6.1.4.3, using germanium doped silica surrounded by a pure silica cladding.† Each core was able to be individually illuminated by coupling light into the proximal end of the fibre, using the set up described in Chapter 6, Section 6.1.4.1 (**Figure 3.17**).

With the objective of loading single TG-AuNP particles into individual cores of the fibre, small pits were created in each core at the distal end of the fibre. The pits were created by chemical etching using hydrofluoric acid (HF).‡ The HF selectively etched the Ge-doped silica to create cavities in the glass cores at the distal surface (**Figure 3.18**). To prepare the TG-AuNP-MBA for loading into the pits, a small aliquot containing approximately 1800 beads was prepared, and washed twice in 70% EtOH. As much supernatant as possible was removed from the sample leaving a pellet of beads. The etched fibre could then be gently pressed into the pellet, with simultaneous "live" monitoring of a core to check for loading. Typically, around 14-15 out of 19 cores would afford signal after loading (**Figure 3.18**).

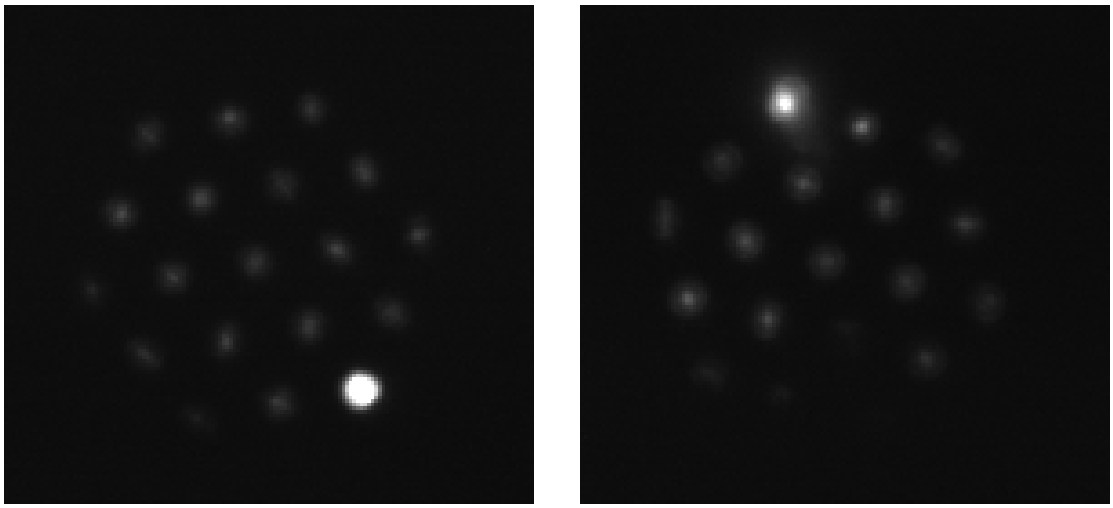

Figure 3.17 Illumination of single core in 19-core multimode fibre.

† Fibres designed and fabricated by K. Harrington and H. Wood, University of Bath, UK
‡ HF etching carried out by Dr D. Choudhury, Heriot-Watt University, UK

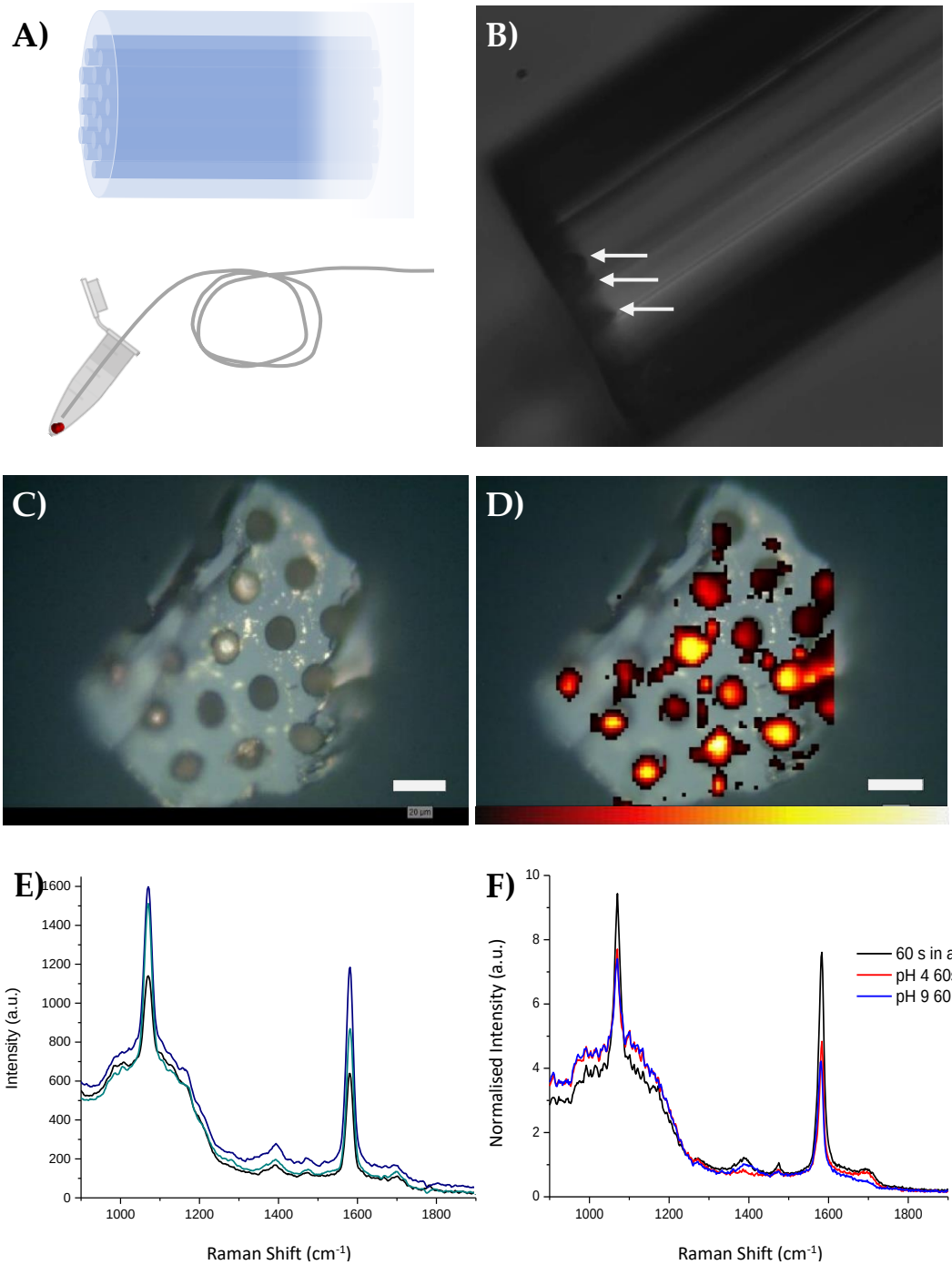

Figure 3.18 19 core, multimode etched fibre loaded with TG-AuNP-MBA (10 μm TG beads; 150 nm AuNP). A) Illustration of "force loading" fibre by pushing into a pellet in minimal solution volume (~10 μL). (B) Lateral view of HF etched fibre with arrows indicating pits. Taken with whitelight microscope (C) White light image of the distal end of a 10 μm TG-AuNP-MBA loaded fibre. (D) Raman intensity map of (C), StreamLine configuration used with 785 nm excitation, 2 s integration, 10 mW, 50x objective. Colour bar represents 1587 cm^{-1} peak intensity. (E) Representative spectra obtained through fibre, 0.2 mW, 10 s integration. (F) Spectra obtained through fibre, after submersion in pH 4 and 9 buffers, 0.2 mW, 60 s integration

3.5.2 Redox Sensors

As the individual microspheres can generate a high signal, this aspect lends itself to the ability of multiplexing. Each bead functionalised with separate SERS sensor can be loaded into separate etched cores of the fibre affording a multiplexed sensing fibre, capable of sensing different physiological parameters. Redox potential can be used as a metric of assessing health status.[199] Previous work by the group have demonstrated the use of SERS redox sensors in biological applications.[23,110,112] TG-AuNP conjugates were functionalised with napthaquinone derivative 1,8-diaza-4,5-dithian-1,8-di(2-chloro-[1,4]-naphthoquinone-3-yl)octane (NQ), a dimer which is thought to dissociate on the conjugation to surface of the nanosensors. This reporter molecule is sensitive to redox potential (**Figure 3.19**).[110,112,200]

The multiplexing of a multicore fibre was by combining equal volumes of TG-AuNP-MBA and TG-AuNP-NQ (10 μm, 0.1 mL), washing in 70% EtOH, followed by the removal of much of the supernatant, leaving a pellet. The distal end of an etched fibre (19-core, 20 μm core diameter) was dipped into the TG mixture, resulting in NQ and MBA filled cores, where A-F denotes the corresponding through-fibre spectra in (A) and the core positions in (B) (**Figure 3.20**).

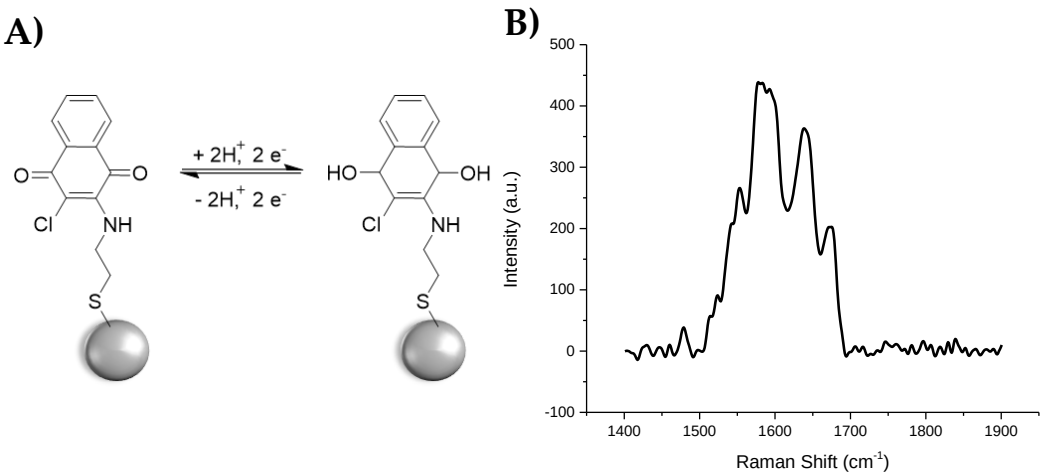

Figure 3.19 NQ: Redox potential sensor. A) Structure of NQ on AuNP. B) SER spectrum of NQ functionalised TG-AuNP.

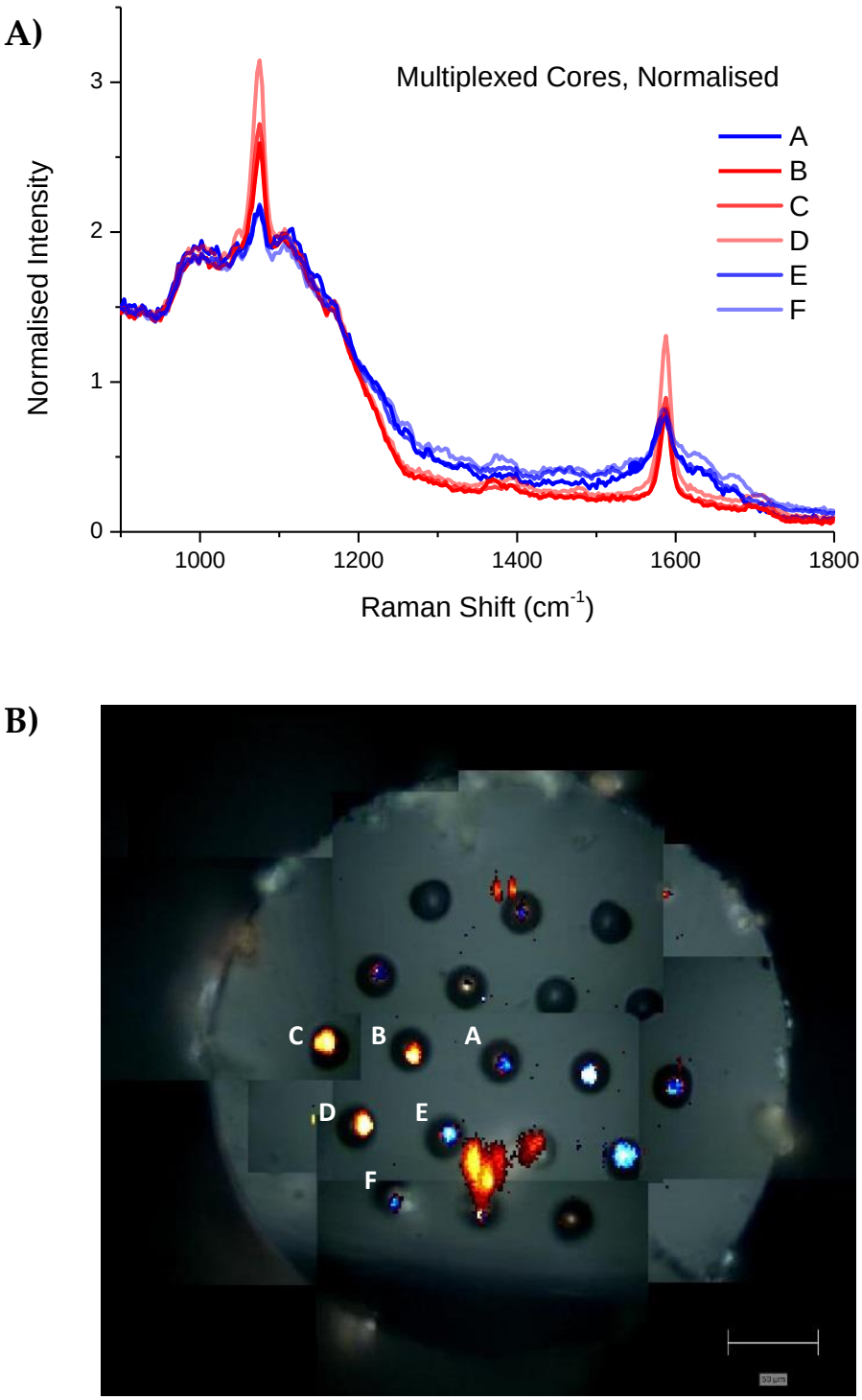

Figure 3.20 Multiplexed fibre with redox and pH SERS reporters. 19-core multimode fibre loaded with TG-AuNPs (10 μm TG beads; 150 nm AuNP) functionalised with NQ (blue) or 4-MBA (red). A) Spectra recorded through fibre, B) Raman map of distal end. A-F denotes the corresponding through-fibre spectra in A) and the core positions in B). A) Recorded using Ocean Optics QE Pro spectrometer with 785 nm excitation source, 30 s integration. B) Maps obtained using Renishaw In Via spectrometer with 785 nm excitation.

Although loading of beads into the etched pits was a simple process, the ability to retain them on the end of a fibre proved difficult, as most of the beads were removed upon contact with solution. A range of chemical (glues: sol-gels, Araldite, Nafion, cell-tac) and physical (nylon meshes) approaches to holding the beads on fibre were attempted, unfortunately these attempts did not result in prolonged retention.

3.6 Fabrication of Single Core pH Sensing Fibre

The multicore fibre would be of great interest to develop further as it demonstrates obvious multiplexing capabilities. However, as retention of the particles within the etched pits proved more complex than anticipated, a simpler option was developed.

Moving towards a strategy which circumvents the requirement for advanced instrumentation or engineered components, the polymer-SERS conjugates were employed with a commercially available single core fibre (200 μm core diameter).

The so-called "SERS chamber", comprised a large core fibre combined with large TG-AuNP-MBA conjugates (~200 μm). The rationale for this approach was that larger TG beads would be easier to manipulate into position onto the distal end of the fibre, as well as being easily held by simple and abundantly available materials: nylon mesh from cell strainers. It was thought that simply using mesh to hold the SERS particles in place would negate the need for a layer such as sol-gel, which could produce uneven thicknesses with variable porosity.

The fabrication of the packaged distal end is illustrated in **Figure 3.21**. A section of nylon mesh (100 μm pore size) was placed on top of a rubber ring. A ceramic fibre ferrule suitable for a 200 μm core diameter fibre was pushed through the ring, resulting in the mesh flush across the top of the ferrule. **Table 3.4** highlights the components used to fabricate the packaged end portion.

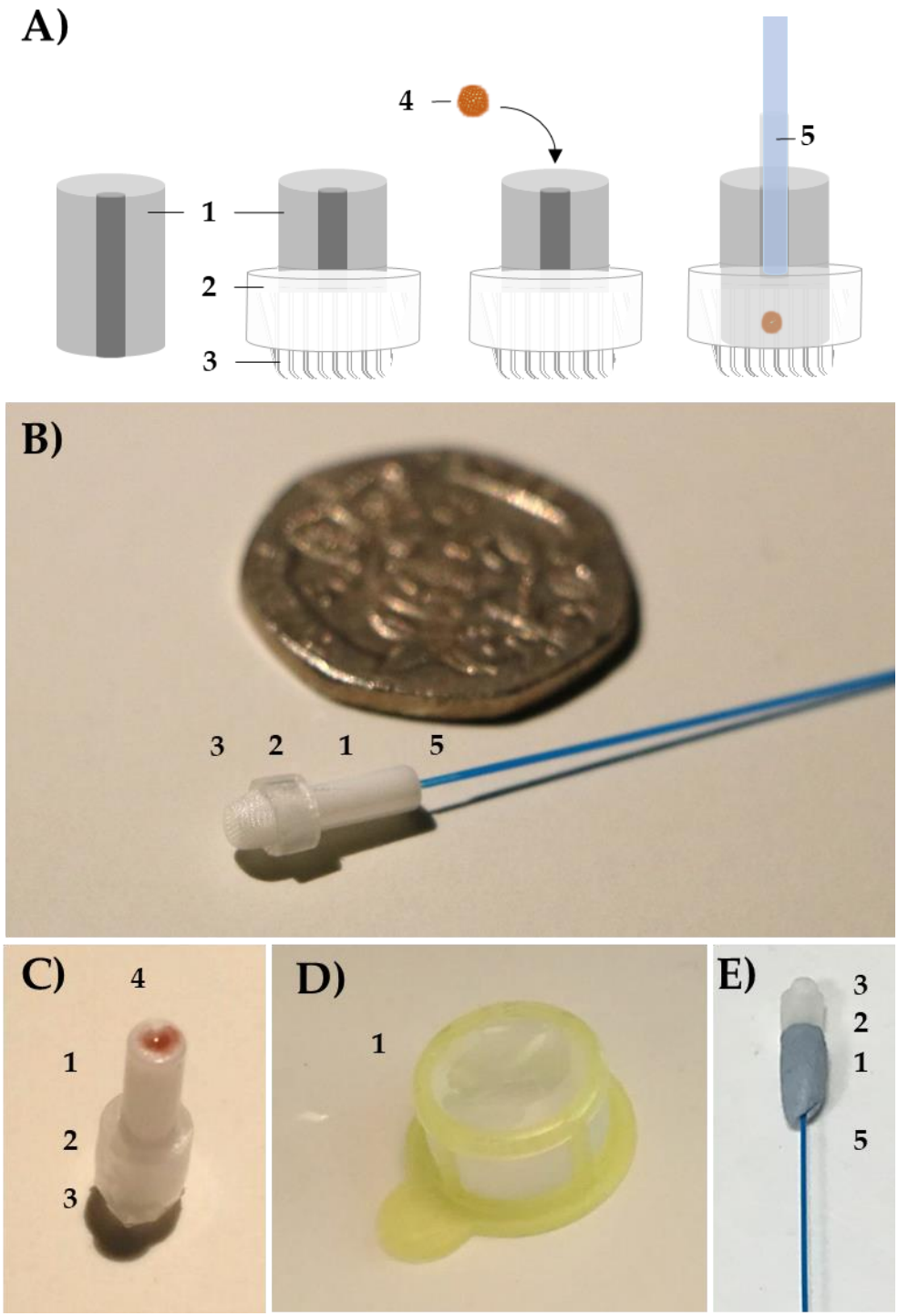

Figure 3.21 Fabrication of the SERS Chamber. A) Illustrating of the fabrication of the complete "SERS chamber" fibre. B) Packaged distal end of the fibre and 20 pence for scale. C) Packaged ferrule with TG-AuNP-MBA placed atop to flow down centre. D) Nylon mesh (100 μm pores) used to hold the TG-AuNP-MBA in place. E) Fibre secured against TG/mesh in ferrule with Blu-Tac. Numbered items represent components in Table 3.4

Table 3.4 Components of SERS Chamber

Number	Component
1	Fibre ferrule for 200 μm core diameter fibre
2	Section of rubber used to secure mesh in place
3	100 μm pore nylon mesh from cell strainer (Corning Falcon™)
4	~200 μm TG beads with 150 nm AuNP-MBA
5	200 μm single core fibre (ThorLabs)

Fibre optic sensing of pH has been demonstrated previously,[8,161] and it is known that the background Raman scattering from the fibre can overpower the SERS signal. Although some of these issues may be lessened using complex fibre designs, these are often bulky, necessitating sophisticated manufacturing.[8,128,201] Additionally, as shown in **Chapter 2**, many fibres for use with SERS sensing are prepared by dipping the fibre into nanoparticle solutions, leading to unknown and inconsistent concentrations at the distal end.[8,128,161,201] With the SERS Chamber approach, the signal was easily seen over the fibre background (**Figure 3.22**), with observable changes at the pH sensitive peaks (1400 cm^{-1} and 1700 cm^{-1}).

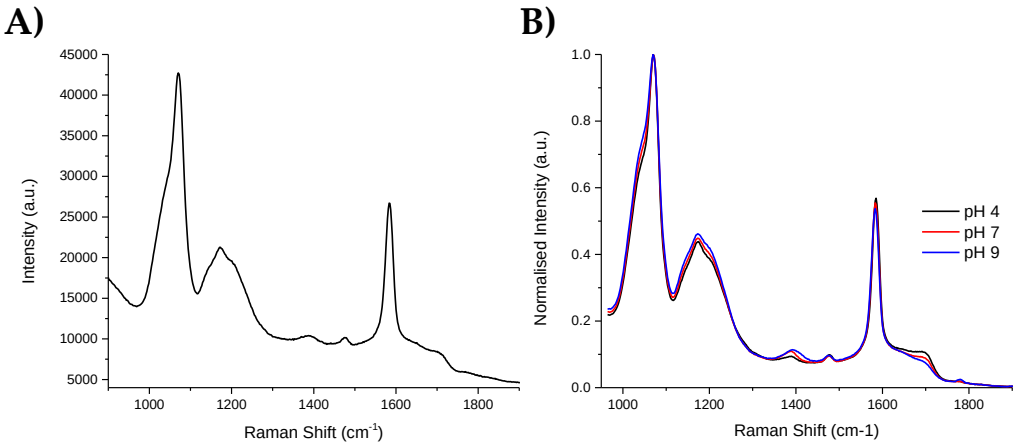

Figure 3.22 Spectra from SERS Chamber recorded in air A), and B) averaged spectra recorded with distal end submerged in pH 4, 7, and 9 buffers. 785 nm, 30 s integration time, 0.8 mW output.

Aqueous pH buffers were prepared from pH 4-9 and verified with an electrochemical pH meter (Mettler-Toledo). The packaged distal end of the fibre was submerged in buffer and the spectrum recorded continuously for 5 min (30 s integration time). Between readings the SERS chamber was rinsed in dH_2O. The fibre had three replicate calibrations where the pHs were measured in a random order. The spectra were analysed by first normalising the spectra to the magnitude of a reference peak (1070 cm^{-1}), followed by measuring the area under the curve (AUC) within ± 25 cm^{-1} of the peaks at 1380 cm^{-1} and 1700 cm^{-1}. Plotting pH against the AUC ratio, the fibre demonstrated variation within the physiological range (**Figure 3.23**).

While proving a simple method for pH sensing, one limitation of this approach is the observed hysteresis. During pH calibration measurements it was noticed that changes to the spectra were often delayed after changing from one pH buffer to the next. This lagging effect was more obvious going from an acidic environment to a more basic environment, with the reverse direction changing quickly. **Figure 3.23 (A)** shows the sensing capability after submerging the distal end in buffer for 5 min, while **Figure 3.23 (B)** results after 30 s submersion. While using this device does not exhibit instant dynamic changes, it may pose more valuable in situations where the device may remain in place for an extended period of time.

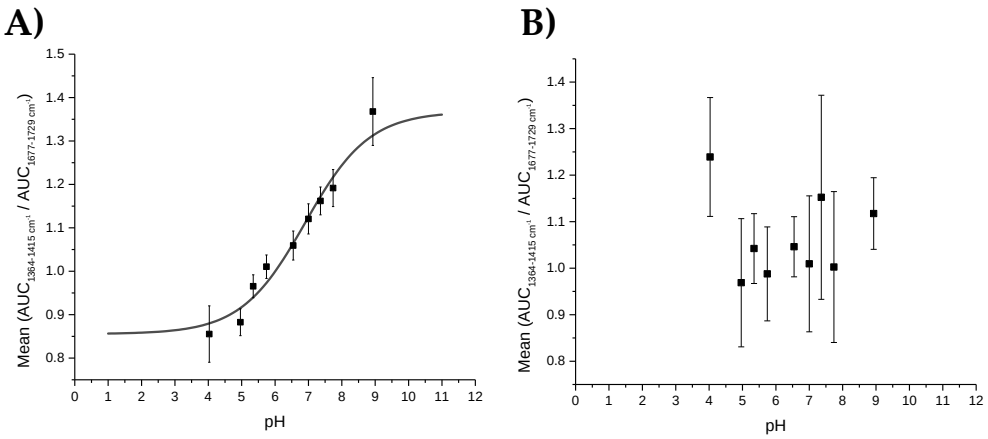

Figure 3.23 pH measurements with respect to time submerged. (A) Distal end of fibre submerged in pH buffer for 5 min before recording spectra, (B) submerged for 30 s before recording measurement in. 785 nm laser, 30 s integration time, 0.8 mW output, Ocean Optics QE Pro spectrometer used.

3.7 Conclusions

The use of TentaGel beads as a substrate for nanoparticles to facilitate pH sensing has been shown.

The use of 3D scaffolds as a sensor in spatially sensitive regions within 3D cell culture, as well for loading on to the distal end of an optical fibre has been demonstrated.

These beads have also been used in the measurement of extracellular pH within MTS. It has been shown that the central and outer regions of the MTS have different pHs, and the monitoring of extracellular pH could prove a useful tool in the assessment of novel drug development. Further to this, the scaffolds as used for 3D cell culture could be extended to simultaneously investigate intra- and extracellular pH/redox potentials with carefully selected nanosensors.

Initial studies have proven the capabilities of using the TG-AuNP beads to provide multiplexed fibres, capable generating signal intensities large enough to overcome the Raman fibre background. Future investigations into precision positioning of the scaffolds into the etched cores provides the potential to multiplex the 19-core fibre with a larger variety of SERS sensors than demonstrated here (redox and pH). Special consideration into retaining particles on the end of the fibre would prove valuable in the furthering of this work.

4 Dual Purpose Fibres – pH Sensing Combined with Bacterial Analysis

While physiological sensing through fibre can afford of wealth of information, it rarely negates the requirement for the analysis of a physical sample. This chapter describes a method by which both sensing, and fluid extraction can be carried out to gain information on both physiological environment and the pathogen. Much of the work presented in this chapter can be found in the Analyst publication "Dual purpose fibre – SERS pH sensing and bacterial analysis" (DOI: 10.1039/C8AN01322E).

4.1 Introduction

4.1.1 Current Identification and Analysis of Pulmonary Bacteria

With the rising global challenge of antimicrobial resistance, there is an urgent need to reduce unnecessary antimicrobial prescriptions.[202] Ventilator-associated pneumonia (VAP) is a common infection found in the critically unwell in intensive care units (ICUs), with *Pseudomonas aeruginosa* behind many of these infections.[203] The treatment strategy for suspected VAP in patients is typically to administer broad spectrum antibiotics, however, using broad spectrum antibiotics in an indiscriminate manner is implicated in the development of antimicrobial resistance.[204] Tailoring treatments to target the specific strain of bacteria would help reduce the elimination of healthy bacteria within the lung,[205,206] but also help reduce the formation of antimicrobial resistant strains.

Studies have shown that standard methods used to identify specific infectious agents, often by the interpretation of non-specific clinical or radiological features combined with culture techniques from sputum samples, are not able to diagnose lower tract respiratory infection which requires processing of bronchoalveolar lavage fluid (BALF) samples.[207]

However, culture from BALF typically takes several days and suffers from a lack of both sensitivity and specificity due to aspirated fluid being prone to contamination from the upper respiratory tract. Molecular sequencing, which often employs polymerase chain reactions (PCR) to overcome issues concerning sample size, can be overly sensitive, potentially leading to patient overtreatment. Overtreatment combined with poor sampling techniques, can result in a significantly negative impact on patient health.[208–211]

The correct identification of pathogens causing respiratory infections and the monitoring of their antimicrobial sensitivity is of great importance in assisting with diagnosis and treatment choice. Recently, major advances in pulmonary investigation methods have demonstrated the *in situ* detection of Gram-negative bacteria in human lungs.[212] In addition to identification, knowing details of the physiological environment at the site of interest can hold great value. pH is tightly regulated within cells and tissues, with deviations indicative of disease. Within the lung, an acidic pH can encourage the growth of bacteria, reduce the efficiency of endogenous cationic antimicrobial peptides and inactivate some antibiotics - all factors that contribute to antimicrobial resistance and worsening patient outcome.[15,213]

4.1.2 Paper Based Sensing

Introduced as a scientific tool in the early 1800s by Swedish chemist Jöns Berzelius, filter paper is a widely used and versatile tool for analysing and handling fluids, in a

broad range of applications from molecular separation in chromatography, swabs for biological samples and as a microfluidic device.[214–216] It's attractiveness as a substrate stems from its abundance, inexpensiveness, and compatibility in many biological and chemical environments, and due its wicking ability does not require external forces for the transport of fluid through the paper.

Analysis through an optical fibre has been previously reported, however, challenges include difficulties in reproducibility from fibre to fibre, as well as generating SERS signals dominated by the intrinsic silica fibre background. As a result, much of the focus in this area has been on background suppression through complex fibre designs and correction methods.[8,161,169]

Paper based substrates utilising NPs for analyte detection and SERS sensing are gaining traction as point-of-care systems due to their low cost and flexible nature.[217–220] One of the difficulties of using paper is directing the deposition of NPs, due to the inherent wicking ability of filter paper which is both quick and uncontrolled. The use of patterning with a hydrophobic ink can assist with some of these issues, by defining a specified SERS sensing region.[221,222]

Here, a facile and cost-effective method of using AuNPs on a wax patterned paper is demonstrated. This substrate is capable of ratiometrically measuring pH using SERS, whilst retrieving a biological fluid sample through the combination of paper attached to a fibre-based system. The advantages of a wax patterned paper sensing substrate are two-fold, it allows simple control of particle deposition and also facilitates an easy way to retrieve biological samples. The paper-fibre combination was designed to be small enough to be bronchoscope deployable with the ability to reach alveolar regions within the lung, allowing for site specific information to be gathered about both host and pathogen. This approach has also overcome many of the outlined challenges with SERS applications, by achieving an easily repeatable fabrication process and generating reproducible high signal to noise ratios.

4.2 Paper SERS Substrate Design

The main goal of this research was to provide a simple SERS substrate to combine with a fibre-based approach to sensing, specifically pH. For this purpose, filter paper was chosen as the preferred material due to its wide availability and porous nature.

4-Mercaptobenzoic acid functionalised AuNPs (4-MBA; 150 nm, $3.6x10^8$ particles/μL) were pipetted on to filter paper. Repeated depositions of AuNPs (2 μL) were applied, to a final volume of 2-8 μL, with drying stages in between, to avoid a loss of AuNPs through soaking and washing through the paper. The sizes of the spots were defined by the volume of the solution, however there was much variance in shape and spread, or wicking, of the AuNPs within the spots (**Figure 4.1 (A) I**).

In an effort to overcome the influence of non-uniform capillary wicking, and therefore the low reproducibility, a hydrophobic wax mask was printed onto the filter paper (**Figure 4.1 (A) II**).§ Wax printing is a simple, inexpensive, and quick method, amenable to mass production. Patterning paper with a wax mask allows containment of the wicking action, confining the dispersion to hydrophilic areas.[221–223] By limiting the solution containing the AuNPs to a defined area, there was a reduction in variability in the AuNP concentration at any point within the hydrophilic area. A substantial difference between applying the AuNPs to filter paper with and without the wax barrier could be clearly seen by eye (**Figure 4.1 (A)**). The image shows both an increasing spot size, as well as a non-uniform spread of AuNPs across the filter paper where a wax barrier was not used. SERS mapping (1587 cm^{-1} peak intensity, **Figure 4.1 (B)**) was used to reveal the unevenness further (**Figure 4.1 (C)**). The patterned paper allowed the AuNPs to be deposited to the filter paper in a controlled manner, filling the entire hydrophilic area evenly (**Figure 4.1 (D)**). SEM images from paper substrates

§ Prepared by Angus Marks, University of Edinburgh

with the printed wax barrier show a high density of AuNPs on the cellulose fibres, which may help in the formation of SERS "hot-spots", further enhancing signal intensity (**Figure 4.2**).

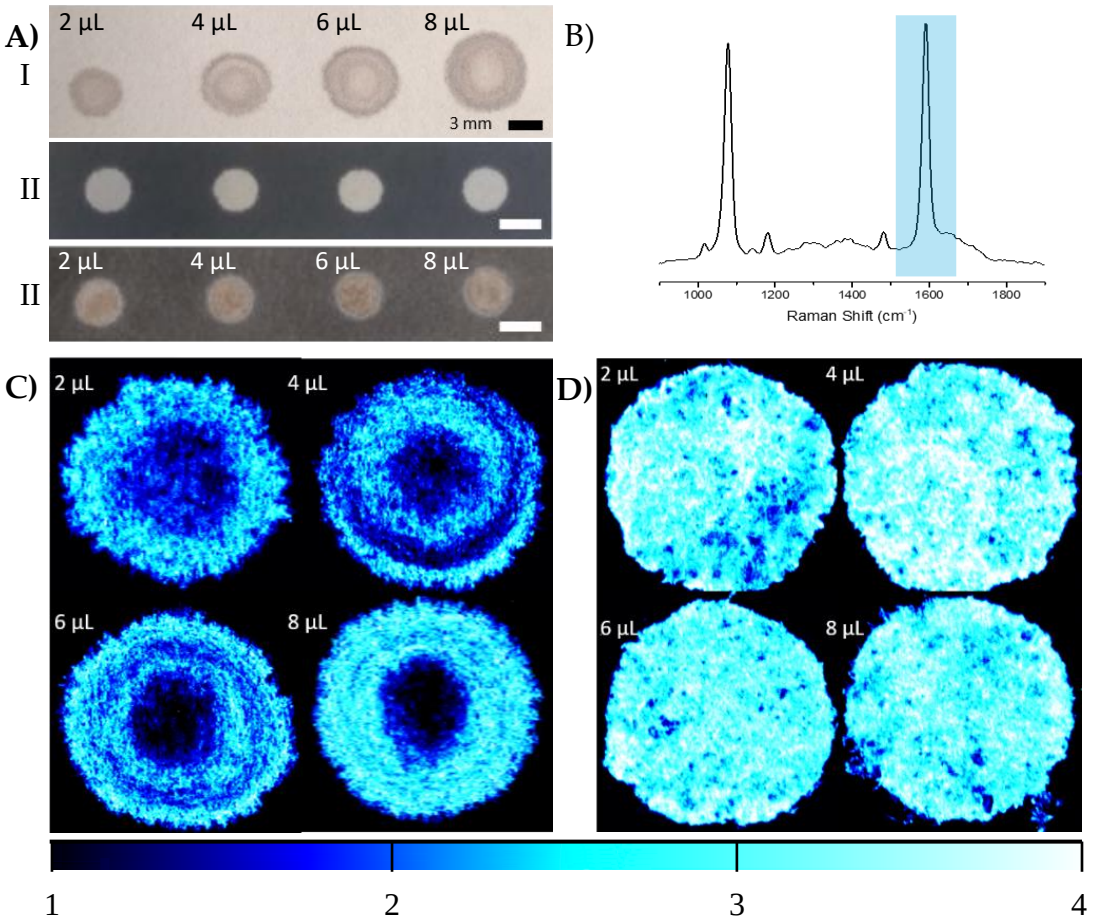

Figure 4.1 Differences between filter paper with waxed boundaries and no boundary.

A) I: Solutions of AuNPs were pipetted onto filter paper without a defined wax boundary, II: images of the filter paper with wax boundaries printed, III: AuNPs deposited onto waxed-masked features. All AuNPs depositions used 2 µL drops with 3.6×10^8 particles/µL. B) SERS spectra of 4-MBA, with the highlighted peak at 1587 cm^{-1} used for intensity comparisons. C) and D) Raman intensity maps of filter paper and patterned filter paper (respectively), deposited with varying levels of deposited AuNPs.

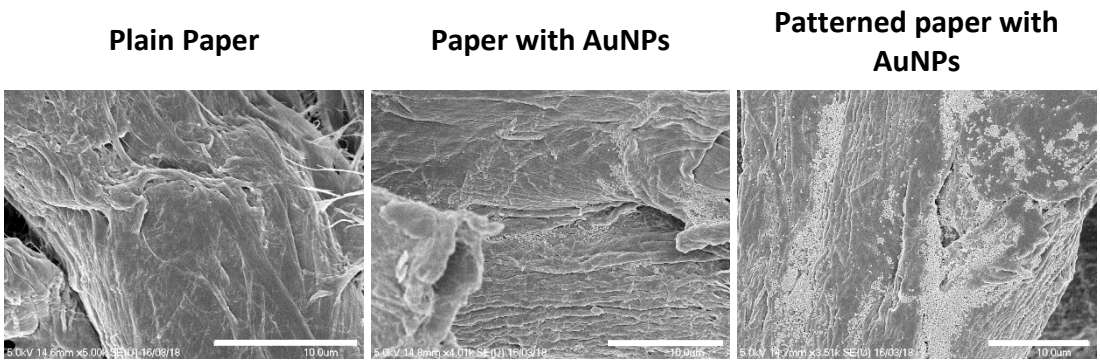

Figure 4.2 Scanning electron microscopy (SEM) images of plain filter paper (without AuNPs), 2 μL droplet AuNPs (with $3.6x10^8$ particles/μL) on filter paper fibres, and wax patterned filter paper with a 2 μL droplet AuNPs. Scale bar 10 μm. Images show a higher density of AuNPs using the wax patterned paper.

4.3 Fibre Sensing

4.3.1 Translation to fibre.

While pH sensing using an optical fibre has been demonstrated previously,[8,161] the background Raman signal from this fibre is strong and can overwhelm the SERS signal from the deposited particles on the distal end. Although some of these issues can be alleviated using sophisticated fibre designs, these are often bulky and require multiple fibres or fibres with large bores.[8,128,201] Additionally, as shown in **Chapter 2**, typically fibres for use with SERS sensing are prepared by dipping the distal end into concentrated nanoparticle solutions, leading to unknown and variable concentrations on the fibre tip.[8,128,161,201] This has an impact on how irreproducible, and therefore scalable, the production of the fibre sensors can be. Keeping in mind the possible applications, the ideal set-up would consist of a single fibre being bronchoscope deployable, with simple fabrication steps and minimal packaging requirements.

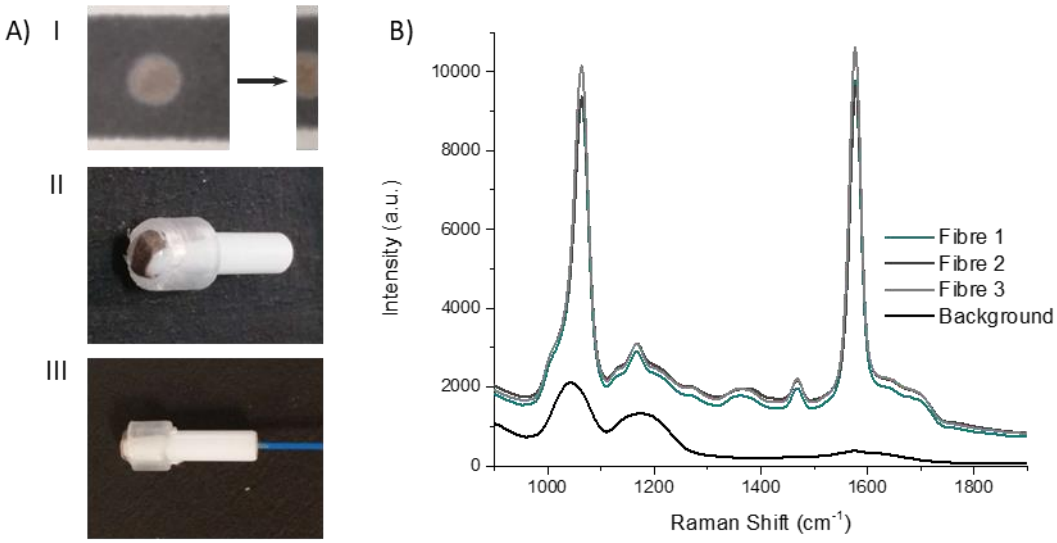

Figure 4.3 Translation of the paper SERS substrate to the end of a fibre**.** A) The fabrication process to combine the AuNP containing paper with a 200 μm core optical fibre. I: 2 mm section of AuNP paper was cut, II: AuNP paper secured across a fibre ferrule, III: fibre threaded through and secured in place. B) SERS spectra obtained from 3 separate fibres showing similar signal intensities. Intrinsic fibre background represented by the spectrum in black (which is much smaller than the generated SERS signals). Illumination using 785 nm, 1 mW, 1 s integration time.

The fabrication of the packaged ferrule end was a simple process (**Figure 4.3 (A)**), whereby a 2 mm wide strip of the wax printed AuNP paper was placed, facing upwards, on to a ring-shaped section of rubber. The ferrule was pushed through the ring with the paper flush across the top surface. A commercially available 200 μm single core (NA 0.39), multi-mode fibre was then threaded through the ferrule until it abutted against the paper and was secured in place at the base of the ferrule.

Through combining the fibre with the paper-based SERS substrate, a controlled particle deposition was achieved, providing confidence that the same signal intensity can be reached in any location where the fibre tip is placed on the AuNP paper. This extends to being able to reliably reproduce a strong signal when moving between fibres. Three separate fibres with packaged distal ends were prepared and their

spectra recorded in air. It can be seen that across the three fibres reproducibility of the paper-based system was demonstrated by strong signals of similar intensities (**Figure 4.3 (B)**). Moreover, the strong signal intensity generated by the paper-based SERS sensor easily overcomes the intrinsic fibre background using relatively low laser power and integration time (1 mW and 1 s respectively). Importantly, the fibre background did not impose significantly on the pH sensitive peaks at 1380 cm^{-1} and 1700 cm^{-1}.

4.3.2 pH Sensing.

The reporter molecule, 4-MBA, has been shown in previous chapters to be sensitive to pH, and has been previously demonstrated as a suitable choice for biologically and clinically relevant pH sensing.[8,23,51,224] The peaks observed at 1380 cm^{-1} and 1700 cm^{-1} (**Figure 4.4 (A)-(B)**) are spectral features most dependent on pH. Under basic conditions (pH 9 and above), AuNP-MBA will be in the anionic form, affording a strong response in the 1380 cm^{-1} peak. Conversely, under acidic conditions (pH 5 and below), the carboxylic acid (neutral form) will be the dominant species, generating a clear response in the peak found at 1700 cm^{-1}.

Aqueous pH buffers were prepared from pH 4-10 and verified with an electrochemical pH meter (Mettler-Toledo). The packaged distal end of the fibre was submerged in the buffers and the spectrum recorded after 10 s. Between readings the AuNP-paper substrate was rinsed in dH_2O and blotted dry. Each fibre had three replicate calibrations with the pHs used in random order, with three sensing fibres in total measured. The spectra were analysed by first normalising the spectra to the magnitude of a reference peak (1070 cm^{-1}), followed by evaluating the area under the curve (AUC) within a ± 25 cm^{-1} window of the peaks at 1380 cm^{-1} and 1700 cm^{-1}. Plotting pH against the AUC ratio, demonstrated consistent variation within the physiological range for all three fibres (**Figure 4.4 (C)**), indicating the suitability of the paper SERS substrate for fibre sensing and possible *in vivo* application.

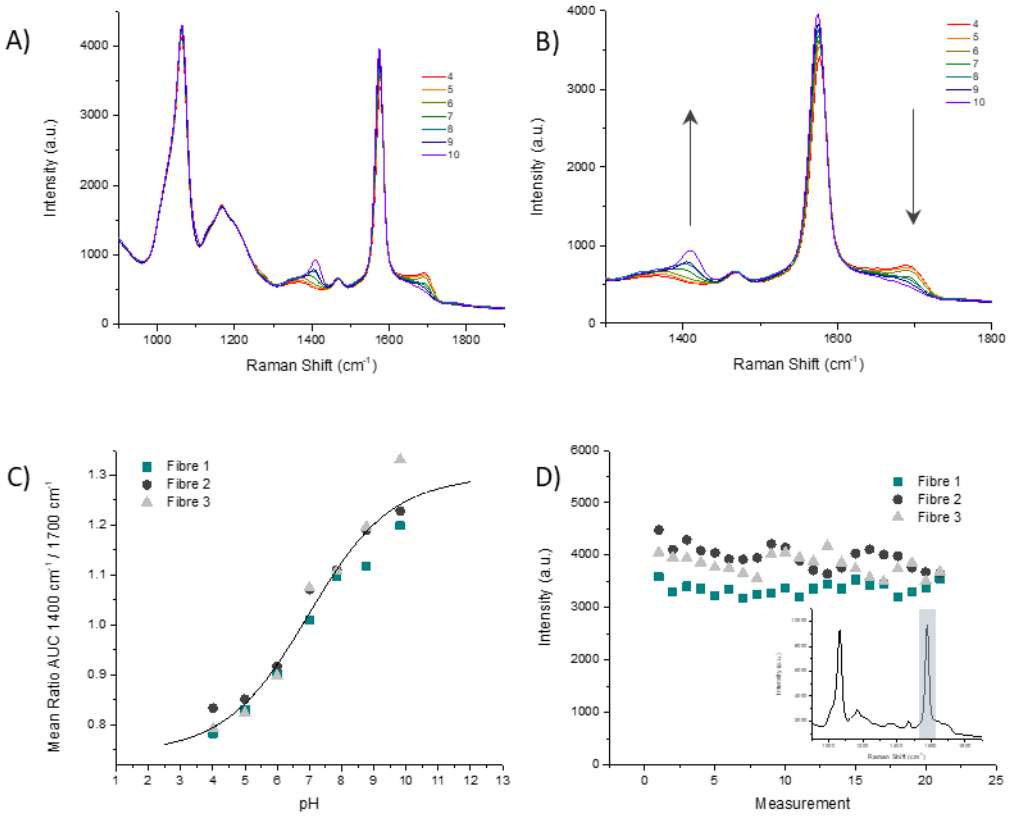

Figure 4.4 pH responses from the sensing fibre. A) SERS spectra of 4-MBA, through an optical fibre between pH 4-10; B) zoomed peaks of interest at 1380 cm^{-1} and 1700 cm^{-1} at pH 4-10 (arrows indicate changes with increasing pH). C) Ratio of AUC within a ± 25 cm^{-1} window of 1380 cm^{-1} and 1700 cm^{-1} plotted against pH with data shown for 3 fibres. Boltzmann curve fitted to data. Each measurement was taken with illumination at 785 nm, 1mW, 10 s integration time. D) Intensity of the 1587 cm^{-1} reference peak (inset) obtained during each measurement of the pH calibration plotted in chronological order.

The loss of nanoparticles over time from the distal end of the fibre would be problematic, not only due to loss of signal, but also because loss of AuNPs would not be possible for use in *in vivo* applications. With the fibres which have been dip-coated into nanoparticles, typically, a porous sol-gel layer is used to protect the distal end. However, this coating can also suffer from variations in both coating depth and the porosity of the sol-gel layer, which may affect the speed at which measurements can

be acquired. The paper-based SERS substrate showed no significant signal loss over the course of the pH measurements (approximately 60 min per fibre). The intensity of the 1587 cm^{-1} peak was plotted over time, with the slight oscillations being attributed to the drying and wetting of the SERS samples. The average intensities between the first and last sets of pH measurements differed by less than 10% of the overall signal intensity (**Figure 4.4 (D)**).

4.4 Extraction and Culture of *P. aeruginosa*

There has been a considerable increase in the number of infections with lower respiratory tract infections responsible for the second highest burden of disease globally.[225–227] Within ICUs, the development of pneumonia is associated with high mortality rates.[228] The investigation of respiratory disease can involve biopsies, an invasive procedure, and the collection of BALF, which can become contaminated by bacteria found in the upper respiratory tract. The ability to sample fluid at specific sites can alleviate issues related to contamination. The optical fibre presented here has been designed keeping in mind that it should be deployable through a conventional bronchoscope, once encased in an outer sheath. In this way, it could be extended and retracted at specific regions of interest, with visualisation to allow for positioning, therefore minimising the contact between the distal end of the probe and the upper respiratory tract.

The porous nature of the filter paper not only provides a suitable substrate for the capturing of nanoparticles but also lends itself to retrieving a sample of fluid. Herein, it was demonstrated that using waxed patterned paper, in a packaged ferrule device, is capable of sampling liquid containing bacteria. These samples can then be cultured

and counted or extracted and imaged. A clinical isolate of *P. aeruginosa 3284* was cultured and used is this study.

4.4.1 Sample Retrieval Efficiency

To evaluate whether samples containing bacteria could be retrieved using waxed patterned paper, and to investigate the limit of detection, 10-fold serial dilutions of *PA3284* ranging from 6 x10^8 – 6 x10^0 CFUs (colony forming units)/mL were prepared. The paper was dipped briefly into the solution of bacteria and pressed gently 4 times across a lysogeny broth (LB) agar plate (**Figure 4.5**). This process was repeated for each of the dilutions alongside control plates consisting of 3x 20 μL droplets of each dilution. The plates were incubated overnight (37 °C) and counted manually the following morning (**Figure 4.5 (B)-(C)**). It was observed that colonies formed *via* pressing paper onto a plate matched that of the control plates, with the lowest colonies formed as low as 60 CFUs/mL.

This demonstrates the ability of the paper to be used as a so called "sponge" regarding retrieving a fluid sample.

In a similar manner, the ferrule tip containing the AuNPs soaked paper was dipped into the bacterial containing solutions and gently pressed into LB agar plates, with three presses per dip. This process was repeated a total of three times per dilution. After an overnight incubation the colonies were counted and compared to the control, consisting of 3x 20 μL droplets at each dilution (**Figure 4.6**). It was again observed that a similar number of colonies were formed between the packaged ferrule and standard methods, with a LOD of 60 CFUs/mL in both the paper-based methods and the control (Miles and Misra) method, thus efficiently detecting below the clinical cut off which is considered infectious above 10^4 CFUs/mL.[208,229]

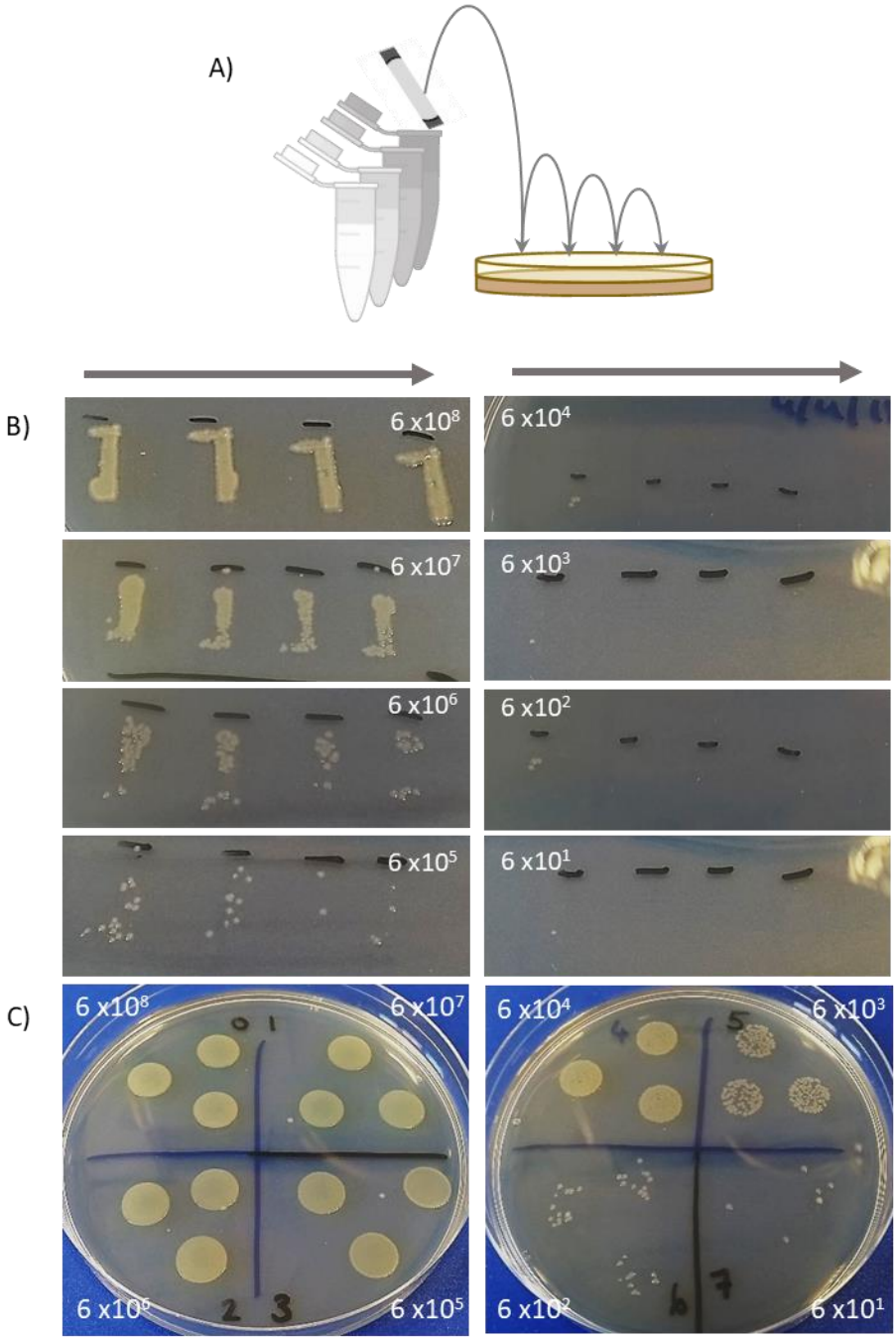

Figure 4.5 Assessing bacterial retrieval using waxed masked paper. A) Illustration showing method by which bacteria were sampled by dipping a strip of waxed masked paper into serial dilutions of PA3284 and pressing into LB agar plates followed by overnight culture. B) PA3284 cultures from paper pressing at serial dilutions of 6 x10^8 – 6 x10^1 CFU/mL. C) Control cultures. 3x 20 µL droplets of each dilution cultured overnight and counted manually the following day.

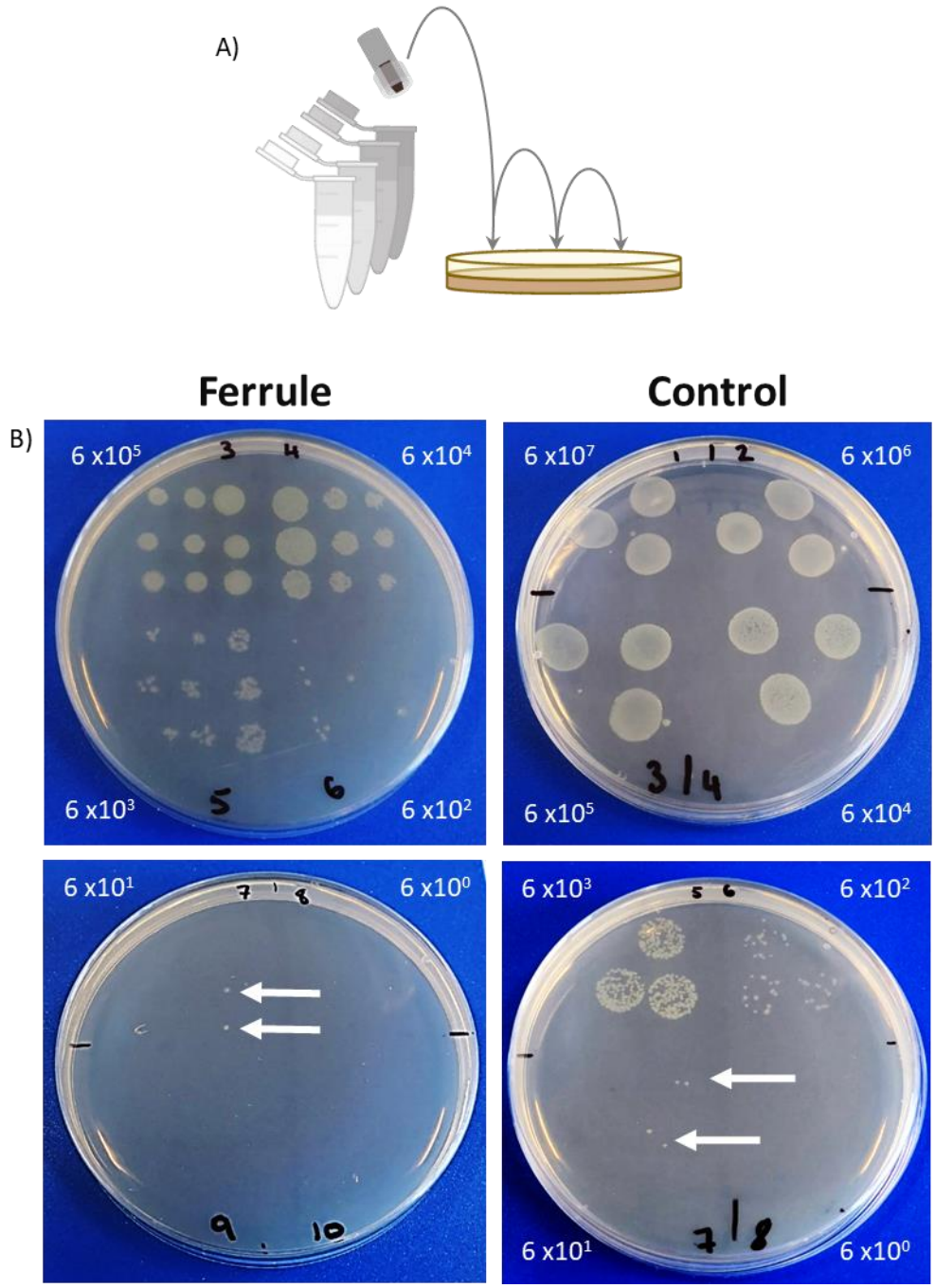

Figure 4.6 Assessing bacterial retrieval using the packaged ferrule. A) Illustration showing the packaged ferrule (with AuNP soaked paper) dipped into serial dilutions of PA3284 and pressing into LB agar plates followed by overnight culture. B) Plated cultures from serial dilutions of 6 x10^8 – 6 x10^1 CFU/mL using the ferrule, and control method of 3x 20 µL droplets of each dilution. Colonies were counted manually following overnight culture.

4.4.2 Imaging Extracted Bacteria

While culture techniques provide a platform for analysis and analysis of treatment pathways (i.e. drug responsiveness treatment), there is still a delay in the analysis pathway (requires overnight culturing). Being able to both perform culture and imaging techniques from the same extracted sample allows for a quick determination on whether or not bacteria is present. Extraction of bacteria from the paper was carried out after pressing the paper into agar by placing the paper strip in PBS (500 μL) and lightly vortexing. Using an in-house ubiquicidin based bacterial stain (5 μM),[230] it was possible to image the live bacteria shortly after retrieval, without the need for a washing step, by confocal laser scanning microscopy (CLSM; **Figure 4.7**).[230–232]

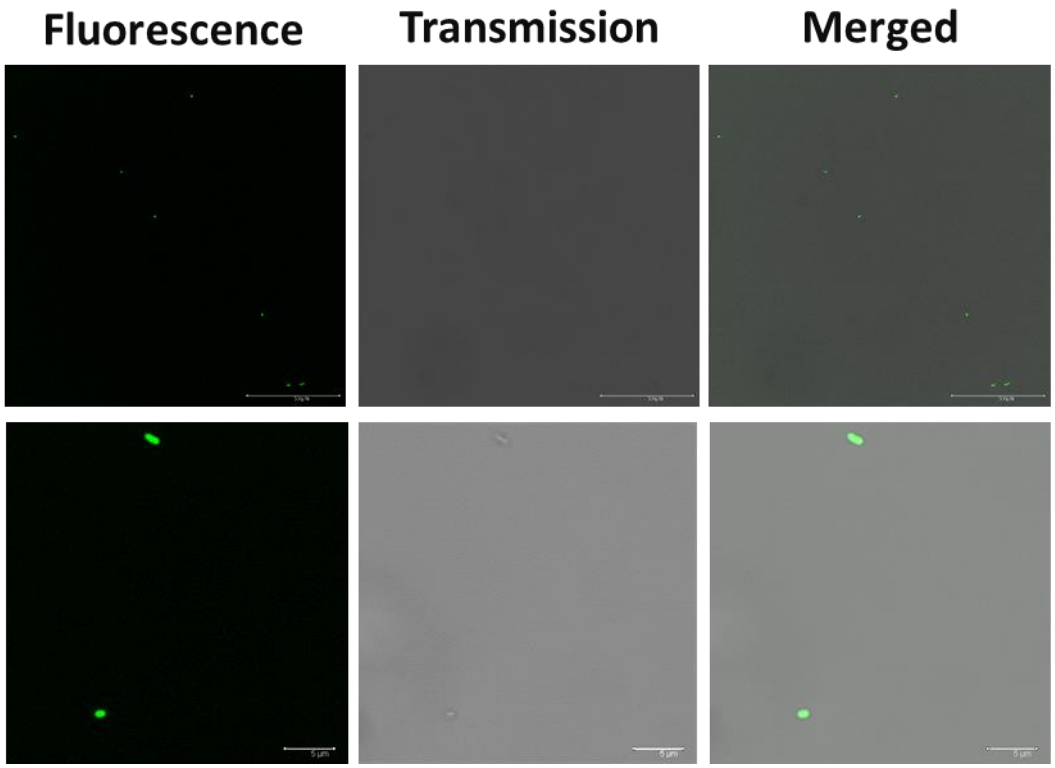

Figure 4.7 CLSM fluorescence images from extracted and labelled P. aeruginosa in PBS. The ferrule was dipped into bacteria (6 x10^2 CFU/mL), pressed into agar, then submerged in PBS. The "extracted" bacteria was stained with UBI-based dye (5 μM). Top panel, wide field view, bottom panel, zoom in of P. aeruginosa. Leica SP8, 488 nm excitation, 63x oil immersion. Images were brightness and contrast enhanced with proprietary software.

4.4.3 Direct Imaging of Bacteria on Paper

Imaging bacteria directly on the paper itself was investigated. Unfortunately, the filter paper used exhibits high autofluorescence (**Figure 4.8**), limiting the imaging approach due to difficulties in imaging "green on green". However, shifting the excitation wavelength to image the bacteria with a far-red dye proved to be beneficial. Thus, the bacteria were labelled with a Syto60 (5 µM), a red fluorescent nuclear stain,

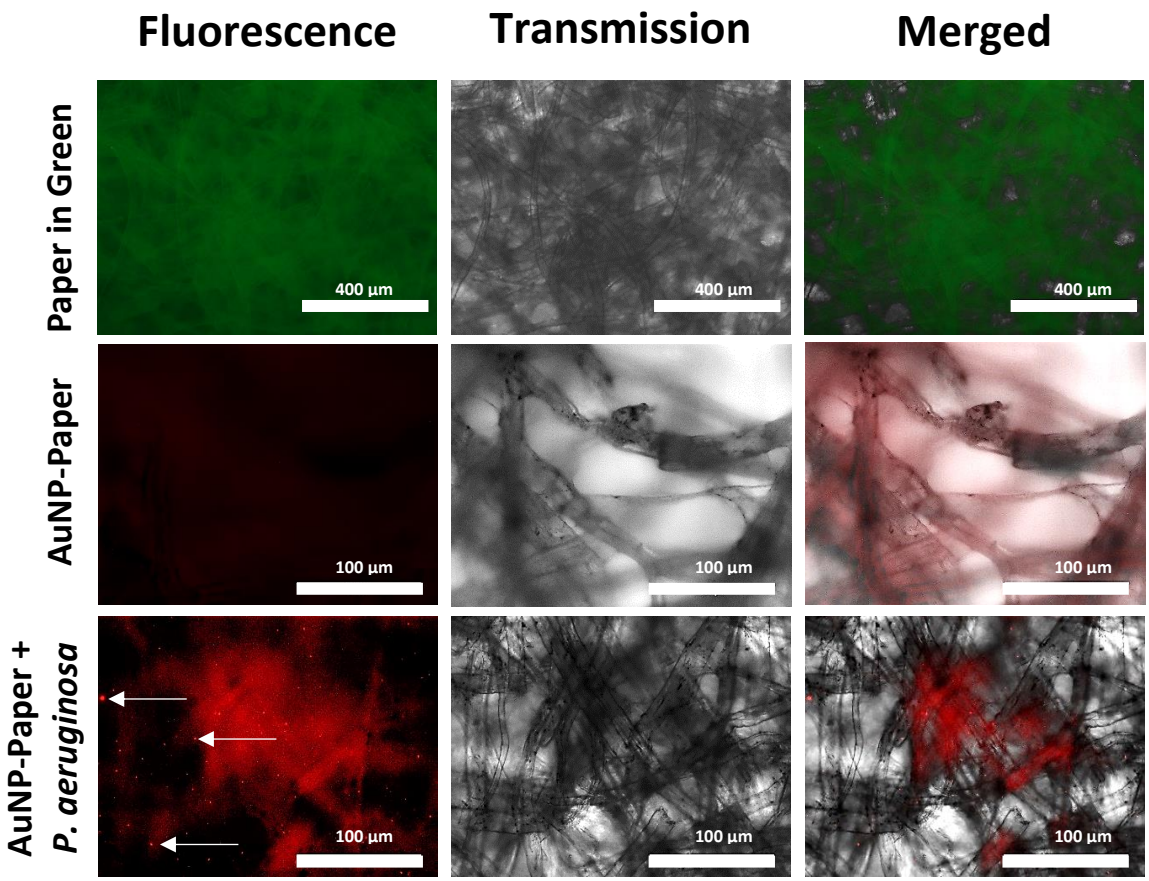

Figure 4.8 Widefield fluorescence images of AuNP soaked paper. Top row: Waxed paper without AuNP imaged using green channel displaying intense autofluorescence. Middle row: AuNP-paper without bacteria, imaged using Cy5 channel. Bottom row: AuNP-paper dipped in 6x 10^5 CFU/mL bacterial solution of *P. aeruginosa*, stained with Syto60 (λ_{ex}652 nm, λ_{em}678 nm). Speckle indicate bacteria, highlighted by arrows. Imaged using an EVOS microscope equipped with a Cy5 light cube.

before introducing the AuNP-paper strips into the solution containing bacteria at 6 x10^5 CFUs/mL. While this approach moved away from the autofluorescence seen in the green channel, there was still some autofluorescece signal observed in the cy5 fluorescence channel. Nevertheless, despite the background signal the labelled bacteria could clearly be detected by widefield imaging, indicating that augmenting the collected samples with an appropriate far-red bacteria-specific stain could enable *in situ* bacterial detection without any need for a processing step. This could pave the way for simultaneous measurements for bacteria and pH through a single fibre.

4.5 Conclusions

In this study, a facile, inexpensive and reproducible paper-based SERS sensor has been integrated with optical fibre technology for use in pH sensing across a physiological relevant range. Using a patterned wax printed stencil to control the wicking boundary of AuNPs, the distribution of particles can be controlled across the paper. In addition, due to the wicking nature of the filter paper, it was possible to extract the bacteria, *P. aeruginosa,* demonstrating the dual-purpose ability of the paper substrate to acquire physiological and pathogenic information.

5 Conclusions

In this work, the aim was to develop a range of substrates to extend the use of SERS nanosensors in several pH sensing applications: combining nanosensors with an optical fibre for remote sensing and to also use them within an *in vitro* tumour model – multicellular tumour spheroids (MTS). pH is a tightly regulated and vitally important cellular characteristic, any disruption of the finely balanced pH state in cells can result in the widespread disorder of cell function which has been implicated in disease progression. While research regarding pH is often focused on intracellular pH as a detrimental factor in maintaining healthy cell functioning, this research is directed towards the extracellular pH of cells. Additionally, fibre-based physiological sensing, particularly within the lungs to reach the alveolar space, presents as a challenge for *in vivo* sensing applications as they are still limited by the size of the sensors.

In Chapter 2, a suitable SERS reporter molecule sensitive to environmental pH was selected for physiological pH sensing. Following nanosensors selection, AuNP-MBA were deposited on the end of an optical fibre for remote sensing. During this process some limitations were overcome: preventing the loss of AuNPs from the distal end of the fibre and the removal of the intense signal from the fibre background. The application of a sol-gel layer provided a porous layer enabling AuNP retention while allowing fluid exchange to occur. The intrinsic fibre background was overcome through the utilisation of time correlated single photon counting spectroscopy (TCSPC). TCSPC facilitated the temporal selection of the SERS signal thereby diminishing the impact of the signal generated by the silica fibre. TCSPC clearly demonstrated a strong improvement in sensing capabilities over conventional Raman spectroscopy despite the sophisticated set up.

Macroscopic polymer beads employed as scaffolds for nanosensors was presented in Chapter 3, demonstrating the first example of *in situ* extracellular pH sensing SERS measurements within MTS. MTS are an important tool in cell culture, mimicking the *in vivo* tumour microenvironment more closely than traditional monolayer culture techniques. However, much of the research employing SERS sensing in biological applications focusses on the delivery of nanoparticles intracellularly, measurements concerning the extracellular spaces are somewhat lacking. These 3D scaffolds were used to measure pH in spatially sensitive regions within the MTS, showing a pH gradient between the central and outer regions of the MTS. The quantitative monitoring of extracellular pH could prove a useful tool in the assessment of novel drug development, drug delivery or other types of cancer therapy. Further, these scaffolds as used for 3D cell culture could be extended to simultaneously investigate intra- and extracellular pH/redox potentials with carefully selected nanosensors.

In addition to measuring pH gradients in MTS, initial studies have proven the capabilities of using the AuNP loaded beads in multicore fibres, extending from a single-plexed pH sensing fibre to a multiplexed pH and redox potential sensing fibre. These beads were capable of generating signal intensities large enough to overcome the intrinsic Raman fibre background. Future investigations could include looking into precision positioning of the scaffolds into the etched cores providing the potential to multiplex the 19-core fibre with a larger variety of SERS sensors than are demonstrated here (redox and pH). Special consideration into retaining particles on the end of the fibre would prove valuable in the furthering of this work.

Chapter 4 presented a simple, low-cost and reproducible paper-based SERS nanosensor substrate combined with an optical fibre for use in pH sensing across a physiological relevant range. A patterned wax printed stencil was used to control the wicking boundary of AuNPs controlling the distribution of particles across the paper. In addition, due to the wicking nature of the filter paper, it was possible to extract

and image the bacteria, *P. aeruginosa,* demonstrating the dual-purpose ability of the paper substrate to acquire physiological and pathogenic information.

Overall, this project has employed SERS for the quantitative and dynamic measurements of pH. This research demonstrates the first example of *in situ* extracellular pH sensing SERS measurements within MTS, and also presents the development of simple substrates for SERS-based optical-fibre sensors to provide a compact and miniaturised sensing system, capable of measuring pH at locations remote to the optical system.

However, there are several improvements that could be investigated to expand the application of these sensors:

For all sensing applications, the selection and evaluation of different sensing targets could be employed to extend the range of physiological parameters such as hydrogen peroxide or oxygen concentration, or the redox potential.[109,114] This would enable multiple measurements to be conducted simultaneously on the same sample.

For the fibre-based work, the dual-purpose pH sensing and sample retrieval fibre could be combined with a time resolved spectrometer to facilitate both Raman and fluorescence measurements through a single-fibre, including the quantitative determination of pH, with a qualitative analysis of the presence of bacteria. The development of a single fibre capable of obtaining fluorescence and Raman data would greatly aid in the development of small and compact sensors.

6 Materials and Methods

6.1 General

6.1.1 Chemicals and Solvents

All chemicals were purchased from Sigma Aldrich Co. and were used without further purification, unless stated otherwise. The redox active compound 1,8-diaza-4,5-dithian-1,8-di(2-chloro[1,4]-napthaquinone-3-yl)octane (NQ) was synthesised by Dr. P. I. Thomson. All solid gold nanoparticles were purchased from Sigma Aldrich Co, sizes were selected based on their SERS activity using a 785 nm excitation wavelength.

6.1.2 pH Calibration Buffers

All pH calibration buffers were prepared at room temperature in distilled water using the hydrochloric acid (HCl, 0.2 M) and potassium chloride (KCl, 0.2 M) (pH 1.0 – 2.5), potassium hydrogen phthalate (0.1 M) and HCl (0.1 M) (pH 3.0 – 4.0), citric acid (0.2 M) and sodium citrate (0.2 M) (pH 4.0 – 5.5), KH_2PO_4 (0.1 M) and sodium hydroxide (NaOH, 0.1 M) (pH 6.0 – 8.0), Tris(hydroxymethyl)aminomethane (tris, 0.1 M) and HCl (0.1 M) (pH 8.0 – 9.0), sodium bicarbonate (0.05 M) and NaOH (0.1 M) (pH 10.0 – 11.0), and KCl (0.2 M) and NaOH (0.2 M) (pH 12.0 – 13.0). The pH values were measured using a glass-electrode pH meter (Mettler Toledo), and where necessary adjusted using the appropriate acid or base.

6.1.3 Instruments

6.1.3.1 Bright Field Microscopy

- An Olympus CK2 was used for general cell culture and an Olympus CK2 with attached QCapture software to record images.

6.1.3.2 Confocal Fluorescence Microscopy

- Leica TCS SP8 - laser scanning confocal microscope

6.1.3.3 Fluorescence Microscopy

- Life Technologies EVOS FL Auto Cell Imaging System equipped with GFP and Invitrogen Cy5 light cubes (GFP excitation = 470⁄22 nm, emission 510/42 nm, and Cy5 excitation = 628/40, emission = 692/40 nm).

6.1.3.4 Plate Reader

- BIOTEK Synergy HT plate reader

6.1.3.5 Scanning Electron Microscopy

- Hitachi 4700 II cold Field-emission Scanning Electron Microscope
- EmScope sputter coater

6.1.3.6 Transmission Electron Microscopy

- Philips / FEI CM120 Biotwin transmission electron microscope

6.1.3.7 Zeta Potential

- Malvern Zetasizer Nano ZS using a Dip Cell accessory as necessary.

6.1.4 Raman Spectroscopic Measurements

6.1.4.1 Instrumentation

SERS spectra were recorded using four different instruments:

- A Renishaw in Via confocal Raman microscope and spectrometer
- An Ocean Optics QE Pro
- An Ocean Optics QE Pro combined with an optical fibre set up (**Figure 6.1**)
- Custom-built spectrometer combined with optical fibre set up (**Figure 6.1**) for TCSPC measurements**

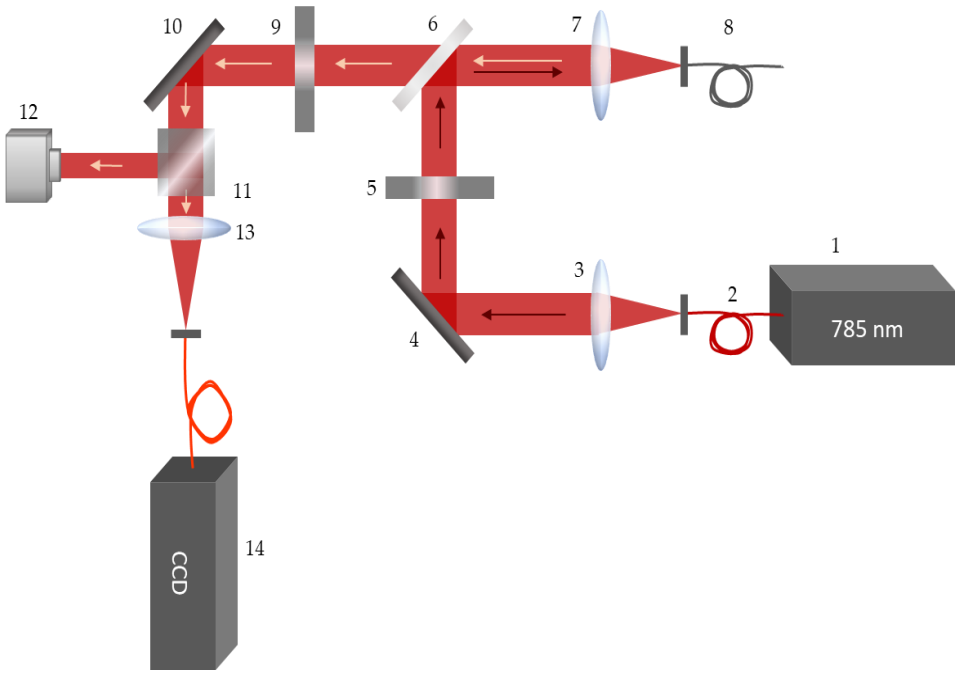

Figure 6.1 Optical fibre rig set up for fibre-based Raman measurements. See **Table 6.1** for a list of components.

** Built by Katjana Ehrlich, Heriot Watt University

Table 6.1 List of optical components for fibre-based Raman measurements

Number	Component
1	Continuous-wave 785 nm laser (Thorlabs)
2	Single mode fibre patch cable (1 m, 785 nm)
3	Moulded glass aspheric lenses (650 – 1100nm broadband antireflective (AR) coating). In all cases, compact aspheric lenses were used, where identical lenses were used in all locations to give unity magnification of the laser source
4	Mirror
5	Short pass filter
6	Long pass dichroic mirror
7	Lens
8	Fibre to sample (single core multimode fibre in chapters 2 and 4; multicore-multimode fibre as described in chapter 3)
9	Long pass filter
10	Mirror
11	Beamsplitter
12	Compact USB 2.0 CMOS camera connected to display. For imaging distal end of sample fibre
13	Lens
14	Spectrometer collection (Ocean Optics QEPro)

6.1.4.2 SERS Glass Substrate

Characterisation of SERS substrates were carried out on gold coated glass microscope slides. These were prepared by first cutting microscope slides into approximately 1 x 1.5 cm glass chips, soaking them in potassium hydroxide (KOH) overnight. The following day, the chips were rinsed in dH_2O and dried under a stream of air. The chips were placed in a petri dish and coated first with a 3 nm layer of chromium, then with 150 nm layer of gold, by Andrew Garrie, School of Physics and Astronomy, University of Edinburgh.

6.1.4.3 Optical Fibres

Several different fibres were used. Single core multimode 200 μm core diameter (NA 0.39) fibres were used in chapters 2-4.

Custom made fibres were made by Jim Stone (University of Bath) *via* the stack and draw process. First, a Ge-doped optical fibre preform surrounded by a thin pure silica jacket, with a parabolic refractive index profile (ø = 32 mm, numerical aperture = 0.3, Draka-Prysmian) was drawn down to form smaller rods (ø = 5.75 mm). The Ge-doped rods were surrounded by pure silica tubing (outer ø = 10 mm), to increase the core-to-core separation within the resulting fibre. The jacketed rods were then drawn down further (ø = 2.4 mm). Subsequently, 19 of the rods were then stacked in a hexagonal, close-packed formation, positioned within a jacket tube, and drawn under vacuum to form the 19-core fibre with a final core diameter of 10 μm, and an outer diameter of 125 μm.

For etching the distal ends of the fibres, 1 m lengths of fibre were cut. At the end of the fibre to be etched, a 5 cm portion of the plastic coating was removed with a razor blade. The fibres were then cleaved to leave a flat surface. The prepared fibres were then cleaned in deionized water within an ultrasonic bath for 3 min prior to etching

with 40% hydrofluoric acid (HF) for 60 s.[††] The etched fibres were subsequently placed in deionized water within an ultrasonic bath for 5 min. Caution - hydrofluoric acid (HF) is a highly corrosive inorganic acid. It must be handled with extreme caution.

6.2 General Techniques

6.2.1 General Cell Culture Procedures

The majority of the cell work was carried out using the MCF-7 human breast cancer cell line. Cells were cultured in Dulbecco's modified eagle's medium (DMEM; Gibco), supplemented with 10% heat in-activated foetal calf serum (FCS), L-glutamine (200 nM), 1% penicillin/streptomycin (10,000 U/mL), and incubated at 37 °C in a humidified 5% CO_2 environment. Cells were regularly passaged after reaching confluency in T75 flasks. Cells were gently washed with warmed phosphate buffered solution (PBS; Gibco), followed by the addition of warmed trypsin with ethylenediaminetetraacetic acid (0.5%; EDTA, 1 mL) added and incubated for 3-5 min. The flasks were tapped to detach cells, before adding DMEM (9 mL) and transferring the cell solution to a centrifuge tube before centrifugation (2000*g*, 4 min). The medium was removed, and the cell pellet resuspended in fresh medium (10 mL). Cells were then transferred to a new flask containing fresh medium.

For storage, cells were trypsinised as for passaging, with the cell pellet resuspended in a "freeze mixture" consisting of 10% dimethyl sulfoxide (DMSO) and 90% FCS. Aliquots of the cell suspension were transferred to cryovials and stored at -80 °C.

[††] Etching was carried out by D. Choudhury, Heriot Watt University, UK.

Cells were thawed by removing from -80 °C storage, wiping vials with 70% EtOH, and allowing the cells to thaw. The thawed cell suspension was transferred to a centrifuge tube containing medium, centrifuged (2000*g*, 4 min) before resuspending in fresh media and seeding for culture as required.

6.2.2 Cell Counting

Cells were counted either by using haemocytometry or by automation using a NucleoCounter.

Using haemocytometry to determine the number of cells, an aliquot (10 μL) of cell suspension was combined with 0.2% trypan blue (10 μL) on a surface (e.g. parafilm). The mixture was transferred to a Bright Line™ Haemocytometer for counting.

The cell concentration was determined by equation 2.1, where C = cell concentration (cells/mL), N = number of cells, and Q = number of quadrants counted (5).

$$C = \frac{N}{Q} \times 2 \times 10^4$$

The cell concentration was also determined by using a NucleoCounter, where a sample of the cell suspension (100 μL) was lysed and stabilised using proprietary solutions (Chemometec), followed by analysis using a microfluidic device which could take up a sample of the cell suspension, and contained the stain propidium iodide (PI).

6.2.3 MTT Assay

Cells were seeded at 15,000 per well in supplemented medium (100 μL) into a 96-well plate. Cells were allowed to adhere to the well plate overnight at 37 °C and 5% CO_2 in a humidified environment. The assays 10 μm TGs and 150 nm AuNPs were used. The addition of TGs in medium (100 μL, 15 mg/ mL TG particle concentration), TG-

AuNP (100 μL, 15 mg/ mL TG particle concentration, 5.4 x10^{10} particles/ mL AuNPs), TG-AuNP-MBA (100 μL, 15 mg/ mL TG particle concentration, 5.4 x10^{10} particles/ mL AuNPs, and was incubated overnight. The following day, a solution of 3-(4,5-dimethylthiazol-2-yl)-2,5-diphenyltetrazolium bromide (MTT) in PBS and medium (7:3, v/v; 1.7 mM). The cells were washed twice with PBS (2x 100μL), with the MTT solution (100 μL) added and incubated for 4 hours. Solubilising solution (100 μL), comprising 10% Triton-X 100 in acidic isopropanol (0.1N HCl), was added to the cells, covered in foil and shaken for 45 min. The absorbance was measured while shaking.

6.3 Chapter 2 Experimental – Nanoparticle Functionalisation

6.3.1 AuNP Functionalisation with 4-MBA

AuNPs were functionalised overnight with 0.1 mM 4-MBA in 10% EtOH. The 0.1 mM solution was prepared by first dissolving 4-MBA (*ca.* 2 mg) in EtOH to make a 1 mM solution. A 1 mL aliquot of AuNPs (3.6 x10^{9} particles/mL) was centrifuged (5500 rpm, 10 min) and the supernatant (900 μL) removed, leaving the pellet of AuNPs undisturbed. To the pellet, dH_2O (800 μL) was added, followed by the 4-MBA solution (100 μL, final concentration 0.1 mM). The AuNPs were sonicated to force resuspension and left overnight. The following day, the AuNPs were washed by centrifugation (5500 rpm, 10 min), the supernatant removed (900 μL) and resuspended in dH_2O (900 μL). The washings were repeated twice more before use.

6.3.2 AuNP Functionalisation with 4-MPY

AuNPs were functionalised overnight with 0.1 mM 4-MPY in 10% EtOH. The 0.1 mM solution was prepared by first dissolving 4-MPY (*ca.* 1 mg) in EtOH to make a 1 mM solution. A 1 mL aliquot of AuNPs was centrifuged (5500 rpm, 10 min) and the supernatant (900 μL) removed, leaving the pellet of AuNPs undisturbed. To the pellet, dH_2O (800 μL) was added, followed by the 4-MPY solution (100 μL, final concentration 0.1 mM). The AuNPs were sonicated to force resuspension and left overnight. The following day, the AuNPs were washed by centrifugation (5500 rpm, 10 min), the supernatant removed (900 μL) and resuspended in dH_2O (900 μL). The washings were repeated twice more before use.

6.3.3 AuNP Functionalisation with 4-ATP

AuNPs were functionalised overnight with 0.1 mM 4-ATP in 10% EtOH. The 0.1 mM solution was prepared by first dissolving 4-ATP (*ca.* 1 mg) in EtOH to make a 1 mM solution. A 1 mL aliquot of AuNPs was centrifuged (5500 rpm, 10 min) and the supernatant (900 μL) removed, leaving the pellet of AuNPs undisturbed. To the pellet, dH_2O (800 μL) was added, followed by the 4-ATP solution (100 μL, final concentration 0.1 mM). The AuNPs were sonicated to force resuspension and left overnight. The following day, the AuNPs were washed by centrifugation (5500 rpm, 10 min), the supernatant removed (900 μL) and resuspended in dH_2O (900 μL). The washings were repeated twice more before use.

6.3.4 pH Calibrations

Gold coated glass chips (as described in Section 2.2.1) were used as a substrate for the AuNP during pH calibrations. A single chip was glued to a microscope slide and an adhesive PDMS chamber placed surrounding the gold-coated chip.

A droplet of poly-L-lysine (PLL; 50 μL; MW 30 000–70 000; 0.1 mg/mL) was pipetted onto the gold-coated glass and left under cover for around 2h. The excess PLL was rinsed off using dH_2O and the AuNPs (50 μL, ~1.5 $x10^8$ particles) pipetted on to the now PLL coated area. The sample was allowed to dry overnight under ambient conditions before use.

For each of the calibrations, buffers between pH 1-12 were used. For each pH, buffer solution (0.5 mL) was placed within the PDMS chamber, the spectra recorded, and the buffer removed. Between each pH buffer the chip was rinsed with dH_2O. Each calibration composed of three replicates, with the pH solutions being used in a random order.

6.3.5 Fibre preparation

6.3.5.1 Nanoparticle Loading

Three commercial optical fibres (200 μm core diameter, 0.39 NA) were functionalised with poly-L-lysine and placed in the fibre rig (**Figure 6.1**). While "live", each fibre was dipped into a concentrated solution of AuNP-MBA (~3.6 $x10^{11}$ particles mL^{-1}) and the resulting spectra recorded after each dip up to a total of 5 dips, using 785 nm laser source, 0.8 mW output power and 30 s integration time.

6.3.5.2 Effects of Contact

After the initial addition of AuNP-MBA to the fibre, the AuNPs were left to dry. Following this, the fibres were dipped in H_2O, gently blotted on to filter paper and their spectra through fibre recorded. This was repeated a total of 3 times. Similarly, white light images and distal end Raman maps were taken of a fibre tip between blots, using a Renishaw In Via spectrometer, StreamLine function, 785 nm laser with ~10 mW power.

6.3.5.3 Sol-Gel Coating

Sol-Gel layer was prepared *via* the method set out by Grant et al.[170] Tetramethyl orthosilicate (TMOS, 0.5 mL) was added to milliQ water (1.0 mL) and HCl (10 μL, 0.04 M) and sonicated on ice for 30 min. Following sonication, 0.5 mL of the solution was added to PBS (1.0 mL). The Sol-Gel was applied in a similar way to the AuNP deposition, by briefly dipping the distal end of the fibre into the iced solution of the Sol-Gel mixture and allowed to dry overnight under ambient conditions.

6.3.6 Time Correlated Single Photon Counting

6.3.6.1 Instrumentation

Two spectrometers were used for comparative purposes: a custom-built spectrometer containing an in-house CMOS SPAD line sensor[163,171], and an Ocean Optics QE Pro spectrometer. For fibre measurements with either spectrometer, the fibre set up described in Section 6.1.4.1 was used (**Figure 6.1**).

6.3.6.2 Fibre Preparation

The distal end of a fibre (2.7 m, 50 μm diameter, 0.22 NA) was functionalised with poly-L-lysine, followed by dipping the end into a concentrated solution of 4-MBA functionalised gold nanoshells while monitoring the signal intensity using the fibre imaging set up described in Section 6.1.4.1, and a commercial spectrometer. A sol-gel layer (as described in Section 6.3.5.3) was applied before recording pH measurements.

6.3.6.3 pH Calibration

For the calibrations, buffers between pH 4.5-9.0 were used. For each pH, the distal end of the fibre would be gently placed in an Eppendorf containing the buffer solution (0.5 mL) and the spectra recorded using 785 nm laser source, 0.8 mW output power, and either 10 s or 60 s integration time. Between each pH buffer the fibre was rinsed with dH_2O. Each calibration composed of three replicates, with the pH solutions being used in a random order.

6.4 Chapter 3 Experimental – TG Substrates

6.4.1 TentaGel-Nanoparticle Scaffolds

Amine functionalised TentaGel® beads (TG; 5, 10, 20, 30, 100, 200, and 300 μm) were purchased from Rapp-Polymere. Typically, 10 μm TGs with a loading of 0.2-0.3 mmol/g were used unless stated otherwise.

A portion of TGs were weighed, and AuNPs added from stock, in general, to 1 mg of TGs, 3 mL of AuNPs (to give 1:3 w/v ratio) from stock would be added and left overnight. The following day, the supernatant was removed and the TG-AuNPs resuspended in 70% EtOH (final concentration of 1mg/mL TGs).

6.4.2 TG-AuNP Functionalisation with 4-MBA or NQ

For TG-AuNP beads, the AuNPs were functionalised overnight (after TG conjugation) with either 4-MBA (0.8 mM) or NQ (0.8 mM) in 10% EtOH. The 0.8 mM solution was prepared by first dissolving 4-MBA (ca. 2 mg) in EtOH to make a 5 mM solution. A 1 mL aliquot of TG-AuNPs (1 mg/mL) was centrifuged (7000 rpm, 1 min) and 900 μL of the supernatant removed, leaving a pellet in the centrifuge tube. The 4-MBA (5 mM) solution was added to the pellet, the conjugates were sonicated to force

resuspension and left overnight. The following day, the AuNPs were washed by centrifugation (7000 rpm, 1 min), the supernatant removed (900 μL) and the beads resuspended in dH_2O (900 μL). The washings were repeated twice more before use.

The same process was followed for the functionalisation of the varying sizes of TG beads (5-300 μm), as shown in Section 3.3.3.

6.4.3 TG Modifications

6.4.3.1 Adipic Acid Coupling

A solution containing adipic acid (1.5 eq) in anhydrous dimethylformamide (DMF) (10 mg/mL) was activated with N,N,N',N'-Bis(tetramethylene)-O-(N-succinimidyl)uranium hexafluorophosphate (HSPyU) (2.1 eq) and DIPEA (6 eq) at 40^0C for 1h. Once the activation is complete the solution is added to the TG resin beads together with DIPEA (3 eq) and shaken at rt overnight. The reaction was monitored *via* the ninhydrin test. The solution containing the resin was washed with DMF until colourless wash solution, DCM (3x5 mL) and MeOH (3x5 mL). The zeta potential of the beads was then measured.

6.4.3.2 Polyethylene Glycol Diacid Coupling

A solution containing polyethylene glycol diacid (HO_2C-PEG-COOH, M.W 600) (1.5 eq) in anhydrous dimethylformide (DMF) (10 mg/mL) was activated with N,N,N',N'-Bis(tetramethylene)-O-(N-succinimidyl)uranium hexafluorophosphate (HSPyU) (2.1 eq) and DIPEA (6 eq) at 40^0C for 1h. Once the activation is complete the solution is added to the TG resin beads together with DIPEA (3 eq) and shaken at rt overnight. The reaction was monitored *via* the ninhydrin test. The solution was drained, and the resin washed with DMF until colourless wash solution, DCM (3×5 mL) and MeOH (3×5 mL). The zeta potential of the beads was then measured.

6.4.3.3 Acetylation

A solution containing TG resin beads, acetic anhydride (2 eq), pyridine (3 eq) DMF (15 eq) was shaken at room temperature for 30 min. The reaction was monitored *via* the ninhydrin test. The solution was drained, and the resin washed with DMF until colourless wash solution, DCM (3×5 mL) and MeOH (3×5 mL). The zeta potential of the beads was then measured.

6.4.4 AuNP Functionalisation with 4-MBA

AuNPs were functionalised as described in Section 6.3.1. The zeta potential of the beads was then measured.

6.4.5 AuNP Functionalisation with PLL

AuNPs were functionalised overnight with PLL (0.1 mg/mL; MW 30 000–70 000) in dH_2O. A 1 mL aliquot of AuNPs (3.6 $x10^9$ particles) was centrifuged (5500 rpm, 10 min) and the supernatant (900 μL) removed, leaving the pellet of AuNPs undisturbed. To the pellet, dH_2O (800 μL) was added, followed by the PLL solution (100 μL, final concentration 0.1 mg/mL). The AuNPs were sonicated to force resuspension and left overnight. The following day, the AuNPs were washed by centrifugation (5500 rpm, 10 min), the supernatant removed (900 μL) and resuspended in dH_2O (900 μL). The washings were repeated twice more before use. The zeta potential of the beads was then measured.

6.4.6 pH Calibration

Gold coated glass chips (as described in Section 2.2.1) were used as a substrate for AuNP during pH calibrations. A single chip was glued to a microscope slide and an adhesive PDMS chamber placed surrounding the gold-coated chip.

A droplet of PLL (50 μL; MW 30 000–70 000; 0.1 mg/mL) was pipetted onto the gold coated glass and left under cover for approximately 2h. The PLL was rinsed off using dH_2O and the TG-AuNP-MBA sample pipetted on to the PLL coated area. The sample was allowed to dry overnight under ambient conditions.

For each of the calibrations, buffers between pH 1-12 were used. For each pH, buffer solution (0.5 mL) was placed in the PDMS chamber, the spectra recorded, and the buffer removed. Between each pH buffer the chip was rinsed with dH_2O. Each calibration composed of three replicates, with the pH solutions being used in a random order.

6.4.7 Monolayer Cell Culture

In a sterile environment, CaF_2 windows were cleaned and soaked in 70% EtOH for 1 hr, the solution removed, and the windows allowed to dry within a laminar flow hood. Each window was coated with PLL (50 μL; MW 30 000–70 000; 0.1 mg/mL; 0.1 mg/ml) and left for approximately 2 hr. The windows were rinsed with sterile tissue culture (TC) water and allowed to dry.

TG-AuNP-MBA (10 μm, 1 mg mL^{-1}) were soaked in 70% EtOH overnight, followed by 3 washings by centrifugation (7500 rpm, 5 min), the supernatant removed (950 μL) and resuspended in 70% EtOH (950 μL), with sonication to aid resuspension. A sample of the suspension (20 μL) was pipetted onto the pre-functionalised CaF_2 windows and allowed to dry completely in a sterile environment.

Each window was placed in a separate well of a 6-well plate, to which a suspension of cells in medium (1 x10^5 cells, 2 mL) was added. The cells were incubated overnight at 37 °C in a humidified 5% CO_2 environment to allow adhesion to the windows.

6.4.7.1 Drug Responses

Staurosporine (STS) was used to induce apoptosis. Following overnight incubation of cells on the CaF_2 windows, each CaF_2 window was placed into 35 mm petri dish, and a solution of STS in medium (1 μM, 2 mL) added. One sample was left untreated as a control, with fresh medium added instead. All samples were placed in an incubator at 37 °C in a humidified 5% CO_2 environment for at least 30 min prior to imaging. Each STS dosed sample was incubated for either 0-1, 1-2, 2-3, 4-5, 5-6, or 6-7 hours, and imaged immediately upon removal from the incubator.

6.4.7.2 Measuring Extracellular pH of Monolayer Culture

TG-AuNP-MBA beads which were surrounded by at least 3 cells were used for measuring pH. All spectra were recorded using the Renishaw In Via spectrometer, using Edge 785 nm laser, 5x objective, ~100 mW, 7s integration time with 5 accumulations.

All data was processed using WiRe 4.4, Origin9 software, and Excel.

6.4.8 Multicellular Tumour Spheroids (MTS)

The hanging drop technique was used to prepare MTS. Cells were first grown in a 2D monolayer. The cells were trypsinised, and the cell solution transferred to a centrifuge tube before centrifugation (2000*g*, 4 min). The medium was removed, and the cell pellet resuspended in fresh medium (4 x10^4 cells/mL). Droplets (15 μL) of the cell

suspension were pipetted onto the lid of a plastic Petri dish. The lid was placed on the bottom of the dish containing medium (10 mL) and incubated at 37 °C in a humidified 5% CO_2 environment. The MTS were typically grown over a period of 7 days, with the droplets containing the MTS having fresh medium exchanged on days 4 and 6.

6.4.8.1 Incorporation of TG into Multicellular Tumour Spheroids (MTS)

TG-AuNP-MBA (10 μm, 0.01 mg mL^{-1} TG) were soaked in 70% EtOH overnight, followed by 3 washings by centrifugation (7500 rpm, 5 min), the supernatant removed (450 μL) and resuspended in sterile PBS (450 μL). On the last centrifugation step, as much supernatant was removed as possible, leaving a pellet of TG-AuNP-MBA in <10 μL sterile PBS. To the pellet, 1 mL of cells in medium was added (4 $x10^4$ cells mL^{-1}), pipetting the solution gently to resuspend the pellet of beads. Droplets (15 μL) of the cell/bead mixture was pipetted onto the lid of a plastic Petri dish. The lid was placed on the bottom of the dish containing medium (10 mL) and incubated at 37 °C in a humidified 5% CO_2 environment. The MTS were typically grown over a period of 7 days, with the droplets containing the MTS having fresh medium exchanged on days 4 and 6.

6.4.8.2 Drug Responses

Staurosporine (STS) was used to induce apoptosis in the MTS. After 7 days of growth, the medium containing the droplets was removed and replaced with either fresh medium (20 μL), or STS in medium (10 μM, 20 μL). All samples were placed in an incubator at 37 °C in a humidified 5% CO_2 environment for at least 30 min prior to imaging. Each STS dosed sample was incubated for either 0-1, 1-2, 2-3, 4-5, 5-6, 6-7 hours, or overnight, and imaged immediately upon removal from the incubator.

6.4.8.3 Imaging of TGs incorporated in MTS

After approximately 7 days of growth, the MTS formed *via* the hanging drop method were harvested for imaging.

Mapping whole MTSs was possible *in situ* using the Renishaw In Via spectrometer. The MTS were mapped using the StreamLine 785 nm laser, 5x objective, ~100 mW, 2s integration time. A 20 x 14.2 μm (x,y) step size in each direction was used. A single spectrum was extracted from each TG bead (approximately in the centre) and categorised as either "Centre" or "Outer" depending on location of the particle.

All data was processed using WiRe 4.4, Origin9 software, and Excel.

6.4.8.4 Setting MTS in Matrigel®

All equipment (Matrigel®, pipette tips, CaF_2 windows) was chilled on ice prior to introduction of the MTS. MTS were gently pipetted into desired volume of chilled Matrigel® onto a CaF_2 window, and allowed to set in an incubator at 37 °C with 5% CO_2 for 30 min.

6.4.9 MTS TEM

MTS were fixed in 0.5% glutaraldehyde in PBS for 2 hours. Osmium tetroxide staining of the fixed samples were carried out by Steve Mitchell (School of Biological Science, University of Edinburgh). The samples were sectioned, transferred to copper imaging grids, and examined using a Jeol JEM transmission electron microscope.

6.4.10Multicore Multimode Fibre

Fabrication of the 19 core, multimode fibre was carried out *via* the "stack and draw" process as described in Section 6.1.4.3. Through fibre Raman measurements were carried out using the fibre set up as shown in **Figure 6.1** coupled to an Ocean Optics QE Pro spectrometer. Raman mapping of the distal fibre end was carried out using a Renishaw InVia system.

Functionalised TG-AuNPs (10 μm / 150 nm) were loaded into etched cores of the multicore fibre *via* force loading. A sample of TG-AuNPs containing approximately 1800 microspheres, and comprising either only TG-AuNP-MBA, or a mixture of TG-AuNP-MBA and TG-AuNP-NQ in 70% EtOH were allowed to settle into a loose pellet. The supernatant was removed as much as possible to leave <10 μL. The distal end of the fibre was then pressed gently into the pellet of microspheres. Typically, loading was carried out with live monitoring of a single core.

6.4.11Single Core Fibre

6.4.11.1 Fabrication

A single core, multimode, silica based optical fibre (1 m length, core diameter of 200 μm, NA 0.39) was used for the SERS chamber work (Section 3.6). Both the optical fibre (200 μm core diameter, NA 0.39) and fibre ferrules were purchased from Thorlabs.

Larger TG-AuNP-MBA (~200 μm TG bead size) conjugates were prepared for the SERS chamber work in the same way as outlined in Section 6.4.2.

Fabrication of the chamber in which a single TG-AuNP-MBA bead would sit was prepared by first cutting a strip from a cell strainer mesh (Falcon Corning™; ~2 mm wide, 100 μm pore size). This was placed on top of a rubber ring, and a fibre ferrule was pushed through resulting in the mesh placed flush on the top of the ferrule. A

single TG-AuNP-MBA bead was pipetted into the open end of the ferrule and pushed into place by the fibre and secured in place.

6.4.11.2 pH Sensing

For the calibrations, buffers between pH 4.0-9.0 were used. For each pH, the distal end of the fibre would be gently placed in an Eppendorf containing the buffer solution (0.5 mL) and the spectra recorded using a 785 nm laser source, with an output power of 0.8 mW, and a 30 s integration time. Between each pH buffer the fibre was rinsed with dH_2O. Each calibration composed of three replicates, with the pH solutions being used in a random order.

6.5 Chapter 4 Experimental – Paper substrates

6.5.1 General

Filter paper (Whatman, grade 114) was purchased from Scientific Laboratory Supplies Ltd. Lysogeny Broth was purchased from Thermofisher. Both the Optical fibre (200 μm core diameter, NA 0.39) and fibre ferrules were purchased from Thorlabs.

6.5.1.1 Preparation of functionalised nanoparticles

Gold nanoparticles (5 x 1 mL aliquots, 3.6 $x10^9$ particles/mL, ~150 nm) were prepared for functionalisation by centrifuged at 5500 rpm for 10 min. For functionalising the particles, following centrifugation, the supernatant (900 μL) from each aliquot was removed without disturbing the pellet. The pellet was resuspended in deionised water (800 μL) and 4-MBA (100 μL, 1 mM in EtOH) and left overnight. Unbound 4-

MBA was removed via washing and centrifugation at 5500 rpm for 10 min. The supernatant (900 μL) was removed without disturbing the pellet, followed by resuspension in dH2O (900 μL). The samples were vortexed and sonicated to ensure the particles were forced back into suspension. The washing and centrifugation process was completed a total of 3 times.

The functionalised nanoparticles were then concentrated and combined. The samples were centrifuged at 5500 rpm for 10 min, and the supernatant (950 μL) was removed without disturbing the pellet. The AuNPs were forced back into suspension in the remaining volume of dH2O (~50 μL) through sonication and vortexing. The 5 aliquots were combined, centrifuged at 5500 rpm for 10 min, and the appropriate amount of supernatant was removed to give a final volume of 50 μL (1.8×10^{10} particles).

6.5.2 Fabrication of paper SERS substrate

Preparation of the filter paper: an array of circular stencils was designed.[‡‡] A Xerox ColourQube8580 was used to print in standard waxed based ink on to the surface of the filter paper, leaving 3 mm diameters disks of bare paper. The wax printed paper was placed on a hotplate (150 °C) and compressed with a weight for 60s.

For fabrication of the SERS-active substrate, 2 μL droplets of the concentrated 4-MBA functionalised AuNPs were pipetted on to the filter paper disk and allowed to dry at room temperature for an hour. A further 6 μL of AuNPs was dropped on to each disk in 2 μL aliquots with drying in between to a total of 8 μL (2.9×10^{9} total particles deposited).

‡‡ Drawn and printed by Angus Marks, University of Edinburgh

6.5.3 Fibre sensing

For preparation of the fibre-based sensor: Silica based optical fibres (3 x 1 m length, core diameter of 200 μm, NA 0.39) were used throughout. The filter paper disks containing functionalised AuNPs had a 1 mm wide strip down the centre of the disk. The "top side" (the side of the filter paper to which AuNPs had been applied) was placed facing upwards on top of a rubber ring. A fibre ferrule was pushed through the ring resulting in the filter paper placed flush on the top of the ferrule. Following the preparation of the packaged ferrule, the fibre tip was threaded through to meet the filter paper and secured in place. A total of 3 fibres were prepared for calibration.

A SERS spectrum was obtained using the packaged distal end of the fibre from 7 separate pH buffers from pH 4-10. SERS spectra were acquired while the fibre tip was fully submerged in each buffer for the total period of the spectral acquisition time. 3 independent fibres were used each with 3 replicate measurements between pH 4-10, with the order of the measurements within each replicate being random.

6.5.4 Bacterial Culture and Extraction of *P. aeruginosa 3284*

An inhouse clinical isolate *Pseudomonas aeruginosa 3284* was used for this investigation. A single colony was inoculated in Lysogeny Broth (LB; 10 mL) and incubated overnight (37 °C, 250 RPM), followed by a further subculture (100 μL of overnight culture in 10 mL LB) and incubated at the same conditions for 4 hours until mid-log phase growth was reached.

The optical density at 595 nm (OD_{595}) of the resulting culture was measured and adjusted to a value of 1 to give an approximate bacterial concentration of 6 $x10^8$ CFU/mL. Serial dilutions (6 x 10^8 to 6 x 10^0 CFU/mL) were prepared with sterile PBS.

For each dilution, the packaged ferrule was dipped into the bacteria containing solution and pressed in succession across an LB agar plate. To compare, 3 x 20 μL

samples of each dilution was dropped on lysogeny broth (LB) agar plates for CFU analysis. Plates were incubated at 37 °C with 5% CO_2 overnight, with CFUs manually counted as a standard method.

6.5.5 Fluorescence Imaging of Bacteria

Bacteria were stained with either an in-house ubiquicidin based fluorescent dye (5 μM)[212], or nuclear stain (Syto60, 5μM, Thermofisher).

The ferrule was dipped into bacteria (6 $x10^2$ CFU/mL), pressed into agar, then submerged in PBS. The "retrieved" bacteria were stained with UBI-based dye (5 μM), and imaged using a Leica SP8 CSLM, 488 nm excitation, 63x oil immersion objective. Images were brightness and contrast enhanced with proprietary software.

Widefield fluorescence images of bacteria on filter paper AuNP soaked paper. Before the introduction of the paper, a bacterial solution of *P. aeruginosa* (6x 10^5 CFU/mL), was stained with Syto60 (5 μm, λex652 nm, λem678 nm) as per manufacturer's instructions. Waxed paper without AuNP or bacteria was imaged using the GFP lightcube with the EVOS FL Auto Cell Imaging System. AuNP-paper without bacteria, imaged using Cy5 light cube. Waxed paper containing AuNPs was dipped into the stained bacterial solutions and imaged on the using the Cy light cube.

7 References

1 H. N. Po and N. M. Senozan, 5.

2 Overview of pH Regulation, /overview-of-ph-regulation, (accessed 18 February 2019).

3 Q. Yan, *Methods Mol. Biol. Clifton NJ*, 2010, **637**, 1–21.

4 M. Chen, C. Chen, Z. Shen, X. Zhang, Y. Chen, F. Lin, X. Ma, C. Zhuang, Y. Mao, H. Gan, P. Chen, X. Zong and R. Wu, *Oncotarget*, 2017, **8**, 45759–45767.

5 Y. Kato, S. Ozawa, C. Miyamoto, Y. Maehata, A. Suzuki, T. Maeda and Y. Baba, *Cancer Cell Int.*, 2013, **13**, 89.

6 Respiratory diseases statistics - Statistics Explained, https://ec.europa.eu/eurostat/statistics-explained/index.php/Respiratory_diseases_statistics#Deaths_from_diseases_of_the_respiratory_system, (accessed 26 March 2019).

7 J. D. Salciccioli, D. C. Marshall, J. Shalhoub, M. Maruthappu, G. D. Carlo and K. F. Chung, *BMJ*, 2018, **363**, k4680.

8 D. Choudhury, M. G. Tanner, S. McAughtrie, F. Yu, B. Mills, T. R. Choudhary, S. Seth, T. H. Craven, J. M. Stone, I. K. Mati, C. J. Campbell, M. Bradley, C. K. I. Williams, K. Dhaliwal, T. A. Birks and R. R. Thomson, *Biomed. Opt. Express*, 2017, **8**, 243.

9 E. L. Vukovac, M. Lozo, K. Mise, I. Gudelj, Ž. Puljiz, A. Jurcev-Savicevic, A. Bradaric, J. Kokeza and J. Mise, *Med. Sci. Monit. Int. Med. J. Exp. Clin. Res.*, 2014, **20**, 255–261.

10 E. Lozo Vukovac, K. Miše, I. Gudelj, I. Perić, D. Duplančić, I. Vuković, Z. Vučinović and M. Lozo, *J. Int. Med. Res.*, 2019, **47**, 791–802.

11 M. J. Pugia, *Lab. Med.*, 2000, **31**, 92–96.

12 A. W. Ng, A. Bidani and T. A. Heming, *Lung*, 2004, **182**, 297–317.

13 C. R. Bodem, L. M. Lampton, D. P. Miller, E. F. Tarka and E. D. Everett, *Am. Rev. Respir. Dis.*, 1983, **127**, 39–41.

14 S. Garneau-Tsodikova and K. J. Labby, *MedChemComm*, 2016, **7**, 11–27.

15 A. Dalhoff, S. Schubert and U. Ullmann, *Infection*, 2005, **33**, 36–43.

16 D. Hanahan and R. A. Weinberg, *Cell*, 2000, **100**, 57–70.

17 D. Hanahan and R. A. Weinberg, *Cell*, 2011, **144**, 646–674.

18 Y. A. Fouad and C. Aanei, *Am. J. Cancer Res.*, 2017, **7**, 1016–1036.

19 M. Damaghi, J. W. Wojtkowiak and R. J. Gillies, *Front. Physiol.*, , DOI:10.3389/fphys.2013.00370.

20 P. Swietach, R. D. Vaughan-Jones, A. L. Harris and A. Hulikova, *Philos. Trans. R. Soc. B Biol. Sci.*, , DOI:10.1098/rstb.2013.0099.

21 A. I. Hashim, X. Zhang, J. W. Wojtkowiak, G. V. Martinez and R. J. Gillies, *NMR Biomed.*, 2011, **24**, 582–591.

22 C. Corbet and O. Feron, *Nat. Rev. Cancer*, 2017, **17**, 577–593.

23 L. E. Jamieson, V. L. Camus, P. O. Bagnaninchi, K. M. Fisher, G. D. Stewart, W. H. Nailon, D. B. McLaren, D. J. Harrison and C. J. Campbell, *Nanoscale*, 2016, **8**, 16710–16718.

24 B. Thakur, S. Jayakumar and S. N. Sawant, *Chem. Commun.*, 2015, **51**, 7015–7018.

25 J. Zhou, L. Zhang and Y. Tian, *Anal. Chem.*, 2016, **88**, 2113–2118.

26 M. C. Frost and M. E. Meyerhoff, *Annu. Rev. Anal. Chem.*, 2015, **8**, 171–192.

27 M. C. Frost, A. K. Wolf and M. E. Meyerhoff, in *Detection Challenges in Clinical Diagnostics*, 2013, pp. 129–155.

28 C. V. Raman and K. S. Krishnan, *Nature*, 1928, **121**, 501–502.

29 E. Smith and G. Dent, *Modern Raman Spectroscopy – A Practical Approach*, John Wiley & Sons, Ltd, 2005.

30 P. Atkins and J. De Paula, *Atkins' Physical Chemistry*, Oxford University Press, Oxford, 9th edn., 2010.

31 S. I. Stoeva, J.-S. Lee, C. S. Thaxton and C. A. Mirkin, *Angew. Chem. Int. Ed.*, 2006, **45**, 3303–3306.

32 S. Shikha, T. Salafi, J. Cheng and Y. Zhang, *Chem. Soc. Rev.*, 2017, **46**, 7054–7093.

33 M. Fleischmann, P. J. Hendra and A. J. McQuillan, *Chem. Phys. Lett.*, 1974, **26**, 163–166.

34 D. L. Jeanmaire and R. P. Van Duyne, *J. Electroanal. Chem. Interfacial Electrochem.*, 1977, **84**, 1–20.

35 M. G. Albrecht and J. A. Creighton, *J. Am. Chem. Soc.*, 1977, **99**, 5215–5217.

36 A. A. Stacy and R. P. V. Duyne, *Chem. Phys. Lett.*, 1983, **102**, 365–370.

37 L. A. Lane, X. Qian and S. Nie, *Chem. Rev.*, 2015, **115**, 10489–10529.

38 A. Campion and P. Kambhampati, *Chem. Soc. Rev.*, 1998, **27**, 241–250.

39 K. Faulds, A. Hernandez-Santana and W. E. Smith, in *Spectroscopic Properties of Inorganic and Organometallic Compounds*, 2010, pp. 1–21.

40 K. L. Wustholz, A.-I. Henry, J. M. McMahon, R. G. Freeman, N. Valley, M. E. Piotti, M. J. Natan, G. C. Schatz and R. P. Van Duyne, *J. Am. Chem. Soc.*, 2010, **132**, 10903–10910.

41 S. M. Asiala and Z. D. Schultz, *The Analyst*, 2011, **136**, 4472–4479.

42 N. H. Kim, W. Hwang, K. Baek, Md. R. Rohman, J. Kim, H. W. Kim, J. Mun, S. Y. Lee, G. Yun, J. Murray, J. W. Ha, J. Rho, M. Moskovits and K. Kim, *J. Am. Chem. Soc.*, 2018, **140**, 4705–4711.

43 E. C. Le Ru and P. G. Etchegoin, in *Principles of Surface-Enhanced Raman Spectroscopy*, Elsevier, 2009.

44 X. Zhao and M. Chen, *RSC Adv.*, 2014, **4**, 63596–63602.

45 P. C. Lee and D. Meisel, *J. Phys. Chem.*, 1982, **86**, 3391–3395.

46 L.-P. Ding and Y. Fang, *Spectrochim. Acta. A. Mol. Biomol. Spectrosc.*, 2007, **67**, 767–771.

47 C. H. Munro, W. E. Smith, M. Garner, J. Clarkson and P. C. White, *Langmuir*, 1995, **11**, 3712–3720.

48 K. F. Gibson, D. Correia-Ledo, M. Couture, D. Graham and J.-F. Masson, *Chem. Commun.*, 2011, **47**, 3404–3406.

49 H. Park, S. Lee, L. Chen, E. K. Lee, S. Y. Shin, Y. H. Lee, S. W. Son, C. H. Oh, J. M. Song, S. H. Kang and J. Choo, *Phys. Chem. Chem. Phys.*, 2009, **11**, 7444–7449.

50 C. L. Zavaleta, B. R. Smith, I. Walton, W. Doering, G. Davis, B. Shojaei, M. J. Natan and S. S. Gambhir, *Proc. Natl. Acad. Sci. U. S. A.*, 2009, **106**, 13511–13516.

51 S. W. Bishnoi, C. J. Rozell, C. S. Levin, M. K. Gheith, B. R. Johnson, D. H. Johnson and N. J. Halas, *Nano Lett.*, 2006, **6**, 1687–1692.

52 R. Smith, K. L. Wright and L. Ashton, *The Analyst*, 2016, **141**, 3590–3600.

53 K. Majzner, A. Kaczor, N. Kachamakova-Trojanowska, A. Fedorowicz, S. Chlopicki and M. Baranska, *Analyst*, 2012, **138**, 603–610.

54 S. McAughtrie, K. Lau, K. Faulds and D. Graham, *Chem. Sci.*, 2013, **4**, 3566.

55 P. Heraud, K. M. Marzec, Q.-H. Zhang, W. S. Yuen, J. Carroll and B. R. Wood, *Sci. Rep.*, 2017, **7**, 8945.

56 S. Yerolatsitis, F. Yu, S. McAughtrie, M. G. Tanner, H. Fleming, J. M. Stone, C. J. Campbell, T. A. Birks and J. C. Knight, in *Advanced Photonics 2018 (BGPP, IPR, NP, NOMA, Sensors, Networks, SPPCom, SOF) (2018), paper SoW3H.2*, Optical Society of America, 2018, p. SoW3H.2.

57 S. Pahlow, K. Weber, J. Popp, B. R. Wood, K. Kochan, A. Rüther, D. Perez-Guaita, P. Heraud, N. Stone, A. Dudgeon, B. Gardner, R. Reddy, D. Mayerich and R. Bhargava, *Appl. Spectrosc.*, 2018, **72**, 52–84.

58 C. A. Lieber, S. K. Majumder, D. L. Ellis, D. D. Billheimer and A. Mahadevan-Jansen, *Lasers Surg. Med.*, 2008, **40**, 461–467.

59 H. Lui, J. Zhao, D. McLean and H. Zeng, *Cancer Res.*, 2012, **72**, 2491–2500.

60 L. M. Almond, J. Hutchings, G. Lloyd, H. Barr, N. Shepherd, J. Day, O. Stevens, S. Sanders, M. Wadley, N. Stone and C. Kendall, *Gastrointest. Endosc.*, 2014, **79**, 37–45.

61 L. M. Almond, J. C. Hutchings, C. A. Kendall, G. R. Lloyd, J. C. Day, O. A. Stevens, N. A. Shepherd, H. Barr and N. Stone, *J. Biomed. Opt.*, 2012, **17**, 081421.

62 S. Duraipandian, W. Zheng, J. Ng, J. J. H. Low, A. Ilancheran and Z. Huang, *Analyst*, 2011, **136**, 4328–4336.

63 S. McAughtrie, K. Faulds and D. Graham, *J. Photochem. Photobiol. C Photochem. Rev.*, 2014, **21**, 40–53.

64 K. Buckley, J. G. Kerns, P. D. Gikas, H. L. Birch, J. Vinton, R. Keen, A. W. Parker, P. Matousek and A. E. Goodship, *IBMS BoneKEy*, 2014, **11**, 602.

65 S. Kloß, B. Lorenz, S. Dees, I. Labugger, P. Rösch and J. Popp, *Anal. Bioanal. Chem.*, 2015, **407**, 8333–8341.

66 G. Rusciano, P. Capriglione, G. Pesce, P. Abete, V. Carnovale and A. Sasso, *Laser Phys. Lett.*, 2013, **10**, 075603.

67 C. A. Jenkins, R. A. Jenkins, M. M. Pryse, K. A. Welsby, M. Jitsumura, C. A. Thornton, P. R. Dunstan and D. A. Harris, *Analyst*, 2018, **143**, 6014–6024.

68 C. A. Jenkins, P. D. Lewis, P. R. Dunstan and D. A. Harris, *World J. Gastrointest. Oncol.*, 2016, **8**, 427–438.

69 A. Sahu, S. Sawant, H. Mamgain and C. M. Krishna, *Analyst*, 2013, **138**, 4161–4174.

70 H. J. Butler, L. Ashton, B. Bird, G. Cinque, K. Curtis, J. Dorney, K. Esmonde-White, N. J. Fullwood, B. Gardner, P. L. Martin-Hirsch, M. J. Walsh, M. R. McAinsh, N. Stone and F. L. Martin, *Nat. Protoc.*, 2016, **11**, 664–687.

71 V. O. Baron, M. Chen, S. O. Clark, A. Williams, R. J. H. Hammond, K. Dholakia and S. H. Gillespie, *Sci. Rep.*, 2017, **7**, 9844.

72 K. Kneipp, A. S. Haka, H. Kneipp, K. Badizadegan, N. Yoshizawa, C. Boone, K. E. Shafer-Peltier, J. T. Motz, R. R. Dasari and M. S. Feld, *Appl. Spectrosc.*, 2002, **56**, 150–154.

73 K. Bando, N. I. Smith, J. Ando, K. Fujita and S. Kawata, *J. Opt.*, 2015, **17**, 114023.

74 A. Huefner, W.-L. Kuan, K. H. Müller, J. N. Skepper, R. A. Barker and S. Mahajan, *ACS Nano*, 2016, **10**, 307–316.

75 D. Cialla-May, X.-S. Zheng, K. Weber and J. Popp, *Chem. Soc. Rev.*, 2017, **46**, 3945–3961.

76 F. Lussier, T. Brulé, M. Vishwakarma, T. Das, J. P. Spatz and J.-F. Masson, *Nano Lett.*, 2016, **16**, 3866–3871.

77 F. Lussier, T. Brulé, M.-J. Bourque, C. Ducrot, L.-É. Trudeau and J.-F. Masson, *Faraday Discuss.*, 2017, **205**, 387–407.

78 K. Lin, J. Xu, L. Li, F. Liao, X. Dong and J. Lin, *Laser Phys. Lett.*, 2018, **15**, 125601.

79 K. Zhang, C. Hao, Y. Huo, B. Man, C. Zhang, C. Yang, M. Liu and C. Chen, *Lasers Med. Sci.*, , DOI:10.1007/s10103-019-02781-w.

80 K. Faulds, W. E. Smith and D. Graham, *Anal. Chem.*, 2004, **76**, 412–417.

81 M. B. Wabuyele and T. Vo-Dinh, *Anal. Chem.*, 2005, **77**, 7810–7815.

82 K. Ryu, A. J. Haes, H.-Y. Park, S. Nah, J. Kim, H. Chung, M.-Y. Yoon and S.-H. Han, *J. Raman Spectrosc.*, 2010, n/a-n/a.

83 A. Huefner, W.-L. Kuan, R. A. Barker and S. Mahajan, *Nano Lett.*, 2013, **13**, 2463–2470.

84 S. Lee, S. Kim, J. Choo, S. Y. Shin, Y. H. Lee, H. Y. Choi, S. Ha, K. Kang and C. H. Oh, *Anal. Chem.*, 2007, **79**, 916–922.

85 S. Lee, H. Chon, M. Lee, J. Choo, S. Y. Shin, Y. H. Lee, I. J. Rhyu, S. W. Son and C. H. Oh, *Biosens. Bioelectron.*, 2009, **24**, 2260–2263.

86 H. Kearns, R. Goodacre, L. E. Jamieson, D. Graham and K. Faulds, *Anal. Chem.*, 2017, **89**, 12666–12673.

87 T. Vo-Dinh, K. Houck and D. L. Stokes, *Anal. Chem.*, 1994, **66**, 3379–3383.

88 N. R. Isola, D. L. Stokes and T. Vo-Dinh, *Anal. Chem.*, 1998, **70**, 1352–1356.

89 P. L. White, S. J. Hibbitts, M. D. Perry, J. Green, E. Stirling, L. Woodford, G. McNay, R. Stevenson and R. A. Barnes, *J. Clin. Microbiol.*, 2014, **52**, 3536–3543.

90 M. Chisanga, H. Muhamadali, D. I. Ellis and R. Goodacre, *Appl. Spectrosc.*, 2018, **72**, 987–1000.

91 K. Duval, H. Grover, L.-H. Han, Y. Mou, A. F. Pegoraro, J. Fredberg and Z. Chen, *Physiology*, 2017, **32**, 266–277.

92 B. M. Baker and C. S. Chen, *J Cell Sci*, 2012, **125**, 3015–3024.

93 Alhaque Sharmin, Themis Michael and Rashidi Hassan, *Philos. Trans. R. Soc. B Biol. Sci.*, 2018, **373**, 20170216.

94 Y. Fang and R. M. Eglen, *Slas Discov.*, 2017, **22**, 456–472.

95 Schmidt Sara, Lilienkampf Annamaria and Bradley Mark, *Philos. Trans. R. Soc. B Biol. Sci.*, 2018, **373**, 20170223.

96 R. Santoro, S. Venkateswaran, F. Amadeo, R. Zhang, M. Brioschi, A. Callanan, M. Agrifoglio, C. Banfi, M. Bradley and M. Pesce, *Biomater. Sci.*, 2017, **6**, 154–167.

97 N. Noor, A. Shapira, R. Edri, I. Gal, L. Wertheim and T. Dvir, *Adv. Sci.*, 2019, **0**, 1900344.

98 L. E. Jamieson, D. J. Harrison and C. J. Campbell, *Analyst*, 2015, **140**, 3910–3920.

99 J. Z. Zhang, N. S. Bryce, R. Siegele, E. A. Carter, D. Paterson, M. D. de Jonge, D. L. Howard, C. G. Ryan and T. W. Hambley, *Integr. Biol. Quant. Biosci. Nano Macro*, 2012, **4**, 1072–1080.

100 L. H. Tucker, A. Conde-González, D. Cobice, G. R. Hamm, R. J. A. Goodwin, C. J. Campbell, D. J. Clarke and C. L. Mackay, *Anal. Chem.*, 2018, **90**, 8742–8749.

101 F. Nicolson, L. E. Jamieson, S. Mabbott, K. Plakas, N. C. Shand, M. R. Detty, D. Graham and K. Faulds, *Analyst*, 2018, **143**, 5965–5973.

102 M. Altunbek, D. Çetin, Z. Suludere and M. Çulha, *Talanta*, 2019, **191**, 390–399.

103 O. Lyandres, N. C. Shah, C. R. Yonzon, J. T. Walsh, M. R. Glucksberg and R. P. Van Duyne, *Anal. Chem.*, 2005, **77**, 6134–6139.

104 H.-Z. Yu, N. Xia and Z.-F. Liu, *Anal. Chem.*, 1999, **71**, 1354–1358.

105 J. Kneipp, H. Kneipp, B. Wittig and K. Kneipp, *J. Phys. Chem. C*, 2010, **114**, 7421–7426.

106 A. Pallaoro, G. B. Braun, N. O. Reich and M. Moskovits, *Small*, 2010, **6**, 618–622.

107 A. Jaworska, L. E. Jamieson, K. Malek, C. J. Campbell, J. Choo, S. Chlopicki and M. Baranska, *The Analyst*, 2015, **140**, 2321–2329.

108 V. Mallikarjun, D. J. Clarke and C. J. Campbell, *Free Radic. Biol. Med.*, 2012, **53**, 280–288.

109 P. I. T. Thomson, V. L. Camus, Y. Hu and C. J. Campbell, *Anal. Chem.*, 2015, **87**, 4719–4725.

110 C. A. R. Auchinvole, P. Richardson, C. McGuinnes, V. Mallikarjun, K. Donaldson, H. McNab and C. J. Campbell, *ACS Nano*, 2012, **6**, 888–896.

111 J. Jiang, C. Auchinvole, K. Fisher and C. J. Campbell, *Nanoscale*, 2014, **6**, 12104–12110.

112 L. E. Jamieson, A. Jaworska, J. Jiang, M. Baranska, D. J. Harrison and C. J. Campbell, *The Analyst*, 2015, **140**, 2330–2335.

113 R. Li, Z. Jia and M. A. Trush, *React. Oxyg. Species Apex NC*, 2016, **1**, 9–21.

114 L.-L. Qu, Y.-Y. Liu, S.-H. He, J.-Q. Chen, Y. Liang and H.-T. Li, *Biosens. Bioelectron.*, 2016, **77**, 292–298.

115 X. Gu, H. Wang, Z. D. Schultz and J. P. Camden, *Anal. Chem.*, 2016, **88**, 7191–7197.

116 R. Motterlini and L. E. Otterbein, *Nat. Rev. Drug Discov.*, 2010, **9**, 728–743.

117 M. J. D. Griffiths and T. W. Evans, *N. Engl. J. Med.*, 2005, **353**, 2683–2695.

118 Y. Cao, D.-W. Li, L.-J. Zhao, X.-Y. Liu, X.-M. Cao and Y.-T. Long, *Anal. Chem.*, 2015, **87**, 9696–9701.

119 J. Cui, K. Hu, J.-J. Sun, L.-L. Qu and D.-W. Li, *Biosens. Bioelectron.*, 2016, **85**, 324–330.

120 S. Schlücker, B. Küstner, A. Punge, R. Bonfig, A. Marx and P. Ströbel, *J. Raman Spectrosc.*, 2006, **37**, 719–721.

121 C. Jehn, B. Küstner, P. Adam, A. Marx, P. Ströbel, C. Schmuck and S. Schlücker, *Phys. Chem. Chem. Phys.*, 2009, **11**, 7499–7504.

122 B. R. Lutz, C. E. Dentinger, L. N. Nguyen, L. Sun, J. Zhang, A. N. Allen, S. Chan and B. S. Knudsen, *ACS Nano*, 2008, **2**, 2306–2314.

123 X. Qian, X.-H. Peng, D. O. Ansari, Q. Yin-Goen, G. Z. Chen, D. M. Shin, L. Yang, A. N. Young, M. D. Wang and S. Nie, *Nat. Biotechnol.*, 2008, **26**, 83–90.

124 S. Keren, C. Zavaleta, Z. Cheng, A. de la Zerda, O. Gheysens and S. S. Gambhir, *Proc. Natl. Acad. Sci. U. S. A.*, 2008, **105**, 5844–5849.

125 R. McQueenie, R. Stevenson, R. Benson, N. MacRitchie, I. McInnes, P. Maffia, K. Faulds, D. Graham, J. Brewer and P. Garside, *Anal. Chem.*, 2012, **84**, 5968–5975.

126 O. Stevens, I. E. Iping Petterson, J. C. C. Day and N. Stone, *Chem. Soc. Rev.*, 2016, **45**, 1919–1934.

127 I. P. Santos, E. M. Barroso, T. C. Bakker Schut, P. J. Caspers, C. G. F. van Lanschot, D.-H. Choi, M. F. van der Kamp, R. W. H. Smits, R. van Doorn, R. M. Verdijk, V. Noordhoek Hegt, J. H. von der Thüsen, C. H. M. van Deurzen, L. B. Koppert, G. J. L. H. van Leenders, P. C. Ewing-Graham, H. C. van Doorn, C. M. F. Dirven, M. B. Busstra, J. Hardillo, A. Sewnaik, I. ten Hove, H. Mast, D. A. Monserez, C. Meeuwis, T. Nijsten, E. B. Wolvius, R. J. Baatenburg de Jong, G. J. Puppels and S. Koljenović, *The Analyst*, 2017, **142**, 3025–3047.

128 P. R. Stoddart and D. J. White, *Anal. Bioanal. Chem.*, 2009, **394**, 1761–1774.

129 T. Kaino, *Appl. Phys. Lett.*, 1986, **48**, 757–758.

130 T. Kaino, K. Jinguji and S. Nara, *Appl. Phys. Lett.*, 1982, **41**, 802–804.

131 C. G. Danny, A. Subrahmanyam and V. V. R. Sai, *J. Raman Spectrosc.*, 2018, **49**, 1607–1616.

132 F. Yu and J. C. Knight, *IEEE J. Sel. Top. Quantum Electron.*, 2016, **22**, 146–155.

133 F. Benabid, J. C. Knight, G. Antonopoulos and P. S. J. Russell, *Science*, 2002, **298**, 399–402.

134 R. Altkorn, M. D. Malinsky, R. P. Van Duyne and I. Koev, *Appl. Spectrosc.*, 2001, **55**, 373–381.

135 Kitao. Fujiwara and Keiichiro. Fuwa, *Anal. Chem.*, 1985, **57**, 1012–1016.

136 A. Ghatak and K. Thyagarajan, *Fundam. PHOTONICS*, 2000, 44.

137 B. Vojnovic and D. Volpi, *Notes on optical fibres and fibre bundles*, University of Oxford, 2012.

138 T. Hutter, S. R. Elliott and S. Mahajan, *Opt. Express*, 2018, **26**, 15539.

139 S. Harmsen, S. Rogalla, R. Huang, M. Spaliviero, V. Neuschmelting, Y. Hayakawa, Y. Lee, Y. Tailor, R. Toledo-Crow, J. W. Kang, J. M. Samii, H. Karabeber, R. M. Davis, J. R. White, M. van de Rijn, S. S. Gambhir, C. H. Contag, T. C. Wang and M. F. Kircher, *ACS Nano*, , DOI:10.1021/acsnano.8b06808.

140 C. L. Zavaleta, E. Garai, J. T. C. Liu, S. Sensarn, M. J. Mandella, D. Van de Sompel, S. Friedland, J. Van Dam, C. H. Contag and S. S. Gambhir, *Proc. Natl. Acad. Sci. U. S. A.*, 2013, **110**, E2288-2297.

141 E. Garai, S. Sensarn, C. L. Zavaleta, N. O. Loewke, S. Rogalla, M. J. Mandella, S. A. Felt, S. Friedland, J. T. C. Liu, S. S. Gambhir and C. H. Contag, *PLOS ONE*, 2015, **10**, e0123185.

142 E. Garai, S. Sensarn, C. L. Zavaleta, D. Van de Sompel, N. O. Loewke, M. J. Mandella, S. S. Gambhir and C. H. Contag, *J. Biomed. Opt.*, 2013, **18**, 096008.

143 R. M. Davis, B. Kiss, D. R. Trivedi, T. J. Metzner, J. C. Liao and S. S. Gambhir, *ACS Nano*, 2018, **12**, 9669–9679.

144 M. A. A. Mamun, S. Juodkazis, A. Mahadevan-Jansen and P. R. Stoddart, in *Optical Diagnostics and Sensing XVIII: Toward Point-of-Care Diagnostics*, International Society for Optics and Photonics, 2018, vol. 10501, p. 1050102.

145 C. Liu, S. Wang, G. Chen, S. Xu, Q. Jia, J. Zhou and W. Xu, *Sens. Bio-Sens. Res.*, 2014, **1**, 8–14.

146 A. Ricciardi, A. Crescitelli, P. Vaiano, G. Quero, M. Consales, M. Pisco, E. Esposito and A. Cusano, *Analyst*, 2015, **140**, 8068–8079.

147 J. P. Scaffidi, M. K. Gregas, V. Seewaldt and T. Vo-Dinh, *Anal. Bioanal. Chem.*, 2009, **393**, 1135–1141.

148 V. Guieu, D. Talaga, L. Servant, N. Sojic and F. Lagugné-Labarthet, *J. Phys. Chem. C*, 2009, **113**, 874–881.

149 X. Zheng, D. Guo, Y. Shao, S. Jia, S. Xu, B. Zhao, W. Xu, C. Corredor and J. R. Lombardi, *Langmuir*, 2008, **24**, 4394–4398.

150 Y. Kitahama, T. Itoh, J. Aoyama, K. Nishikata and Y. Ozaki, *Chem. Commun.*, 2009, 6563.

151 D. Jin, Y. Bai, H. Chen, S. Liu, N. Chen, J. Huang, S. Huang and Z. Chen, *Anal. Methods*, 2015, **7**, 1307–1312.

152 J. Cao, D. Zhao and Q. Mao, *Analyst*, 2017, **142**, 596–602.

153 S. Liu, J. Huang, Z. Chen, N. Chen, F. Pang, T. Wang and L. Hu, *J. Raman Spectrosc.*, 2015, **46**, 197–201.

154 A. Michota and J. Bukowska, *J. Raman Spectrosc.*, 2003, **34**, 21–25.

155 L. Lawson and T. Huser, *Anal. Chem.*, 2012, **84**, 3574–3580.

156 J. Kneipp, H. Kneipp, B. Wittig and K. Kneipp, *Nano Lett.*, 2007, **7**, 2819–2823.

157 Y. Shen, L. Liang, S. Zhang, D. Huang, J. Zhang, S. Xu, C. Liang and W. Xu, *Nanoscale*, 2018, **10**, 1622–1630.

158 K. L. Nowak-Lovato and K. D. Rector, *Int. J. Anal. Chem.*, 2012, **2012**, 390182.

159 D. Ma, J. Zheng, P. Tang, W. Xu, Z. Qing, S. Yang, J. Li and R. Yang, *Anal. Chem.*, 2016, **88**, 11852–11859.

160 K. Kim, K. L. Kim, H. B. Lee and K. S. Shin, *J. Phys. Chem. C*, 2012, **116**, 11635–11642.

161 K. Ehrlich, A. Kufcsák, S. McAughtrie, H. Fleming, N. Krstajic, C. J. Campbell, R. K. Henderson, K. Dhaliwal, R. R. Thomson and M. G. Tanner, *Opt. Express*, 2017, **25**, 30976.

162 N. Krstajić, J. Levitt, S. Poland, S. Ameer-Beg and R. Henderson, *Opt. Express*, 2015, **23**, 5653–5669.

163 A. Kufcsák, A. Erdogan, R. Walker, K. Ehrlich, M. Tanner, A. Megia-Fernandez, E. Scholefield, P. Emanuel, K. Dhaliwal, M. Bradley, R. K. Henderson and N. Krstajić, *Opt. Express*, 2017, **25**, 11103–11123.

164 C. E. Talley, L. Jusinski, C. W. Hollars, S. M. Lane and T. Huser, *Anal. Chem.*, 2004, **76**, 7064–7068.

165 J. S. Suh and J. Kim, *J. Raman Spectrosc.*, 1998, **29**, 143–148.

166 Help Online - Origin Help - Boltzmann, https://www.originlab.com/doc/Origin-Help/Boltzmann-FitFunc, (accessed 23 January 2019).

167 P. Xu, L. Kang, N. H. Mack, K. S. Schanze, X. Han and H.-L. Wang, *Sci. Rep.*, 2013, **3**, 2997.

168 H. Wei, E. P. Vejerano, W. Leng, Q. Huang, M. R. Willner, L. C. Marr and P. J. Vikesland, *Proc. Natl. Acad. Sci.*, 2018, **115**, 7272–7277.

169 J. C. C. Day and N. Stone, *Appl. Spectrosc.*, 2013, **67**, 349–354.

170 S. A. Grant and R. S. Glass, *IEEE Trans. Biomed. Eng.*, 1999, **46**, 1207–1211.

171 K. Ehrlich, H. Fleming, S. McAughtrie, A. Kufcsák, N. Krstajić, C. J. Campbell, R. K. Henderson, K. Dhaliwal, R. R. Thomson and M. G. Tanner, in *Biophotonics: Photonic Solutions for Better Health Care VI*, International Society for Optics and Photonics, 2018, vol. 10685, p. 106850Q.

172 J. Clavadetscher, S. Hoffmann, A. Lilienkampf, L. Mackay, R. M. Yusop, S. A. Rider, J. J. Mullins and M. Bradley, *Angew. Chem. Int. Ed Engl.*, 2016, **55**, 15662–15666.

173 Y. Zhao, J. Feng, L. Hong, Y. Li, C. Wang and S. Ye, *Inorg. Chem. Front.*, 2018, **5**, 1133–1138.

174 J. M. Behrendt, D. Nagel, E. Chundoo, L. M. Alexander, D. Dupin, A. V. Hine, M. Bradley and A. J. Sutherland, *PLOS ONE*, 2013, **8**, e50713.

175 J. M. Behrendt, M. Afzaal, L. M. Alexander, M. Bradley, A. V. Hine, D. Nagel, P. O'Brien, K. Presland and A. J. Sutherland, *J. Mater. Chem.*, 2008, **19**, 215–221.

176 X. Wang, Q. Ma, B. Li, Y. Li and X. Su, *Lumin. J. Biol. Chem. Lumin.*, 2007, **22**, 1–8.

177 T. Franklin-Ford, N. Shah, E. Leiferman, C. S. Chamberlain, A. Raval, R. Vanderby and W. L. Murphy, *Macromol. Biosci.*, 2012, **12**, 1615–1621.

178 Y. Leng, K. Sun, X. Chen and W. Li, *Chem. Soc. Rev.*, 2015, **44**, 5552–5595.

179 R. Pérez-Pineiro, M. A. Correa-Duarte, V. Salgueirino and R. A. Alvarez-Puebla, *Nanoscale*, 2012, **4**, 113–116.

180 J.-H. Kim, H. Kang, S. Kim, B.-H. Jun, T. Kang, J. Chae, S. Jeong, J. Kim, D. H. Jeong and Y.-S. Lee, *Chem. Commun.*, 2011, **47**, 2306–2308.

181 H. Kang, S. Jeong, Y. Koh, M. Geun Cha, J.-K. Yang, S. Kyeong, J. Kim, S.-Y. Kwak, H.-J. Chang, H. Lee, C. Jeong, J.-H. Kim, B.-H. Jun, Y.-K. Kim, D. Hong Jeong and Y.-S. Lee, *Sci. Rep.*, 2015, **5**, 10144.

182 J. Kress, R. Zanaletti, A. Rose, J. G. Frey, W. S. Brocklesby, M. Ladlow and M. Bradley, *J. Comb. Chem.*, 2003, **5**, 28–32.

183 J. Kress, A. Rose, J. G. Frey, W. S. Brocklesby, M. Ladlow, G. W. Mellor and M. Bradley, *Chem. – Eur. J.*, 2001, **7**, 3880–3883.

184 J. Rademann, M. Barth, R. Brock, H.-J. Egelhaaf and G. Jung, *Chem. – Eur. J.*, 2001, **7**, 3884–3889.

185 J. A. Olmos-Asar, M. Ludueña and M. M. Mariscal, *Phys. Chem. Chem. Phys.*, 2014, **16**, 15979.

186 M.-C. Daniel and D. Astruc, *Chem. Rev.*, 2004, **104**, 293–346.

187 J. C. Love, L. A. Estroff, J. K. Kriebel, R. G. Nuzzo and G. M. Whitesides, *Chem. Rev.*, 2005, **105**, 1103–1170.

188 D. V. Leff, L. Brandt and J. R. Heath, *Langmuir*, 1996, **12**, 4723–4730.

189 S. Gomez, K. Philippot, V. Collière, B. Chaudret, F. Senocq and P. Lecante, *Chem. Commun.*, 2000, **0**, 1945–1946.

190 J. W. Hudgens, J. M. Pettibone, T. P. Senftle and R. N. Bratton, *Inorg. Chem.*, 2011, **50**, 10178–10189.

191 H. Qian, W. T. Eckenhoff, M. E. Bier, T. Pintauer and R. Jin, *Inorg. Chem.*, 2011, **50**, 10735–10739.

192 L.-B. Weiswald, D. Bellet and V. Dangles-Marie, *Neoplasia N. Y. N*, 2015, **17**, 1–15.

193 P. Vaupel, *Semin. Radiat. Oncol.*, 2004, **14**, 198–206.

194 M. K. Danquah, X. A. Zhang and R. I. Mahato, *Adv. Drug Deliv. Rev.*, 2011, **63**, 623–639.

195 L. Q. Chen and M. D. Pagel, *Adv. Radiol.*, , DOI:10.1155/2015/206405.

196 M. Xu, X. Ma, T. Wei, Z.-X. Lu and B. Ren, *Anal. Chem.*, 2018, **90**, 13922–13928.

197 S. Cao, P. Liu, H. Zhu, H. Gong, J. Yao, Y. Sun, G. Geng, T. Wang, S. Feng, M. Han, J. Zhou and Y. Xu, *PLOS ONE*, 2015, **10**, e0137221.

198 K. Rajamäki, T. Nordström, K. Nurmi, K. E. O. Åkerman, P. T. Kovanen, K. Öörni and K. K. Eklund, *J. Biol. Chem.*, 2013, **288**, 13410–13419.

199 W. H. Watson, J. D. Ritzenthaler and J. Roman, *Redox Biol.*, 2016, **8**, 305–315.

200 L. E. Jamieson, 2016.

201 G. F. S. Andrade, M. Fan and A. G. Brolo, *Biosens. Bioelectron.*, 2010, **25**, 2270–2275.

202 J. O'Neill, *Tackling drug-resistant infections globally: final report and recommendations*, H M Government/Wellcome Trust, 2016.

203 S. Ramírez-Estrada, B. Borgatta and J. Rello, *Infect. Drug Resist.*, 2016, **9**, 7–18.

204 D. Heyland, S. Ewig and A. Torres, *Crit. Care*, 2002, **6**, 117–120.

205 R. P. Dickson, J. R. Erb-Downward, F. J. Martinez and G. B. Huffnagle, *Annu. Rev. Physiol.*, 2016, **78**, 481–504.

206 D. N. O'Dwyer, R. P. Dickson and B. B. Moore, *J. Immunol. Baltim. Md 1950*, 2016, **196**, 4839–4847.

207 R. P. BAUGHMAN, D. A. KEETON, C. PEREZ and R. W. WILMOTT, *Am. J. Respir. Crit. Care Med.*, , DOI:10.1164/ajrccm.156.1.9610059.

208 H. Wang, X. Gu, Y. Weng, T. Xu, Z. Fu, W. Peng and W. Yu, *BMC Pulm. Med.*, , DOI:10.1186/s12890-015-0094-z.

209 J. R. Lentino and D. A. Lucks, *J. Clin. Microbiol.*, 1987, **25**, 758–762.

210 K. C. Carroll, *J. Clin. Microbiol.*, 2002, **40**, 3115–3120.

211 A. Zumla, J. A. Al-Tawfiq, V. I. Enne, M. Kidd, C. Drosten, J. Breuer, M. A. Muller, D. Hui, M. Maeurer, M. Bates, P. Mwaba, R. Al-Hakeem, G. Gray, P. Gautret, A. A. Al-Rabeeah, Z. A. Memish and V. Gant, *Lancet Infect. Dis.*, 2014, **14**, 1123–1135.

212 A. R. Akram, S. V. Chankeshwara, E. Scholefield, T. Aslam, N. McDonald, A. Megia-Fernandez, A. Marshall, B. Mills, N. Avlonitis, T. H. Craven, A. M. Smyth, D. S. Collie, C. Gray, N. Hirani, A. T. Hill, J. R. Govan, T. Walsh, C. Haslett, M. Bradley and K. Dhaliwal, *Sci. Transl. Med.*, 2018, **10**, eaal0033.

213 W. F. Walkenhorst, J. W. Klein, P. Vo and W. C. Wimley, *Antimicrob. Agents Chemother.*, 2013, **57**, 3312–3320.

214 J. Wisniak, *Chem. Educ.*, 2000, **5**, 343–350.

215 P. W. Smit, I. Elliott, R. W. Peeling, D. Mabey and P. N. Newton, *Am. J. Trop. Med. Hyg.*, 2014, **90**, 195–210.

216 X. Li, D. R. Ballerini and W. Shen, *Biomicrofluidics*, 2012, **6**, 011301-011301–13.

217 E. P. Hoppmann, W. W. Yu and I. M. White, *Methods*, 2013, **63**, 219–224.

218 C. H. Lee, M. E. Hankus, L. Tian, P. M. Pellegrino and S. Singamaneni, Highly Sensitive Surface Enhanced Raman Scattering Substrates Based on Filter Paper Loaded with Plasmonic Nanostructures, https://pubs.acs.org/doi/abs/10.1021/ac2016882, (accessed 6 April 2018).

219 H. Torul, H. Çiftçi, D. Çetin, Z. Suludere, I. H. Boyacı and U. Tamer, *Anal. Bioanal. Chem.*, 2015, **407**, 8243–8251.

220 R. P. Gandhiraman, D. Nordlund, V. Jayan, M. Meyyappan and J. E. Koehne, *ACS Appl. Mater. Interfaces*, 2014, **6**, 22751–22760.

221 R. Derda, S. K. Y. Tang, A. Laromaine, B. Mosadegh, E. Hong, M. Mwangi, A. Mammoto, D. E. Ingber and G. M. Whitesides, *PLoS ONE*, , DOI:10.1371/journal.pone.0018940.

222 D. A. Bruzewicz, M. Reches and G. M. Whitesides, *Anal. Chem.*, 2008, **80**, 3387–3392.

223 A. W. Martinez, S. T. Phillips, M. J. Butte and G. M. Whitesides, *Angew. Chem. Int. Ed Engl.*, 2007, **46**, 1318–1320.

224 F. Wang, R. G. Widejko, Z. Yang, K. T. Nguyen, H. Chen, L. P. Fernando, K. A. Christensen and J. N. Anker, *Anal. Chem.*, 2012, **84**, 8013–8019.

225 R. P. Dickson, J. R. Erb-Downward and G. B. Huffnagle, *Lancet Respir. Med.*, 2014, **2**, 238–246.

226 A.-P. Magiorakos, C. Suetens, D. L. Monnet, C. Gagliotti and O. E. Heuer, *Antimicrob. Resist. Infect. Control*, 2013, **2**, 6.

227 R. Lozano, M. Naghavi, K. Foreman, S. Lim, K. Shibuya, V. Aboyans, J. Abraham, T. Adair, R. Aggarwal, S. Y. Ahn, M. A. AlMazroa, M. Alvarado, H. R. Anderson, L. M. Anderson, K. G. Andrews, C. Atkinson, L. M. Baddour, S. Barker-Collo, D. H. Bartels, M. L. Bell, E. J. Benjamin, D. Bennett, K. Bhalla, B. Bikbov, A. B. Abdulhak, G. Birbeck, F. Blyth, I. Bolliger, S. Boufous, C. Bucello, M. Burch, P. Burney, J. Carapetis, H. Chen, D. Chou, S. S. Chugh, L. E. Coffeng, S. D. Colan, S. Colquhoun, K. E. Colson, J. Condon, M. D. Connor, L. T. Cooper, M. Corriere, M. Cortinovis, K. C. de Vaccaro, W. Couser, B. C. Cowie, M. H. Criqui, M. Cross, K. C. Dabhadkar, N. Dahodwala, D. De Leo, L. Degenhardt, A. Delossantos, J. Denenberg, D. C. Des Jarlais, S. D. Dharmaratne, E. R. Dorsey, T. Driscoll, H. Duber, B. Ebel, P. J. Erwin, P. Espindola, M. Ezzati, V. Feigin, A. D. Flaxman, M. H. Forouzanfar, F. G. R. Fowkes, R. Franklin, M. Fransen, M. K. Freeman, S. E.

Gabriel, E. Gakidou, F. Gaspari, R. F. Gillum, D. Gonzalez-Medina, Y. A. Halasa, D. Haring, J. E. Harrison, R. Havmoeller, R. J. Hay, B. Hoen, P. J. Hotez, D. Hoy, K. H. Jacobsen, S. L. James, R. Jasrasaria, S. Jayaraman, N. Johns, G. Karthikeyan, N. Kassebaum, A. Keren, J.-P. Khoo, L. M. Knowlton, O. Kobusingye, A. Koranteng, R. Krishnamurthi, M. Lipnick, S. E. Lipshultz, S. L. Ohno, J. Mabweijano, M. F. MacIntyre, L. Mallinger, L. March, G. B. Marks, R. Marks, A. Matsumori, R. Matzopoulos, B. M. Mayosi, J. H. McAnulty, M. M. McDermott, J. McGrath, Z. A. Memish, G. A. Mensah, T. R. Merriman, C. Michaud, M. Miller, T. R. Miller, C. Mock, A. O. Mocumbi, A. A. Mokdad, A. Moran, K. Mulholland, M. N. Nair, L. Naldi, K. M. V. Narayan, K. Nasseri, P. Norman, M. O'Donnell, S. B. Omer, K. Ortblad, R. Osborne, D. Ozgediz, B. Pahari, J. D. Pandian, A. P. Rivero, R. P. Padilla, F. Perez-Ruiz, N. Perico, D. Phillips, K. Pierce, C. A. Pope, E. Porrini, F. Pourmalek, M. Raju, D. Ranganathan, J. T. Rehm, D. B. Rein, G. Remuzzi, F. P. Rivara, T. Roberts, F. R. De León, L. C. Rosenfeld, L. Rushton, R. L. Sacco, J. A. Salomon, U. Sampson, E. Sanman, D. C. Schwebel, M. Segui-Gomez, D. S. Shepard, D. Singh, J. Singleton, K. Sliwa, E. Smith, A. Steer, J. A. Taylor, B. Thomas, I. M. Tleyjeh, J. A. Towbin, T. Truelsen, E. A. Undurraga, N. Venketasubramanian, L. Vijayakumar, T. Vos, G. R. Wagner, M. Wang, W. Wang, K. Watt, M. A. Weinstock, R. Weintraub, J. D. Wilkinson, A. D. Woolf, S. Wulf, P.-H. Yeh, P. Yip, A. Zabetian, Z.-J. Zheng, A. D. Lopez and C. J. Murray, *The Lancet*, 2012, **380**, 2095–2128.

228 J. Chastre and J.-Y. Fagon, 2002, **165**, 37.

229 J. B. J. Scholte, H. A. van Dessel, C. F. M. Linssen, D. C. J. J. Bergmans, P. H. M. Savelkoul, P. M. H. J. Roekaerts and W. N. K. A. van Mook, *J. Clin. Microbiol.*, 2014, **52**, 3597–3604.

230 A. R. Akram, N. Avlonitis, A. Lilienkampf, A. M. Perez-Lopez, N. McDonald, S. V. Chankeshwara, E. Scholefield, C. Haslett, M. Bradley and K. Dhaliwal, *Chem. Sci.*, 2015, **6**, 6971–6979.

231 N. Krstajić, B. Mills, I. Murray, A. Marshall, D. Norberg, T. H. Craven, P. Emanuel, T. R. Choudhary, G. O. S. Williams, E. Scholefield, A. R. Akram, A. Davie, N. Hirani, A. Bruce, A. Moore, M. Bradley and K. Dhaliwal, *J. Biomed. Opt.*, 2018, **23**, 076005.

232 B. Mills, A. R. Akram, E. Scholefield, M. Bradley and K. Dhaliwal, *JoVE J. Vis. Exp.*, 2017, e56284–e56284.

8 Appendices

8.1 Supporting data from Chapter 2

8.1.1 4-MPY Calibration Plots

All spectra were normalised to between 0-1 before integrating pH changing regions. The black curve represents a Boltzmann fit to the plotted data, the red curve is the theoretical Henderson-Hasselbach plot derived using the experimentally determined pKa (x0). Spectra obtained using a Renishaw In Via system, with 785 nm illumination, at 0.5 mW, 60x objective, and 1s integration time.

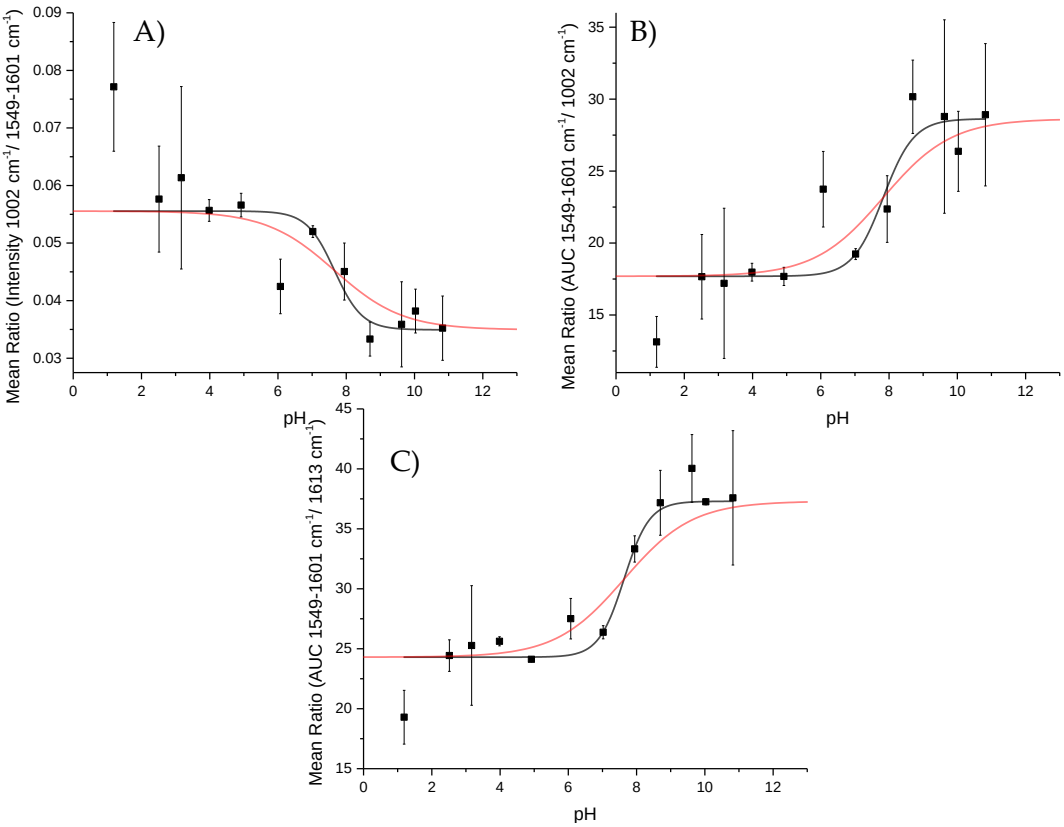

Figure 8.1 4-MPY **c**alibration plots using peak intensities and area under the curve (AUC) calculations. Plot (A) represents the ratio between the 1002 cm^{-1} peak against the AUC between 1549-1601 cm^{-1}. (B) represents the ratio between the AUC between 1549-1601 cm^{-1} and the 1002 cm^{-1} peak. (C) represents the ratio between the AUC between 1549-1601 cm^{-1} and the 1613 cm^{-1} peak.

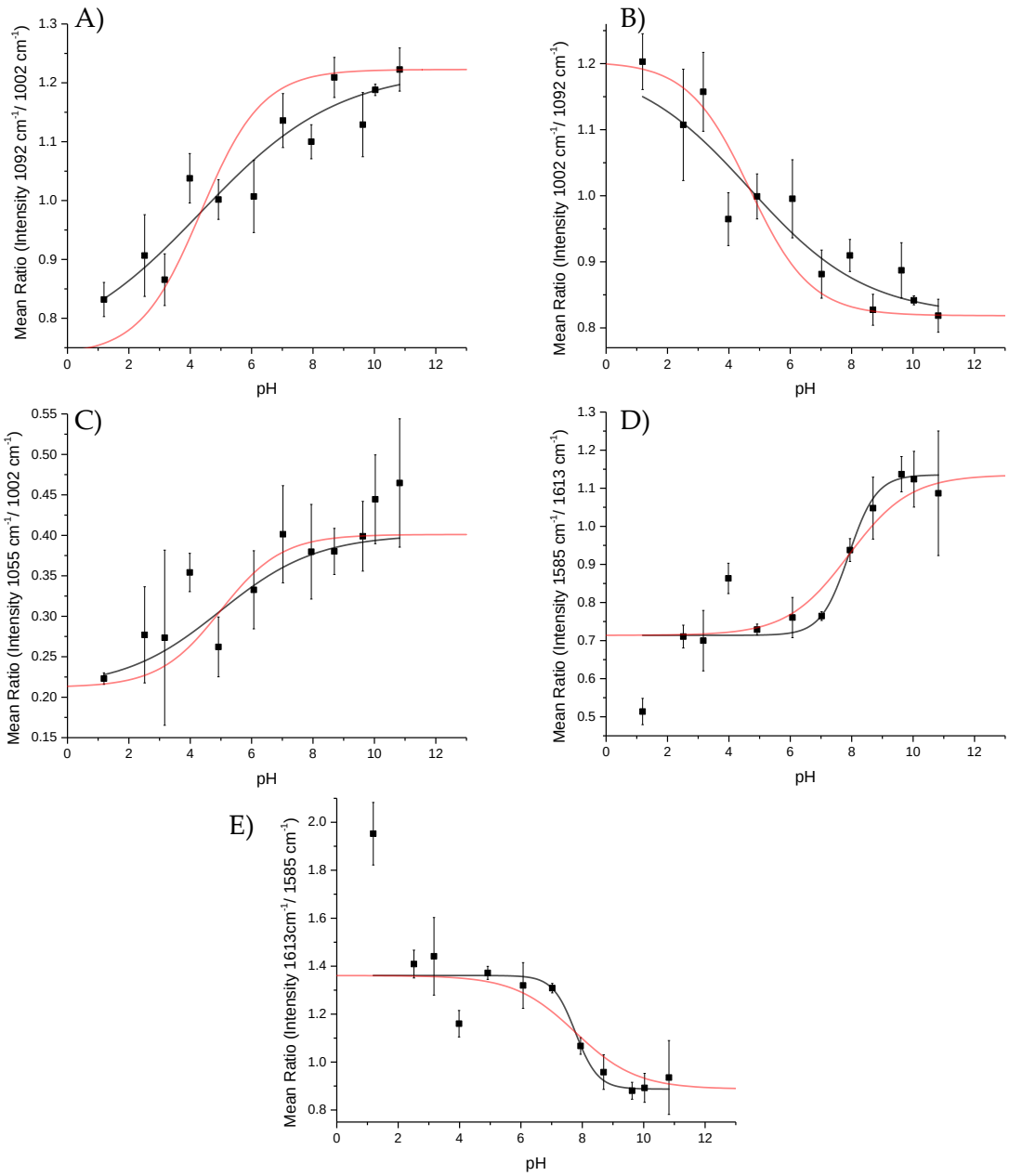

Figure 8.2 4-MPY **c**alibration plots using peak intensities calculations. Plot (A) represents the ratio between the 1092 cm^{-1} peak against the 1002 cm^{-1} peak. (B) represents the ratio between the 1002 cm^{-1} peak against the 1092 cm^{-1} peak. (C) represents the ratio between the 1055 cm^{-1} peak against the 1002 cm^{-1} peak. (D) represents the ratio between the 1585 cm^{-1} peak against the 1613 cm^{-1} peak. (E) represents the ratio between the 1613 cm^{-1} peak against the 1585 cm^{-1} peak.

8.1.2 4-ATP Calibration Plots

All spectra were normalised to between 0-1 before integrating pH changing regions. The black curve represents a Boltzmann fit to the plotted data, the red curve is the theoretical Henderson-Hasslebach plot derived using the experimentally determined pKa (x0). Spectra obtained using a Renishaw In Via system, with 785 nm illumination, at 0.5 mW, 60x objective, and 1s integration time.

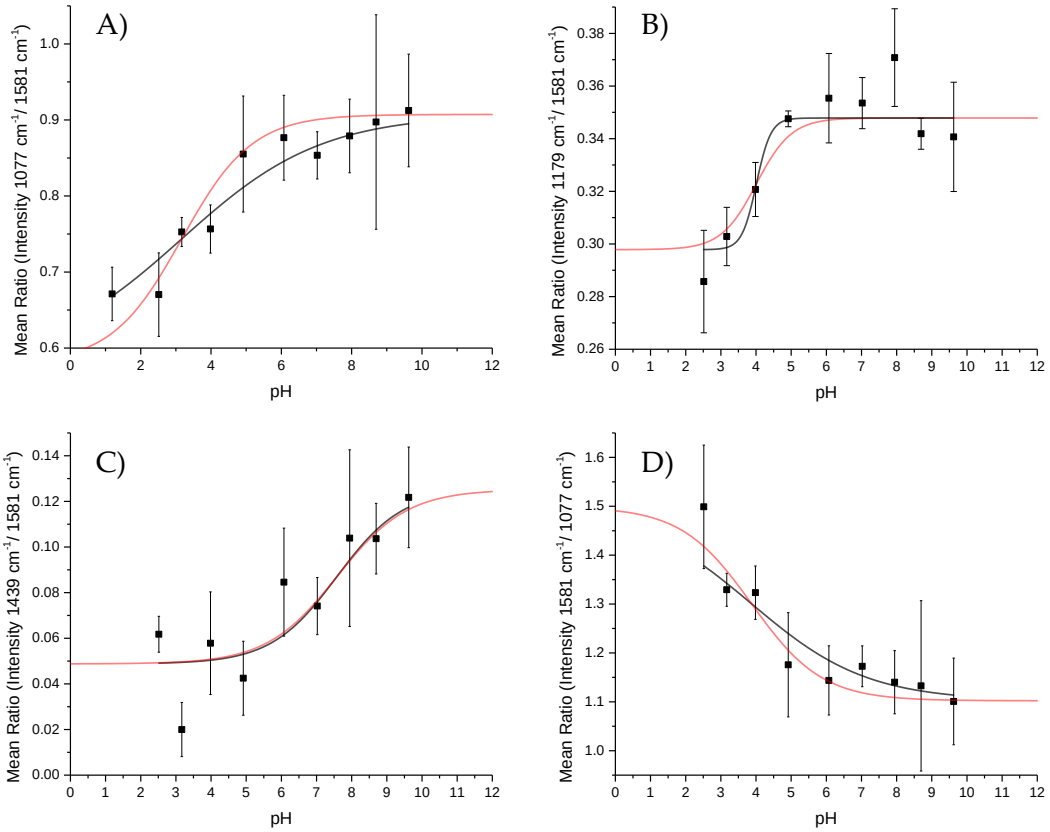

Figure 8.3 4-ATP **c**alibration plots using peak intensities calculations. Plot (A) represents the ratio between the 1077 cm^{-1} peak against the 1581 cm^{-1} peak. (B) represents the ratio between the 1179 cm^{-1} peak and the 1581 cm^{-1} peak. (C) represents the ratio between the 1439 cm^{-1} peak and the 1581 cm^{-1} peak. (D) represents the ratio between the 1581 cm^{-1} peak and the 1077 cm^{-1} peak.

8.2 Publications

Reproduced from:

- K. Ehrlich, A. Kufcsák, S. McAughtrie, H. Fleming, N. Krstajić, C. J. Campbell, R. K. Henderson, K. Dhaliwal, R. R. Thomson, and M. G. Tanner, ***Optics Express***, 2017, **25**, 25: 30976-30986

Reproduced with permission from OSA Publishing *via* the Creative Common Attribution 4.0 License.

- K. Ehrlich, H. Fleming, S. McAughtrie, A. Kufcsák, N. Krstajić, C. J. Campbell, R. K. Henderson, K. Dhaliwal, R. R. Thomson, and M. G. Tanner, ***Proc. SPIE 10685, Biophotonics: Photonic Solutions for Better Health Care VI,*** 2018, **106850Q**

Reproduced with permission from SPIE Biophotonics

- H. Fleming, S. McAughtrie, B. Mills, M. G. Tanner, A. Marks, C. J. Campbell, ***Analyst***, 2018, **143**, 5918-5925

Reproduced with permission from Royal Society of Chemistry *via* the Creative Common Attribution 3.0 Unported License.

Research Article | Vol. 25, No. 25 | 11 Dec 2017 | OPTICS EXPRESS 30976

Optics EXPRESS

pH sensing through a single optical fibre using SERS and CMOS SPAD line arrays

K. Ehrlich,[1,2,*] A. Kufcsák,[3] S. McAughtrie,[2,4] H. Fleming,[4] N. Krstajic,[2,3] C. J. Campbell,[4] R. K. Henderson,[3] K. Dhaliwal,[2] R. R. Thomson,[1,2] and M. G. Tanner[1,2,5]

[1]*Scottish Universities Physics Alliance (SUPA), Institute of Photonics and Quantum Science, Heriot-Watt University, Edinburgh EH14 4AS, UK*
[2]*EPSRC IRC Hub in Optical Molecular Sensing & Imaging, MRC Centre for Inflammation Research, Queen's Medical Research Institute, University of Edinburgh, 47 Little France Crescent, Edinburgh EH16 4TJ, UK*
[3]*Institute for Integrated Micro and Nano Systems, School of Engineering, University of Edinburgh, King's Buildings, Alexander Crum Brown Road, Edinburgh EH9 3FF, UK*
[4]*School of Chemistry, EaStChem, University of Edinburgh, Joseph Black Building, West Mains Road, Edinburgh EH9 3FF, UK*
[5]*M.Tanner@hw.ac.uk*
[*]*ke9@hw.ac.uk*

Abstract: Full exploitation of fibre Raman probes has been limited by the obstruction of weak Raman signals by background fluorescence of the sample and the intrinsic Raman signal of the delivery fibre. Here we utilised functionalised gold nanoshells (NS) to take advantage of the surface-enhanced Raman spectroscopy (SERS) effect to enhance the pH responsive spectrum of 4-mercaptobenzoic acid (MBA). However, the fibre background is still dominant. Using the photon arrival time-resolving capability of a CMOS single-photon avalanche diode (SPAD) based line sensor, we recover the SERS spectrum without a fibre background in a 10 s measurement. In this manner, pH sensing through a multimode fibre at a low excitation power that is safe for future *in vivo* applications, with short acquisition times (10 or 60 s), is demonstrated. A measurement precision of ± 0.07 pH units is thus achieved.

OCIS codes: (300.6500) Spectroscopy, time-resolved; (030.5260) Photon counting.

References and links

1. N. Stone, C. Kendall, J. Smith, P. Crow, and H. Barr, "Raman spectroscopy for identification of epithelial cancers," Faraday Discuss. **126**, 141–157, discussion 169–183 (2004).
2. P. Crow, B. Barrass, C. Kendall, M. Hart-Prieto, M. Wright, R. Persad, and N. Stone, "The use of Raman spectroscopy to differentiate between different prostatic adenocarcinoma cell lines," Br. J. Cancer **92**(12), 2166–2170 (2005).
3. C. A. Lieber, H. E. Nethercott, and M. H. Kabeer, "Cancer field effects in normal tissues revealed by Raman spectroscopy," Biomed. Opt. Express **1**(3), 975–982 (2010).
4. E. B. Hanlon, R. Manoharan, T.-W. Koo, K. E. Shafer, J. T. Motz, M. Fitzmaurice, J. R. Kramer, I. Itzkan, R. R. Dasari, and M. S. Feld, "Prospects for in vivo Raman spectroscopy," Phys. Med. Biol. **45**(2), R1–R59 (2000).
5. O. Stevens, I. E. Iping Petterson, J. C. C. Day, and N. Stone, "Developing fibre optic Raman probes for applications in clinical spectroscopy," Chem. Soc. Rev. **45**(7), 1919–1934 (2016).
6. M. G. Shim, B. C. Wilson, E. Marple, and M. Wach, "Study of Fiber-Optic Probes for in Vivo Medical Raman Spectroscopy," Appl. Spectrosc. **53**, 619–627 (1999).
7. D. Wei, S. Chen, and Q. Liu, "Review of Fluorescence Suppression Techniques in Raman Spectroscopy," Appl. Spectrosc. Rev. **50**, 387–406 (2015).
8. U. Utzinger and R. R. Richards-Kortum, "Fiber optic probes for biomedical optical spectroscopy," J. Biomed. Opt. **8**(1), 121–147 (2003).
9. J. C. C. Day and N. Stone, "A Subcutaneous Raman Needle Probe," Appl. Spectrosc. **67**(3), 349–354 (2013).
10. D. Choudhury, M. G. Tanner, S. McAughtrie, F. Yu, B. Mills, T. R. Choudhary, S. Seth, T. H. Craven, J. M. Stone, I. K. Mati, C. J. Campbell, M. Bradley, C. K. I. Williams, K. Dhaliwal, T. A. Birks, and R. R. Thomson, "Endoscopic sensing of alveolar pH," Biomed. Opt. Express **8**(1), 243–259 (2016).

#307131 https://doi.org/10.1364/OE.25.030976
Journal © 2017 Received 14 Sep 2017; revised 27 Oct 2017; accepted 30 Oct 2017; published 27 Nov 2017

11. I. Gusachenko, M. Chen, and K. Dholakia, "Raman imaging through a single multimode fibre," Opt. Express **25**(12), 13782–13798 (2017).
12. W. Becker, *Advanced Time-Correlated Single Photon Counting Techniques* (Springer Berlin Heidelberg, 2005).
13. A. Campion and P. Kambhampati, "Surface-enhanced Raman scattering," Chem. Soc. Rev. **27**, 241 (1998).
14. P. R. Stoddart and D. J. White, "Optical fibre SERS sensors," Anal. Bioanal. Chem. **394**(7), 1761–1774 (2009).
15. S. W. Bishnoi, C. J. Rozell, C. S. Levin, M. K. Gheith, B. R. Johnson, D. H. Johnson, and N. J. Halas, "All-optical nanoscale pH meter," Nano Lett. **6**(8), 1687–1692 (2006).
16. T. Rojalin, L. Kurki, T. Laaksonen, T. Viitala, J. Kostamovaara, K. C. Gordon, L. Galvis, S. Wachsmann-Hogiu, C. J. Strachan, and M. Yliperttula, "Fluorescence-suppressed time-resolved Raman spectroscopy of pharmaceuticals using complementary metal-oxide semiconductor (CMOS) single-photon avalanche diode (SPAD) detector," Anal. Bioanal. Chem. **408**(3), 761–774 (2016).
17. J. Kostamovaara, J. Tenhunen, M. Kögler, I. Nissinen, J. Nissinen, and P. Keränen, "Fluorescence suppression in Raman spectroscopy using a time-gated CMOS SPAD," Opt. Express **21**(25), 31632–31645 (2013).
18. I. Nissinen, J. Nissinen, P. Keränen, A. K. Länsman, J. Holma, and J. Kostamovaara, "A Multitime-Gated SPAD Line Detector for Pulsed Raman Spectroscopy," IEEE Sens. J. **15**, 1358–1365 (2015).
19. C. Zhang, L. Zhang, R. Yang, K. Liang, and D. Han, "Time-Correlated Raman and Fluorescence Spectroscopy Based on a Silicon Photomultiplier and Time-Correlated Single Photon Counting Technique," Appl. Spectrosc. **67**(2), 136–140 (2013).
20. K. Ehrlich, A. Kufcsák, N. Krstajić, R. K. Henderson, R. R. Thomson, and M. G. Tanner, "Fibre optic time-resolved spectroscopy using CMOS-SPAD arrays," Proc. SPIE **10058**, 100580H (2017).
21. E. A. G. Webster, L. A. Grant, and R. K. Henderson, "A High-Performance Single-Photon Avalanche Diode in 130-nm CMOS Imaging Technology," IEEE Electron Device Lett. **33**, 1589–1591 (2012).
22. N. Krstajić, J. Levitt, S. Poland, S. Ameer-Beg, and R. Henderson, "256 × 2 SPAD line sensor for time resolved fluorescence spectroscopy," Opt. Express **23**(5), 5653–5669 (2015).
23. A. Kufcsák, A. Erdogan, R. Walker, K. Ehrlich, M. Tanner, A. Megia-Fernandez, E. Scholefield, P. Emanuel, K. Dhaliwal, M. Bradley, R. K. Henderson, and N. Krstajić, "Time-resolved spectroscopy at 19,000 lines per second using a CMOS SPAD line array enables advanced biophotonics applications," Opt. Express **25**(10), 11103–11123 (2017).
24. A. T. Erdogan, R. Walker, N. Finlayson, N. Krstajic, G. O. S. Williams, and R. K. Henderson, "A 16.5 giga events/s 1024 x 8 SPAD line sensor with per-pixel zoomable 50ps-6.4ns/bin histogramming TDC," in *2017 Symposium on VLSI Circuits* (2017), pp. C292–C293.
25. P. Matousek, M. Towrie, C. Ma, W. M. Kwok, D. Phillips, W. T. Toner, and A. W. Parker, "Fluorescence suppression in resonance Raman spectroscopy using a high-performance picosecond Kerr gate," J. Raman Spectrosc. **32**, 983–988 (2001).
26. J. Holma, I. Nissinen, J. Nissinen, and J. Kostamovaara, "Characterization of the Timing Homogeneity in a CMOS SPAD Array Designed for Time-Gated Raman Spectroscopy," IEEE Trans. Instrum. Meas. **66**, 1837–1844 (2017).
27. S. A. Grant and R. S. Glass, "Sol-gel-based biosensor for use in stroke treatment," IEEE Trans. Biomed. Eng. **46**(10), 1207–1211 (1999).

1. Introduction

Raman spectroscopy, based on exploiting the inelastic scattering of light from a sample, is often used for histochemical analysis such as discrimination of malignant and benign tissue [1–3]. The advantages for *in vivo* investigations are that it is non-destructive and minimally invasive, exhibits high spatial resolution, is chemically sensitive and has a rapid response which is important for *in situ* diagnosis [4]. However, the small cross section of the Raman scattering results in a weak signal, especially when exciting in the near-infrared regime ($1/\lambda^4$-dependency). The signal is often further obscured by fluorescence from surrounding regions e.g. tissue in medical applications. Additionally, *in vivo* measurements require optical fibre probes to reach the position of interest in the body. The optical fibre exhibits a high Raman scattering from the core material which contrary to other fluorescence background, is constant and scales with the fibre length itself [5,6]. This combination of unwanted background signals makes *in vivo* Raman spectroscopy extremely challenging, especially with a miniaturized fibre probe.

Efforts in recent years in response to the challenge have included methods of fluorescent background suppression [7]. However, while some are not applicable for *in vivo* applications, others suffer from sophisticated and expensive set-ups or long acquisition times. Meanwhile several commercial and non-commercial fibre Raman probes have been developed with methods for background suppression ranging from advanced fibre designs [8–10] to complex correction methods [11].

We demonstrate a time-correlated single photon counting (TCSPC) [12] spectrometry technique in combination with surface-enhanced Raman spectroscopy (SERS) [13] to overcome the challenges and enable a background free Raman spectrum with an ultra-miniaturised single fibre probe. The size and simplicity (moving the advanced and costly apparatus outside the fibre probe) enables endoscopic application in size restricted regions (e.g. the distal lung) with a disposable sensing probe. We exemplify the system for pH sensing with 4-mercaptobenzoic acid (MBA). pH is a key marker for the acid-base balance in metabolism which is tightly regulated but can be locally changed by pathologies such as inflammation and cancer. As an example, generation of an acidic environment increases growth of bacteria and inhibits antibiotics [10]. Quantifying and monitoring the environmental pH *in vivo* as enabled by this work has potential to improve diagnostics and therapy.

In this paper, we produce a sensing probe through the deposition of MBA functionalised gold nanoshells (NS) on the tip of the delivery fibre optic [10,14]. The gold NS have been designed as optical nanosensors for localized measurements of pH *in vivo*. They are robust, designed for use in the near-infrared spectral region, avoiding distortion from excessive autofluorescence from tissue and blood, and exhibit a continuous signal over a wide range of pH [15].

We remove fluorescent and fibre backgrounds through post-processing time-gating using the TCSPC capabilities of a complementary metal-oxide semiconductor (CMOS) single-photon avalanche diode (SPAD) based line sensor. We exploit the different time profiles of background fluorescence, fibre Raman scattering and the SERS signal to separate signal from background [16–19].

The TCSPC capable CMOS SPAD line sensor detects single photons and generates histograms according to their arrival time for 256 pixels simultaneously which are correlated to different wavelengths [20]. The advantages are high efficiency [21] and high time resolution (< 500 ps time stamping resolution) to record luminescent kinetics down to the nanosecond regime. This enables the utilisation of low excitation power (< 1 mW) and short exposure times (10 s - 60 s) thus enabling further development towards the *in vivo* sensing of physiological parameters. The technique is only limited by photon statistic constraints known as counting loss and pile-up, and inherent limitations on the performance of the SPADs; detector dead-time, dark count rate, varying photon detection probabilities, crosstalk and afterpulsing [12]. The exploitation of this advanced measurement system enables suppression of the unwanted background in the fibre-based Raman probe, facilitating the recovery of the background free spectrum. We demonstrate how this enables low power, rapid pH sensing through a multi-mode fibre with functionalised gold NS achieving improved measurement precision.

2. Material and methods

2.1. Optical setup

The measurements were performed using the time-resolved spectrometer shown schematically in Fig. 1. It consists of four parts: i) The excitation source was a 785 nm pulsed laser (LDH-D-F-N-780 and PDL 800-D, PicoQuant, spectral FWHM < 0.35 nm). The laser when operated at maximum power has a short leading pulse with a FWHM of 30 ps as stated in the manual specific to this laser, however it exhibits a long tail with a FWHM of 1.5 ns containing ¾ of the power. The average power was reduced with neutral density filters to 0.8 mW, this is safe for *in vivo* measurement and below the damage threshold for the sensors in continuous operation. The repetition rate was 20 MHz, as such, a full measurement of light transiting the length of a 2.7 m fibre and being backscattered to the detector was completed before the next laser pulse. ii) An optical coupling and collection system which was based on the same arrangement as standard for epi-fluorescence measurement. iii) A spectrometer based on a collimation lens, f = 50 mm, a transmission grating (1624 grooves / mm, Wasatch)

and a focusing lens, f = 30 mm (both Achromat Doublets, Thorlabs), ensuring a spectral range of 80 nm across the line array centred at 870 nm and a throughput of 78%, measured with a photodiode (S120C Thorlabs). iv) The in-house made CMOS SPAD sensor consisted of 256 pixels in a single line manufactured with 130 nm CMOS technology. The sensor timestamps the single photon events internally and simultaneously for all pixels. For further information about this sensor see [22,23]. This and the lack of any scanning element [16,17], for scanning along the spectral or temporal axis, ensures short measurement times. The dispersion was 0.3 nm/pixel and the spectral resolution was 1.6 nm or 25 cm^{-1}, limited by entrance slit width, grating density and lens combination. The temporal resolution set by the time-to-digital converter (TDC) was 423 ± 3 ps. The signal level was kept low to ensure a detector count rate of < 1% of the laser excitation rate and < 50% of the detector readout frame rate. The fibre-coupled design is extremely versatile and flexible for a broad range of applications and with the potential to be compact and mobile, suitable for *in situ* applications.

Two lengths of delivery optical fibres were used to act as passive fibre sensors with functionalised gold NS deposit at the fibre tip: a 2.7 m and an 18 m multimode fibre (both FG050LGA, Thorlabs). The protocol for the SERS preparation can be found in Section A.2.

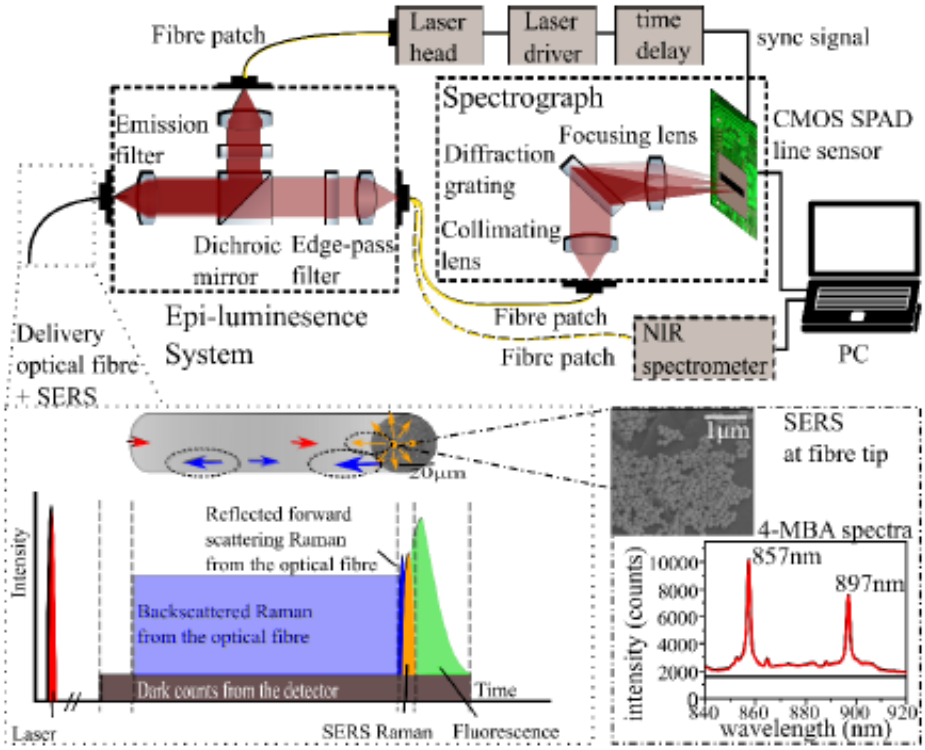

Fig. 1. A schematic of the time-resolved spectrometer and the principles of time-resolved measurements through an optical fibre with gold NS deposited on the fibre tip. The fibre tip of the multimode optical fibre (NA 0.22, 50 µm, Thorlabs) is covered with functionalised gold NS (150 nm, Bare Auroshell), as shown in the SEM image. The free-space spectrum of the functionalised MBA molecule taken with a Raman Probe and a QEPro spectrometer (OceanOptics). The integration time is 10 s and excitation power is 0.8 mW comparable to the experimental settings later. The schematic of the evolution of the signals in time is not to scale, the separation bars are guidance for the eye.

Optics EXPRESS

2.2 Data analysis

Utilizing the experimental setup and procedure outlined, a single measurement yields a 2-dimensional data array consisting of the spectral axis, the temporal axis and intensity data in terms of number of counts per pixel and per time bin. For gathering the spectral information, each pixel is correlated to a certain wavelength range. The temporal information is gained by measuring the arrival time of the photons and histogramming them for each pixel with the on-chip TCSPC functionality of the sensor.

"Noisy pixels" exhibit excessively high dark count rates due to fabrication variations and being electronically closer to their avalanche condition. The data of these pixels are removed from the measurement to avoid introducing excessive noise in the result. An average of 26% of the 256 pixels are identified as 'noisy pixels' through two identification methods: i) For a homogenous background (e.g. in Fig. 2(b) where there is a region of only dark counts), the average dark count level is taken as a threshold and the data of all pixels above this threshold are removed. ii) For a non-homogenous background, for example with an underlying signal (e.g. if the time of travel through the fibre or a fluorescent decay exceeds the measurement period as discussed later), a moving average method is used. The moving average is calculated over a window size of 5 adjacent pixels. If the data of one pixel is greater than the average plus the standard deviation of this subset, it is removed.

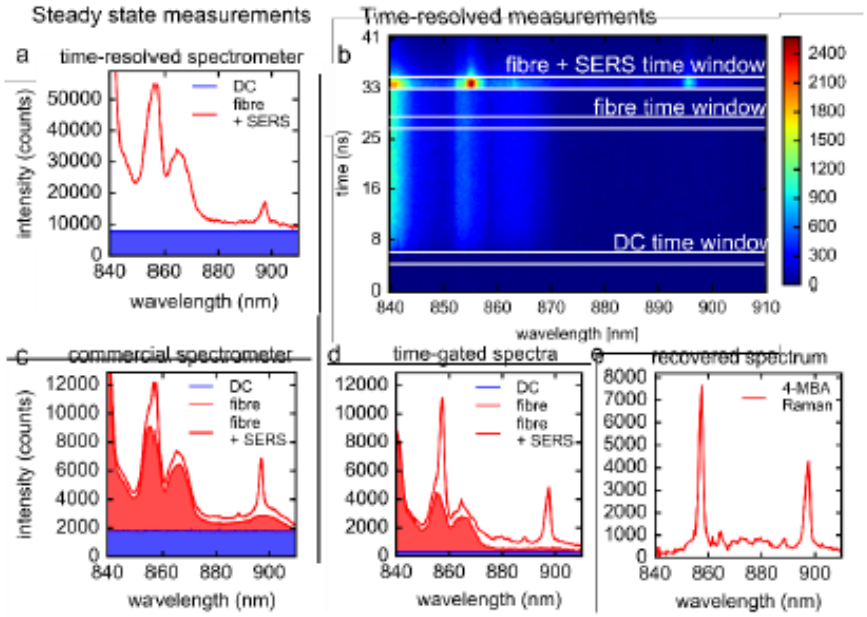

Fig. 2. 10 s measurement of a 2.7 m multimode optical fibre with functionalised gold NS at the fibre tip. (a) Non time-resolved measurement of the time-resolved spectrometer. (b) A 3-dimensional representation of the time-resolved measurement. Noisy pixels are removed and dark counts are subtracted. (c) Non time-resolved measurement with a commercial spectrometer (QEPro, Ocean Optics). (d) Time-gated spectra originating from the time windows indicated in (b). Time window width is 5 time bins or 2.1 ns. (e) A recovered spectrum from the MBA molecule.

As seen in Figs. 2(b) and 2(d), a full data analysis from one measurement is enabled by slicing the data into three time windows along the histogram axis. The average background count level per pixel is derived from the dark count 'DC' time window shown in Fig. 2(b) and subtracted pixel-wise as detector pixels exhibit differing count rates. Note that in the case of a signal that exceeds the duration of the measurement period determined by the repetition rate,

this time window contains not only detector background but also any other background signal such as fibre Raman or long lived fluorescence. The photon shot noise from these counts is still present in the final data. The 'fibre' time window contains the information about the backscattered fibre Raman spectral shape which can be used with a scaling factor to subtract the remaining fibre Raman signal from the 'fibre + SERS' time window (largely from the forward scattered fibre Raman) and thus the spectral information of MBA (as seen in Fig. 2(e)) can be recovered without a fibre background. Because of the uniformity of the fibre Raman, the time window can be placed anywhere along the fibre Raman signal. The scaling factor is needed to account for the reflection of the forward scattered fibre Raman on the multiple surfaces (fibre, NS, sol-gel).

3. Results and discussions

3.1 Enhanced visibility of the Raman signal through post-processing time-gating

Figure 2(a) and 2(c) demonstrate that the time-resolved spectrometer, without applying the time windows, offers visually similar spectra to the commercial spectrometer with some important differences. The time-resolved spectrometer has a higher efficiency (producing larger overall signal amplitudes) but a lower spectral resolution leading to broadening and lower peak visibility for the SERS features at ~860 nm and ~900 nm compared to the commercial spectrometer. Meanwhile, the ratio of detector dark counts to signal is comparable between the reference measurement and the time-resolved spectrometer measurement (as shown in Figs. 2(a) and 2(c)). Through post-processing time-gating, the detector dark counts and the unwanted fibre Raman can be significantly suppressed and the visibility of the SERS Raman signal can be significantly increased (see Fig. 2(d)). For clearer observation of the Raman spectra, the measured fibre background (from the 'fibre' time window) is subtracted, demonstrating clear recovery of the true spectra from the fibre tip (see Fig. 2(e)).

When time-gating the data the background counts are clearly reduced, thus reducing the background photon shot noise. For the purpose of this paper, we choose a time window of 5 time bins. This maximizes the signal-to-background (S/B) by removing the majority of the fibre background while additionally collecting the desired Raman signal over multiple time bins. However, increasing the time window width further than 5 time bins decreases S/B (see Appendix A.1.). For a fibre Raman dominant background, the S/B obtained was 4 × better in the time-gated result than that measured with the commercial spectrometer (integrated over the 857 nm peak). For a dark count dominated background, the S/B was 19 × better in the time-gated result than with the commercial spectrometer (897 nm peak), see Figs. 2(c) and 2(d).

These results could be improved if the instrument response function of the detector [23,24] and the pulse width of the laser were shorter (as discussed in Appendix A.1.), since the laser exhibits a long tail when operated at high power. The time-gating method in this paper is achieved by recording a whole TCSPC measurement and applying time windows to the data during post-processing. Others have presented time domain gating techniques such as streak cameras, electronically time-gated CCDs or CMOS detectors and optical driven Kerr gates [25]. While the latter achieves a time resolution of picoseconds, the setup is costly and measurement times lengthy (min). Electronic time-gating introduces additional jitter to the measurement through the enabling and disabling of the detector but potentially decreases the measurement time. However, we believe that time-gating in single photon counting (SPC) modality has no time advantage over TCSPC measurements in low light scenarios such as expected for *in vivo* sensing as measurement rate is limited by photon budget, not detector readout.

In biological applications, measurement of the SERS signal can be complicated further by fluorescence from delivered fluorophores or tissue autofluorescence which is always present. Figures 3(a)-3(c) shows how applying the time windows reduces the influence of the

fluorescent background due to the differing time scales of Raman and fluorescence, demonstrating how the MBA spectrum can be successfully recovered. In Fig. 3(a) the spectrum is dominated by a large broad fluorescence response, successfully removed in Fig. 3(b), with a clear recovered spectrum in Fig. 3(c). For other applications, such as remote environmental sensing, longer fibre lengths are useful. In TCSPC methodology, the laser repetition rate determines the temporal duration of the measurement. The time of travel for the photons through the optical fibre can be calculated with $t = (2nL)/c$, where L is the fibre length, n is the refractive index of the fibre core material and c the speed of light in vacuum. Modal dispersion in multimode fibres can be expected to be in the order of tens of picoseconds per metre. We collect signal in a 2.1 ns time window, as such broadening through modal dispersion does not contribute to our measurements of 3 m or 18 m fibres, but if longer multimode fibres were used it would affect the S/B and a longer time window width would be required. If the repetition rate is shorter than the time of travel, photons are counted against the following sync signal and the measurement seems to be 'wrapped around' the histogram axis. In Figs. 3(d)-3(f) an 18 m optical fibre with functionalised gold NS deposited at the fibre tip was measured within a 50 ns measurement period. The excitation power was reduced to 0.12 mW to ensure a single photon counting regime and the integration time was increased to 60 s. The fibre Raman signal is 'wrapped' around 3.6 times, increasing the unwanted background, before the SERS signal is seen in the histogram. This means photons are arriving from subsequent laser pulses in the same TDC bin, due to insufficient delay between pulses. The MBA spectrum can be recovered but suffers from higher shot noise and the use of the lower excitation power decreases the signal from the NS. However, it is clear that the SERS peaks not visible in Fig. 3(d) have been recovered in Fig. 3(f).

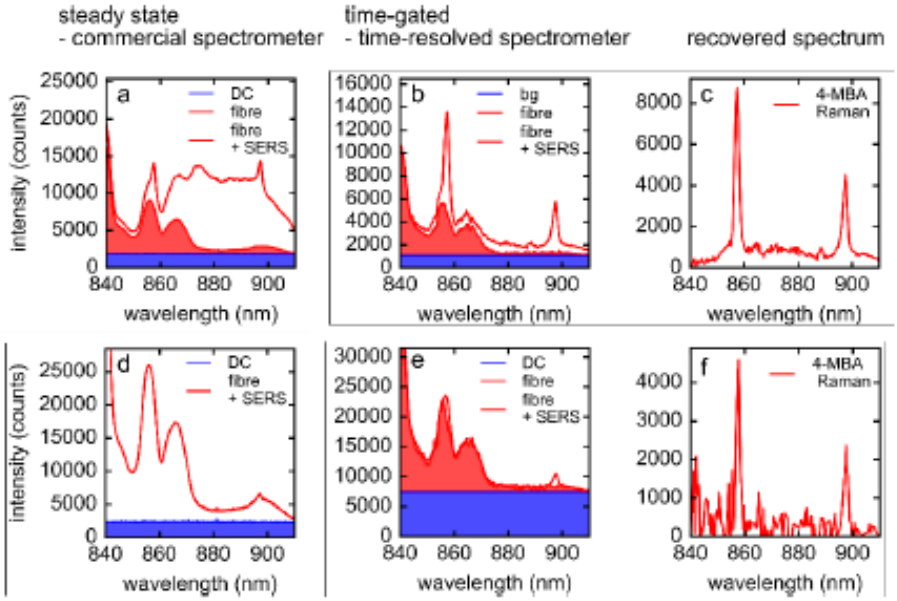

Fig. 3. (a)–(c) 10 s measurement of a 2.7 m multimode optical fibre with functionalised gold NS at the fibre tip and a high fluorescent background from a 3% phosphate Neodymium glass. (d)–(f) 60 s measurement of a 18 m multimode optical fibre with functionalised gold NS at the fibre tip. The excitation power is reduced to 0.12 mW. (a),(d) Reference measurement (QEPro, OceanOptics), (b),(e) time-gated measurement (5 time bins) (c),(f) recovered spectra of the MBA molecule.

As an alternate to the data in Figs. 3(d)-3(f), the same fibre can be measured with a 5 MHz repetition rate ensuring the time of travel does not exceed the measurement period or the

repetition rate of the laser. The expansion of the measurement period leads to a lower dark count level per time point (as DC are spread out over more time bins) but will increase the effect of the timing inhomogeneity of the CMOS SPADs [26], reducing the ability to accurately apply a narrow time window.

Additionally, to guarantee a single photon counting regime without pile-up [12], the average excitation power has to be decreased leading to both lower fibre Raman and SERS signal. If time is no constraint, a longer total measurement time compensates for the lower excitation power, and increases the accuracy of the measurement. However, for long fibres the combination of these factors results in a better recovered spectrum in the case of a short measurement period (high repetition rate) allowing the fibre background to wrap around, thus this method was chosen for the data shown here.

3.2. Application: pH sensing

The spectra of the MBA molecule is sensitive to environmental pH variations and has been previously demonstrated as a pH sensor [9, 21]. Ratiometric changes of the areas under the curve (AUC), within a 4.75 nm spectral window, around the peaks of 880 nm (1380 cm^{-1}) and 906 nm (1700 cm^{-1}) respectively, show the greatest pH sensitivity. Figure 4 shows that time-gating the data greatly increases the selectivity and reduces the standard deviation of the mean over 3 replicates in comparison to a non time-resolved measurement. Increasing the integration time from 10 s (as shown in Fig. 4(a)) to 60 s (as shown in Fig. 4(b)) increases the accuracy of the system further and hence the selectivity.

The precision of the time-resolved spectrometer was evaluated by obtaining the AUC ratios for pH 6 and 8 for 50 consecutively acquired measurements. For a 10 s measurement a repeatability of 0.14 and 0.19 pH units, for pH 6 and 8 respectively, was achieved with time-gating. For an integration time of 60 s this could be improved to 0.05 and 0.07 pH units, for pH 6 and 8 respectively. The precision of the pH sensor was determined by obtaining the AUC ratios while switching iteratively between pH 6 and 8 for 20 repeat measurements. For a 10 s measurement a repeatability of 0.25 and 0.30 pH units, for pH 6 and 8 respectively, was achieved with time-gating. Whilst, for an integration time of 60 s, this could be increased to 0.11 and 0.15 pH units, for pH 6 and 8 respectively.

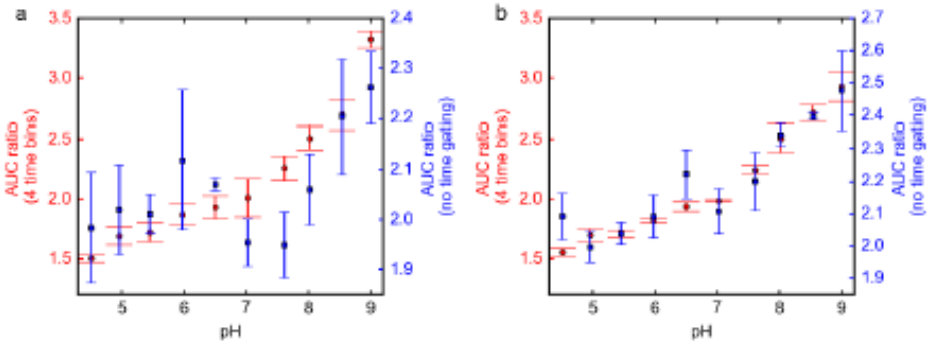

Fig. 4. Variation of area under the curve (AUC) ratio as a function of pH within the pH range of 4.5 to 9, the error bars represent the standard deviation of the mean over 3 replicate measurements. Each measurement was obtained using an average excitation power of 0.8 mW and 20 MHz pulse repetition rate, the integration was increased from a) 10 s to b) 60 s time-resolved measurement.

These results show that we are able to reach the same systematic stability which has been demonstrated earlier using the functionalised NS with a dual-core fibre and an adaptive iterative reweighted penalized least squares (airPLS) algorithm [10]. Decreased precision observed when switching between pH suggests some instability in the SERS sensors when

moving repeatedly over large pH changes. The observed limits in measurement repeatability are larger than those expected from counting statistics after post-processing time-gating, and are instead believed to be due to detector fluctuation (varying pixel dark counts and photon detection probabilities), bias voltage fluctuations or thermal instabilities. Active temperature stabilisation as applied to commercial detectors could offer improved results. We also believe that cooling would greatly reduce the dark counts of the detector, reducing the shot noise and leading to better stability and accuracy. Improved timing accuracy and laser pulse width would offer further improved S/B.

4. Conclusion

A time-resolved system for recovering the spectra of weak Raman signals without fibre or fluorescent backgrounds has been demonstrated. pH sensing through a single core multimode optical fibre using short measurement times was achieved as an example of application. This methodology has high potential for ultra-miniaturized Raman probes for *in vivo* endoscopic sensing of physiological parameters such as pH, oxygen or glucose concentration as well as for remote environmental sensing. In terms of accuracy, the limit of the line sensor was reached and improvement has to include further detector calibrations such as photon-detection variations and reduction of the dark counts through cooling. As time is crucial for *in situ* diagnosis scenarios, the already short integration time can be reduced further through on-chip time-gating capabilities which has been demonstrated with this specific CMOS SPAD line sensor elsewhere [23].

Appendix

A. 1. Signal-to-background investigation

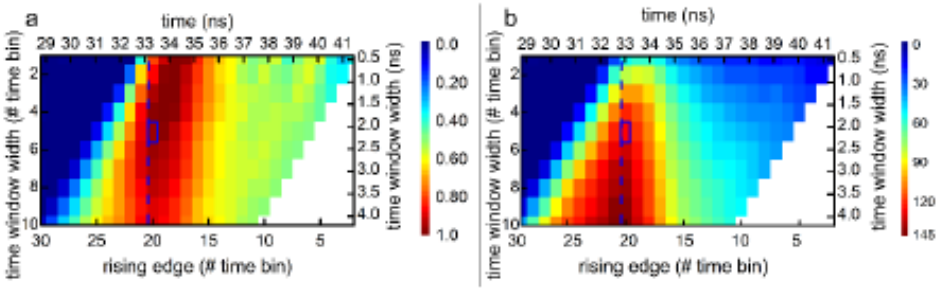

Fig. 5. (a) S/B and (b) S/N plotted against the rising edge of the time window and the width of the time window for the area under the 857 nm SERS peak. The blue vertical dashed line is shown to label the time onset of the signal from the end of the fibre. The blue box shows the chosen timing of bins selected for the other plots in this paper.

The S/B quantifies the 'visibility' of the Raman photons in comparison to the unwanted background photons, which includes the detector dark counts and fibre background. The signal-to-noise (S/N) is a measure for the noise present in the measurement of Raman photons within the whole signal.

$$\frac{S}{B}=\frac{N_R}{N_F+N_{DC}} \; and \; \frac{S}{N}=\frac{N_R}{(N_R+N_F+N_{DC})^{1/2}} \qquad (1)$$

where N_R is the integrated number of counts in the area under the SERS peak at 857 nm, N_F and N_{DC} are the integrated number of counts in the same area of the Raman scattering of the fibre and the detector noise, respectively. The area under the peak was chosen as representative of the Raman signal strength, allowing direct comparison between spectrographs of differing resolution.

While naively the shortest time window may seem to be optimum for improved signal to background or noise [17,26], this is not the case due to extended laser pulse and detector jitter. If the rising edge of the time window is kept constant at the onset of photon counts from the fibre tip, and the width of time window increased (as shown by following the line in Fig. 5) increased SERS signal photons are initially collected, due to the extended IRF of the measurement system, offering improved signal to background (as shown in Fig. 5(a)). However, as the time window is further increased, DC become more dominant than the decreasing tail of the SERS signal, and signal to background decreases. S/N follows a similar trend (see Fig. 5(b)), although a slightly longer time window gives optimum S/N due to the square root in Eq. (1)

Meanwhile, if the time window is misaligned to the SERS signal photon arrival (e.g. moving on the x axis of Fig. 5), or the window is increased in size in both directions around the SERS photon arrival (e.g. from a less accurate measurement system) both S/B and S/N are observed to rapidly decrease due to greater photon counts from the fibre Raman background being included in the data.

A time window of 5 bins was chosen as previously discussed for data in this paper, producing a compromise of good S/B and S/N. This can also be seen as marked visually as the 'fibre + SERS' time window in Fig. 2(b) to capture well the extent of the photons from the fibre tip. However, this once more indicates that a system (both laser and detector) with a shorter IRF would offer an improved measurement result as the time window could be reduced. In this work the limit was the laser pulse shape, extending for ~2 ns (from manufacturer specifications specific to our laser), matching to the optimal time-window determined analytically.

A.2. pH nanosensor preparation

Preparation of the functionalised NS: Gold NS (5 x 1 mL aliquots, $2x10^9$ particles/mL, ~ 150 nm, Bare AuroShell™ Particles in deionised water, Nanospectra Biosciences Inc.) were prepared for functionalisation by centrifugation at 5500 rpm for 10 min. Following centrifugation all or as much as possible of the supernatant was removed without disturbing the pellet. For functionalisation, the pellet was resuspended with distilled water (900 µL) and 4-MBA (100 µL, 1 mM in EtOH) and the samples were left overnight. The NS were washed to remove unbound molecule by centrifuging at 5500 rpm for 10 min. Following centrifugation all or as much as possible of the supernatant was removed without disturbing the pellet. The functionalised particles were then resuspended with 500 µL dH_2O and the samples were sonicated and vortexed to force the particles back into suspension. This washing procedure was repeated a total of 3×. Following washing the particle suspensions were centrifuged at 5500 rpm for 10 min and 450 µL of the supernatant was removed. The final volume remaining in each of the aliquots was measured by pipette and noted. Samples were again centrifuged at 5500 rpm for 10 min and the appropriate volume of supernatant was removed from each to leave a final volume of 5 µL. The individual aliquots (5 aliquots) were then combined to give a particle suspension with a final volume of 25 µL.

Loading of the fibre with functionalised NS: Binding of the functionalised NS and the fibre tip can be increased by enhancing their electrostatic interaction. To achieve this the fibre tip was soaked overnight in positively-charged poly-L-lysine (0.1 mg/mL in distilled water, 30000-70000 MW, Sigma Aldrich) The fibre tip was then removed from the poly-L-lysine solution and dried under nitrogen. The fibre tip was directly dipped into the functionalised NS suspension to coat the fibre. NS were added to the fibre tip until a maximized SERS Raman signal was observed. Currently, there is no control over the packaging density and distribution of the NS through this protocol (as seen in Fig. 1).

Sol-gel preparation for the fibre tip: After the NS had dried on to the fibre tip they were secured by dip coating a protective sol-gel. The sol-gel was prepared *via* the method set out

by Grant *et al.* [27] with MilliQ water being used instead of deionised water. The sol-gel was left to dry overnight.

Funding

UK Engineering and Physical Sciences Research Council (EPSRC, United Kingdom) Interdisciplinary Research Collaboration (EP/K03197X/1); Engineering and Physical Sciences Research Council and Medical Research Council (EP/L016559/1); James-Watt Scholarship from Heriot-Watt University.

Acknowledgments

We would like to further thank STMicroelectronics, Imaging Division, Edinburgh, for their support in manufacturing of the CMOS SPAD line sensors. The experimental data is available via Edinburgh DataShare (http://dx.doi.org/10.7488/ds/2241).

Time-resolved single photon spectroscopy through a single optical fibre for miniaturised medical probe design

K. Ehrlich[*a,b], H. Fleming[d], S. McAughtrie[b,d], A. Kufcsák[c], N. Krstajic[b,c], C. J. Campbell[d], R. K. Henderson[c], K. Dhaliwal[b], R. R. Thomson[a,b], M. G. Tanner[a,b]

[a]Scottish Universities Physics Alliance (SUPA), Institute of Photonics and Quantum Science, Heriot-Watt University, Edinburgh EH144AS, UK,
[b]EPSRC IRC Hub in Optical Molecular Sensing & Imaging, MRC Centre for Inflammation Research, Queen's Medical Research Institute, University of Edinburgh, 47 Little France Crescent, Edinburgh EH164TJ, UK,
[c]Institute for Integrated Micro and Nano Systems, School of Engineering, University of Edinburgh, King's Buildings, Alexander Crum Brown Road, Edinburgh EH93FF, UK,
[d]School of Chemistry, EaStChem, University of Edinburgh, Joseph Black Building, West Mains Road, Edinburgh EH93FF, UK

ABSTRACT

We present a spectroscopic system and an optical fibre probe which enable the full exploitation of the temporal evolution and spectral information of a weak Raman signal against background fluorescence and intrinsic fibre Raman. The system consists of a single multimode fibre and a CMOS single-photon avalanche diode (SPAD) line sensor capable of resolving and histogramming the arrival times of photons for 256 pixels simultaneously, offering improved signal to background compared to a non-time resolved measurement modality. The capabilities of the system are tested for intrinsic Raman standards such as cyclohexane and for pH sensing with functionalised gold nanoshells exploiting surface enhanced Raman scattering (SERS). The nanoshells are functionalised with the pH responsive 4-mercaptobenzoic acid (MBA) enabling demonstration of wide range pH sensing with low excitation power (< 1 mW) and short acquisition times (10 s), achieving a measurement precision of ± 0.07 pH units.

Keywords: Fibre optic sensors, Time-resolved spectroscopy, Photon counting, Raman spectroscopy, Surface-enhanced Raman scattering, Detector arrays

1. INTRODUCTION

In 2012, respiratory diseases were accountable for an average of 20.1 % of all deaths in the UK, with numbers stagnating for the last 10 years while numbers for heart diseases decreased[1]. The total costs in the UK in 2014 were £11.1 bn for treatment and loss to the wider economy[2]. Recent development to tackle this problem include optical imaging through flexible fibre imaging bundles in combination with optical molecular probes based on environmental fluorophores to identify pulmonary infections and inflammation *in vivo*[3,4]. Additionally, the image-guided diagnosis can be supported with localized measurements of key physiological parameters such as pH, oxygen saturation or glucose concentration. We investigate pH as a key marker in this paper, which is tightly regulated in the human body but can locally change due to inflammations and cancerous environments. Furthermore, in the dawn of antimicrobial resistance (AMR), the monitoring and quantification of pH could potentially help clinicians to improve diagnosis and treatment because the growth of bacteria are enhanced in acidic environments while certain antibiotics are inhibited in acidic environments.

Raman spectroscopy investigates the chemical fingerprint of a molecule through its vibrational energy levels by exploiting the inelastic scattering of light when the sample is interacting with light. The advantages are its non-destructiveness, it is minimally invasive, being label-free, and has a rapid response which is important for *in situ* diagnosis[5]. However, the Raman scattering is an inherently weak signal due to the small cross section of the Raman

* Send correspondence to K. Ehrlich: ke9@hw.ac.uk

Biophotonics: Photonic Solutions for Better Health Care VI, edited by Jürgen Popp, Valery V. Tuchin, Francesco Saverio Pavone, Proc. of SPIE Vol. 10685, 106850Q
 · doi: 10.1117/12.2307334

scattering and the fact that its intensity scales inversely with the excitation wavelength ($1/\lambda^4$-dependency). The *in vivo* Raman signal is further obscured by the background from the optical fibre and the fluorescence of the environment. The optical fibre which is required to gain access to remote hollow areas such as the alveoli region of the lung generates fluorescence and Raman scattering, depending on the excitation wavelength, in its core material. This fibre background, contrary to the fluorescence background from tissue, is constant and scales with the fibre length. The fluorescence from surrounding regions e.g. the autofluorescence of endogenous tissue fluorophores, is heterogeneous within and across samples, and hence very difficult to calibrate out. Efforts in recent years in response to the challenge have included complex set ups and computational methods for fluorescent background suppression[6] and advanced Raman probe designs[7–9]. However, while some are not applicable for *in vivo* applications, others suffer from sophisticated and expensive set-ups or long acquisition times.

To overcome the challenges and enable a background free Raman spectroscopy, we demonstrate a time-correlated single photon counting (TCSPC)[10] spectrometry technique. This approach moves the focus away from advanced and costly endoscopic probe design development because it enables endoscopic spectrometry with a standard single core multimode optical fibre. The fibre is small enough to reach otherwise size restricted regions and simple and cheap enough to be used as a disposable sensing probe. TCSPC capable complementary metal-oxide semiconductor (CMOS) single-photon avalanche diodes (SPAD) line sensors are able to detect single photons and histogram them according to their arrival time for 256 pixels simultaneously which are correlated to different wavelengths[11]. The advantages of these line sensors are high efficiency with a fill-factor of 48 % and high time resolution (< 500 ps time stamping resolution) to record luminescent kinetics down to the nanosecond regime[12,13]. By using the additional information about the temporal evolution we can exploit the different time profiles of background fluorescence, fibre Raman scattering and the Raman from the end of fibre to separate the wanted Raman signal from unwanted background[14–16]. This is done through post-processing time-gating. The technique is currently only limited by photon statistic constraints known as counting loss and pile-up, and inherent limitations on the performance of the SPADs; detector dead-time, dark count rate, varying photon detection probabilities, crosstalk and afterpulsing[10(chap6.2, 7.8, 7.9)]. Others have presented time domain gating techniques such as streak cameras, electronically time-gated CCDs[16] or CMOS detectors[13,17] and optical driven Kerr gates[18]. While the latter achieves a time resolution of picoseconds, the setup is costly and measurement times lengthy – on the order of minutes.

The system is exemplified for pH sensing with 4-mercaptobenzoic acid (MBA) in this paper. Gold nanoshells were functionalised with MBA and then deposited on the distal end of the delivery fibre. These nanosensors have been designed for localized measurements of pH in vivo as they can be used in the near-infrared spectral region, avoiding distortion from excessive autofluorescence from tissue and blood. They are also robust and exhibit a continuous signal over a wide range of pH[19]. The SERS effect enhances the Raman signal and allows low excitation power (< 1 mW) and short exposure times of 10 s with a measurement precision of ± 0.07 pH units is thus achieved. The enhanced signal to background achieved in a time resolved modality is also used to investigate the observation of weak intrinsic Raman signals.

2. MATERIALS AND METHODS

2.1 Experimental Setup

A schematic of the time-resolved spectrometer is shown in Fig. 1.

The whole system is comprised of four parts: a pulsed excitation source, an optical coupling and collection system, a spectrometer and an in-house made CMOS SPAD line sensor. The fibre-coupled design is versatile and flexible for a broad range of applications, a fluorescence spectrometer version of this setup is presented elsewhere[11], and with the potential to be compact and mobile, suitable for *in situ* applications. The excitation source was a 785 nm pulsed laser (LDH-D-F-N-780 and PDL 800-D, PicoQuant, spectral FWHM < 0.35 nm) using the near-infrared window for biological tissue to minimise tissue fluorescence background. In TCSPC methodology the repetition rate of the laser determines the duration of the measurement window. To gather all information within one measurement window, it must be ensured that a full measurement of light transiting the length of the fibre and being backscattered to the detector is completed before the next laser pulse. For a 2.7m fibre used in these experiments, this is achieved with a repetition rate of 20 MHz. The optical coupling and collection system ensures efficient coupling into the delivery fibre and the spectrometer by using a 1:1 imaging system and a fluorescence filter set consisting of an excitation filter, a dichroic

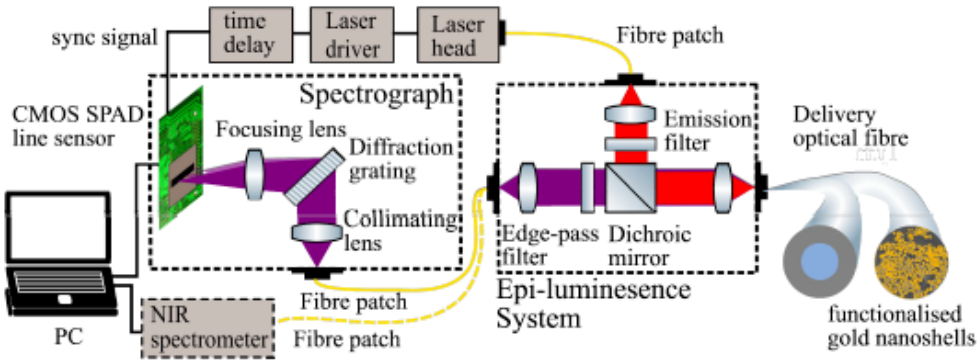

Figure 1: A schematic of the time-resolved spectrometer consisting of a pulsed laser source, an optical coupling and collection system, a transmission spectrograph and a CMOS SPAD line sensor. The delivery optical fibre is a 2.7 m standard step-index single core fibre (FG050LGA, Thorlabs). For the pH sensing, functionalised gold nanoshells are deposit onto the distal end of the fibre.

beam splitter and an emission filter. The spectrometer determines the spectral resolution which is limited by the entrance slit, a multimode fibre with a core diameter of 50 um, the transmission grating (1624 grooves / mm, Wasatch) density the lens combination, a collimation lens (f = 50 mm) and a focusing lens (f = 30 mm, both Achromat Doublets, Thorlabs). The resulting spectral resolution is 1.6 nm or 25 cm^{-1}. A throughput of 78 % at the centre wavelength was measured with a photodiode (S120C Thorlabs). The in-house made CMOS SPAD sensor consists of 256 pixels in a single line manufactured with 130 nm CMOS technology. The whole electronics needed for TCSPC is integrated on a printed circuit board (PCB) exploiting a robust and compact 'system on a chip' design. The sensor timestamps the single photon events internally and simultaneously for all pixels. The average power was reduced with neutral density filters to 0.8 mW which is safe for *in vivo* measurement and ensures single photon regime at a detector count rate of < 1 % of the laser excitation rate and < 50 % of the detector readout frame rate to avoid pile-up distortions. While a high spectral resolution is important to resolve the fine Raman peaks, the temporal resolution determines the capability of separating the Raman signal from the unwanted background signal from the fibre and the environmental fluorescence. The temporal resolution of this system is determined by the time-to-digital converter (TDC) which is 423 ± 3 ps, the full width half maximum (FWHM) of the SPAD which is 0.8 ns and the FWHM of the laser source. When operated at maximum power, the laser has a short leading pulse with a FWHM of 30 ps as stated by the manufacturer, however it exhibits a long tail with a FWHM of 1.5 ns containing ¾ of the power. This greatly limits the temporal resolution and influences the window width in the data analysis.

2.2 Data Analysis

TCSPC is considered a slow method as only one photon per integration time is counted, and as the accuracy of the pH sensing is increasing with the number of counted photons, the number of cycles or measurement time to gather the necessary statistics can be long. In single photon counting (SPC) mode every photon is registered during the integration time, only limited by the dead time of the detector, however the timing information is not available. A combination of TCSPC and SPC is the gating of the signal where a narrow time windows is provided so that the signal of interest, in our case the Raman at the end of the fibre tip, is selected against others. Time-gating can be done either on-chip where the electronics or the SPADs itself are disabled during certain times or during post-processing when the time-resolved data are sliced into certain time windows. In photon starving regimes (approximately 1 photon per laser cycles), which are likely in *in vivo* measurements, there is no advantages of SPC mode over TCSPC mode in terms of measurement time, while TCSPC modality acquires more information.

A single measurement yields a 3-dimensional data cube consisting of the spectral axis, the temporal axis and intensity data in terms of number of counts per pixel and per time bin. For gathering the spectral information, each pixel is correlated to a certain wavelength range. The temporal information is gained by measuring the arrival time of the photons and histogramming them for each pixel with the on-chip TCSPC functionality of the sensor. The full measurement with SERS at the fibre tip can be seen in Figure 2 a). The full measurement is then sectioned into certain time windows depending on the information they contain. The data analysis consists of three steps: i) "Noisy pixels" are

identified and the data removed from the measurement. These pixels are electronically closer to their avalanche condition and hence exhibit a higher dark count (DC) rate. There is a balance to maintain as every pixel for which data is removed worsens the spectral resolution which is critical with the fine Raman peaks. We determine the average DC level from the 'DC' time window, indicated in Figure 2 a), as a threshold and remove pixels which DC rate is 2 times above the average. ii) The 'fibre' window contains solely the information from the backscattered fibre Raman which can be used to determine the spectral shape of the fibre Raman background. This, with a scaling factor, is subtracted from the remaining fibre Raman signal derived from the 'fibre + SERS' time window and thus allows the background free recovering of the MBA Raman spectra. The scaling factor accounts for the forward Raman scattering fibre background reflected on the several surfaces at the fibre tip. Knowing the backscattering fibre Raman spectral shape from every point along the fibre can be used for distributed temperature sensing[20] or checking the integrity of the fibre if not accessible otherwise.

3. RESULTS AND DISCUSSIONS

3.1 Molecular reporter based on surface enhanced Raman scattering (SERS)

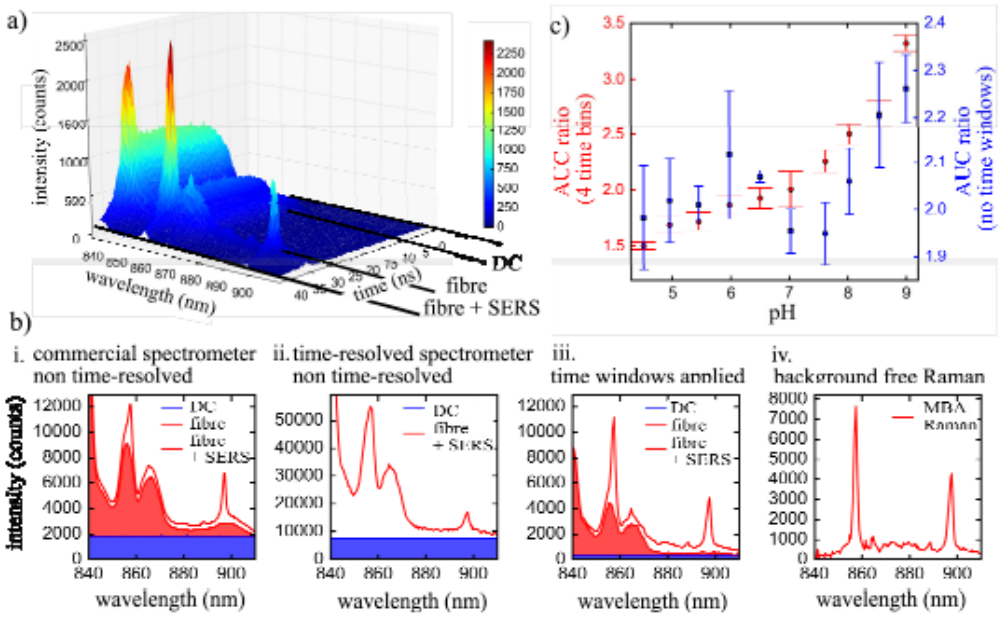

Figure 2. a) 3-dimensional representative of a 2.7 m multimode optical fibre with functionalised gold nanoshells at the fibre tip. Noisy pixels are removed and dark counts are subtracted. The time window used in the further analysis are indicated. (b) from left to right: i) Non time-resolved measurement with a commercial spectrometer (QEPro, Ocean Optics). ii) Non time-resolved measurement with the time-resolved spectrometer. iii) Spectra originate when the time windows indicated in (a) are applied. Time window width is 5 time bins or 2.1 ns. iv.) A recovered spectrum from the MBA molecule. Each measurement was obtained using an average excitation power of 0.8 mW and 20 MHz pulse repetition rate and an integration time of 10 s. (c) pH sensing using the variation of area under the curve (AUC) ratio, the error bars represent the standard deviation of the mean over 3 replicate measurements.

Figure 2 b) i. and ii. shows that the time-resolved spectrometer arrives at visually similar spectra when compared to a commercial spectrometer. However, it also offers a higher efficiency but a lower spectral resolution which leads to a broadening and a lower peak visibility for the SERS features at ~860 nm and ~900 nm. At the same time, the ratio of DC to signal is comparable between both spectrometers. Through post-processing time-gating, the detector dark counts and the unwanted fibre Raman can be significantly suppressed and the visibility of the SERS Raman signal can be significantly increased, as shown in Figure 2 b) iii. with a temporal window of 5 time bins or 2.1 ns, the S/B improves by 4× for a dark count dominated background, around the 857 nm peak, and by 19× around the 897 nm peak when

comparing the time-gated results with the measurements from a commercial spectrometer. When applying the time windows to the data, the background photon shot noise is reduced by a factor equal to the square root of the number of which the time bins are reduced from the full time-resolved measurement. The background free MBA Raman spectra (Figure 2 b) iv. can be used for pH sensing by using the area under the curve (AUC) ratio of the two pH sensitive spectral features of MBA around 880 nm and 906 nm. The results shown in Figure 2 c) are for a 10 s measurement time and show that the sensitivity can be greatly increased through applying the time windows. The repeatability of the system was measured through 50 consecutive measurements of pH 6 and pH 8 to be 0.14 and 0.19, respectively. The sensitivity and repeatability can be further increased through a longer integration time. Suppression of environmental fluorescence with this methodology is show elsewhere[21]. The limitations of this analysis are the IRF function of the laser and the temporal stability of the CMOS SPAD line sensor. As mentioned above the time profile of the laser is ~2 ns which was shown to be the best time window width size for our analysis. If the pulse width of the laser and the IRF of the SPADs, which have been shown to be 0.8 ns[13] were shorter then shorter time window width is achievable and favorable in terms of distinguishing Raman and fluorescence background. In terms of accuracy, the limits of the line sensor were reached and improvements have to include further detector calibrations such as photon-detection variations and reduction of the dark counts and shot noise through cooling and active temperature stabilization. The time-gating method in this paper is achieved by recording a whole TCSPC measurement and applying time windows to the data during post-processing. Electronic time-gating introduces additional jitter to the measurement through the enabling and disabling of the detector but potentially decreases the measurement time.

3.2 Intrinsic Raman

The surface-enhancing effect of the gold nanoshells enables strong and easily detectable MBA Raman signal, however, label-free sensing would rely on the intrinsic Raman. The near-infrared window for biological tissue exhibits low tissue Raman, and would be useful for deep tissue Raman which requires higher excitation powers than we can achieve with

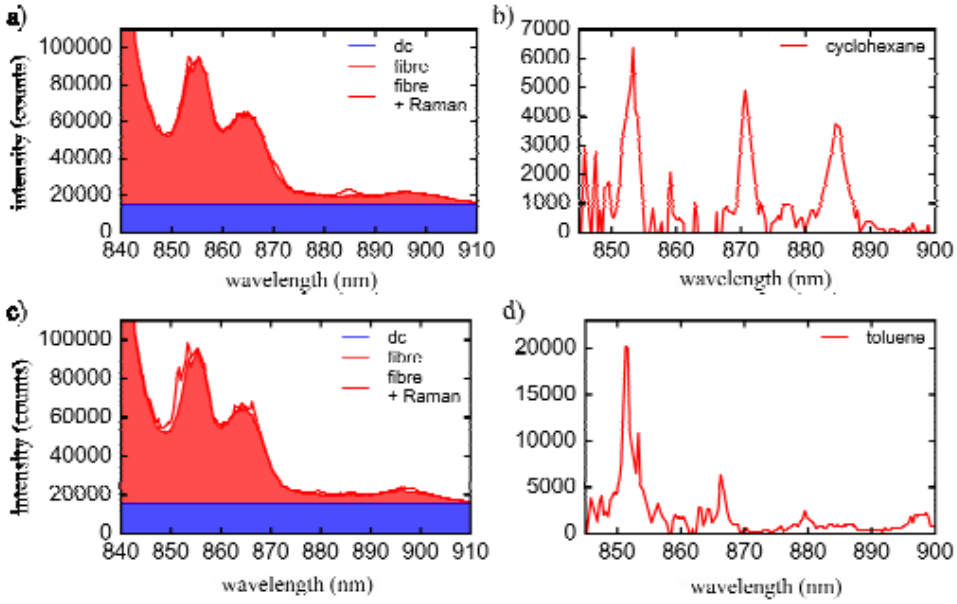

Figure 3. a) Time resolved measurement of Raman scattering from cyclohexane through a 2.7m optical fibre. The time windows are applied as shown in Fig. 2 with a time window width of 6 time bins or 2.5 ns. b) Background free Raman spectra from cyclohexane c) Time resolved measurement of Raman scattering from toluene through a 2.7m optical fibre. The time window width is 6 time bins or 2.5 ns. (d) Background free Raman spectra from toluene. The data analysis followed the same methodology as presented in Figure 2 b). Each measurement was obtained using an average excitation power of 1.2 mW and 20 MHz pulse repetition rate and an integration time of 300 s.

our laser. Instead, we demonstrate the capabilities of our system with standard Raman example chemicals which have a strong intrinsic Raman signal – cyclohexane and toluene. To compensate for the weak signal, the integration time was increased to 300 s, otherwise the experimental conditions are identical to the SERS measurements. A time window width of 6 time bins or 2.5 ns was used which reduces the background count rate and the background noise by a factor of 19.

In Figure 3, the same data analysis method of post-processing time-gating was applied to the raw data and we were able to retrieve the background free Raman spectra of cyclohexane and toluene. In Figure 3 c), the three strong Raman lines of cyclohexane at 854 nm (1027 cm^{-1}), 871 nm (1266 cm^{-1}) and 885 nm (1443 cm^{-1}) are visible in similar peak intensities which is expected from literature[22]. Small variations to the intensities are due to chromatic aberration in the spectrometer's optical system. The smaller peak at 863 nm (1157 cm^{-1}) is hardly visible as it is just above the noise level. In Figure 3 d), the Raman lines of toluene are shown. The two close peaks around 852 nm and 854 nm, 1003 cm^{-1} and 1030 cm^{-1} respectively, are visible as a double peak because the peak separation is the same order as the spectral resolution of the spectrometer and hence not resolvable. The Raman lines of lower intensity at 867 nm (1200 cm^{-1}), 880 nm (1380 cm^{-1}) and 897 nm (1600 cm^{-1}) are visible. We show that we can see the strong peaks of the intrinsic Raman samples. While we are limited by the noise level for observation of the weaker peaks, it is clear there is a great improvement in visibility of intrinsic Raman features through the time resolved methodology As discussed above further improvement in terms of reducing the dark counts, enhancing the temporal stability of the detector and increasing the laser power will help to enhance the sensitivity of the system for intrinsic Raman measurement.

4. CONCLUSION

A time-resolved system and methodology for recovering the spectra of inherently weak Raman signals measured through a single core multimode optical fibre has been demonstrated. We were able to enhance the visibility of the Raman spectra through post-processing time-gating as well as recover them free from background signals such as the fibre Raman and fluorescent environments. As an example, the methodology was applied to standards of intrinsic Raman spectroscopy and to pH-sensing with nanosensors deposited on the distal end of the fibre tip. It has high potential as an ultra-miniaturized and simplified Raman probe for *in vivo* endoscopic sensing of physiological parameters such as pH, oxygen or glucose concentration. While using the SERS effect for the pH nanosensors, measurement times as short as 10 s were used while intrinsic Raman spectra were recorded over a 300 s integration time. Shorter acquisition times are crucial for real-time in situ diagnosis scenarios and the system can be further improved by increasing the collection efficiency through reducing the information the system gathers. Instead of acquiring the full temporal and spectral information, one can bin pixels together and only record the two narrow spectral bands which show the pH sensitive response. However, we believe that time-gating in single photon counting (SPC) modality has no time advantage over TCSPC measurements in low light scenarios such as expected for *in vivo* sensing as measurement rate is limited by photon budget, not detector readout. In applications which are not limited by the photon budget, the on-chip time-gating capabilities of this detector which have been previously demonstrated[13], can be used to further decrease the integration time. To keep the advantage of automatic calibration, multiple time windows would be preferable. The exploitation of this advanced measurement system enables suppression of the unwanted background in the fibre-based Raman probe, facilitating the recovery of the background free spectrum in a single fibre probe.

REFERENCES

[1] "The battle for breath - the impact of lung disease in the UK.", Br. Lung Found., 26 May 2016, <https://www.blf.org.uk/policy/the-battle-for-breath-2016> (16 April 2018).

[2] "The battle for breath - the economic burden of lung disease.", Br. Lung Found., 9 March 2017, <https://www.blf.org.uk/policy/economic-burden> (16 April 2018).

[3] Thiberville, L., Salaün, M., Lachkar, S., Dominique, S., Moreno-Swirc, S., Vever-Bizet, C. and Bourg-Heckly, G., "Human in vivo fluorescence microimaging of the alveolar ducts and sacs during bronchoscopy," Eur. Respir. J. 33(5), 974–985 (2009).

[4] Craven, T. H., Walsh, T. S. and Dhaliwal, K., "Emerging Technology Platforms for Optical Molecular Imaging and Sensing at the Alveolar Level in the critically ill," [Annual Update in Intensive Care and Emergency Medicine 2018], Springer, Cham, 247–262 (2018).

[5] Hanlon, E. B., Manoharan, R., Koo, T. W., Shafer, K. E., Motz, J. T., Fitzmaurice, M., Kramer, J. R., Itzkan, I., Dasari, R. R. and Feld, M. S., "Prospects for in vivo Raman spectroscopy," Phys. Med. Biol. **45**(2), R1-59 (2000).
[6] Wei, D., Chen, S. and Liu, Q., "Review of Fluorescence Suppression Techniques in Raman Spectroscopy," Appl. Spectrosc. Rev. **50**(5), 387–406 (2015).
[7] Utzinger, U. and Richards-Kortum, R. R., "Fiber optic probes for biomedical optical spectroscopy," J. Biomed. Opt. **8**(1), 121–147 (2003).
[8] Stevens, O., Petterson, I. E. I., Day, J. C. C. and Stone, N., "Developing fibre optic Raman probes for applications in clinical spectroscopy," Chem. Soc. Rev. **45**(7), 1919–1934 (2016).
[9] Choudhury, D., Tanner, M. G., McAughtrie, S., Yu, F., Mills, B., Choudhary, T. R., Seth, S., Craven, T. H., Stone, J. M., Mati, I. K., Campbell, C. J., Bradley, M., Williams, C. K. I., Dhaliwal, K., Birks, T. A. and Thomson, R. R., "Endoscopic sensing of alveolar pH," Biomed. Opt. Express **8**(1), 243–259 (2017).
[10] Becker, W., [Advanced Time-Correlated Single Photon Counting Techniques], Springer Berlin Heidelberg, Berlin, Heidelberg (2005).
[11] Ehrlich, K., Kufcsák, A., Krstajić, N., Henderson, R. K., Thomson, R. R. and Tanner, M. G., "Fibre optic time-resolved spectroscopy using CMOS-SPAD arrays," Proc. SPIE **10058**, 100580H (2017).
[12] Krstajić, N., Levitt, J., Poland, S., Ameer-Beg, S. and Henderson, R., "256 × 2 SPAD line sensor for time resolved fluorescence spectroscopy," Opt. Express **23**(5), 5653–5669 (2015).
[13] Kufcsák, A., Erdogan, A., Walker, R., Ehrlich, K., Tanner, M., Megia-Fernandez, A., Scholefield, E., Emanuel, P., Dhaliwal, K., Bradley, M., Henderson, R. K. and Krstajić, N., "Time-resolved spectroscopy at 19,000 lines per second using a CMOS SPAD line array enables advanced biophotonics applications," Opt. Express **25**(10), 11103–11123 (2017).
[14] Rojalin, T., Kurki, L., Laaksonen, T., Viitala, T., Kostamovaara, J., Gordon, K. C., Galvis, L., Wachsmann-Hogiu, S., Strachan, C. J. and Yliperttula, M., "Fluorescence-suppressed time-resolved Raman spectroscopy of pharmaceuticals using complementary metal-oxide semiconductor (CMOS) single-photon avalanche diode (SPAD) detector," Anal. Bioanal. Chem. **408**(3), 761–774 (2016).
[15] Kostamovaara, J., Tenhunen, J., Kögler, M., Nissinen, I., Nissinen, J. and Keränen, P., "Fluorescence suppression in Raman spectroscopy using a time-gated CMOS SPAD," Opt. Express **21**(25), 31632–31645 (2013).
[16] Nissinen, I., Nissinen, J., Keränen, P., Länsman, A. K., Holma, J. and Kostamovaara, J., "A Multitime-Gated SPAD Line Detector for Pulsed Raman Spectroscopy," IEEE Sens. J. **15**(3), 1358–1365 (2015).
[17] Erdogan, A. T., Walker, R., Finlayson, N., Krstajic, N., Williams, G. O. S. and Henderson, R. K., "A 16.5 giga events/s 1024 x 8 SPAD line sensor with per-pixel zoomable 50ps-6.4ns/bin histogramming TDC," 2017 Symp. VLSI Circuits, C292–C293 (2017).
[18] Matousek, P., Towrie, M., Ma, C., Kwok, W. M., Phillips, D., Toner, W. T. and Parker, A. W., "Fluorescence suppression in resonance Raman spectroscopy using a high-performance picosecond Kerr gate," J. Raman Spectrosc. **32**(12), 983–988 (2001).
[19] Bishnoi, S. W., Rozell, C. J., Levin, C. S., Gheith, M. K., Johnson, B. R., Johnson, D. H. and Halas, N. J., "All-optical nanoscale pH meter," Nano Lett. **6**(8), 1687–1692 (2006).
[20] Dyer, S. D., Tanner, M. G., Baek, B., Hadfield, R. H. and Nam, S. W., "Analysis of a distributed fiber-optic temperature sensor using single-photon detectors," Opt. Express **20**(4), 3456 (2012).
[21] Ehrlich, K., Kufcsák, A., McAughtrie, S., Fleming, H., Krstajic, N., Campbell, C. J., Henderson, R. K., Dhaliwal, K., Thomson, R. R. and Tanner, M. G., "pH sensing through a single optical fibre using SERS and CMOS SPAD line arrays," Opt. Express **25**(25), 30976–30986 (2017).
[22] "NIST Chemistry WebBook.", <https://webbook.nist.gov/chemistry/> (17 April 2018).

Analyst

COMMUNICATION

View Article Online
View Journal

Cite this: DOI: 10.1039/c8an01322e

Received 16th July 2018,
Accepted 29th September 2018

DOI: 10.1039/c8an01322e

rsc.li/analyst

Dual purpose fibre – SERS pH sensing and bacterial analysis†

Holly Fleming,[a,b] Sarah McAughtrie,[a,b] Bethany Mills,[b] Michael G. Tanner,[b,c] Angus Marks[a] and Colin J. Campbell *[a]

The exploitation of fibre based Raman probes has been challenged by often complicated fabrication procedures and difficulties in reproducibility. Here, we have demonstrated a simple and cost-effective approach for sensing pH through an optical fibre, by employing a wax patterned filter paper-based substrate for surface enhanced Raman spectroscopy (SERS). Through this method, high reproducibility between fibres was achieved. In addition to sensing pH, it was possible to extract fluid samples containing *P. aeruginosa* for further analysis. This dual purpose fibre is bronchoscope deployable, and is able to gather information about both the host and pathogen, which may lead to an improved treatment plan in future *in vivo* applications.

Introduction

With the rising global challenge of antimicrobial resistance, there is an urgent need to reduce unnecessary antimicrobial prescriptions.[1] Ventilator-associated pneumonia (VAP) is the most common infection among the critically unwell in intensive care units (ICUs), with *Pseudomonas aeruginosa* behind many of these infections.[2]

Studies have shown that using the standard methods to identify the infectious agents, often by interpreting non-specific clinical or radiological features combined with culture techniques from sputum samples, was not adequate to diagnose lower tract respiratory infection but required processing of bronchoalveolar lavage fluid (BALF) samples.[3] However, even the use of these samples has a number of limitations. Bacterial cultures typically take up to 3 days for results, but specifically, these samples can suffer from a lack of sensitivity due to aspirated fluid being prone to contamination from the upper respiratory tract. Molecular sequencing methods such as polymerase chain reactions (PCR) can be overly sensitive, potentially leading to overtreatment of patients. Combined with poor sampling techniques, there is a significant impact on the treatment and management of patients.[4–7]

The correct identification of pathogens causing respiratory infections and the monitoring of their antimicrobial sensitivity is of great importance. In addition to identification, knowing the physiological environment of the site of interest can also hold great value. pH is tightly regulated within cells and their microenvironments, with any deviations from the homeostasis indicating disease processes. Within the lung, an acidic pH can encourage the growth of bacteria, reduce the efficiency of endogenous cationic antimicrobial peptides and inactivate some antibiotics – all factors that contribute to antimicrobial resistance and worsening patient outcome.[8,9]

The need for bed-side based monitoring has driven research efforts with a focus on robust and rapidly responding optical sensor devices. Fibre-based Raman spectroscopy is becoming a popular method for *in vivo* investigations due to its being a non-destructive and minimally invasive technique. Furthermore, it exhibits high spatial resolution and chemical sensitivity, important factors for *in situ* monitoring. However, as Raman scattering is an inherently weak phenomenon, its use for dynamic physiological sensing can be somewhat limited.

Surface enhanced Raman spectroscopy (SERS), where a reporter molecule is adsorbed on to the surface of a metal nanoparticle (NP), can increase the signal intensity by several orders of magnitude over conventional Raman scattering. SERS has been used in many applications, from intracellular physiological sensing, drug delivery sensing, explosive detection and many more.[10,11]

SERS has been demonstrated through fibre previously, however, it has been challenged by difficulties in reproducibility from fibre to fibre, as well as generating SERS signal inten-

[a]EaStCHEM, School of Chemistry, University of Edinburgh, Edinburgh, EH9 3FJ, UK. E-mail: colin.campbell@ed.ac.uk
[b]Centre for Inflammation Research, Queen's Medical Research Institute, University of Edinburgh, Edinburgh, EH16 4TJ, UK
[c]Scottish Universities Physics Alliance (SUPA), Institute of Photonics and Quantum Science (IPAQS), Heriot-Watt University, Edinburgh EH14 4AS, UK
†Electronic supplementary information (ESI) available. See DOI: 10.1039/c8an01322e

sities great enough to overcome the intrinsic silica fibre background. As a result, much of the focus in this area has been on background suppression through complex fibre designs and correction methods.[12–14]

Paper based substrates for SERS sensing and detection are gaining traction as point-of-care systems due to their low cost and flexible nature.[15–17] One of the difficulties is directing the deposition of NP, due to the inherent wicking ability of filter paper which is both quick and uncontrolled. The use of patterning with a hydrophobic ink can assist with some of these issues, by defining a specified SERS sensing region.[18,19]

Here, we demonstrate a facile and cost-effective SERS substrate capable of ratiometrically measuring pH using SERS, whilst retrieving a biological fluid sample through combining paper and fibre-based systems. The advantages of a wax patterned paper sensing substrate are two-fold, it allows simple controlling of particle deposition and also facilitates an easy way to retrieve biological fluid samples. Our method has been designed to be small enough to be bronchoscope deployable with the ability to reach alveolar regions within the lung, allowing for site specific information to be gathered and so gaining information about both host and pathogen. This approach has also overcome many of the outlined challenges by achieving an easily repeatable fabrication process and generating high signal to noise ratios.

Results and discussion

Paper SERS substrate design

The main goal of this research was to provide a simple SERS substrate to combine with a fibre-based approach to sensing, in particular pH. For this purpose, filter paper was chosen as the preferred substrate due to its wide availability and porous nature.

4-Mercaptobenzoic acid functionalised AuNPs (4-MBA; 150 nm, 3.6×10^8 particles per μL) were pipetted on to filter paper substrates. Repeated depositions of a low volume of AuNPs (2 μL droplets) were applied, to a final volume of 2–8 μL, with drying stages in between, to avoid a loss of AuNPs through soaking and washing through the paper. The size of the spots that contain AuNPs was defined by the volume of the solution, however there is much variance in shape and the spread, or wicking, of the AuNPs within the spots (Fig. 1A, I).

In an effort to overcome the influence of non-uniform capillary wicking, and therefore the low reproducibility of using a filter paper-based SERS substrate, a hydrophobic wax surround was printed onto the filter paper. Solid wax printing is a simple, inexpensive, and quick method, amenable to mass production. Patterning paper with a wax surround allows control of the wicking action of aqueous solutions, confining the dispersion to the hydrophilic areas.[18–20] By limiting the solution containing the AuNPs to a defined area, there is a reduction in variability in AuNP concentration at any point within the hydrophilic area. A substantial difference between applying AuNPs to filter paper with and without a wax barrier

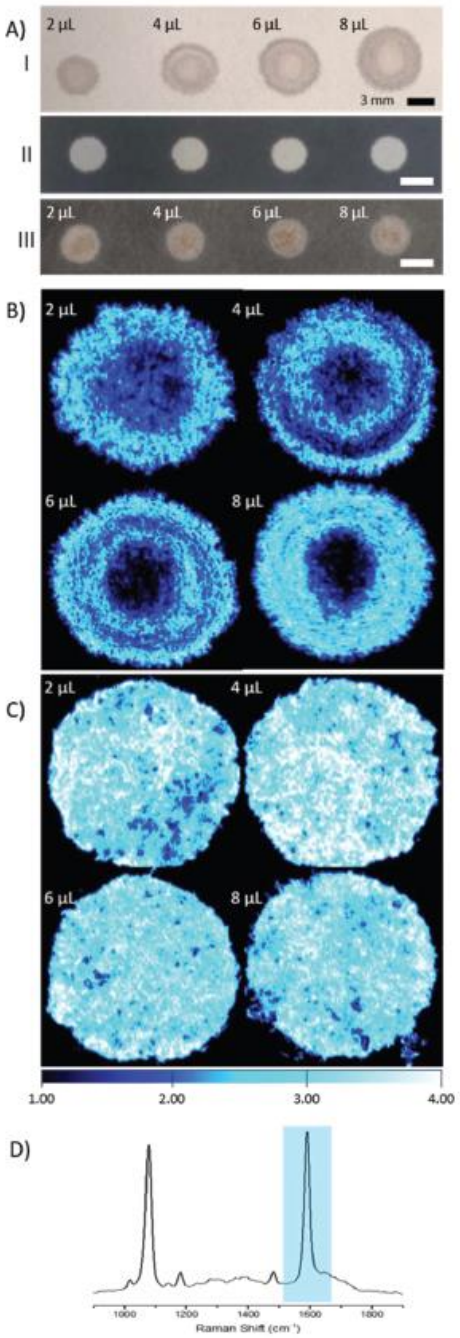

Fig. 1 Differences between filter paper with waxed boundary and no boundary. (A) I: AuNPs deposited onto filter paper without defined wax boundaries, II: images of filter paper with wax boundary, III: AuNPs deposited onto paper with defined wax boundary. All AuNPs depositions using 2 μL drops. (B) and (C) Raman intensity maps of filter paper and patterned filter paper (respectively), deposited with varying volumes of AuNPs. (D) SERS spectra of 4-MBA, with highlighted peak at 1587 cm^{-1} used for intensity comparisons.

can be clearly seen by eye (Fig. 1A). The image shows both an increasing spot size, as well as an uneven spread of AuNPs across the filter paper where a wax barrier was not used. The unevenness is further revealed by SERS mapping (Fig. 1B). The patterned paper allows AuNPs to be deposited on the filter paper in a controlled manner, filling the entire hydrophilic area evenly (Fig. 1C). SEM images from paper substrates with a printed wax barrier show a high density of AuNPs on the cellulose fibres, which may help in the formation of SERS "hot-spots", further enhancing the signal intensity (Fig. S1†).

Fibre sensing

Translation to fibre. While pH sensing using an optical fibre has been demonstrated previously,[12,13] the background Raman scattering from the fibre is strong and can overwhelm the SERS signal from particles deposited on the distal end. Although some of these issues can be alleviated using sophisticated fibre designs, these are often bulky and require multiple fibres or fibres with large bores.[12,21,22] Additionally, many fibres for use with SERS sensing are prepared by dipping the distal end into concentrated nanoparticle solutions, leading to unknown and variable concentrations on the fibre tip.[12,13,21,22] This has an impact on how reproducible, and therefore scalable, the production of the fibre sensors can be. Keeping in mind the future translation of fibre-based sensors into clinic, the ideal instrument would consist of a single fibre being bronchoscope deployable, with simple fabrication steps and minimal packaging requirements.

The fabrication of the packaged ferrule end is a simple process (Fig. 2A), whereby a 2 mm wide strip of the wax printed AuNP paper was placed, facing upwards, on a ring-shaped section of rubber. The ferrule was pushed through the ring with the paper flush across the top surface. A commercially available 200 μm single core (NA 0.39), multi-mode fibre was then threaded through the ferrule until abutted against the paper, and secured in place at the base of the ferrule.

Through combining the fibre with the paper-based SERS substrate, a controlled particle deposition is achieved, provid-

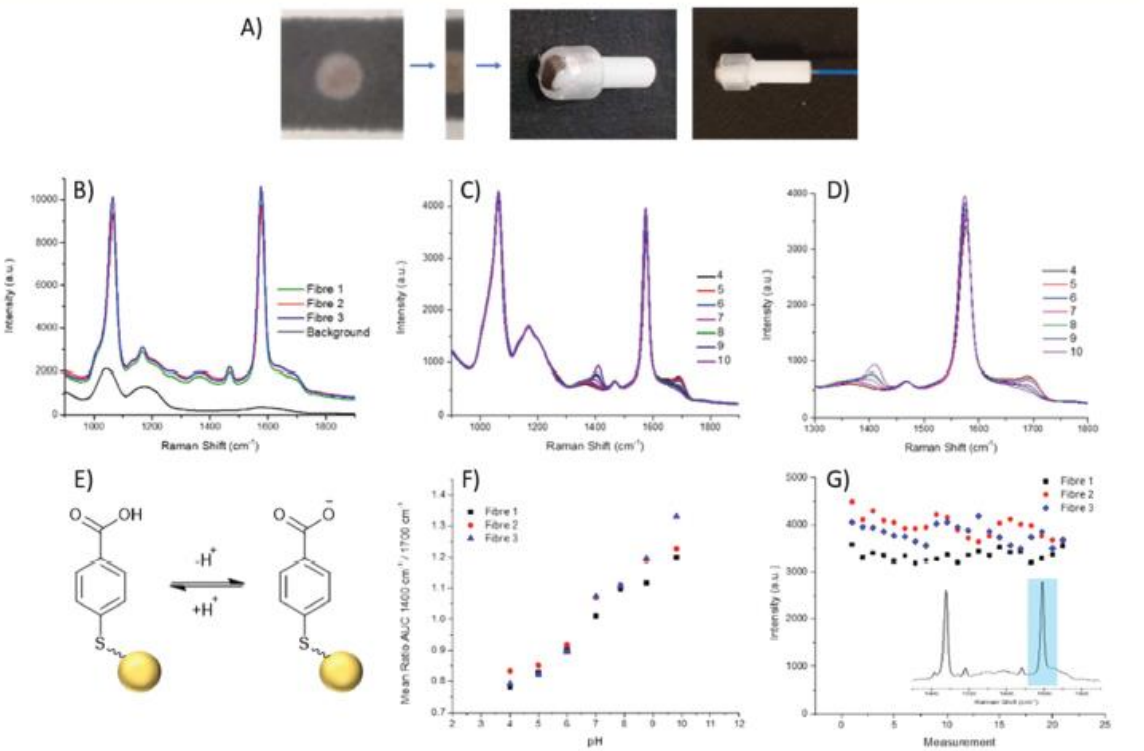

Fig. 2 (A) Process of fabrication to combine paper SERS substrate with 200 μm core optical fibre. Centre strip of AuNP paper cut and secured across a fibre ferrule, fibre threaded through and secured in place. (B) SERS spectra from 3 separate fibres, displaying similar signal intensities. Black spectrum represents intrinsic fibre background (which is easily overcome by SERS signals), 785 nm, 1 mW, 1 s integration time. (C) SERS spectra of 4-MBA, through fibre, over pH 4–10; (D) shows zoomed range of peaks of interest at 1380 cm^{-1} and 1700 cm^{-1} changing over pH 4–10. (E) NP-MBA nanosensors, equilibrium between MBA and its deprotonated form attached to a gold NP (yellow sphere, not to scale. (F) Ratio of Area under Curve (AUC) between 1380 cm^{-1} and 1700 cm^{-1} plotted against pH over 3 fibres. Each measurement was taken using 785 nm, 1 mW, 10 s integration time. (G) Intensity of 1587 cm^{-1} reference peak (inset) obtained during each measurement of the pH calibration plotted in chronological order.

ing confidence that the same signal intensity can be reached in any location where the fibre tip is placed on the AuNP paper. This extends to being able to reliably reproduce a strong signal when moving between fibres. Three separate fibres with packaged distal ends were prepared and their spectra recorded in air. It can be seen that across the three fibres reproducibility of the paper-based system is demonstrated by strong signals of similar intensities (Fig. 2B). Moreover, the strong signal intensity generated by the paper-based SERS sensor easily overcomes the intrinsic fibre background using relatively low laser power and integration time (1 mW and 1 s respectively). Importantly, the fibre background does not impose significantly on the pH sensitive peaks at 1380 cm^{-1} and 1700 cm^{-1}.

pH sensing. The reporter molecule, 4-MBA, has long been known as sensitive to environmental pH variations, and has been previously demonstrated as a suitable choice for biologically and clinically relevant pH sensing.[11,12,23,24] The peaks observed at 1380 cm^{-1} and 1700 cm^{-1} are spectral features most dependent on pH. Under basic conditions (pH 9 and above), 4-MBA is known to be in the anionic form, affording a strong response in the 1380 cm^{-1} peak. Conversely, under acidic conditions (pH 5 and below), 4-MBA is mostly in the neutral form, generating a clear response in the peak found at 1700 cm^{-1}.

Aqueous pH buffers were prepared from pH 4–10 and verified with an electrochemical pH meter (Mettler-Toledo). The packaged distal end of the fibre was submerged in buffer and the spectrum recorded after 10 s. Between readings the AuNP-paper substrate was rinsed in dH_2O and blotted dry. Each fibre had three replicate calibrations where pHs were recorded in a random order. Three fibres in total were measured. The spectra were analysed by first normalising the spectra to the magnitude of a reference peak (1070 cm^{-1}), followed by evaluating the area under the curve (AUC) within a ±25 cm^{-1} window of the peaks at 1380 cm^{-1} and 1700 cm^{-1}. Plotting pH against the AUC ratio, all fibres demonstrated consistent variation within the physiological range (Fig. 2F), again indicating the suitability of the paper SERS substrate for fibre sensing in future *in vivo* applications.

The loss of nanoparticles over time from the distal end of the fibre would be problematic, not only due to loss of signal, but also because loss of AuNPs is undesirable for use in *in vivo* applications. With the fibres which have been dip-coated with nanoparticles, typically, a porous sol–gel layer is used to protect the distal end. However, this coating can also suffer from variations in both coating depth and the porosity of the sol–gel layer, which may affect the speed at which measurements can be acquired. The paper SERS substrate showed no significant signal loss from over the course of the pH measurements (approximately 60 min per fibre). The intensity of the 1587 cm^{-1} peak was plotted over time, with the slight oscillations being attributed to the drying and wetting of the SERS samples. The average intensities between the first and last sets of pH measurements differ by less than 250 counts, less than 10% of overall signal intensity (Fig. 2G).

Extraction and culture of *P. aeruginosa*

There has been a considerable increase in the number of infections due to antimicrobial resistant bacteria with lower respiratory tract infections responsible for the second highest burden of disease globally.[25–27] Within ICUs, the development of pneumonia is associated with high mortality rates.[28] The investigation of respiratory disease can involve biopsies, an invasive procedure, and the collection of BALF, which can become contaminated by bacteria found in the upper respiratory tract. The ability to sample fluid at specific sites can alleviate issues related to contamination. This fibre has been designed keeping in mind that it should be deployable through a conventional bronchoscope. In this way, it can be extended and retracted at specific region of interest, therefore minimising the contact between the distal end of the probe and upper respiratory tract.

The porous nature of the filter paper not only provides a suitable substrate for the deposition of nanoparticles but also lends itself to retrieving a sample of fluid. We demonstrate that the filter paper is capable of sampling liquid containing bacteria which can then be cultured and counted. A clinical isolate of *P. aeruginosa 3284* was cultured and prepared for this study.

Sample retrieval efficiency. To evaluate whether samples containing bacteria could be retrieved using this method, and to investigate the limit of detection, 10-fold serial dilutions of *PA3284* ranging from 6×10^8–6×10^0 CFUs (colony forming units) per mL were prepared. The ferrule tip containing the AuNPs soaked paper substrate was dipped in to the bacterial containing solutions and gently pressed into lysogeny broth (LB) agar plates, with three presses per dip. This process was repeated a total of three times per dilution. After an overnight incubation period (37 °C, 5% CO_2), the colonies were counted and compared to the control (consisting of 3x 20 μL droplets of each dilution) (Fig. 3). We observed a similar number of colonies between the paper and standard methods, with a LOD of 60 CFUs per mL in both the paper-based method and the Miles and Misra method, efficiently detecting below the clinical cut off (above 10^4 CFUs per mL to be considered pathogenic).[4,29]

Direct imaging. We were able to further extract bacteria from the paper after pressing into agar by placing the paper strip in PBS (500 μL) and lightly vortexing. Using an in-house ubiquicidin based bacterial stain (5 μM),[30] it was possible to image the live bacteria shortly after retrieval, without the need for a washing step, by confocal laser scanning microscopy (CLSM; Fig. 3B). Using bacteria specific probes enables the *in situ* optical detection of live bacteria in human alveolar lung tissue.[30–32]

In addition, we investigated imaging bacteria directly on the paper itself (Fig. 4). Due to the autofluorescence of the paper (Fig. S2†), a far-red dye was used. The bacteria were labelled with a Syto60 (5 μM), a fluorescent nuclear stain, before introducing the AuNP-paper strips into the solution containing 6×10^5 CFUs per mL. While this strategy sup-

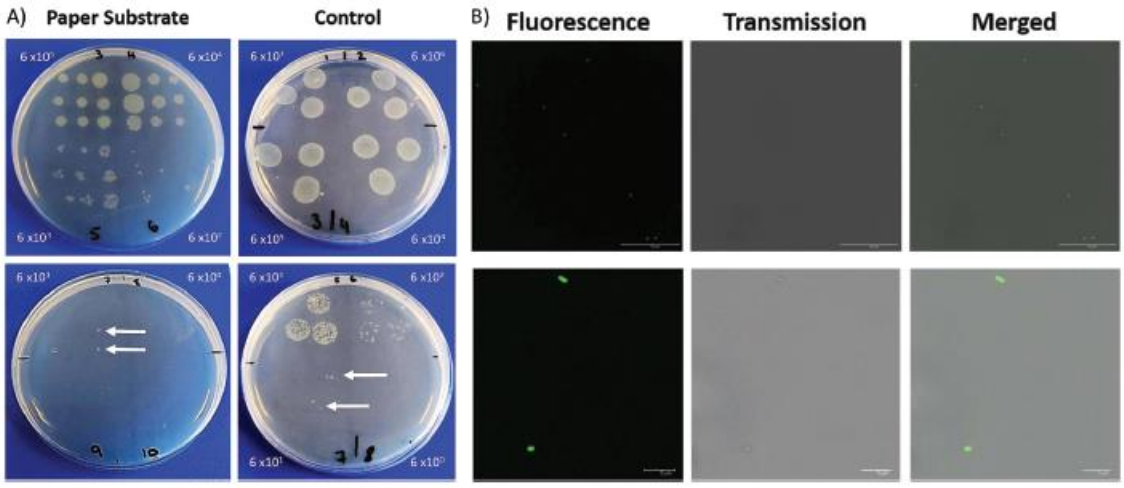

Fig. 3 (A) *P. aeruginosa* colonies on LB agar. Packaged fibre ferrule dipped into solutions containing ten-fold serial dilutions of bacteria and pressed into plate. Similarly, for the control plates, 3 × 20 μL droplets pipetted on to the plates. CFUs grown from a concentration above 6×10^0 in both the paper ferrule and control samples. White arrows indicate colonies formed at a concentration of 6×10^1. Both conditions incubated overnight at 37 °C, 5% CO_2. Dilutions of *P.* aeruginosa were between, paper substrate: 6×10^5–6×10^0 CFU mL^{-1}; control: 6×10^7–6×10^0 CFU mL^{-1}. (B) Fluorescence images from extracted *P. aeruginosa* in PBS. Ferrule pressed into agar, followed by submerging in PBS, stained with UBI-based dye (5 μM). 6×10^2 CFU mL^{-1} concentration used. Top panel, wide field view, bottom panel, zoom in of *P. aeruginosa*.

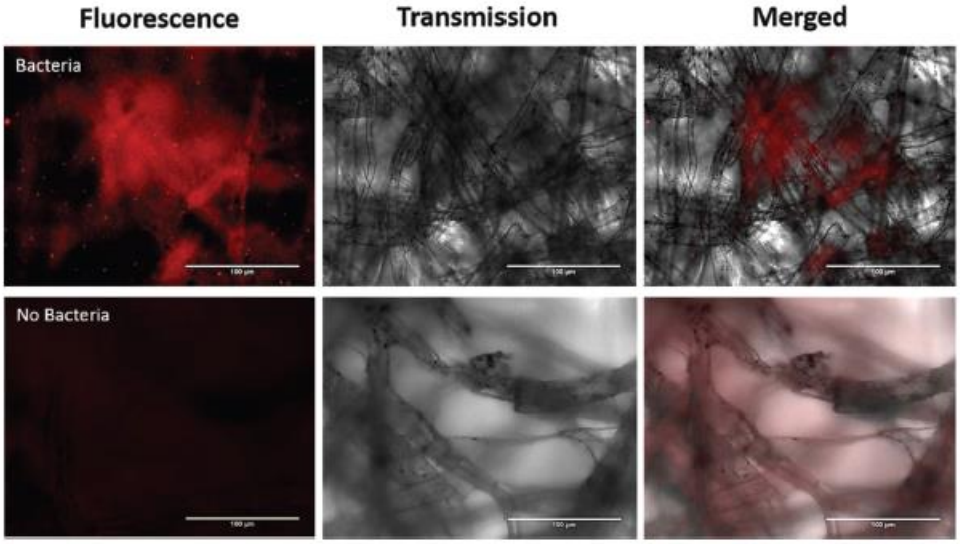

Fig. 4 Fluorescence images showing bacteria on AuNP-paper substrates. Bacteria were treated with Syto60 (5 μM), the top row consists of AuNP-paper containing bacteria, merged, transmission, and fluorescence images. The bottom row corresponds to AuNP-paper without bacteria.

pressed much of the autofluorescence seen in the green channel, there is still some homogeneous signal observed in the Cy5 fluorescence channel. However, despite the background signal, the labelled bacteria can clearly be detected by widefield imaging, indicating that augmenting collected samples with an appropriate far-red bacteria-specific stain could enable *in vivo* bacterial detection on fibre without any need for a processing step. This could pave the way for simultaneous measurements for bacteria and pH through a single fibre.

Experimental section

Materials and reagents

Gold nanoparticles in citrate buffer (AuNPs, 150 nm, put concentration), poly-L-lysine (30 000–70 000 MW), 4-mercaptobenzoic acid (4-MBA) were all purchased from Sigma-Aldrich. Filter paper (Whatman, grade 114) was purchased from Scientific Laboratory Supplies Ltd. Lysogeny Broth was purchased from Thermofisher. Both the optical fibre (200 μm core diameter, NA 0.39) and fibre ferrules were purchased from Thorlabs.

Instrumentation

Solid wax printing was carried out using a Xerox ColourQube8580.

SERS maps were collected on a Renishaw In Via system, using a 785 nm laser, 5× objective, at ~1.5 mW laser power with a 1.4 s integration time.

The fibre-based SERS spectra were collected using a home built optical set up specifically for optical fibres.[12] A 785 nm laser line (Thorlabs) was used as the excitation source, coupled to an OceanOpticsPro spectrometer. The output of the laser power was set as 1 mW, and an integration time of 10 s was used.

Images of bacteria extracted from paper fluorescent were taken by confocal laser scanning microscopy (Leica SP8, 488 nm excitation, 63× oil immersion). Images were brightness and contrast enhanced with proprietary software. Bacteria imaged directly on waxed AuNP paper were taken using an EVOS® microscope with GFP and Cy5 light cubes, images were brightness and contrast enhanced using ImageJ software.

Methods

Preparation of functionalised nanoparticles. Gold nanoparticles (5 × 1 mL aliquots, 3.6×10^9 particles per mL, ~150 nm) were prepared for functionalisation by centrifuged at 5500 rpm for 10 min. For functionalising the particles, following centrifugation, the supernatant (900 μL) from each aliquot was removed without disturbing the pellet. The pellet was resuspended in deionised water (800 μL) and 4-MBA (100 μL, 1 mM in EtOH) and left overnight. Unbound 4-MBA was removed *via* washing and centrifugation at 5500 rpm for 10 min. The supernatant (900 μL) was removed without disturbing the pellet, followed by resuspension in dH_2O (900 μL). The samples were vortexed and sonicated to ensure the particles were forced back into suspension. The washing and centrifugation process was repeated a total of 3 times.

The functionalised nanoparticles were then concentrated and combined. The samples were centrifuged at 5500 rpm for 10 min, and the supernatant (950 μL) was removed without disturbing the pellet. The AuNPs were forced back into suspension in the remaining volume of dH_2O (~50 μL) through sonication and vortexing. The 5 aliquots were combined, centrifuged at 5500 rpm for 10 min, and the appropriate amount of supernatant was removed to give a final volume of 50 μL.

Fabrication of paper SERS substrate. Preparation of the filter paper: an array of circular stencils was designed. A Xerox ColourQube8580 was used to print in standard wax based ink on to the surface of the filter paper, leaving 3 mm diameter disks of bare paper. The wax printed paper was placed on a hotplate (150 °C) and compressed with a weight for 60s to ensure that the wax fully penetrated the paper.

For fabrication of the SERS-active substrate, 2 μL droplets of the 4-MBA functionalised AuNPs were pipetted on to the filter paper disk and allowed to dry at room temperature for an hour. A further 6 μL of AuNPs was dropped on to each disk in 2 μL aliquots with drying in between to a total of 8 μL (2.9×10^9 total particles deposited).

Fibre sensing. For preparation of the fibre-based sensor: silica based optical fibres (3 × 1 m length, core diameter of 200 μm, NA 0.39) were used throughout. The filter paper disks containing functionalised AuNPs had a 1 mm strip cut. The "top side" (the side of the filter paper to which AuNPs had been applied) was placed facing upwards on top of a rubber ring. A fibre ferrule was pushed through the ring resulting in the filter paper placed flush on the top of the ferrule. Following the preparation of the packaged ferrule, the fibre tip was threaded through to meet the filter paper and secured in place. A total of 3 fibres were prepared for calibration.

A SERS spectrum was obtained using the packaged distal end of the fibre from 7 separate pH buffers from pH 4–10. SERS spectra were acquired while the fibre tip was fully submerged in each buffer. Each of the 3 fibres were used for 3 replicate measurements between pH 4–10, with the order of the measurements within each replicate being random.

Bacterial culture and extraction of *P. aeruginosa* 3284. An inhouse clinical isolate *Pseudomonas aeruginosa 3284* was used. A single colony was inoculated in Lysogeny Broth (LB; 10 mL) and incubated overnight (37 °C, 250 RPM), followed by a further subculture (100 μL of overnight culture in 10 mL LB) and incubated at the same conditions for 4 hours until mid-log phase growth was reached.

The optical density at 595 nm (OD_{595}) of the resulting culture was measured and adjusted to a value of 1 to give an approximate bacterial concentration of 6×10^8 CFU mL^{-1}. Serial dilutions (6×10^8 to 6×10^0 CFU mL^{-1}) were prepared with sterile PBS.

For each dilution, the packaged ferrule was dipped into the bacteria containing solution and pressed in succession across an LB agar plate. To compare, 3 × 20 μL samples of each dilution was dropped on lysogeny broth (LB) agar plates for CFU analysis. Plates were incubated at 37 °C with 5% CO_2 overnight, with CFUs manually counted.

After the paper ferrule had been pressed into LB agar, it was placed in an Eppendorf containing PBS (0.5 mL) and lightly vortexed. The paper and ferrule were removed and the bacteria containing solution labelled with a ubiquicidin-based probe (5 μM), without a washing step. Immediately following the addition of the label, the solutions were placed in a confocal imaging chamber, pre-coated with poly-D-lysine (0.1 mg mL^{-1}) and imaged by confocal laser scanning microscopy.

For direct imaging of bacteria on the paper, bacteria were first stained with Syto60 (5 μM; Thermofisher), as per manu-

facturer's instructions, and washed twice with PBS by centrifugation at 13 000 rpm for 1 min. The AuNP paper was dipped into the stained bacterial solution containing 6×10^5 CFUs per mL and imaged using widefield microscopy.

Conclusions

In this study, a facile, inexpensive and reproducible paper-based SERS sensor has been integrated with optical fibre technology for use in pH sensing across a physiological relevant range. Using a patterned wax printed stencil to control the wicking boundary of AuNPs, the distribution of particles can be controlled across the paper. In addition, due to the wicking nature of the filter paper, it was possible to extract the bacteria, *P. aeruginosa*, demonstrating the dual-purpose ability of the paper substrate to acquire physiological and pathogenic information.

Conflicts of interest

The authors have no conflicts to declare.

Acknowledgements

This work was supported by the Engineering and Physical Sciences Research Council (EPSRC) and Medical Research Council (MRC) under grant number EP/L016559/1 (OPTIMA), and the School of Chemistry, University of Edinburgh; and the EPSRC Interdisciplinary Research Collaboration (EP/K03197X/1).

References

1 J. O'Neill, *Tackling drug-resistant infections globally: final report and recommendations*, H M Government/Wellcome Trust, 2016.
2 S. Ramírez-Estrada, B. Borgatta and J. Rello, *Infect. Drug Resist.*, 2016, 9, 7–18.
3 R. P. Baughman, D. A. Keeton, C. Perez and R. W. Wilmott, *Am. J. Respir. Crit. Care Med.*, 1997, 156, 286–291.
4 H. Wang, X. Gu, Y. Weng, T. Xu, Z. Fu, W. Peng and W. Yu, *BMC Pulm. Med.*, 2015, 15, 94.
5 J. R. Lentino and D. A. Lucks, *J. Clin. Microbiol.*, 1987, 25, 758–762.
6 K. C. Carroll, *J. Clin. Microbiol.*, 2002, 40, 3115–3120.
7 A. Zumla, J. A. Al-Tawfiq, V. I. Enne, M. Kidd, C. Drosten, J. Breuer, M. A. Muller, D. Hui, M. Maeurer, M. Bates, P. Mwaba, R. Al-Hakeem, G. Gray, P. Gautret, A. A. Al-Rabeeah, Z. A. Memish and V. Gant, *Lancet Infect. Dis.*, 2014, 14, 1123–1135.
8 A. Dalhoff, S. Schubert and U. Ullmann, *Infection*, 2005, 33, 36–43.
9 W. F. Walkenhorst, J. W. Klein, P. Vo and W. C. Wimley, *Antimicrob. Agents Chemother.*, 2013, 57, 3312–3320.
10 A. Jaworska, L. E. Jamieson, K. Malek, C. J. Campbell, J. Choo, S. Chlopicki and M. Baranska, *Analyst*, 2015, 140, 2321–2329.
11 L. E. Jamieson, V. L. Camus, P. O. Bagnaninchi, K. M. Fisher, G. D. Stewart, W. H. Nailon, D. B. McLaren, D. J. Harrison and C. J. Campbell, *Nanoscale*, 2016, 8, 16710–16718.
12 D. Choudhury, M. G. Tanner, S. McAughtrie, F. Yu, B. Mills, T. R. Choudhary, S. Seth, T. H. Craven, J. M. Stone, I. K. Mati, C. J. Campbell, M. Bradley, C. K. I. Williams, K. Dhaliwal, T. A. Birks and R. R. Thomson, *Biomed. Opt. Express*, 2017, 8, 243.
13 K. Ehrlich, A. Kufcsák, S. McAughtrie, H. Fleming, N. Krstajic, C. J. Campbell, R. K. Henderson, K. Dhaliwal, R. R. Thomson and M. G. Tanner, *Opt. Express*, 2017, 25, 30976.
14 J. C. C. Day and N. Stone, *Appl. Spectrosc.*, 2013, 67, 349–354.
15 R. P. Gandhiraman, D. Nordlund, V. Jayan, M. Meyyappan and J. E. Koehne, *ACS Appl. Mater. Interfaces*, 2014, 6, 22751–22760.
16 E. P. Hoppmann, W. W. Yu and I. M. White, *Methods*, 2013, 63, 219–224.
17 C. H. Lee, M. E. Hankus, L. Tian, P. M. Pellegrino and S. Singamaneni, *Anal. Chem.*, 2011, 83, 8953–8958.
18 R. Derda, S. K. Y. Tang, A. Laromaine, B. Mosadegh, E. Hong, M. Mwangi, A. Mammoto, D. E. Ingber and G. M. Whitesides, *PLoS One*, 2011, 6, 5.
19 D. A. Bruzewicz, M. Reches and G. M. Whitesides, *Anal. Chem.*, 2008, 80, 3387–3392.
20 A. W. Martinez, S. T. Phillips, M. J. Butte and G. M. Whitesides, *Angew. Chem., Int. Ed.*, 2007, 46, 1318–1320.
21 P. R. Stoddart and D. J. White, *Anal. Bioanal. Chem.*, 2009, 394, 1761–1774.
22 G. F. S. Andrade, M. Fan and A. G. Brolo, *Biosens. Bioelectron.*, 2010, 25, 2270–2275.
23 S. W. Bishnoi, C. J. Rozell, C. S. Levin, M. K. Gheith, B. R. Johnson, D. H. Johnson and N. J. Halas, *Nano Lett.*, 2006, 6, 1687–1692.
24 F. Wang, R. G. Widejko, Z. Yang, K. T. Nguyen, H. Chen, L. P. Fernando, K. A. Christensen and J. N. Anker, *Anal. Chem.*, 2012, 84, 8013–8019.
25 R. P. Dickson, J. R. Erb-Downward and G. B. Huffnagle, *Lancet Respir. Med.*, 2014, 2, 238–246.
26 A.-P. Magiorakos, C. Suetens, D. L. Monnet, C. Gagliotti and O. E. Heuer, *Ant. Res. Infect. Control*, 2013, 2, 6.
27 R. Lozano, M. Naghavi, K. Foreman, S. Lim, *et al.*, *Lancet*, 2012, 380, 2095–2128.
28 J. Chastre and J.-Y. Fagon, *Am. J. Respir. Crit. Care Med.*, 2002, 165, 867–903.
29 J. B. J. Scholte, H. A. van Dessel, C. F. M. Linssen, D. C. J. J. Bergmans, P. H. M. Savelkoul, P. M. H. J. Roekaerts and W. N. K. A. van Mook, *J. Clin. Microbiol.*, 2014, 52, 3597–3604.

30 A. R. Akram, N. Avlonitis, A. Lilienkampf, A. M. Perez-Lopez, N. McDonald, S. V. Chankeshwara, E. Scholefield, C. Haslett, M. Bradley and K. Dhaliwal, *Chem. Sci.*, 2015, 6, 6971–6979.
31 N. Krstajić, B. Mills, I. Murray, A. Marshall, D. Norberg, T. H. Craven, P. Emanuel, T. R. Choudhary, G. O. S. Williams, E. Scholefield, A. R. Akram, A. Davie, N. Hirani, A. Bruce, A. Moore, M. Bradley and K. Dhaliwal, *J. Biomed. Opt.*, 2018, 23, 076005.
32 B. Mills, A. R. Akram, E. Scholefield, M. Bradley and K. Dhaliwal, *J. Visualized Exp.*, 2017, 129, e56284.